Dendrimer and Cadmium free Quantum Dots Fluorescent Nanocomposites

Bruno José Brandão Campos
Doutoramento em Química
Departamento de Química da Faculdade de Ciências
da Universidade do Porto
2017

Orientador
Joaquim C.G. Esteves da Silva, Professor Catedrático,
Faculdade de Ciências da Universidade do Porto

Coorientador
Manuel Algarra Gonzalez, Investigador,
Faculdade de Ciências da Universidade de Málaga

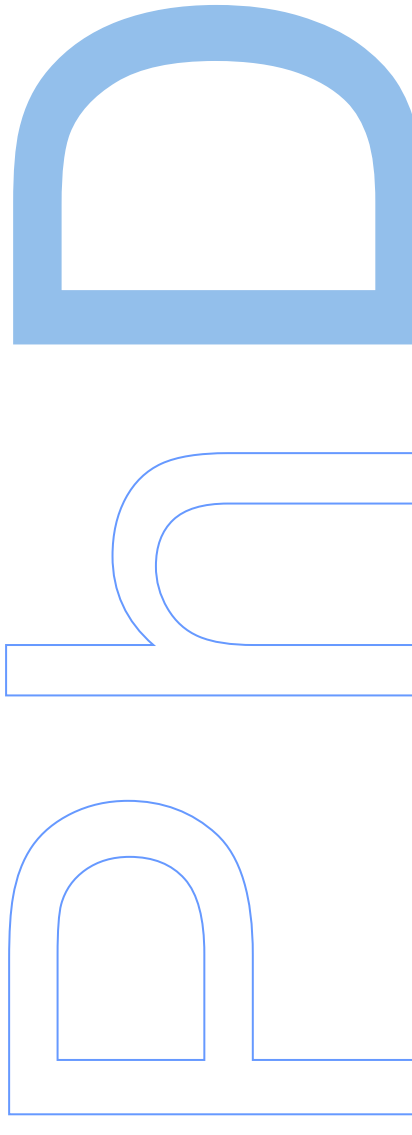

This project was supported by a Ph.D. scholarship with the reference SFRH/BD/84318/2012, co-funded by the European Social Fund (Fundo Social Europeu, FSE), through Programa Operacional Potencial Humano – Quadro de Referência Estratégico Nacional (POPH – QREN), and by national funds from the Ministry of Education and Science through the Portuguese Fundação para a Ciência e a Tecnologia, I.P. (FCT). Also, this work was made in part under project PTDC/QEQ-QFI/0289/2014 and PTDC/QEQ-QAN/5955/2014 and it was supported within Project 3599 – "Promover a Produção Científica e Desenvolvimento Tecnológico e a Constituição de Redes Temáticas (3599-PPCDT) e comparticipado pelo Fundo Comunitário Europeu FEDER". We thank project CTQ2015-68951-C3-3-R (Ministerio de Economía y Competitividad, Spain) and FEDER funds, project P12-RNM-1565 (Excelencia, Junta de Andalucía, Spain). Project CTQ2015-68951-C3-3-R supported by MINECO (Spain) and FEDER funds.

Agradecimentos

Um doutoramento é mais do que um título académico, é uma fase da vida de um estudante que nos permite uma descoberta mais profunda sobre nós mesmos e da importância do nosso papel na sociedade. E apercebi-me que somos uma espécie de "eternos peregrinos do conhecimento". Como em todas as caminhadas existem vários desafios e que desde já quero agradecer a todas as pessoas que me acompanharam nesta viagem e me ajudaram a potenciar as minhas qualidades. Desta forma quero expressar o meu sincero agradecimento:

Ao meu orientador Professor Doutor Joaquim C. G. Esteves da Silva por todo o apoio, conhecimento transmitido e confiança prestada.

Ao meu co-orientador Doutor Manuel Algarra por me acompanhar sempre de uma forma muito próxima e atenta sobre meu trabalho.

À Fundação para a Ciência e Tecnologia (FCT) pelo investimento no meu crescimento científico e académico.

Aos meus pais Manuela Brandão e José Campos por serem desde sempre os meus pilares que tornaram tudo isto possível. E a todos os meus familiares pelo apoio dado com amor.

À minha esposa Jéssica Campos pelos bons conselhos, amor recebido e acima de tudo pelo exemplo de ser humano que me faz acreditar e ver as coisas boas da vida.

Em especial, mais do que agradecer quero dedicar este meu trabalho aos meus avós José Ribeiro de Campos e José Augusto Pereira Brandão por serem os meus impulsionadores e a força motriz para continuar a investigar.

Resumo

Durante o período de trabalho do doutoramento foram sintetizados, caracterizados e aplicados sete nanosensores químicos baseados em QDs de zinco, silício e carbono, dos quais quatro conjugados com dendrímeros e outros três sem dendrímero. A aplicação destes nanosensores passou pela determinação quantitativa de metais pesados a compostos orgânicos, alguns deles com elevado impacto na saúde ambiental (em diferentes tipos de matrizes).

O nanosensor de zinco dopado com manganês foi funcionalizado com o dendrímero PAMAM-OH de terceira geração (ZnS:Mn@PAMAM-$OH_{G=3}$) resultando num nanocompósito fluorescente adequado para determinação seletiva e raciométrica do catião Cd^{2+} em solução aquosa. O ZnS:Mn@PAMAM-$OH_{G=3}$ em termos de propriedades ópticas do nanosensor apresentava um rendimento quântico de 0.15 e duas bandas de emissão a 448 nm e a 595 nm. A resposta do sensor ao aumento da concentração de Cd^{2+}, em diferentes tipos de amostras aquosas, dava-se através do aumento de fluorescência da banda de emissão a 448 nm e diminuição da banda a 595 nm ($I_{448/595}$).

Os seguintes nanosensores sintetizados basearam-se em carbono (CQDs), onde se estudaram alguns dos parâmetros que influenciam a formação de nanopartículas de carbono fluorescentes, entre os quais o processo de carbonização, os agentes desidratantes e os diferentes percursores de carbono.

Um dos primeiros a ser sintetizado foi os CQDs funcionalizados com ácido mercaptosuccínico (MSA), com a lactose em refluxo de ácido sulfúrico concentrado. A funcionalização dos CQDs com MSA (CQDs-MSA) aumentou significativamente tanto o comprimento de onda de emissão como o rendimento quântico, 472 nm e 0.46 respetivamente. Em termos de aplicabilidade, mostrou elevada seletividade na deteção de catiões prata em dissoluções contendo nanopartículas de prata.

Também se estudou o efeito da dopagem nos CQDs através da adição de uma solução aquosa de NH_3 a uma solução de lactose, sem a necessidade de adicionar um ácido, por aquecimento hidrotermal. Os N-CQDs apresentaram um aumento do rendimento quântico (0.11) e uma diminuição do tamanho médio (7.7 nm), relativamente aos CQDs convencionais. O XPS e a espectroscopia RAMAM demonstraram o efeito da dopagem na formação dos CQDs, indicando a presença de

grupos amino e amido na superfície dos N-CQDs. A presença destes grupos permitiu que os N-CQDs se tornassem seletivos na determinação da piridina.

No seguimento destas experiências, realizou-se a funcionalização dos CQDs com a vitamina B_{12}. Este nanocompósito fluorescente apresenta duas bandas de emissão a 417 nm e a 550 nm conferindo a este nanosensor propriedades raciométricas devido ao efeito de transferência de energia de ressonância por fluorescência (FRET) entre os CQDs (doador) e a Vitamina B_{12} (aceitador). Este nanosensor raciométrico demonstrou elevada seletividade na determinação de um pesticida metabolito fenólico do carbofurano, o 3-cetofenolcarbofurano, tanto em solução como em amostras reais de molho de soja.

Após estes trabalhos, procedeu-se a primeira funcionalização de CQDs com dendrímeros. Os CQDs foram sintetizados através do ácido fólico, o percursor de carbono, e o ácido fosfórico. A funcionalização ocorreu com a adição do dendrímero PAMAM-NH_2. Os CQDs funcionalizados com o dendrímero PAMAM-NH_2 levaram a uma diminuição do comprimento de onda de emissão (451 nm) e um aumento do rendimento quântico (0.27). Os ensaios demonstraram que a intensidade de fluorescência dos CQDs@PAMAM-NH_2 na presença do ião cloroplatinato diminuía significativamente e seletivamente, mesmo quando testado em amostras de nanopartículas de platina em solução.

Procedeu-se à segunda funcionalização de CQDs também com o dendrímero PAMAM-NH_2 mas utilizando como percursor de carbono o carvão ativado onde foi submetido a uma exfoliação química com ácidos e oxidantes fortes. Também neste caso observou-se um aumento do rendimento quântico (0.06) e a formação de agregados (65 nm). Os CQDs@PAMAM-NH_2 demonstraram enorme seletividade para um dos constituintes dos explosivos, o 4-cloro-2,6-dinitroanilina. A sua elevada seletividade deve-se à particularidade do nanosensor de carbono responder à presença do analito através da diminuição desproporcional de duas bandas de emissão a 465 nm e 507 nm. O rácio de intensidades de emissão destas duas bandas torna os CQDs@PAMAM-NH_2 um promissor nanosensor raciométrico na deteção seletiva do 4-cloro-2,6-dinitroanilina.

O nanosensor de silício foi igualmente funcionalizado com o dendrímero PAMAM com grupos terminais hidroxilo da quinta geração (SiQDs@PAMAM-$OH_{G=5}$). A síntese baseou-se num processo hidrotermal do APTES e do PAMAM-$OH_{G=5}$, em solução aquosa. Os SiQDs@PAMAM-$OH_{G=5}$ apresentavam um rendimento quântico de

0.15 e uma banda de emissão a 446 nm, demonstrando seletividade para o catião Cr^{6+} em amostras reais colhidas em efluentes de indústrias eletroquímicas.

De forma a avaliar a potencial utilização dos nanosensores de silício em componentes electroquímicos foram imobilizados SiQDs e SiQDs@PAMAM-$OH_{G=5}$ numa membrana de celulose regenerada pelo método "*dip coating"*. A estabilidade termal e a condutividade das membranas foram otimizadas com a imobilização dos SiQDs, não se observando um melhoramento substancial das propriedades físicas com a presença do dendrímero PAMAM-$OH_{G=5}$. Em ambos os nanosensores de silício observou-se que as características optoelectrónicas eram favorecidas em meio seco em vez de um meio aquoso.

Abstract

During the period of the PhD work were synthesized, characterized and applied seven chemical nanosensors based on QDs of zinc, silicon and carbon, of which four were conjugated with dendrimers and three without dendrimer. The application of these nanosensors aimed the quantitative determination of heavy metals to organic compounds, some with high impact on environmental health (in different matrices).

The manganese-doped zinc nanosensor was functionalized with the dendrimer PAMAM-OH of third generation (ZnS:Mn@PAMAM-$OH_{G=3}$) resulting in a fluorescent nanocomposite suitable for the selective and ratiometric determination of Cd^{2+} cation in aqueous solution. The ZnS:Mn@PAMAM-$OH_{G=3}$ nanosensor presents in terms of optical properties a quantum yield of 0.15, and two emission bands at 448 nm and 595 nm. The response of the nanosensor to the increasing concentration of Cd^{2+}, in different types of aqueous samples, was observed by an increasing of the fluorescence emission band at 448 nm and the decreasing at 595 nm ($I_{448/595}$).

The next nanosensors synthesized were based on carbon (CQDs), concomitantly was studied some parameters that influence the formation of fluorescent carbon nanoparticles, including the carbonization process, the dehydrating agents and various carbon precursors.

The firstly CQDs synthesized was functionalized with mercaptosuccinic acid, with the lactose refluxed in concentrated sulfuric acid. The functionalization of the CQDs with MSA (CQDs-MSA) increased significantly the wavelength emission and the quantum yield, 472 nm and 0.46 respectively. Concerning to the application, they showed high selectivity in the sensing of silver cations dissolutions containing silver nanoparticles.

Was also studied the effect of doping on CQDs by the addition of NH3 aqueous solution to a lactose solution, without the need to add an acid, by hydrothermal heating. The N-CQDs showed an increasing in the quantum yield (0.11) and a decreasing in the average size (7.7 nm), comparatively to raw CQDs. The XPS and Raman spectroscopy showed the effect of doping in the CQDs formation, indicating the presence of amino and amido groups on the surface of the N-CQDs. The presence of these groups enabled N-CQDs to be selective in the determination of pyridine.

Following these experiments, the functionalization of CQDs with vitamin B_{12} was done. This fluorescent nanocomposite shows two emission bands at 417 nm and 550 nm

giving to this nanosensor a ratiometric property due to the fluorescence resonance energy transfer (FRET) effect between the CQDs (donor) and Vitamin B_{12} (acceptor). This ratiometric nanosensor demonstrated high selectivity in the determination of a pesticide phenolic metabolite of carbofuran, the carbofuran phenol 3-Keto, both in solution and in real samples of soy sauce.

After this work, was performed the first functionalization of CQDs with dendrimers. The CQDs were synthesized using folic acid, the carbon precursor, and the phosphoric acid. The functionalization occurred with the addition of PAMAM-NH_2 dendrimer. The CDs functionalized with PAMAM-NH_2 dendrimer led to a decrease of the wavelength emission (451 nm) and an increase in the quantum yield (0.27). The tests showed that the fluorescence intensity of CQDs@PAMAM-NH_2 in the presence chloroplatinate ion decreased significantly and selectively, even when tested on samples containing platinum nanoparticles in solution.

Was proceeded the second functionalization of CQDs also with PAMAM-NH_2 dendrimer, using activated carbon as carbon precursor, which was subjected to a chemical exfoliation with strong acids and oxidants. Also in this case it was observed an increase in the quantum yield (0.06) and the formation of aggregates (65 nm). CQDs@ PAMAM-NH_2 showed great selectivity for one of the explosives components, the 4-chloro-2,6-dinitroaniline. The high selectivity of the carbon nanosensor is related to the particular response, in the presence of the analyte, through the unequal decreasing of two emission bands at 465 nm and 507 nm. The emission intensity ratio of these two bands makes CQDs@PAMAM-NH_2 a promising ratiometric nanosensor in the selective detection of 4-chloro-2,6-dinitroaniline.

The silicon nanosensor was also functionalized with a PAMAM dendrimer with hydroxyl end groups of the fifth generation (SiQDs@PAMAM-$OH_{G=5}$). The synthesis is based on a hydrothermal process of the APTES and PAMAM-OH in aqueous solution. The SiQDs@PAMAM-$OH_{G=5}$ had a quantum yield of 0.15 and a band emission at 446 nm, showing selectivity for Cr^{6+} cation in real samples collected in wastewaters of electrochemical industries.

In order to evaluate the potential use of silicon nanosensors for electrochemical devices were immobilized SiQDs and SiQDs@PAMAM-$OH_{G=5}$ in a regenerated cellulose membrane by dip coating. The thermal stability and conductivity of membranes were optimized with the immobilization of SiQDs, was not observed a substantial improvement of the physical properties in the presence of PAMAM-$OH_{G=5}$ dendrimer.

In both silicon nanosensors was observed that the optoelectronic characteristics were favored in a dry medium instead of an aqueous medium.

Table of Contents

List of Abbreviations

AFM	Atomic Force Microscopy
APTES	(3-aminopropyl)triethoxysilane
ATR	Attenuated Total Reflectance
CQDs	Carbon Quantum Dots
DLS	Dynamic Light Scattering
EDS	Energy-Dispersive X-ray Spectroscopy
FTIR	Fourier Transform Infrared Spectroscopy
MCR-ALS	Multivariate Curve Resolution-Alternating Least Squares
MSA	Mercaptosuccinic acid
PAMAM-NH_2	Polyamidoamine dendrimer with amine surface groups
PAMAM-OH	Polyamidoamine dendrimer with hydroxyl surface groups
PARAFAC	Parallel Factor analysis
QDs	Quantum Dots
SEM	Scanning Electron Microscopy
SiQDs	Silicon Quantum Dots
TEM	Transmission Electron Microscopy
UV-VIS	Ultraviolet–Visible spectroscopy
XPS	X-ray Photoelectron Spectroscopy
XRD	X-Ray Diffraction

Preface

The nanochemistry opened a new branch with the discovery of QDs [1]. QDs are nanoparticles of a semiconducting material with 1-12 nm in diameter. Due to the confinement effects, they possess distinctive emitting properties that are being proved as allied tools for labeling biological systems and for the basis of chemical/biochemical sensors [2]. Compared with organic fluorophores, QDs presents considerable advantages as emission tunability, narrow half width wavelength (20-40 nm), broad excitation bands, resistant to photobleaching, blinkness, up and downconversion and improved brightness [3]. Our research group has synthesized several QDs based on cadmium, proving that they are an interesting fluorescent platform for immobilization of molecules, such as dendrimers and cyclodextrins, which conferred sensing properties to different analytes. However, the use of cadmium as sensors opened a new discussion in the sensing field due to the inherent toxicity problems associated to cadmium in the human body, otherwise the demanding of research in nontoxic biocompatible nanoparticles increased [4]. For that the synthesis of QDs focused on low toxic QDs with elements such as zinc, silicon and carbon. They can be functionalized [5] by chemical modification of their surface, resulting a hybrid organic/inorganic nanocomposite. Dendrimers are artificial polymers [6], with star-shaped highly branched macromolecules with a well defined composition and monodispersity which results in multitude of physical properties [7]. Moreover, dendrimers are a particularly interesting class of emerging nano-pharmaceuticals [5, 8]. The conjugation of QDs coated with dendrimers has demonstrated remarkable and attractive optoelectronic characteristics specially suited to analytical [9-14] and bio-analytical [15, 16] applications. Depending of the terminal groups on the edge sites of dendrimers, the QDs-dendrimers nanocomposites could presents an improved biocompatibility and biostablility which renders them important roles in biomedical and bio/chemical sensing [17, 18]. In this context, the conjugation of QDs-dendrimers structures is considered an interesting innovation by providing new fluorescent nanomaterials dendrimer based, with a huge potential in the development of fluorescent probes to act as luminescent markers [19].

References

1. I. Ekimov, A. A. Onushenko, JETP Lett. 34 (1981) 345.
2. P. Ling, Trends in Quantum dots research, Nova Science 2005.
3. H. Mattoussi H, G. Palui, H.B, Adv Drug Deliv Rev 64 (2012) 138.
4. C.B. Murray, C.R. Kagan, M.G. Bawendi, Annu. Rev. Mater. Sci. 30 (2000) 545.
5. J.G. Rouse et al., J. Investigation Derm. 127 (2007) 143.
6. D.A. Tomalia, et al., Polym. J. 17 (1985) 117.
7. U. Boas, P.M. H. Heegaard, Chem. Soc. 33 (2004) 43.
8. F. Sánchez-Sancho, et al. Bioconjugate Chem. 13 (2002) 647.
9. B.B. Campos, M. Algarra, J.C.G. esteves da Silva Analyst 134 (2009) 244
10. B.B. Campos, M. Algarra, J.C.G. esteves da Silva J. Fluoresc. 20 (2010) 143.
11. M. Algarra, B.B. Campos et al., Talanta 83 (2011) 1335.
12. M. Algarra, R. Moreno-Tost et al., Opt. Mat. 33 (2011) 893.
13. M. Algarra, B.B. Campos et al., Talanta 88 (2012) 403.
14. M. Algarra, B.B. Campos et al., Mat Sci Eng. C 32 (2012) 799.
15. D. Gomes, M. Algarra, et al., Talanta 93 (2012) 411.
16. M. Algarra, B.B. Campos, D. Gomes, et al. Talanta 99 (2012) 574.
17. W.E. Bawarski et al. Nanomedicine: Nanotech. Biol Med. 4 (2008) 273.
18. A. Wisher, I. Bronstein, V. Chechik, Chem. Commun. 15 (2008) 1637.
19. X. Michalet, et al. Science 307 (2005) 538.

Goals Proposed

In general, the PhD project was planned to be focused on the synthesis, characterization and application of fluorescent nanoparticles:

I. **Synthesis** of novel fluorescent chemical nanosensors based on QDs cadmium free (ZnS:Mn, Silicon and Carbon dots) functionalized with organic molecules such as Dendrimers, MSA and Vitamin B_{12}. Achieving highly soluble and less toxic systems for analytical purposes.

II. **Characterization** of the synthesized sensors by TEM, SEM, EDS, XPS, AFM, XRD, DLS, FTIR, UV-VIS, Electrochemical, Spectrofluorimetry, Spectral deconvolution, MCR-ALS, PARAFAC and Lifetime.

III. **Application** of the sensors by selective determination of organic molecules and inorganic metal ions known by their harmful characteristics to the environment and healthcare, collected in real samples.

Thesis Layout

The framework of this thesis was elaborated by a compilation of papers published throughout the four years of PhD. The work done resulted in one book chapter and eight scientific articles published in international scientific journals with peer review system. Which published paper is designed by a chapter. Wherefore the thesis layout is ordered as follow:

Chapter 1 is the Introduction of this thesis, with highlights up to nanocomposites made of dendrimers and quantum dots. This chapter is a kind of review with emphasis to some works which were performed during my master degree. The nanocomposites referred in this chapter are mainly composed by inorganic quantum dots of Cadmium and Zinc. This chapter was published in the book *Dendrimers: Synthesis, Applications and Role in Nanotechnology* by Nova Science Publishers with the reference Chapter 9, 2013, pages 215-228.

Chapter 2 is the paper concerned to a PAMAM-OH dendrimer and a doped QD made of zinc and manganese. Following a synthesis strategy towards to a less toxic QD, the zinc doped QD was the first to be synthesized and the application was pointed to Cd(II) sensing. This paper was published in *Talanta* (4.16 impact factor) with the reference Vol. 135, 2015, pages 317-324.

Chapter 3 is the article related to CQDs functionalized with MSA. Was the first CQD to be synthesized and were tested various passivating agents, except dendrimers. The enhancement obtained by the functionalization of CQDs by MSA originated nanocomposites available to sensing silver nanoparticles. This paper was published in *Journal of Materials Chemistry A* (8.87 impact factor) with the reference Vol. 2, 2014, pages 8342-8351.

Chapter 4 is the work concerned to CQDs doped with nitrogen. Was studied the formation of fluorescent nanoparticles in a basic mild, instead of the ordinary acidic mild. The N-CQDs synthesized showed selectivity in the determination of benzene homologous, the pyridine. This paper was published in *Journal of Colloid and Interface Science* (3.91 impact factor) with the reference Vol. 458, 2015, pages 209-216.

Chapter 5 is the article related to CQDs functionalized with Vitamin B_{12}. Were the first CQDs synthesized with ratiometric properties attributed to the FRET phenomenon between CQDs and Vitamin B_{12}. Even the application was oriented to the sensing of harmful pesticides, belonging to the family of metabolites carbofuran. This ratiometric nanosensor showed high selectivity to carbofuran phenol 3-Keto. This paper was published in Sensors and Actuators B (5.08 impact factor) with the reference Vol. 239, 2017, pages 553–561.

Chapter 6 is the first paper of CQDs functionalized with dendrimers, the PAMAM-NH_2. Using a Vitamin B9, the acid folic, as the carbon precursor because the existence of amino groups in the acid folic structure. A similar strategy to the previous chapter but in this case the nitrogen elements are present in the carbon precursor. The addition of PAMAM-NH_2 rendered the fluorescent nanocomposites available for sensing chloroplatinate ions. This paper was published in *Journal of Colloid and Interface Science* (3.91 impact factor) with the reference Vol. 465, 2016, pages 165-173.

Chapter 7 is the second paper with functionalization of CQDs also with PAMAM-NH_2 dendrimer. The carbon precursor used was the activated carbon and for the formation of fluorescent nanoparticles were needed to submit the activated carbon to extreme acidic and oxidation conditions. The fluorescent nanocomposites synthesized allowed the selective sensing of 4- chloro-2,6-dinitroaniline, an explosive component. This paper was published in *Carbon* (5.89 impact factor) with the reference Vol. 106, 2016, pages 171-178.

Chapter 8 is the work related to QDs of silicon also functionalized with a PAMAM-OH dendrimer. Was the first attempt to synthesize QDs different from the conventional inorganic QDs. The results were optically satisfactory and the application is environmentally interesting due to the sensing of an hazard pollutant, the Cr(VI). This paper was published in *Talanta* (4.16 impact factor) with the reference Vol. 144, 2015, pages 862-867.

Chapter 9 is the paper where SiQDs and SiQDs@PAMAM-$OH_{G=5}$ synthesized in the above work were immobilized into a regenerated cellulose membrane, trying to give a more practical use of the fluorescent nanoparticles, potentially for electrochemical devices. This paper was published in *Carbohydrates Polymers* (4.31 impact factor) with the reference Vol. 151, 2016, pages 939-946.

Chapter 1

Dendrimers Quantum Dots Nanocomposites for Chemical Sensing

1.1 Contribution to this Paper

My contribution to this paper included the bibliographic research and writing of contents related with the dendrimers, QDs and the dendrimers:QDs nanocomposites, in order to scaffold the state of the art. This paper was submitted as a book chapter and until the acceptation it passes through some adjustments required by the reviewers and under supervision of my advisor Professor Joaquim Esteves da Silva and co-advisor Doutor Manuel Algarra.

In: Dendrimers
Editors: Heather B. Harris and Brian L. Turner
ISBN: 978-1-62808-604-1

Chapter 9

DENDRIMER-MODFIED QUANTUM DOTS NANOCOMPOSITES FOR CHEMICAL SENSING

M. Algarra, B. B. Campos and J. C. G. Esteves da Silva
Centro de Investigação em Química, Departamento de Química e Bioquímica,
Ciências da Universidade do Porto, Porto, Portugal

ABSTRACT

Dendrimers are characterized, among other quite interesting properties, by heterogeneity of zones inside their molecules and for a high local concentration of functionalities. These two particularly properties of dendrimers confer them a potential selective and sensitive recognition of guest molecules. On the other side, semiconductor nanoparticles (quantum dots), which are highly fluorescent nanomaterials, can be conjugated with numerous molecules including dendrimers, just by chemically modification of their surface. The coupling of dendrimers and quantum dots result in hybrids organic/inorganic nanocomposites, which can alter the charge, functionality and reactivity, based, for example, in the fluorescence changes induced by molecular recognition at their surfaces. This can simultaneously enhance the stability and dispersion of the nanocomposites. Here we review the advantages of dendrimers modified quantum dots as nanoprobes, to investigate their feasibility to be used as analytical tool in a wide variety of ions and molecules.

INTRODUCTION

Dendrimers

Dendrimers derive their name from the Greek words *dendron* and *meros* meaning reminiscent of a tree which corresponds to compounds having a tree-like branched structure and is replacing the former designation of this class of compounds as cascade molecules [1]. The dendrimers designation was first reported in 1985 by Tomalia and coworkers, who synthesized three-dimensional polyamindoamine (PAMAM) dendrimers containing tertiary

amines and amide linkages [1, 2]. However, previous work of others pioneers about one decade before, like the research groups of Vogtle, Denkwalter and Newkome led to the development of the scientific background of dendrimers [3, 4]. Over 100 different types of dendrimers with over 1000 types of surface modifications have been described [5].

Dendrimers are polymeric molecules composed of hyperbranched monomers, tree-like structures, which emanate radially from a central core. They consist of three critical architectural domains: (a) the multivalent surface, containing a larger number of potentially reactive sites, (a) the interior shells, branch cell layers defined by dendrons, surrounding the core, and (c) the core to which the dendrons are attached. The initiator core is in the heart of the molecule, and branches extend outward from it. The monomers attached to the core (G_0), are called first generation monomers (G_1) and two second generation monomers (G_2) are attached to the each first generation monomers. Successive generations will form in this same manner, being two monomers attached to the monomer from the previous generation. The molecular weight of the dendrimer nearly doubles with each additional generation [6]. At higher generations (greater than five) dendrimers resemble spheres with countless cavities within their branches. Furthermore, terminal groups can be modified to obtain both a charged, and hydrophilic or lipophilic function for a desired a function and/or application [7].

Dendrimers can be functionalized with groups such as carbohydrates, peptides, and silicon to form glycodendrimers, peptide dendrimers, and silicon-based dendrimers, respectively [8, 9]. Different linkages such as polyamines (ie: polypropylene imine, PPI dendrimer) or a mix of polyamides and amines (ie: polyamido amine, PAMAM dendrimer) can make up the dendrimer design. They can be tailored or modified into biocompatible compounds with low cytotoxicity and high biopermeability. In addition, dendrimers are manufactured in high purities with few structural defects, and are easily analyzed by standard methods as mass spectrometry, infrared spectroscopy and NMR spectroscopy.

The advantage of dendrimers is that they can be synthesized and designed for specific applications. The properties of dendrimers include [5]:

(1) Small dimensions that allow them to act at a subcellular level,
(2) A defined number of terminal groups that can be used for bioconjugation with drugs, signaling and targeting components,
(3) Surfaces that may be designed with functional groups to augment or resist trans-cellular, epithelial or vascular biopermeability.
(4) A well-defined 'interior void space' which can encapsulate and isolate components such as small molecule (ie: drugs, metals, or signaling groups). Encapsulating in that void space reduces the drug toxicity and facilitates controlled release.
(5) Positive biocompatibility patterns that are associated with lower generation anionic or neutral polar terminal surface groups as compared to higher generation neutral apolar and cationic surface groups.
(6) Low immunogenicity by coating with PEGylated modification of the surface that make the dendrimer a very versatile nano scaffolding particle [10].
(7) Surface groups that can be modified to optimize biodistribution; receptor mediated targeting, therapy dosage or controlled release of drug from the interior space.
(8) Ability to arrange excretion mode from body, as a function of nanoscale diameter.

Quantum Dots

Quantum dots (QDs), discovered by Louis E Brus, constitute an important class of nanomaterials [11]. QDs are fluorescent semiconductor nanocrystals with unique optical and electrical properties [12-14], whose excitons are confined in all three spatial dimensions. They exploit a quantum effect related to particle size, which retains incoming energy inside the particle in the form of "excitons". The energy of the exciton is determined by its wavelength and this, in turn, is constrained by the size of the particle. When the energy of the exciton is emitted from the particle, it appears as a photon of precisely defined wavelength, so that quantum dots generate extremely pure monochromatic emitted light. They also do this with extremely high quantum efficiencies, which can exceed 60%. Upon their interaction with photon, they get excited and emit energy in UV, visible, or near-infrared (IR) regions, which can be detected [15].

QDs are nanomeric semiconductors composed by elements of periodic groups II-VI, III-V, or IV-VI which range from about 2 to 10 nm in diameter. Different sized QDs emit radiation with different wavelength due to quantum confinement effects and thus they have properties that are intermediate between those of bulk semiconductors and discrete molecules [16]. Compared with organic dyes and fluorescent proteins, QDs possess near-unity quantum yields and much greater brightness than most dyes. QDs have broad excitation profiles and narrow emission peaks, commonly 25-35 nm full width at half-maximum, allowing quantification and simultaneous identification of multiple markers using single wavelength activation [17, 18], continuous and tunable emission maxima due to quantum size effects, a relatively long fluorescence lifetime (5 to greater than 100 ns compared with 1 to 5 ns in organic dyes), and negligible photobleaching [19]. Due to their long fluorescence lifetime QDs signal could be separated from background auto-fluorescence in cells or tissues. Currently, QDs are commercially available offering significant advantages over conventionally used fluorescent markers, due to their photostability, which allows long-term cell labelling and *in vivo* cell tracking. The most commonly used are cadmium selenide (CdSe), cadmium telluride (CdTe), and indium arsenide (InAs) [20].

Dendrimers-Quantum Dots Nanocomposites

Most chemical applications require water soluble QDs, which could be synthesized directly in water but often, have narrow available size ranges and wide size distribution, affording wide FWHM and a wide emission color ranging from 300-1200 nm, or even more [21]. Hence a challenge is to obtain both, hydrophilic and low toxics QDs when thry are designed for biochemical applications. A new class of emerging fluorescent nanoparticles, metal free can avoid this last disadvantage based in carbon and silica atoms, namely carbon and silicon dots [22-26].

Usually, QDs have been synthesized in organic solvents which were coating with hydrobobic ligands such as trioctylphosphine oxide (TOPO) [27, 28] trioctylphosphine (TOP) [29, 30], tetradecylphosphonic acid (TDPA) [31-33] or oleic acid [34-37]. These hydrophobic ligands could be replaced by some water-soluble bifunctional molecules in which one end connects to quantum dot surface atoms and the other end is hydrophilic and may also be reactive to the target analyte. Examples of some water-soluble bifunctional molecules used

are mercaptoalkyl organic acids [38-42], 2-aminoethanethiol [43], mercaptopyridine [44], dihydrolipoic acid [45], oligomeric phosphines [46, 47], peptides [48, 49], and dendrimers [50-60].

The conjugation of an inorganic-organic hybrid results in a reducing toxicity of the QDs core, because of the shield held by surrounding dendrimers, and increase the photostability, important for long term experiments because polymer coatings seem to enable photooxidation at surface defects of the QDs [61]. The biocompatibility and cytotoxicity of CdTe functionalized with PAMAM nanocomposites, where the viability of the cells assayed (PK15) was around 75.28% after 2 days, compared with the raw CdTe which obtained only 25.23% [62], similar experiments are carried out with dendrimer in different area such as dermis [63] and regenerative applications [64].

These nanocomposites constitute by dendrimers-QDs, show several reactive sites that make them potential chemical sensors, due to the potential for multiple detection and binding sites in dendritic structures, in addition the dendrimers offer the ability to contain a large variety of guest analytes within their 3D structure, such as the mentioned fluorescent nanoparticles, QDs.

The most developed sensing systems based in dendrimer-QDs are PPI (poly(propylene imine)), where CdS-PPI is used as metal cation and pH sensor respectively [65, 66]; similar kind of pH sensor in the range 6-8 is found by means the ratiometric measurements of CdSe/CdZnS QDs coated by PAMAM dendrimers for biological applications [67]. DAB (polypropylenimine tetrahexacontaamine dendrimer) coating CdS QDs was applied for Hg^{2+} analysis, where the linear range obtained by quenching at 535 nm was comprised in the narrow range of 1×10^{-6} - 1×10^{-5} M [51], further chemometric analysis was carried out [68] DAB-CdS QDs was applied for nitromethane [53], and by its quenching effect over the fluorescence at 535 nm of CdS nanoparticles, was obtained a linear range comprised between 4×10^{-3} - 2×10^{-1} M. An extensive study of synthesis, characterization of DAB dendrimers with CdS; CdS:ZnS and ZnS QDs is presented, where is showed the synthesis at room temperature in aqueous media and the different techniques of characterization used for its identification [69].

These systems have been extensively characterized, being studied the different parameters involved in the fluorescence emission such as the Cd^{2+} concentration, which is the most critical parameter when is used PAMAM dendrimer [70], the interference effect of other metallic ions was studied on the fluorescence, was found that Cd^{2+} and Zn^{2+} enhance it while Ag^{+}, Cu^{2+} and Pb^{2+} quench the emission [71]. The lifetime of it was calculated and showed values at 165ps and small dependence of the size when the dendrimer generation does increase [72]. More complex characterization techniques are used, such as x-ray absorption near-edge structure (XANES) and x-ray excited optical luminescence (XEOL), to obtain supplementary data of its stability[73].

PAMAM-CdSe QDs using the same methodology for nitroaromatics (4-methoxy-2-nitrophenol, 2-amine-5-chloro-1,3-dinitrobenzene and 3-methoxy-4-nitrobenzoic acid) using determinations at 570 nm and reaching sensibilities around 5.5×10^{-5} M for all of them [54]. It has been found when the dendrimers are hydroxyl terminated groups (poly(alkyl ether)-dendrons), is observed the protection of the emission of CdSe/CdS QDs from quenching effect of CdSe or CdS QDs [74]. PAMAM-CoTe QDs immobilized in glassy carbon electrode for biphenyl A [75], allowed the development of a amperometric methodology for this environmental pollutant a limit of detection 1×10^{-9} M, with a linear response comprised

between 1.3×10^{-8} M $\times10^{-6}$ M at pH 8; glucose was quantified with CdS QDs/glucose oxidase coupled with PAMAM on a Pt electrode, where was obtained a limit of detection of 1×10^{-6} M [76] or urea by CdS QDs based on molecularly imprinted chitosan matrix as electrochemical sensor, obtaining a sensibility of 1×10^{-12} M [77], this last analytical methods are not based in dendrimers but are involved with complex system.

A modification of the PAMAM dendrimer with thiol terminal groups (Figure 1) was used in the metal cation analysis of Cd^{2+} and Pb^{2+}, where CdSe QDs were coated by this thiol dendrimer [59]. The fluorescence the nanocomposites showed an enhancing of for Cd^{2+} and quenching for Pb^{2+}. The sensor can quantified Cd(II) and Pb^{2+} at 5×10^{-8} M and Pb^{2+} 6×10^{-8} M respectively.

The same methodology has been assessed for the analysis of Cu^{2+} by PAMAM-CdTe, where it was found an enhancement of the fluorescence signal with a limit of detection of 70×10^{-9} M. When PAMAM-CdS was used the signal was quenched due to the reduction to Cu^{+} [78].

Similar procedure was developed for C-reactive protein (C-RP), a cardio vascular and inflammation indicator, determination in human serum by ZnSe QDs coated by thiol dendrimer of 5^{th} generation (Figure 2) [56]. The use of dendrimers as coating agents in chemical analysis, provide to QDs a great stability to their surroundings, yielding reproducible data at 465 nm in the range 0.5-8 mg/L, range of routine in hospital protocols. Here must be highlighted that other coating agent must be included, *o*-phosphorylethanolamine, because if not present in the system there is no interaction with the dendrimer/QD system. The effect of every component in the fluorescence signal in thiol-DAB-ZnSe QDs is deep studied by component analysis, where showed that the presence of dendrimer does not affect the fluorescent properties [79].

Recently it was achieved the assay of cancer cells by PAMAM-CdSe/ZnS QDs using electroluminescence probe, where it shows the feasibility to discriminate them [80], by binding to a specific protein (tenascin-C on the surface of human glioblastoma cells), [81]; PAMAM-CdSe, coated by a battery of units of peptides (arginine-glycine-aspartic acid) was successfully used for detection of melanoma calls [82]. The same system was used for sodium ion analysis in neurons based in the pH sensor, which the main feature was that no alterations in the normal functional properties [83]. PAMAM dendrimer coated by CdS QDs was investigated as probing system for ascorbic acid at detection level of 5×10^{-6} M, based in the quenching effect[84].

In forensic chemistry it has been used as fingerprint detection using PAMAM-CdS QDs as alternative to conventional fluorescent powders [85-87]. Promise photosensitive detectors are being developed in the field of photoelectronic, synthesized with PAMAM-PbS QDs in one step for photoswitching process [88], and a new emerging research area such as the functionalization of water soluble multi wall carbon nanotubes (MWNT) with PAMAM-CdTe QDs, where is enhanced substantially the fluorescence signal by this combination to be sensing to DNA [89, 90]. Other complex system based in ferrocenyl-terminated PAMAM dendrimer is designed as quencher of the cathodic electroluminescence of CdTe QDs for chemical sensor [91].

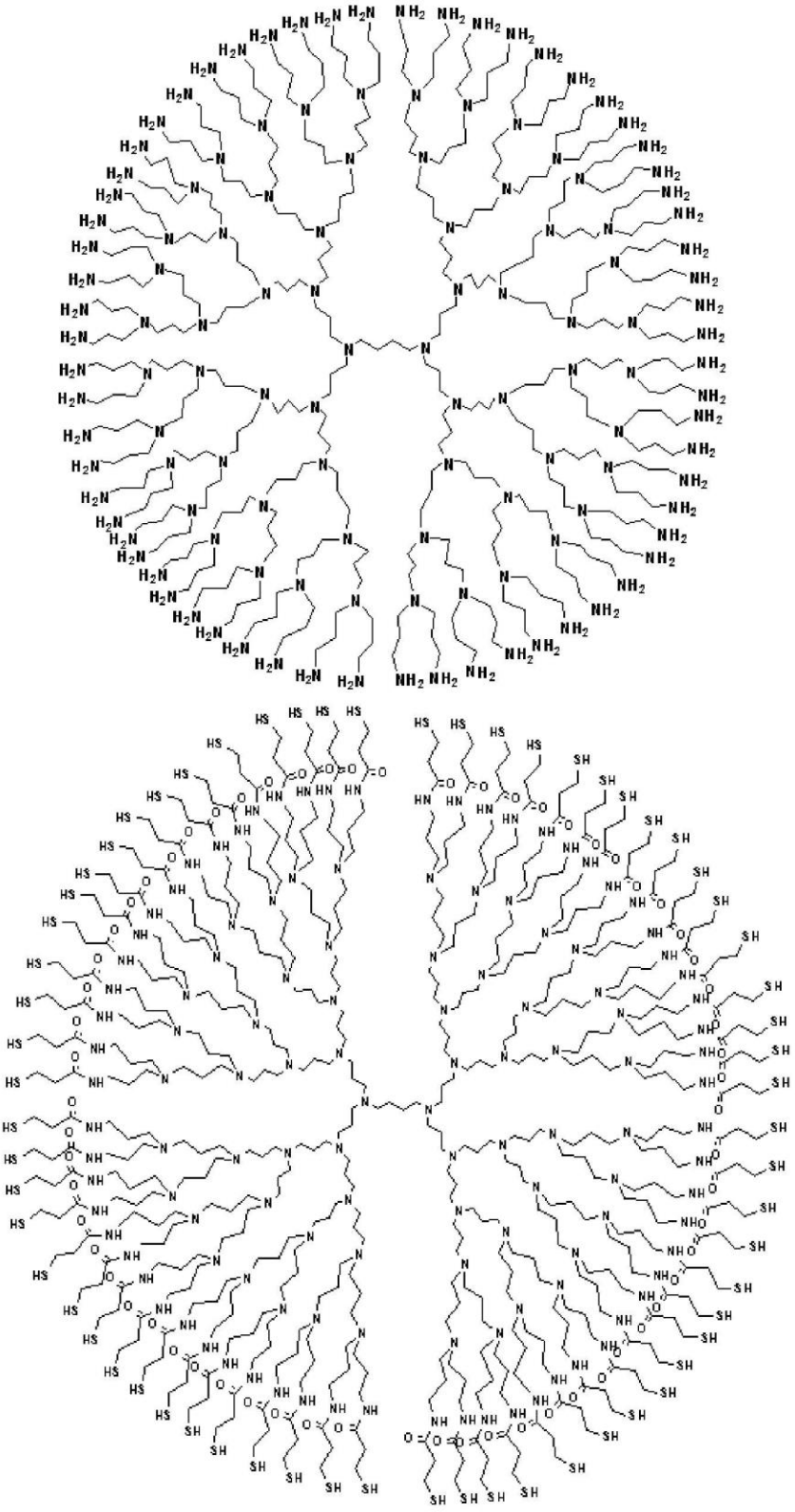

Figure 1. Molecular structures of DAB and thiolated dendrimers generation 5th.

In the research area of immunosensor, the most complex systems, is based the PAMAM-Au QDs, designed for detecting human IgG, mediated by goat-derived anti-human IgG. The response of this sensor is proportional to the quench effect of the fluorescence of the PAMAM-Au QDs [92], with CdSe/ZnS was developed an immunosensor for Escherichia coli O157:H7 and hepatitis B virus, where dendrimers molecules are involved and the detection limits was 2.3 CFU/mL for Escherichia and 5ng/mL for hepatitis B, the aim of these system is provide charge to the carbon nanotubes to be binding to the pathogens, and detected by fluorescence resonance energy transfer process FRET [93].

The system is able to detect human IgG by linear fluorescence quenching over a micromolar to nanomolar concentration range. We have demonstrated the specificity and a wide dynamic range of the proposed immunoassay. The quenching is a result of competitive surface quenching of the AuQDs. Characterization, details of the immunoassay, and the quenching mechanism, are discussed.

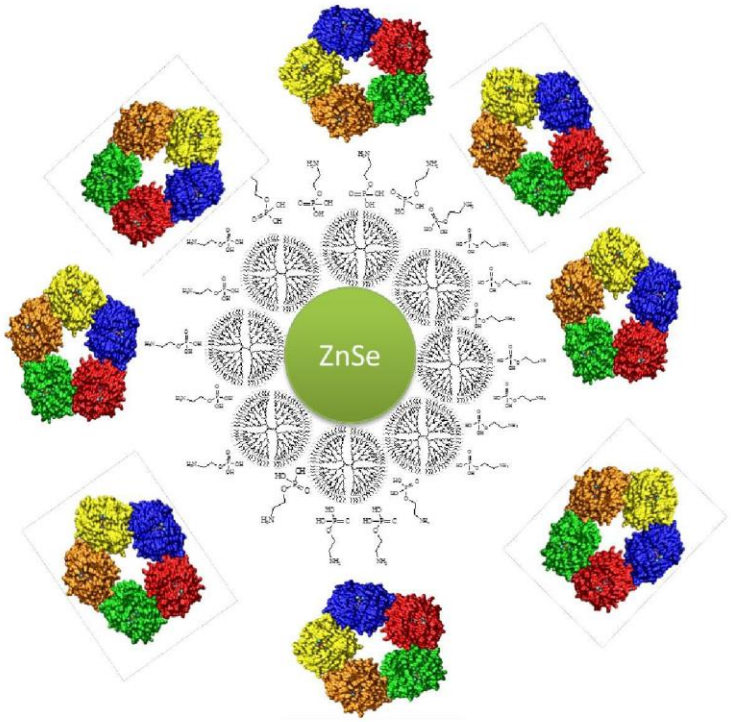

Figure 2. Schematic representation of the interaction of S-DAB-ZnSe with C-RP.

CONCLUSION

The objective of this chapter was to collect the most important applications of the system formed by the different fluorescent nanoparticles the quantum dots with dendrimers. The progresses, both analytical and biomedical application, are in parallel with synthesis of new dendritic molecules, the different and multiple ends groups which can be modified according the target of analysis, at nano sized level, offer a great variety of developments due to their

facile preparation, characterization and manipulation. As consequence of the great current research, quantum dots coated with the different dendrimers are capable to extend their application in a wide range of analytical purpose including spectroscopy, electronic, molecular devices and drug delivery.

REFERENCES

[1] Vogtle, F., Richardt, G. & Werner, N. (2009). *Dendrimer Chemistry: Concepts, Syntheses, Properties, Applications*. Weinheim: Wiley-VCH.

[2] Tomalia, D. A., Baker, H., Dewald, J., Hall, M., Kallos, G., Mar-Tin, S., Roeck, J., Ryder, J. & Smith, P. (1986). Dendritic macromolecules: Synthesis of Starburst dendrimers. *Macromolecules*, *19*, 2466-2468.

[3] Newkome, G. R. & Shreiner, C. D. (2008). Poly(amidoamine), polypropyleneimine, and related dendrimers and dendrons possessing different 1→2 branching motifs: An overview of divergent procedures. *Polymer*, *49*, 1-173.

[4] Moorefield, C. N., Perera, S. & Newkome, G. R. *Dendrimer chemistry: supramolecular perspectives and applications.* In book: *Dendrimer-based drug delivery systems: from theory to practice* (Cheng, Y., ed). Chapter 1. Hoboken, NJ: John Wiley & Sons, 2012.

[5] Tomalia, D. A., Reyna, L. A. & Svenson, S. (2007). Dendrimers as multi-purpose nanodevices for oncology drug delivery and diagnostic imaging. *Biochemical Society Transactions*, *235*, 61-67.

[6] Tomalia, D. A. (2005). Birth of a new macromolecular architecture: dendrimers as quantized building blocks for nanoscale synthetic polymer chemistry. *Progress in Polymer Science*, *30*, 294-324.

[7] Bai, S., Thomas, C., Rawat, A. & Ahsan, F. (2006). Recent progress in dendrimer-based nanocarriers. *Critical Reviews in Therapeutic Drug Carrier Systems*, *23*, 437-495.

[8] Boas, U. & Heegaard, P. M. (2004). Dendrimers in drug research. *Chemical Society Reviews*, *33*, 43-63.

[9] Cloninger, M. J. (2002). Biological applications of dendrimers. (2002). *Current Opinion in Chemical Biology*, *6*, 742-748.

[10] Dufes, C., Uchegbu, I. F. & Schatzlein, A. G. (2005). Dendrimers in gene delivery. *Advanced Drug Delivery Reviews*, *57*, 2177-2202.

[11] Rossetti, R., Nakahara, S. & Brus, L. E. (1983). Quantum size effect in the redox potentials, resonance Raman spectra, and electronic spectra of CdS crystallites in aqueous solution. *Journal of Chemical Physics*, *79*, 1086-1088.

[12] Ekimov, A. I. & Onuschenko, A. A. (1982). Quantum size effect in the optical spectra of semiconductor microcrystals. *Soviet physics: Semiconductors*, *16*, 1215-1219.

[13] Alivisatos, A. P. (1996). Semiconductor clusters, nanocrystals, and quantum dots. *Science*, *271*, 933-937.

[14] Alivisatos, A. P. (1996). Perspectives on the physical chemistry of semiconductor nanocrystals. *Journal of Physical Chemistry*, *100*, 13226-13239

[15] Efros, A. L. & Rosen, M. (2000). The electronic structure of semiconductor nanocrystals. *Annual Review of Materials Science*, *30*, 475-521.

[16] Brus, L. E. (1984). Electron-electron and electron-hole interactions in small semiconductor crystallites: The size dependence of the lowest excited electronic state. *Journal Chemical Physics*, *80*, 4403-4409.

[17] William, W. Y., Chang, E., Drezek, R. & Colvin, V. L. (2006). Water-soluble quantum dots for biomedical applications. *Biochemical and Biophysical Research Communications*, *348*, 781-786.

[18] Chan, W. C. W., Maxwell, D. J., Gao, X. H., Bailey, R. E., Han, M. & Nie, S. (2003). Luminescent quantum dots for multiplexed biological detection and imaging. *Current Opinion in Biotechnology*, *13*, 40-46.

[19] Resch-Genger, U., Grabolle, M., Cavaliere-Jaricot, S., Nitschke, R. & Nann, T. (2008). Quantum dots versus organic dyes as fluorescent labels. *Nature Methods*, *5*, 763-775.

[20] Ashoori, R. C. (1996). Electrons in artificial atoms. *Nature*, *379*, 413-419.

[21] Murray, C. B., Norris, D. J. & Bawendi, M. G. (1993). Synthesis and characterization of nearly monodisperse CdE (E = sulfur, selenium, tellurium) semiconductor nanocrystallites, *Journal of American Chemical Society*, *115*, 8706-8715.

[22] Sun, Y. P., Zhou, B., Lin, Y., Wang, W., Fernando, K. A. S., Pathak, P., Meziani, M. J., Harruff, B. A., Wang, X., Wang, H., Luo, P. L., Yang, H., Kose, M. E., Chen, B., Veca, L. M. & Xie, S. Y. (2006). Quantum-sized carbon dots for bright and colorful photoluminescence. *Journal of American Chemical Society*, *128*, 7756-7757.

[23] Esteves da Silva, J. C. G. & Gonçalves, H. M. R. (2011). Analytical and bioanalytical applications of carbon dots. *Trends in Analytical Chemistry*, *30*, 1327-1336.

[24] Mao, Y., Bao, Y., Han, D., Li, F. & Niu, L. (2012). Efficient one-pot synthesis of molecularly imprinted silica nanospheres embedded carbon dots for fluorescent dopamine optosensing. *Biosensors and Bioelectronics*, *38*, 55-60.

[25] Rosmani, C. H., Abdullah, S. & Rusop, M. (2013). Photoluminescence characteristics of silicon quantum dots nanoparticles (SQDNs) embedded on glass surface. *Procedia Engineering*, *56*, 750-754.

[26] Shiohara, A., Hanada, S., Prabakar, S., Fujioka, K., Lim, T. H., Yamamoto, K., Northcote, P. T. & Tilley, R. D. (2010). Chemical reactions on surface molecules attached to silicon quantum dots. *Journal of American Chemical Society*, *132*, 248-253.

[27] Liu, L., Peng, Q. & Li, Y. (2008). Preparation of CdSe quantum dots with full color emission based on a room temperature injection technique. *Inorganic Chemistry*, *47*, 5022-5028.

[28] Wang, C. H., Chen, C. W., Wei, C. M., Chen, Y. F., Lai, C. W., Ho, M.L. & Chou, P. T. (2009). Resonant energy transfer between CdSe/ZnS type I and CdSe/ZnTe type II quantum dots. *Journal Physical Chemistry C*, *113*, 15548-15552.

[29] Dickerson, B. D., Irving, D. M., Herz, E., Claus, R. O., Spillman, W. B. & Meissner, K. E. (2005). Synthesis kinetics of CdSe quantum dots in trioctylphosphine oxide and in stearic acid. *Applied Physics Letters*, *86*, 171915-171918.

[30] Morris-Cohen, A. J., Donakowski, M. D., Knowles, K. E. & Weiss, E. A. (2010). The effect of a common purification procedure on the chemical composition of the surfaces of cdse quantum dots synthesized with trioctylphosphine oxide. *Journal Physical Chemistry C*, *114*, 897-906.

[31] Peng, X., Manna, U., Yang, W., Wickham, J., Scher, E., Kadavanich, A. & Allvisatos, A. P. (2000). Shape control of CdSe nanocrystals. *Nature 404*, 59-61.

[32] Peng, Z. A. & Peng, X. (2001). Mechanisms of the shape evolution of CdSe nanocrystals. *Journal of American Chemical Society*, *123*, 1389-1395.

[33] Freeman, R., Girsh, J. & Willmer, I., (2013). Nucleic acid/Quantum Dots (QDs) hybrid systems for optical and photoelectrochemical sensing. *Applied Materials and Interfaces*, *5*, 2815-2834

[34] Fritzinger, B., Capek, R. K., Lambert, K., Martins, J. C. & Hens, Z. (2010). Utilizing self-exchange to address the binding of carboxylic acid ligands to CdSe quantum dots. *Journal of American Chemical Society*, *132*, 10195-10201.

[35] Chen, J., Song, J. L., Sun, X. W., Deng, W. Q., Jiang, C. Y., Lei, W, Huang, J. H. & Liu, R. S. (2009). An oleic acid-capped CdSe quantum-dot sensitized solar cell. *Applied Physics Letters*, *94*, *153115-153118.*

[36] Noone, K. M., Anderson, N. C., Horwitz, N. E., Munro, A. M., Kulkarni, A. P. & Ginger, D. S. (2009). Absence of photoinduced charge transfer in blends of PbSe quantum dots and conjugated polymers. *ACS Nano*, *3*, 1345-1352.

[37] Zou, W., Du, Z. J., Li, H. Q. & Zhang, C. (2011). Fabrication of carboxyl functionalized CdSe quantum dots via ligands self-assembly and CdSe/epoxy fluorescence nanocomposites. *Polymer*, *52*, *1938-1943.*

[38] Gomes, D., Algarra, M., Diez de los Rios, M. J., Arrebola, M. M., Herrera-Gutierrez, M. E., Seller-Perez, G. & Esteves da Silva, J. C. G. (2012). CdSe and ZnSe Quantum Dots Capped with PEA for Screening C-Reactive Protein in Human Serum. *Talanta*, *93*, 411-414.

[39] Luan, W., Yang, H., Wan, Z., Yuan, B., Yu, X. & Tu, S. T. (2012). Mercaptopropionic acid capped CdSe/ZnS quantum dots as fluorescence probe for lead(II). *Journal of Nanoparticle Research*, *14*, *762-769.*

[40] Kumar, P., Kukkar, D., Deep, S. & Sharma, S. C. Synthesis of mercaptopropanoic acid stabilized CdS quantum dots for bioimaging in breast cancer. *Advance Material Letters*, *3*, 471-475.

[41] Miranda, M. S., Algarra, M., Jimenez-Jimenez, J., Rodriguez-Castellon, E., Campos, B. B. & Esteves da Silva, J. C. G. (2013). Luminescent behavior of CdTe quantum dots: Neodymium(III) complex-capped nanoparticles. *Journal of Luminescence*, *134*, *408-413*.

[42] Ma, K., Fang, T., Baia, J. & Guo, H. (2013). Regulating properties of quantum dots: effect of methyl side groups of mercapto acids. *RSC Advances*, *3*, 4935-4939.

[43] Wuister, S. F., de Mello Donegá, C. & Meijerink, A. (2004). Luminescence temperature antiquenching of water-soluble CdTe quantum dots: role of the solvent. *Journal of American Chemical Society*, *126*, *10397-10402.*

[44] Wang, Y., Zhang, J., Jia, H., Li, M., Zeng, J., Yang, Bai, Zhao, B., Xu, W. & Lombardi, J. R. (2008). Mercaptopyridine Surface-Functionalized CdTe Quantum Dots with Enhanced Raman Scattering Properties. *Journal Physical Chemistry*, *112*, 996-1000.

[45] Laurino, P., Kikkeri, R. & Seeberger, P. H. (2011). Continuous-flow reactor-based synthesis of carbohydrate and dihydrolipoic acid-capped quantum dots**.** *Nature Protocols*, *6*, 1209-1220.

[46] Kim, S. & Bawendi, M. G. (2003). Oligomeric ligands for luminescent and stable nanocrystal quantum dots. *Journal of American Chemical Society*, *125*, 14652-14653.

[47] Hammer, N. I., Emrick, T. & Barnes, M. D. (2007). Quantum dots coordinated with conjugated organic ligands: new nanomaterials with novel photophysics. *Nanoscale Research Letters*, *2*, 282-290.

[48] Yukawa, H., Kagami, Y., Watanabe, M., Oishi, K., Miyamoto, Y., Okamoto, Y., Tokeshi, M., Kaji, N., Noguchi, H., Ono, K., Sawada, M., Baba, Y., Hamajima, N. & Hayashi, S. (2010). Quantum dots labeling using octa-arginine peptides for imaging of adipose tissue-derived stem cells. *Biomaterials*, *31*, 4094-4103.

[49] Cai, W., Shin, D. W., Chen, K., Gheysens, O., Cao, Q., Wang, S. X., Gambhir, S. S. & Chen, X. (2006). Peptide-labeled near-Infrared quantum dots for imaging tumor vasculature in living subjects. *Nano Letters*, *6*, 669-676.

[50] Lemon, B. I. & Crooks, R. M. (2000). Preparation and Characterization of Dendrimer-Encapsulated CdS Semiconductor Quantum Dots, *Journal of American Chemical Society*, *122*, 12886-12887.

[51] Campos, B. B., Algarra, M., Alonso, B., Casado, C. M., Esteves da Silva, J. C. G. (2009). Mercury(II) sensing based on the quenching of fluorescence of CdS-dendrimer Nanocomposites. *Analyst*, *134*, 2447-2452.

[52] Lee, K. R. & Kang, I. J. (2009). Effects of dopamine concentration on energy transfer between dendrimer–QD and dye-labeled antibody, *Ultramicroscopy*, *109*, 894-898.

[53] Campos, B. B., Algarra, M. & Esteves da Silva, J. C. G. (2010). Fluorescent properties of a hybrid cadmium sulfide-dendrimer nanocomposite and its quenching with nitromethane, *Journal of Fluorescence*, *20*, 143-151.

[54] Algarra, M., Campos, B. B., Miranda, M. S. & Esteves da Silva, J. C. G. (2011). CdSe quantum dots capped PAMAM dendrimer nanocomposites for sensing nitroaromatic compounds. *Talanta*, *83*, 1335-1340.

[55] Divsar, F. & Ju, H. (2011). Electrochemiluminescence detection of near single DNA molecules by using quantum dots-dendrimer nanocomposites for signal amplification. *Chemical Communications*, *47*, 9879-9881.

[56] Algarra, M., Campos, B. B., Gomes, D., Alonso, B., Casado, C. M., Arrebola, M. M., Diez de los Rios, M. J., Herrera-Gutiérrez, M. E, Seller-Pérez, G. & Esteves da Silva, J. C. G. (2012). Thiolated DAB dendrimer/ZnSe nanoparticles for C-reactive protein recognition in human serum. *Talanta*, *99*, 574-579.

[57] Yamamoto, D., Koshiyama, T., Watanabe, S. & Miyahara, MT. (2012). Synthesis and photoluminescence characterization of dendrimer-encapsulated CdS quantum dots. *Colloids and Surfaces A: Physicochemical Engineering Aspects*, *411*, 12-17.

[58] Jie, G., Yuan, J. & Zhang, J. (2012). Quantum dots-based multifunctional dendritic superstructure for amplified electrochemiluminescence detection of ATP. *Biosensors and Bioelectronics*, *31*, 69-76.

[59] Algarra, M., Campos, B. B., Alonso, B., Miranda, M. S., Martínez, A. M., Casado, C. M., Esteves da Silva, J. C. G. (2012). Thiolated DAB dendrimers and CdSe quantum dots nanocomposites for Cd(II) or Pb(II) sensing. *Talanta*, *88*, 403-407.

[60] Algarra, M., Campos, B. B., Alonso, B., Casado, C. M., Esteves da Silva, J. C. G. & Benavente, J. (2013). Inclusion of thiol DAB dendrimer/CdSe quantum dots based in a membrane structure: surface and bulk membrane modification. *Electrochimica Acta*, *89*, 652-659.

[61] Guo, W., Li, J. J., Wang, Y. A. & Peng, X. (2003). Conjugation chemistry and bioapplications of semiconductor box nanocrystals prepared via dendrimer bridging. *Chemistry Material*, *15*, *3125-3133.*

[62] Liu, J., Wei, X., Cao, J. & Jiang, H. (2012). CdTe Quantum dots Modified by Polyamidoamine Dendrimers for Cell Imaging. *E-Journal*, *9*, 171-174.

[63] Schilrreff, P., Mundiña-Weilenmann, C., Romero, E. L. & Morilla, M. J. (2012). Selective cytotoxicity of PAMAM G_5 core-PAMAM $G_{2.5}$ shell tecto-dendrimers on melanoma cells. *International Journal of Nanomedicine*, *7*, 4121-4133.

[64] Oliveira, J. M., Salgado, A. J., Sousa, Mano, J. F. & Reisa, R. L. (2010). Dendrimers and derivatives as a potential therapeutic tool in regenerative medicine strategies-A review. *Progress in Polymer Science*, *35*, 1163-1194.

[65] Fernandes, E. G. R., Vieira, N. C. S., de Queiroz, A. A. A., Guimaraes, F. E. G. & Zucolotto, V. (2010). Immobilization of Poly(propylene imine) dendrimer/nickel phtalocyanine as nanostructured multilayer films to be used as gate membranes for SEGFET pH sensors. *Journal of Physical Chemistry C*, *114*, 6478-6483.

[66] Shiau, S. F, Juang, T. Y, Chou, H. W. & Liang, M. (2013). Synthesis and properties of new water-soluble aliphatic hyperbranched poly(amido acids) with high pH-dependent photoluminescence. *Polymer*, *54*, 623-630.

[67] Somers, R. C., Lanning, R. M., Snee, P. T., Greytak, A. B., Jain, R. K., Bawendi, M. G. & Nocera, D. G. (2012). A nanocrystal-based ratiometric pH sensor for natural pH ranges. *Chemical Science*, *3*, 2980-2985.

[68] Leitão, J. M. M., Tauler, R. & Esteves da Silva, J. C. G. (2011). Chemometric analysis of excitation emission matrices of fluorescent nanocomposites. *Journal of Fluorescence*, *21*, 1987-1996.

[69] Esteves da Silva, J. C. G., Algarra, M. & Campos, B. B. (2011). *Synthesis and analytical applications of Quantum Dots coated with different generations of DAB dendrimers* in Book: *Advances in Nanocomposites: Synthesis*, *characterization and industrial applications* (Reddy, B., ed), Chapter 2, 23-38. Croatia: IN-TECH.

[70] Jin, Y. J., Luo, Y. J., Xu, G. Z. & Yang, B. (2011). Study of photoluminescence property of CdS/PAMAM nanocomposites. *Spectroscopy and Spectral Analysis*, *31*, 3311-3314.

[71] Cong, R. M., Luo, Y. J. & Yu, H. Q. (2007). Effects of metallic ions on the photoluminescence properties of CdS quantum dots poly(amidoamine dendrimer nanocomposites. *Chines Journal of Inorganic Chemistry*, *23*, 1347-1352.

[72] Gayen, S. K., Brito, M., Das, B. B., Comanescu, G., Liang, X. C., Alrubaiee, M., Alfano, R. R., Gonzalez, C., Byro, A. H., Bauer, D. L. V. & Balogh-Nair, V. (2007). Synthesis and optical spectroscopy of a hybrid cadmium sulfide-dendrimer nanocomposite. *Journal of the Optical Society of America B: Optical Physics*, *24*, 3064-3071.

[73] Zhang, P. & Sham, T. K. (2005). The electronic and optical properties of dendrimer-capped CdS quantum dots: A UV-vis and x-ray spectroscopy study. *Physica Scripta T*, *115*, 1019-1021.

[74] Huang, B. & Tomalia, D. A. (2006). Poly(ether) dendrons possessing phosphine focal points for stabilization and reduced quenching of luminescent quantum dots *Inorganica Chimica Acta*, *359*, 1961-1966.

[75] Yin, H., Zhou, Ai, S., Chen, Q., Zhu, X., Liu, X. & Zhu, L. (2010). Sensitivity and selectivity determination of BPA in real water samples using PAMAM dendrimer and CoTe quantum dots modified glassy carbon electrode. *Journal of Hazardous Materials*, *174*, 236–243.

[76] Sun, J., Zhu, Y., Yang, X. & Li, C. (2009). Photoelectrochemical glucose biosensor incorporating CdS nanoparticles. *Particuology*, *7*, 347-352.

[77] Lian, H. T., Liu, B., Chen, Y. P. & Sun, X. Y. (2012). A urea electrochemical sensor based on molecularly imprinted chitosan film doping with CdS quantum dots. *Analytical Biochemistry*, *426*, 40-46.

[78] Ghosh, S., Pryam, A. & Saha, A. (2009). Mechanistic aspects of quantum dot based probing of Cu (II) ions: role of dendrimer in sensor efficiency. *Journal of Fluorescence*, *19*, 723-731.

[79] Algarra, M., Radotić, Kalauzi, A., Alonso, B., Casado, C. M. & Esteves da Silva, J. C. G. (2013). Component analysis of fluorescence spectra of thiol DAB dendrimer/ZnSe-PEA nanoparticles. *Talanta*, *105*, 267-271.

[80] Jie, G., Wang, L., Yuan, J. & Zhang, S. (2011). Versatile Electrochemiluminescence Assays for Cancer Cells Based on Dendrimer/CdSe-ZnS-Quantum Dot Nanoclusters. *Analytical Chemistry*, *83*, 3873-3888.

[81] Li, Z., Huang, P., He, R., Lin, J., Yang, S., Zhang, X., Ren, Q. & Cui, D. (2010). Aptamer-conjugated dendrimer-modified quantum dots for cancer cell targeting and imaging. *Materials Letters*, *64*, 375-378.

[82] Li, Z., Humag, P., Lin, J., He, R., Liu, B., X. Zhang, S. Yang, P. Xi., X. Zhang, Ren, Q. & Cui, D. (2010). Arginine-Glycine-Aspartic Acid-Conjugated Dendrimer-Modified Quantum Dots for Targeting and Imaging Melanoma. *Journal of Nanoscience and Nanotechnology*, *10*, 4859-4867.

[83] Lamy, C. M., Sallin, O., Loussert, C. & Chatton, J. Y. (2012). Sodium sensing in neurons with a dendrimer-based nanoprobe. *ACS Nano*, *6*, 1176-1187.

[84] Ghosh, S., Bhattacharva, S. C. & Saha, A. (2010). Probing of ascorbic acid by CdS/dendrimer nanocomposites: a spectroscopic investigation. *Analytical and Bioanalytical Chemistry*, *397*, 1573-1582.

[85] Menzel, E. R., Takatsu, M., Murdock, R. H., Bouldin, K. K. & Cheng, K. H. (2000). Photoluminescent CdS/Dendrimer Nanocomposites for Fingerprint Detection. *Journal of Forensic Sciences*, *45*, 770-773.

[86] Bouldin, K. K., Menzel, E. R., Takatsu, M. & Murdock, R. H. (2000). Diimide-enhanced fingerprint detection with photoluminescent CdS/dendrimer nanocomposites. *Journal of Forensic Sciences*, *45*, 1239-1242.

[87] Juan, J. Y., Jun, L. Y., Ping, L. G., Jie, L., Feng, W. Y., Qin, Y. Q. & Ting, L. W. (2008). Application of photoluminescent CdS/PAMAM in fingerprint detection. *Forensic Science International*, *179*, 34-38.

[88] Ghosh, S., Khan, A. H. & Acharya, S. (2012). Fabrication of Highly Stable, Hybrid PbS Nanocomposites in PAMAM Dendrimer Matrix for Photodetection. *Journal Physical Chemistry C*, *116*, 6022-6030.

[89] Feng, C. L., Zhong, X. H., Steeinhart, M., Caminade, A. M., Majoral, J. P. & Knoll, W. (2008). Functional Quantum-Dot/Dendrimer Nanotubes for Sensitive Detection of DNA Hybridization. *Small*, *4*, *566-571.*

[90] Zheng, Y., Tang, C., Wang, H., Jiang, J., Tian, M., Shen, G. & Yu, R. (2008). A novel density-tunable nanocomposite of CdTe quantum dots linked to dendrimer-tethered multi-wall carbon nanotubes. *Spectrochimica Acta A: Molecular and Biomolecular Spectroscopy*, *70*, 966-972.

[91] Deng, S. S., Lei, J. J., Liu, Y. Y., Huang, Y. Y. & Ju, H. H. (2013). A ferrocenyl-terminated dendrimer as an efficient quencher via electron and energy transfer for cathodic electrochemiluminescent bioanalysis. *Chemical Communication*, *49*, 2106-2108.

[92] Triulzi, R. C., Micic, M., Orbulescu, J., Giordani, S., Mueller, B. & Leblanc, R. M. (2008). Antibody-gold quantum dot-PAMAM dendrimer complex as an immunoglobulin immunoassay. *Analyst*, *133*, 667-672.

[93] Liu, Y., Brandon, R. Cate, M., Peng, X., Stony, R. & Johnson, M. (2007). Detection of pathogens using luminescent CdSe/ZnS dendron nanocrystals and a porous membrane immunofilter. *Analytical Chemistry*, *79*, 8796-8802.

Chapter 2

ZnS:Mn Nanoparticles Functionalized by PAMAM-OH Dendrimer based Fluorescence Ratiometric Probe for Cadmium

2.1 Contribution to this Paper

My contribution to this paper started with the bibliographic research and writing about zinc QDs, dendrimers and then the experimental planning. The synthesis, purification and functionalization with dendrimers were performed, even all the complementary studies including the effect of some parameters such as pH, ionic strength and the tolerance to some ions on the excitation/emission matrix. The data obtained by the characterization methods was analyzed and interpreted. The determination of analytical parameters and the application to real samples was also performed by collecting real samples *in situ* and assayed with the fluorescent nanosensor. This paper was submitted as a scientific article and until the acceptation it passes through some adjustments required by the reviewers and under supervision of my advisor Professor Joaquim Esteves da Silva and co-advisor Doutor Manuel Algarra.

Talanta 134 (2015) 317–324

Contents lists available at ScienceDirect

Talanta

journal homepage: www.elsevier.com/locate/talanta

ZnS:Mn nanoparticles functionalized by PAMAM-OH dendrimer based fluorescence ratiometric probe for cadmium

Bruno B. Campos [a], Manuel Algarra [b,*], Ksenija Radotić [c], Dragosav Mutavdžić [c], Enrique Rodríguez-Castellón [b], José Jiménez-Jiménez [b], Beatriz Alonso [d], Carmen M. Casado [d], Joaquim C.G. Esteves da Silva [a]

[a] Centro de Investigação em Química, Departamento de Química e Bioquímica, Faculdade de Ciências da Universidade do Porto, Porto, Portugal
[b] Departamento de Química Inorgánica, Facultad de Ciencias, Universidad de Málaga, Campus de Teatinos s/n, 29071 Málaga, Spain
[c] Institute for Multidisciplinary Research, University of Belgrade, KnezaVišeslava 1, 11000 Beograd, Serbia
[d] Departamento de Química Inorgánica, Universidad Autónoma de Madrid, Cantoblanco, 28049 Madrid, Spain

ARTICLE INFO

Article history:
Received 8 July 2014
Received in revised form
3 October 2014
Accepted 8 October 2014
Available online 24 November 2014

Keywords:
Dendrimer
Quantum dots
ZnS:Mn^{2+}
Ratiometric sensor
Cadmium

ABSTRACT

We report a nanocomposite of ZnS:Mn quantum dots and a third generation PAMAM-OH dendrimer (ZnS:Mn@PAMAM-$OH_{G=3}$) which was rationalized to be used as ratiometric nanosensor for Cd^{2+} in aqueous solution. The nanoparticles exhibited a bright yellow-orange emission with peaks at 448 and 595 nm. The structure of ZnS:Mn was not changed after coupling with PAMAM-OH, which was evidenced by the analysis of the emission spectra of the compounds. The results confirm that the prepared fluorescence nanoparticles could selectively detect Cd^{2+} in aqueous solution with a limit of detection of 24.34 μM and RSD 4.07%, obtained by using the ratio I_{448}/I_{595}. The method was applied to different water samples.

1. Introduction

The synthesis of doped quantum dots (QDs) allows the development of nanomaterials with different and improved properties, when compared with the raw QDs, and is receiving much attention [1–6]. A favorable system to be doped is zinc sulfide fluorescent nanoparticles (ZnS QDs) by Mn^{2+} ions, which confers characteristic emission independent of the size of the nanoparticle, due to the lower lying states of Mn^{2+} ions ($^4T_1 \rightarrow {}^6A_1$) [7], permitting larger Stokes shift to avoid self-absorption, longer excited state lifetime, enhanced thermal and chemical stabilities, and minimized toxicity [8–15].

ZnS nanocrystals doped with manganese ions (ZnS:Mn) have attracted great interest on account of their high quantum efficiency and thermal stability, essential properties for chemical applications such as chemical and biosensor, molecular imaging, monitoring drug delivery, etc. [16–20].These properties can be improved substantially by modifying their surfaces with increasing quantum efficiency and stability; therefore ZnS:Mn has been conjugated with different ligand exchange coating agents such as glucose oxidase, for glucose biosensor in biological fluids [21], polyethyleneimine, for heparin assay [22], thioglycerol, for bioimaging [23], chitosan and PEG, for bio-labelling [24,25].

Besides all these nanocomposites materials, dendrimer derivates have been recently exploited for coatings of nanoparticles surfaces which can alter the charge, functionality and reactivity. Simultaneously, the coupling of QDs with dendrimers enhances the stability and dispersion of the nanoparticles as demonstrated by previous results showing that, the dendrimers functionalized CdSe and ZnSe QDs, enhanced their behavior in aqueous solution for quantification of heavy metals and C-Reactive Protein, respectively by means the quenching effect caused to the emission of QDs [26,27]. In the literature, just a few works are found involving fluorescent semiconductors and the terminated OH-poly(amidoamine) dendrimer (PAMAM-OH). As example, CdS QDs were synthesized by using hydroxyl-terminated PAMAM dendrimers as templates and investigated the effects of Cd^{2+} ion/dendrimer ratio, dendrimer generations, and temperatures on the resultant CdS QDs [28]. Due to the harmful cumulative effect of cadmium-containing QDs in the human body [29], arouse a major interest in less toxic fluorescent nanoparticles.

In this work a novel ratiometric chemical nanosensor for Cd^{2+} ions based on terminated OH-poly(amidoamine) dendrimer (PAMAM-OH) of third generation was developed. This nanosensor

* Corresponding author. Tel.: +34 952 131873; fax: +34 952 132000.
E-mail address: malgarra67@gmail.com (M. Algarra).

http://dx.doi.org/10.1016/j.talanta.2014.10.010
0039-9140/

resulted from the research of two different families of dendrimers, functionalized ZnS:Mn QDs, (ZnS:Mn@PAMAM-$OH_{G=3}$). The presence of this ion in the environment raises human health concerns. This Cd^{2+} nanosensor shows minimal interference of environmental conditions when competing with other species, and in the presence of Cd^{2+} an enhancement of the fluorescent intensity is observed. This ratiometric nanosensor, based on QDs functionalized dendrimer, is the first attempt with this of nanomaterial [30,31].

2. Experimental

2.1. Chemicals

Zinc(II) acetate ($ZnAc_2$, %), sodium sulfide ($Na_2S \times 9H_2O$, 99.99%), manganese(II) chloride ($MnCl_2 \times 4H_2O$, 99.99%), *L*-cysteine (Cys, > 97%), mercaptoacetic acid (> 99.0%, MAA), mercaptosuccinic acid (MSA, > 97%) and hydroxyl-terminated poly(amidoamine) dendrimer in methanol of third generation (PAMAM-$OH_{G=3}$) were purchased from Sigma-Aldrich Química S.A. (Spain). In all experiments deionized water was used.

2.2. Synthesis of ZnS:Mn coated with PAMAM-OH dendrimer

To obtain ZnS:Mn QDs, 2.5 mL of $ZnAc_2$ 0.1 M were mixed with 25 mL of Cys and MAA 0.02 M, used as ligand agent; and left stirred for 15 min, when were added 4 mL of $MnCl_2$ 0.01 M with continue stirring for 1 h. After this, previous addition of NaOH 1 M to adjust the pH at 11, was added 3.5 mL of Na_2S 0.1 M to be gently mixed. The crude reaction mixture was heated for 30 min at 90 °C and controlled by its fluorescence at 545 nm. After 48 h, the purification process was followed by the dialyzing of ZnS:Mn QDs for 6 h, precipitated with HCl 0.1 M, centrifuged, filtered and dissolved at pH 8.5, affording a fluorescent a colorless dissolution with at 595 nm.All experiments carried out were prepared with analytical grade reagents supplied from Sigma-Aldrich Química S.A. (Spain).

2.3. Characterization of ZnS:Mn coated with PAMAM-OH dendrimer

Fluorescence measurements were performed using a Jovin Yvon Fluoromax 4 TCSPC (Horiba), and measured between 400 and 700 nm using an integration time of 0.1 s and 5 nm slits for excitation and emission. Fluorescence lifetime analysis was done using an Edinburgh Instruments FLS920, equipped with a Xe lamp (450 W) as excitation source for steady state fluorescence measurements and monocromatics LEDs (PicoQuant PLS), controlled by a PDL 880-B system. Fluorescence decays were interpreted in terms of a multi-exponential: $I(t)=A+\Sigma B_i \exp^{-t/\tau i}$, where A and B_i are the pre-exponential factors and τ_i the decay times. Quantum yields (QY) of ZnS:Mn and ZnS:Mn@PAMAM-$OH_{G=3}$ were obtained using Rhodamine 6 G ($\Phi=0.93$ in methanol, $n=1.329$ and $\lambda_{ex}=535$ nm) as reference; ZnS:Mn and ZnS:Mn@PAMAM-$OH_{G=3}$ were dissolved in deionized water ($n=1.33$) and by 1, leads to obtain the QY of both nanoparticles (UV spectra is showed as Supporting Information Fig. SI1):

$$QY_{CDs} = QY_{st}\left[\frac{(dI/dA)_{CDs}}{(dI/dA)_{st}}\right]\left(\frac{n^2_{CDs}}{n^2_{st}}\right) \quad (1)$$

where *I* is the area under the fluorescence curves and A is the corresponding absorbance [32,33].

Transmission Electron Microscopy (TEM) and Energy Dispersive spectroscopy (EDAX) analysis were carried out with a Philips CM-200. X-ray photoelectron spectroscopic (XPS) studies were performed on a Physical Electronic PHI 5700 spectrometer using non-monochromatic MgK_α radiation (300 W, 15 kV, 1253.6 eV) for analyzing the core-level signals of the elements of interest with a hemispherical multichannel detector. The spectra of powdered samples were recorded with a constant pass energy value at 29.35 eV, using a 720 μm diameter circular analysis area. The X-ray photoelectron spectra obtained were analyzed using PHI ACESS ESCA-V6.0 F software and processed using Multipak 8.2B package. The binding energy values were referenced to adventitious carbon C 1 s signal (284.8 eV). Shirley-type background and Gauss-Lorentz curves were used to determine the binding energy. The size and zeta potential (ζ) of CDs were determined using a Zetasizer Nano ZS (Malvern Instruments, U.K.) equipped with a 4 mWHeNe laser operating at $\lambda=633$ nm. Size measurements were recorded with dynamic light scattering (DLS), at 25 °C in a polystyrene cell (ZEN0040) at a scattering angle of 173° and were average of three tests. The ζ measurements were also performed at 25 °C in polycarbonate folded capillary cells, incorporated with gold plated electrodes (DTS1061) and deionized H_2O was the dispersion medium. Both, size and ζ were automatically obtained by the software, using the Stokes-Einstein and the Henry equation, with the Smoluchowski approximation.

2.4. Fluorescence data analysis

For fluorescence data analysis of the different nanoparticles system which conform the ZnS:Mn coated by PAMAM-OH dendrimer, a series of emission spectra was collected, by excitation at different wavelengths, in the range 300–400 nm with 5 nm step. The emission spectra were measured in the range 400–670 nm, with 3 nm increment. In the analysis we used 4 matrices, corresponding to the pure ZnS, pure PAMAM-$OH_{G=3}$ dendrimer, ZnS:Mn and ZnS:Mn@PAMAM-$OH_{G=3}$. The artificial Raman bands were removed from the raw spectra by using the ale – UV–vis-IR Spectral Software 1.2, FluorTools, www.fluortools.com software. Each matrix was analyzed by using Multivariate Curve Resolution-Alternating Least Squares (MCR-ALS) method [34], which extracted the number of components, as well as their emission profiles. All analyses were performed using The Unscrambler software package (Camo ASA).

2.5. Atomic absorption spectroscopy

All the water samples were analyzed by AAS with a Cadmium (Cd) Lumina Hollow Cathode Lap. In 6 mL of water samples were acidified with 185 μL of 65% HNO_3 and the cadmium stock solutions were prepared by diluting different aliquots of a 1000 μg/mL cadmium standard stock solution. The measurements were done in a concentration range of 0.5–5 mg/L for the calibration curve with a linear regression of 0.9978.

2.6. Metal study

Previous the study of the enhancement effect of cadmium (Cd^{2+}), the metals As^{3+}, Ba^{2+}, Cd^{2+}, Co^{2+}, Cr^{3+}, Cu^{2+}, Fe^{3+}, Hg^{2+}, Mg^{2+}, Ni^{2+}, Pb^{2+}, Sb^{3+}, Tl^{+} and anions CN^-, CO_3^{2-}, SO_4^{2-} were studied by addition of 100 μL of the different metals stock solution (5×10^{-3} M) to 500 μL of ZnS:Mn@PAMAM-$OH_{G=3}$ to the desired concentrations levels in 1 mL of volume, filled up by H_2O. The solution mixture was then equilibrated at room temperature for 5 min before the spectral measurements at 448 and 595 nm. To check the selectivity of this sensor, the experiments were carried out with other metals ions including: Cu^{2+}, Fe^{3+}, Hg^{2+}, Pb^{2+}, Tl^{+} and Zn^{2+}, maintaining the same Cd^{2+} concentration (2.25×10^{-4} M) and ranging the metal ratio concentrations (1:1; 1:5; 5:1). The operation was exactly similar conditions that were used for the detection of Cd^{2+}; Data were obtained by the following

relationship (2):

$$Ratio = \frac{(I_{448}/I_{595})_{ZnS:Mn@PAMAM-OH:Cd-Metal}}{(I_{448}/I_{595})_{ZnS:Mn@PAMAM-OH:Cd}} \quad (2)$$

where ZnS:Mn**@**PAMAM-OH:Cd^{2+}-Metal is the ratio obtained when in dissolution are presented the proposed sensor with Cd^{2+} and the studied metal used as interference, and ZnS:Mn**@**PAMAM-OH:**Cd^{2+}** without metal assayed.

3. Discussion of the results

3.1. Synthesis and analysis of ZnS:Mn nanoparticles

Different parameters were studied to obtain the higher fluorescence intensity, the stabilizing agent, the pH and the concentration of the Mn^{2+} dopant. The planning experiments were drawn in the *Unscrambler* programme. The stabilizing agents studied were the Cys, MSA and MAA, all three had 0.02 M. The reactions were performed at different pH, at 7 and 11, and the concentration of Mn^{2+} was comprised between 0.179 and 0.833 mM, (Fig. SI2A) excited at 405 nm. Cys was selected at pH 11, the optimal value for ZnS nanoparticles. The heating time due to is well known factor to obtain larger size of nanoparticles was studied, and after the results obtained (Fig. SI2B) was observed that a time of 30 min was selected to obtain the best emission intensity. To obtain ZnS:Mn nanoparticles, a range of concentration for Mn^{2+} comprised between 0.179 and 0.833 mM was analyzed, being 0.179 mM the most intense signal under this proposal synthesis (Fig. SI2C).

After the dialyzing purification process, a red shift to 595 nm was observed in the emission spectra, excited at 345 nm (Fig. 1). For ZnS:Mn nanoparticles, two different emission bands are presented in the fluorescence spectra: the first emission band, at about 450 nm, also existed in the emission spectrum of the undoped ZnS nanocrystals. This emission band is due to the host ZnS but not from Mn^{2+} ions. Upon Mn^{2+} doping, a second characteristic emission band centered at around 595 nm is developed for the well-known $^4T_1 \rightarrow {}^6A_1$ d–d transition of Mn^{2+} ions on Zn^{2+} sites, where Mn^{2+} is tetrahedrally coordinated by S^{2-}. This can be explained as Mn^{2+} incorporated into the ZnS lattice led to the Mn^{2+} based orange emission while ZnS with surface bound Mn^{2+} yielded the ultraviolet emission. Thus, it could be concluded that the Mn^{2+} ions in our samples were incorporated into the host ZnS nanocrystals [35,36].

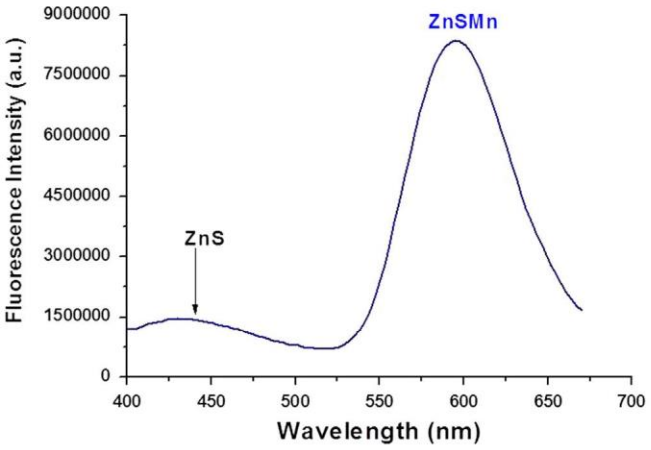

Fig. 1. Fluorescence spectra of dialyzed ZnS:Mn^{2+} with [Mn^{2+}]=0.179 M at pH 11 and coated with Cys (0.02 M) after 30 min of heat. Excitation at 345 nm.

3.2. Characterization of ZnS:Mn nanoparticles

The size and morphology of ZnS:Mn nanoparticles were characterized by TEM (Fig. 2), where nearly monodispersed cores were obtained with an average diameter of 4 nm and revealed packs of parallel willing with a high regular disposition, inset in Fig. 2 is showed the inter-planar distance 0.30 nm which agreed well with obtained previously [37]. The average hydrodynamic size was 17.33 ± 4.97 nm from DLS data (Fig. SI3), thus suggesting that the nanoparticles dispersed well in water. The hydrodynamic diameters were larger than those of the cores due to the solvation layer around the QDs in aqueous solution. Later analysis was obtained the size from DLS data for ZnS:Mn@PAMAM-$OH_{G=3}$, which provided a value of 19.50 ± 4.24 nm. The nanoparticles were subjected to EDAX analysis (Fig. SI4) which shows the general composition of ZnSMn studied, thus clearly shows the presence of Mn^{2+} (0.62%), Zn (19.04%) and S (80.34%), supporting that Mn^{2+} ion was incorporated by substitution into the ZnS host lattice and confirmed by XPS analysis. The negative ζ of ZnS:Mn nanoparticles (-19.90 ± 0.50 mV) is due to the presence of deprotonated cysteine groups on the nanoparticles surface ($pK_a(\alpha\text{–}NH_3^+)=10.78$ and pK_a ($-CH_2$-SH)=8.33, consistent with the pH of the synthesis procedure. The ATR spectra analysis showed (Fig. SI5) three main broad bands which are assigned at 1629 cm^{-1} ($-COO^-$), the band with a shoulder comprised between 3000–3500 cm^{-1} (–OH and N–H) and the weak broad band at 2130 cm^{-1} is assigned at the stretching band of the S-H, which is indication of the low vibration of the covalent bond formed with the ZnS QDs. In the same figure, the spectra of the coated nanoparticles with PAMAM-$OH_{G=3}$ are overlapped, where the only difference is the presence of two bands at 2365 and 2344 cm^{-1}.

3.3. XPS analysis

The XPS study of the ZnS:Mn nanoparticles stabilized with cysteine gives relevant information concerning the surface of the nanoparticles. The C 1*s* core level spectrum (Fig. SI6A) can be decomposed into three contributions at 284.8 eV (75%), 286.1 eV (15%) and 288.1 eV (10%). This spectrum is more or less similar to that of L-cysteine reported in the literature [38] were three contributions at 285.2, 286.7 and 288.5 eV was reported. The first contribution at low binding energy (284.8 eV) is assigned, in addition of adventitious carbon, to C-S- groups. The second at 286.1 eV is mainly due to C-NH_2 and present an area slightly higher than that of the third contribution at 288.1 eV due to the carboxylate group. The S 2*p* core level spectrum (Fig. SI6B) shows a single peak with the doublet S $2p_{3/2}$ and S $2p_{1/2}$ at 161.1 and 162.3 eV, respectively. This signal is assigned to sulfur as thiolated [38], and free thiol groups were not observed in the S 2*p* core level spectrum (signal at about 164 eV). The N 1*s* spectrum (not shown here) shows a maximum at about 400.0 eV and is assigned, as expected, to the amino group of cysteine. The Zn $2p_{3/2}$ core level spectrum shows a single symmetric maximum centered at 1021.2 eV (Fig. SI6C). This peak is not very informative concerning the chemical state of Zn, for this reason the $ZnL_3M_{4,5}M_{4,5}$ Auger spectrum was also registered (Fig. SI6D). In this way is possible to calculate the modified Auger parameter (α') according 3. This Auger signal is sensitive to the chemical state of zinc, and two contribution were observed at 260.9 eV (26%) and 263.7 eV (74%).

$$\alpha' = 1253.6 + KE(ZnLMM) - KE\left(Zn\ 2p_{3/2}\right) \quad (3)$$

where KE(ZnLMM) is the kinetic energy of the Auger electron of ZnLMM and KE(Zn $2p_{3/2}$) the kinetic energy of the photoelectron Zn $2p_{3/2}$, and 1253.6 eV is the energy of the excitation source.

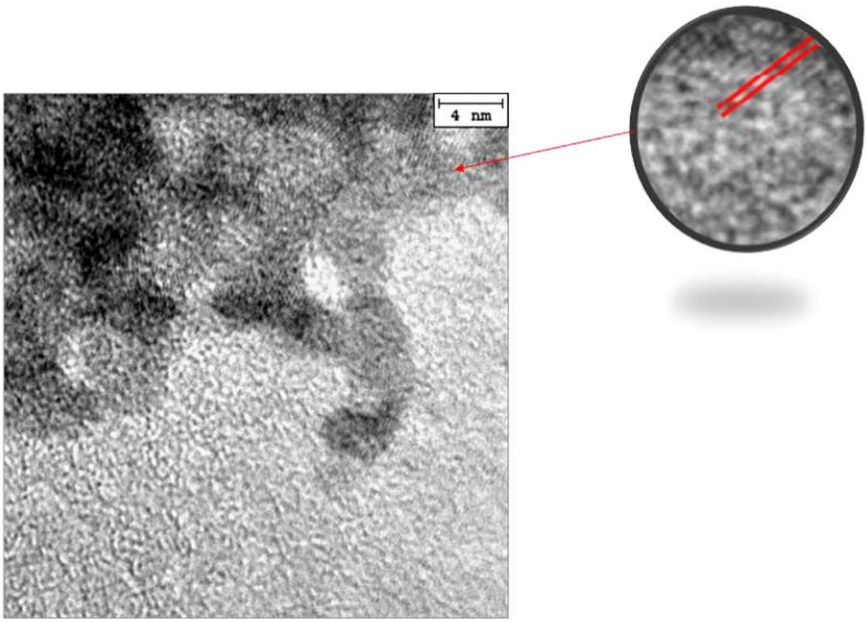

Fig. 2. TEM image of ZnS:Mn 4 nm of average diameter (Inset a magnification of the inter-planar distance of 0.30 nm).

The calculated α' values were 2013.9 and 2011.1 eV, respectively. And using the correspondent Wagner's diagram [39], the presence of a core of ZnS ($\alpha'=2011.2$ eV) in the nanoparticles with Zn bonded to surface cysteine through the thiol group ($\alpha'=2013.9$ eV) is suggested. The Mn 2*p* signal (not shown) is very weak, showing a photoemission Mn $2p_{3/2}$ at 640.3 eV. This value is similar to that reported at 640.4 eV for MnS [39] C: 46.42%, O: 16.31%, N: 3.60, S: 18.15%, Cl 1.49%, Mn: 0.13% and Zn 13.90%. This composition also indicates that part of sulfur is forming part of the metallic sulfide and the excess corresponds to the thiolated groups. The coexistence of metallic Zn and ZnO was confirmed, although it was not possible to distinguish between the single metallic Zn^0 and the alloyed Zn^0.

3.4. Functionalization with PAMAM-$OH_{G=3}$

Two families and generations of dendrimers, PAMAM with hydroxyl terminal groups (PAMAM-$OH_{G=2,\ 3,\ 5}$) and thiol-terminated DAB dendrimers ($DAS_{G=2-5}$) have been assayed, to analyze the influence of the addition to ZnS nanoparticles (Fig. SI7). As observed, all dendrimers conferred a protective environment to ZnS nanoparticles, as observed in the fluorescence intensity, which is most increased in the presence of PAMAM-$OH_{G=2,3}$. It was observed that the hydroxyl dendrimer derivates (PAMAM-$OH_{G=3,5}$) showed fluorescence emission by theirselves, explained by their synthesis procedure (Fig. SI8) [40], being selected PAMAM-$OH_{G=3}$ which showed for a hand a higher fluorescence intensity (Fig. SI9) and low influence on the emission band at 595 nm when added at different concentration to ZnS:Mn nanoparticles (Fig. 3).

The conjugation of PAMAM-$OH_{G=3}$ with ZnS:Mn is not a typically fluorescence resonance energy transfer (FRET) because both raw and coupled bands remained practically immutable, as proof the quantum yield (Φ) for ZnS:Mn and ZnS:Mn@PAMAM-$OH_{G=3}$ are 0.1470 and 0.1509, respectively, in methanol solution. The fluorescence mechanism could not be supported by the donor-acceptor excitons transfer because PAMAM-$OH_{G=3}$ itself presents fluorescence at 448 nm and the doped QD at 595 nm, when the dendrimer is added to the doped QD, the zinc can form stable complexes with dendrimer trough its interior amino groups rather

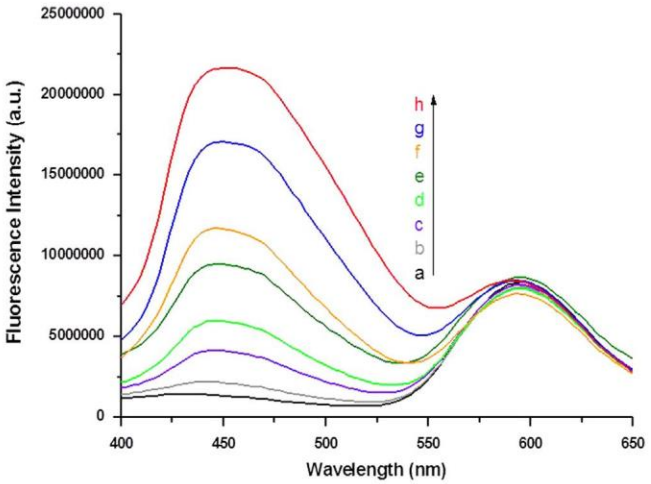

Fig. 3. Influence of the concentration of PAMAM-$OH_{G=3}$ on the fluorescence intensity of $ZnS:Mn^{2+}$: (a) 0 M; (b) 4.07×10^{-8} M; (c) 2.04×10^{-7} M; (d) 4.07×10^{-7} M; (e) 8.14×10^{-7} M; (f) 1.22×10^{-6} M; (g) 2.44×10^{-6} M and (h) 4.07×10^{-6} M. Excitation at 345 nm.

than exterior hydroxyl groups [41]. Probably, due to the binding nature between PAMAM-$OH_{G=3}$ and ZnS:Mn, the chemical relation which they have is mainly about donor-acceptor electrons and at quantum level a reduced donor-acceptor excitons effect, maintaining the fluorescent signals of raw and coupled bands almost equal. The effect of ionic strength on fluorescence was analyzed, by using increasing concentration of NaCl (between 0 and 2 M), showing a decreasing about 57% in the intensity when NaCl concentration does increase, even though at small concentration, indicating the moderate tolerance of ZnS:Mn@PAMAM-$OH_{G=3}$ (Fig. SI10).

The effect of pH (4-11) on the fluorescence intensity was studied, and was compared with ZnS:Mn, showing the similar behavior. With increasing the pH from 6.04 to 6.90 a drastic decreasing of the intensity (60%) is observed, for ZnSMn, but when is analyzed ZnS:Mn@PAMAM-$OH_{G=3}$, this drastic decrease was observed at 8.72 (Fig. SI11). Similar behavior at different values is

found when coated by the dendrimer but, the decrease occurs at slightly high pH, explained that dendrimer coating process protect from the environment.

3.5. Component analysis of ZnS:Mn@PAMAM-$OH_{G=3}$ by MCR-ALS

The results of MCR-ALS analysis of the emission profiles for pure ZnS, pure PAMAM-$OH_{G=3}$ dendrimer, ZnS:Mn and ZnS:Mn@PAMAM-$OH_{G=3}$ are included in Fig. 4. The emission spectrum of ZnS contains four components with the maxima at 439, 493, 535 and 595 nm. After complexation with Mn^{2+}, the first three components of ZnS disappear due to the formation of a new compound, and the new components are formed at 472, 556, 589 and 643 nm. The fourth ZnS component stays unchanged. The PAMAM-OH spectrum contains two contributions at 454 and 465 nm. In the spectrum of ZnS:Mn@PAMAM-$OH_{G=3}$ five components can be observed. The one PAMAM-OH component, at 454 nm, stays unchanged, while its second component is blue shifted for 20 nm, at position 445 nm. The other three components, at 556, 589 and 643 nm come from ZnSMn and are unchanged in the complex with PAMAM-OH. This shows that PAMAM-OH does not change structure of ZnSMn, and change of the one PAMAM-OH component is due to binding to ZnSMn. This is evidence that the formed complex is stable.

3.6. Fluorescence enhancement with Cd^{2+} ions. Ratiometric sensor of Cd^{2+}

Previous the study of the enhancement effect of cadmium (Cd^{2+}), a screening of metals were performed, to analyse the response of the proposed ZnS:Mn@PAMAM-$OH_{G=3}$, used as metal sensor. When no metal ion was added to the solution, the emission profile could be summarized at 448 and 592 nm, being this band where the most interesting results are obtained when added the metals to the solution (Fig. 5).

The effect found are the enhancement due to Tl^{+} (20.2) and Cd^{2+} (32.1), being this metal which offered a significant enhancement of the signal at 595 nm (2 folds), when compared with the others metals added in separated experiments. No significance changes in the intensity was found when added As^{3+} (4.9), Ba^{2+} (1.4), CN^{-} (1.6), CO_3^{2-} (2.8), Mg^{2+} (1.2) and SO_4^{2-} (1.0), moderated for Co^{2+} (11.1), Cr^{3+} (8.6), Ni^{2+} (11.8) and Sb^{3+} (6.2). Metal ions such as Cu^{2+} (18.3), Fe^{3+} (56.9), Hg^{2+} (69.7) and Pb^{2+} (73.1) could cause a larger quenching effect (the values presented in parenthesis represents the mean variation of fluorescence intensity, in percentage, (Fig. 6). Due to the enhancement on the fluorescence intensity effect found and the concern of the Cd^{2+} in the environment was considered the most interesting metal ion to be studied. In Section 2.5 the relationship to obtain the data obtained is detailed.

The concentration effect of Cd^{2+} was studied in the range comprised between 5×10^{-5} and 2.5×10^{-3} M (Fig. SI12A). Under the optimum conditions, the change in the fluorescence intensity at 595 had a prominent linear relationship ($r > 0.999$) with the concentration of Cd^{2+} over the range 1.225×10^{-5}–6.75×10^{-4} M. The inset in Fig. SI12A indicates the correlation of the intensity ratios of emission at 448 nm to 595 nm (I_{448}/I_{595}). When was observed the effect in the two bands studied, is possible to justify that the functionalization of ZnSMn by PAMAM-$OH_{G=3}$ dendrimer is a good approach, (Fig. SI12B and C), where are represented the influence on the fluorescence intensity of ZnS:Mn@PAMAM-$OH_{G=3}$ at different Cd^{2+} concentrations, observed at 595 nm (Fig. SI12B) when compared with raw ZnSMn nanoparticles, and 450 nm (Fig. SI12C) respectively when is compared with raw PAMAM-$OH_{G=3}$, which demonstrated the effective functionalization of ZnSMn and its potential use as ratiometric sensor of Cd^{2+}, always the presence of the dendrimer in the system improve the analytical signal. In both cases, the fluorescence intensity of ZnS:Mn**@**PAMAM-$OH_{G=3}$ increased at 448 nm and 595 nm comparing with raw PAMAM-$OH_{G=3}$ and raw ZnS:Mn bands. At 448 nm, the fluorescence intensity of ZnS:Mn@PAMAM-$OH_{G=3}$ is higher than raw PAMAM-$OH_{G=3}$, even at low concentrations of Cd^{2+}. At 595 nm, the fluorescence intensity of ZnS:Mn@PAMAM-$OH_{G=3}$ is higher than doped QDs from 110 μM of Cd^{2+}, giving the same fluorescent response below. This probably demonstrates the preferential binding of Cd^{2+} for the thiol group of Cys rather than amino groups of PAMAM-$OH_{G=3}$ dendrimer. When the Cd^{2+} ions complexed with thiol groups, the signal of ZnS:Mn and PAMAM-$OH_{G=3}$ is enhanced due to a charge transfer between a Cd^{2+}@ZnS:Mn and the ZnS:Mn@PAMAM-$OH_{G=3}$, until a point where the thiol groups are fully complexed and the remaining Cd^{2+} starts to complex with amino groups of the dendrimer, quenching the signal of PAMAM- $OH_{G=3}$ and saturating the signal of ZnS:Mn. The proposed sensor was optimized to obtain the best sensitivity. The limit of detection (LOD) and quantification (LOQ=3 × LOD) were 24.334 and 81.114 μM, respectively, with an accuracy as relative standard deviation (RSD, $n=10$)=4.07%, as analytical Figures of merit.

Previously to this work, our group did a similar study involving nanocomposites of QDs and dendrimers for the detection of Cd^{2+} ions by using CdSe QDs functionalized with thiolated DAB dendrimer of generation 5. The same fluorescent response behavior of enhancement was obtained and the S-DAB-G5-CdSe sensor emitted a single band at 535 mm (λ_{ex}=408 nm) and a LOD of 10.08 μM [26]. Another analytical example for the detection of Cd^{2+} involved the use of MPA-capped CdTe QDs and the sensing was obtained by enhancing the fluorescent signal with free Cd^{2+} ions at 615 nm (λ_{ex}=350 nm), the LOD founded was 0.5 μM [42]. Beside of the ZnS:Mn@PAMAM-$OH_{G=3}$ sensor has a superior LOD than the S-DAB-G5-CdSe nanocomposites and the MPA-capped CdTe QDs, the proposed sensor for Cd^{2+} detection has a huge advantage of being free of cadmium, avoiding the toxicological problems associated to the cadmium-based QDs (Table 1).

3.7. Tolerance to interferences metal ions

To assess the possibility of analytical application of the present nanosensor, the effects of different concentration ratios of several cations, that may be presented in real samples, on the fluorescence intensity of ZnS:Mn@PAMAM-$OH_{G=3}$ with Cd^{2+} (2.25×10^{-7} M), was studied – Cu^{2+}, Fe^{3+}, Hg^{2+}, Pb^{2+}, Tl^{+} and Zn^{2+}. The fluorescence intensities of ZnS:Mn@PAMAM-$OH_{G=3}$, at different concentration ratios versus M^{n+}, (5:1; 1:1 and 1:5) were measured in separate sets of experiments and summarized in Table 2. Where ZnS:Mn@PAMAM-OH:**Cd**is the ratio obtained when in dissolution are presented the proposed sensor with Cd^{2+} and the studied metal used as interference, and ZnS:Mn@PAMAM-OH:**Cd^{2+}** without metal assayed. In all the cases analyzed, it was found a quenching effect on the signal of ZnS:Mn@PAMAM-OH:**Cd^{2+}**, obtaining a moderate behavior. The most pronounced effect was for Pb^{2+} with a signal decreased over 50–70%.

Fig. SI13A and B shows the results of MCR-ALS analysis of the emission profiles for ZnS:Mn@PAMAM-$OH_{G=3}$ complex in presence of Cd^{2+} ions. The emission spectrum contains three components. The components at 454 and 589 nm have the same position as in the complex in absence of Cd. The components at 454, 556 and 643 nm of the complex disappeared in the presence of Cd, while a new component appeared at 583 nm (Figs. 4 and SI13). This indicates that Cd induced certain structural changes of the complex. A conformation change may be proposed, having in mind a branched structure of the complex due to the PAMAM-OH dendrimer.

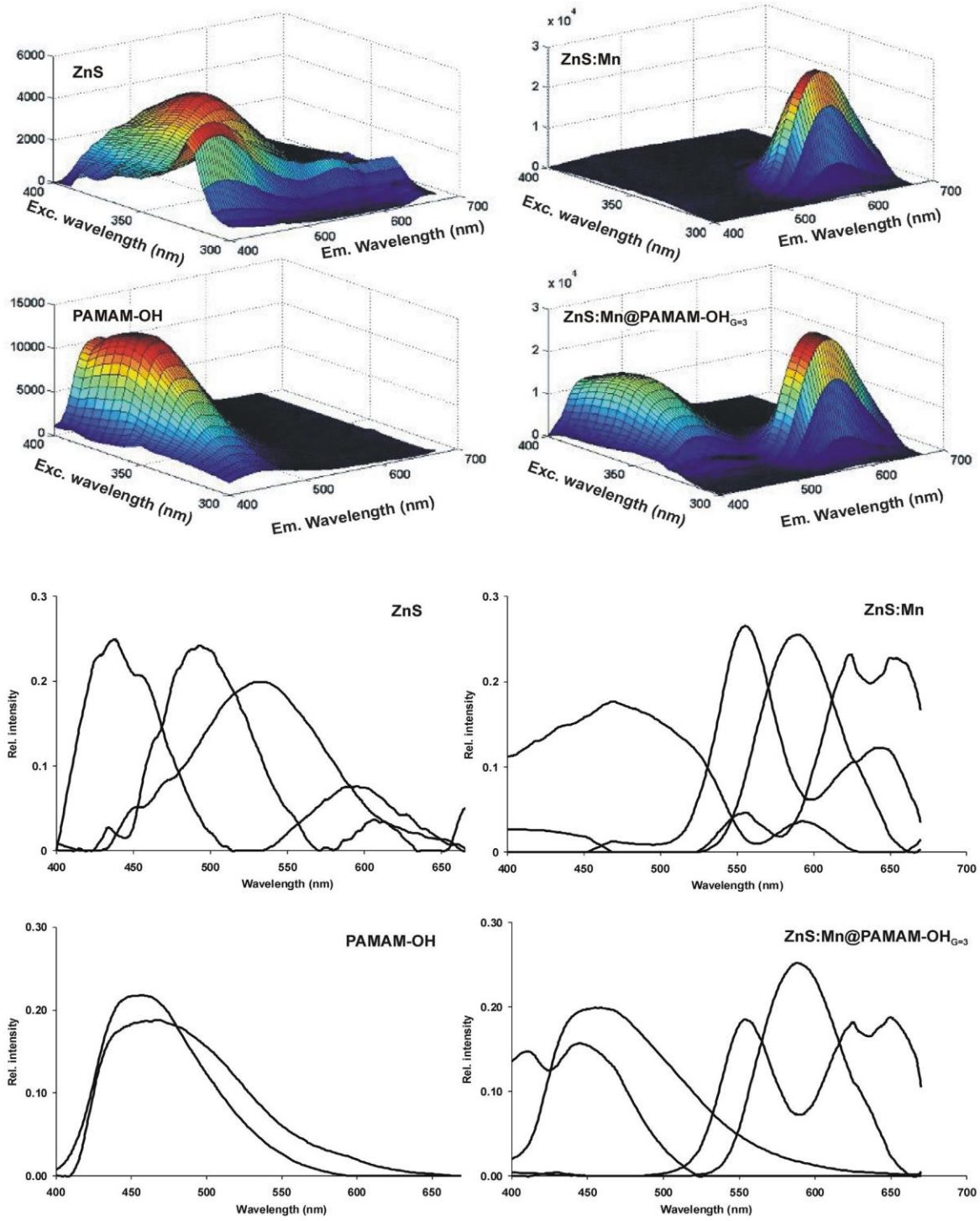

Fig. 4. Upper panel: Excitation-emission matrix for the raw spectra of ZnS, ZnS:Mn, PAMAM-OH and ZnS:Mn@PAMAM-OH$_{G=3}$; Lower panel: Estimated emission profiles for ZnS, ZnS:Mn, PAMAM-OH and ZnS:Mn@PAMAM-OH$_{G=3}$.

3.8. Application to drinking water

Due to the possibility of contamination in drinking water by Cd^{2+}, as result of an impurity from the Zn^{2+} or the galvanized pipes or Cd^{2+} containing solders in fittings, water heaters, water coolers and taps. Therefore, as application, were spiked different concentrations of Cd^{2+} in tap water, bottled water, river water and sewage. The results were compared with Cd^{2+} concentrations measured by Atomic Absorption Spectroscopy (AAS) and are presented in Table 3. In average, the results obtained by the proposed ratiometric sensor have a slight deviation (less than 10%) concerning to the Cd^{2+} concentrations measured by AAS, for the same samples. Comparing the precision of the two analytical methods, the ZnS:Mn@PAMAM-OH$_{G=3}$ sensor showed a mean precision of 5.88% ± 2.45% instead of the 1.41% ± 0.76% for the AAS, this probably occurs because of the huge active sites of dendrimer

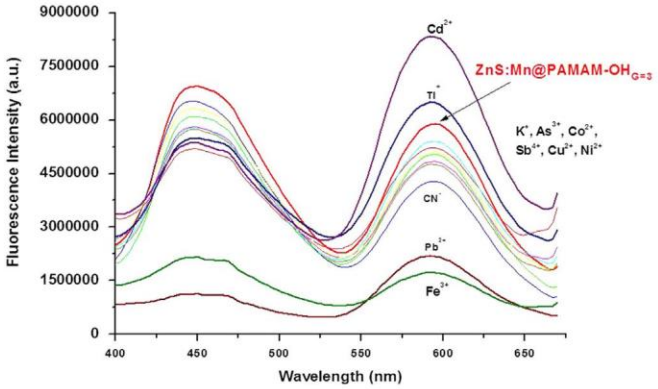

Fig. 5. Fluorescence spectra of ZnS:Mn@PAMAM-OH$_{G=3}$ upon addition of metal ions (7.5×10^{-7} M). excited at 405 nm.

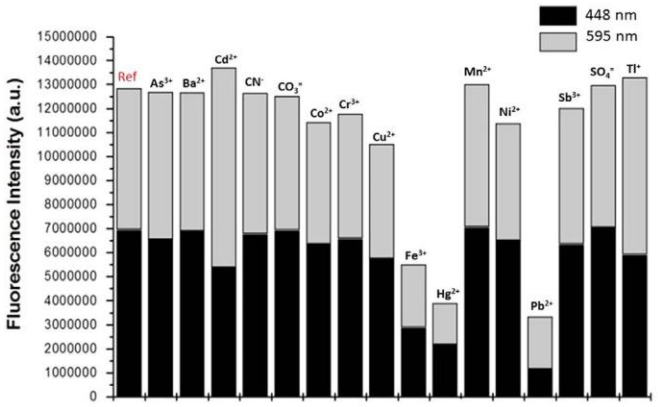

Fig. 6. Ratio of tolerance of the interferences species on the fluorescence spectra at 488 and 595 nm of ZnS:Mn@PAMAM-OH$_{G=3}$ excited at 405 nm.

Table 1
Analytical parameters for Cd^{2+} determination.

LOD (μM)	LOQ (μM)	RSD (%)	Sensitivity
23.44 ± 0.69	78.11 ± 2.26	5.78 ± 2.42	0.034 ± 0.001
Dynamic range: 2.34×10^{-5}–1.10×10^{-3} M			

Table 2
Tolerance ratio of ZnS:Mn@PAMAM-OH$_{G=3}$ when is dissolved Cd^{2+} (2.25×10^{-7} M) versus other metals as interference at different ratios.

	5:1	1:1	1:5
Cu^{2+}	0.65 ± 0.12	0.73 ± 0.09	0.81 ± 0.07
Fe^{3+}	0.84 ± 0.05	0.98 ± 0.02	0.85 ± 0.05
Hg^{2+}	0.61 ± 0.11	0.64 ± 0.12	0.83 ± 0.05
Pb^{2+}	0.53 ± 0.18	0.37 ± 0.32	0.43 ± 0.20
Tl^{+}	0.62 ± 0.10	0.59 ± 0.20	0.56 ± 0.15
Zn^{2+}	0.61 ± 0.12	0.59 ± 0.14	0.53 ± 0.12

were the Cd^{2+} can be complexed, generating signals with light deviations.

4. Conclusions

Summarizing, we have explored the ratiometric behavior of ZnS:Mn^{2+} fluorescent nanoparticles when they are synthesized by a novel method and the further functionalization with hydroxyl terminated PAMAM dendrimer, and used as sensor probe for Cd^{2+}. Two emission bands at 448 and 595 nm were used to obtain the ratiometric ratio (I_{448}/I_{595}). By a wide of analytical techniques was characterized which concluded the presence of Mn^{2+} in the ZnS lattice which produces the orange emission under UV light. The presence of dendrimer in the surface of ZnS:Mn^{2+} increase the QY and the stability when was studied the pH dependence. The main conclusion after fluorescent component analysis was that no influence in the ZnS:Mn structure after coating with dendrimer. When used as sensor probe for Cd^{2+}, an enhancement of the band at 595 nm obtaining prominent linear relationship which was used for metal analysis in water.

An available alternative to fluorescent sensors based on cadmium-made QDs in the detection of free Cd^{2+} ions in real water samples.

Table 3
Comparation of Cd^{2+} measurements in different real water samples by AAS and ZnS:Mn@PAMAM-OH$_{G=3}$ sensor.

Water samples	$[Cd]_{AAS}$ (ppm)	$[Cd]_{Ir}$ (ppm)	Accuracy (%)
Tap	18.48 (0.25)**	16.89 (1.40)	8.59
	27.86 (0.27)	25.26 (1.72)	9.34
	36.49 (0.74)	36.65 (1.50)	0.44
	46.56 (0.19)	46.02 (1.89)	1.15
Bottled	15.07 (0.20)	15.15 (1.35)	0.50
	27.03 (0.57)	25.16 (1.41)	6.93
	37.72 (0.54)	34.33 (1.10)	8.99
	46.88 (0.14)	44.19 (1.28)	5.73
River	14.97 (0.18)	14.30 (1.36)	4.51
	28.12 (0.38)	30.30 (1.79)	7.74
	33.94 (0.20)	31.98 (1.31)	5.80
	45.08 (0.89)	43.57 (1.52)	3.36
Sewage	15.47 (0.49)	17.09 (1.83)	10.50
	27.24 (0.56)	27.77 (2.05)	1.96
	37.45 (0.22)	38.16 (1.91)	1.89
	46.03 (0.81)	42.93 (1.76)	6.72

*Means of three different determinations.
** Standard deviation in parenthesis.

Acknowledgments

Authors are gratefully to Grant SFRH/BD/84318/2012 to FCT (Lisbon, Portugal) and Grant 173017 from the Ministry of Education, Science and Technological development of the Republic of Serbia.

Appendix A. Supporting information

Supplementary data associated with this article can be found in the online version at http://dx.doi.org/10.1016/j.talanta.2014.10.010.

References

[1] D. Mocatta, G. Cohen, J. Schattner, O. Millo, E. Rabani, U. Banin, Science 332 (2011) 77.
[2] R. Zhang, W. Chen, Biosens. Bioelectron. 55 (2014) 83.
[3] J. Ju, W. Chen, Biosens. Bioelectron. 58 (2014) 219.
[4] P. Wu, X.P. Yan, Chem. Soc. Rev. 42 (2013) 5489.
[5] J. Planelles-Aragó, B. Julián-López, E. Cordoncillo, P. Escribano, F. Pellé, B. Viana, C. Sanchez, J. Mater. Chem 18 (2008) 5193.
[6] S. Sarkar, A.R. Maity, N.S. Karan, N. Pradhan, J. Phys. Chem. C 117 (2013) 21988.
[7] D.J. Norris, N. Yao, F.T. Charnock, T.A. Kennedy, Nano Lett. 1 (2001) 3.
[8] M. Behboudnia, P. Sen, Phys. Rev. B 63 (2001) 035316.
[9] A.A. Bol, A. Meijerink, J. Lumin. 87–89 (2000) 315.
[10] A.A. Bol, A. Meijerink, J. Phys. Chem. B 105 (2001) 10197.

[11] C. Jin, J. Yu, L. Sun, K. Dou, S. Hou, J. Zhao, Y. Chen, S. Huang, J. Lumin. 66–67 (1995) 315.
[12] N. Karar, F. Singh, B.R. Mehta, J. Appl. Phys. 95 (2004) 656.
[13] S. Sapra, A. Prakash, A. Ghangrekar, N. Periasamy, D.D. Sarma, J. Phys. Chem. B 109 (2005) 1663.
[14] H. Mattousi, J.M. Mauro, E.R. Goldman, G.P. Anderson, V.C. Sundar, F.V. Mikulec, M.G. Bawendi, J. Am. Chem. Soc. 122 (2000) 12142.
[15] M. Gaceur, M. Giraud, M. Hemadi, S. Nowak, N. Menguy, J.P. Quisefit, K. David, T. Jahanbin, S. Benderbous, M. Boissière, S. Ammar, J. Nanopart. Res. 14 (2012) 932.
[16] Y. Shang, L. Qi, F.Y. Wu, Microchim. Acta 177 (2012) 333.
[17] L. Zhu, S. Ang, W.T. Liu, Appl. Environ. Microbiol. 70 (2004) 597.
[18] W.Y. Xie, W.T. Huang, H.Q. Luo, N.B. Li, Analyst 137 (2012) 4651.
[19] T. Zhao, X. Hou, Y.N. Xie, L. Wu, P. Wu, Analyst 138 (2013) 6589.
[20] B.H. Zhang, L. Qi, F.Y. Wu, Microchim. Acta 170 (2010) 147.
[21] P. Wu, Y. He, H.F. Wang, X.P. Yan, Anal. Chem. 82 (2010) 1427.
[22] H. Yan, H.F. Wang, Anal. Chem. 83 (2011) 8589.
[23] M. Geszke-Moritz, H. Piotrowska, M. Murias, L. Balan, M. Moritz, J. Lulek, R. Schneider, J. Mater. Chem. B 1 (2013) 698.
[24] S. Baruah, G. Tumcharern, J. Dutta, Adv. Mat Res. 55–57 (2008) 589.
[25] H.Y. Kong, B.K. Song, J. Byun, C.S. Hwang, Bull. Kor. Chem. Soc. 34 (2013) 1181.
[26] M. Algarra, B.B. Campos, D. Gomes, B. Alonso, C.M. Casado, M.M. Arrebola, M.J. Diez de los Rios, M.E. Herrera-Gutiérrez, G. Seller-Pérez, J.C.G. Esteves da Silva, Talanta 99 (2012) 574.
[27] M. Algarra, B. Campos, B. Alonso, M.S. Miranda, A.M. Martínez, C.M. Casado, J.C.G. Esteves da Silva, Talanta 88 (2012) 403.
[28] D Yamamoto, T. Koshiyama, S. Watanabe, M.T. Miyahara, Coll. Sur. A: Phsicochem. Eng. Aspects 411 (2012) 12.
[29] N. Chen, Y. He, Y. Su, X. Li, Q. Huang, H. Wang, X. Zhang, R. Tai, C. Fan, Biomaterials 33 (2012) 1238.
[30] Y. Wei, H. Hao, J. Zhang, X. Hao, C. Dong, Anal. Methods 6 (2014) 3227.
[31] Y. Park, C. Koo, H.Y. Chen, A. Han, D.H. Son, Nanoscale 5 (2013) 4944.
[32] A.M. Brouwer, Pure Appl. Chem. 83 (2011) 2228.
[33] G. Weber, F.W.J. Teale, Trans. Faraday Soc. 53 (1957) 646.
[34] M. Algarra, K. Radotić, A. Kalauzi, B. Alonso, C.M. Casado, J.C.G. Esteves da Silva, Talanta 105 (2013) 267.
[35] R. Beaulac, P.I. Archer, D.R. Gamelin, J. Solid State Chem. 181 (2008) 1582.
[36] K. Sooklal, B.S. Cullum, S.M. Angel, C.J. Murphy, J. Phys. Chem. 100 (1996) 4551.
[37] R. Ban, J. Li, J. Cao, P. Zhang, J. Zhang, J.J. Zhu, Anal. Methods 5 (2013) 5929.
[38] O. Cavalleri, L. Oliveri, A. Dacca, R. Paroli, R. Polandi, Appl. Surf. Sci. 175–176 (2001) 357.
[39] J.F. Moulder, W.F. Stickle, P.E. Sobol, K.D. Bomben, J. Chastain (Eds.), Handbook of X-ray Photoelectron Spectroscopy, Perkin-Elmer Corporation Eden Prairie, 1992, p. 204.
[40] D. Wang, T. Imae, J. Am. Chem Soc. 126 (2004) 13204.
[41] A.B. Nepomnyashchii, M.A. Alpuche-Aviles, S. Pan, D. Zhan, F.R.F. Fan, A.J. Bard, J. Electroanal. Chem. 621 (2008) 286.
[42] H. Xu, R. Miao, Z. Fang, X. Zhong, Anal. Chim. Acta 687 (2011) 82.

2.2 Supplementary Data

Supplementary Material

ZnS:Mn Nanoparticles Functionalized by PAMAM-OH Dendrimer based Fluorescence Ratiometric Probe for Cadmium

B.B. Campos, M. Algarra K. Radotić, D. Mutavdžić, E. Rodriguez-Castellón, J. Jiménez-Jiménez, B. Alonso, C. M. Casado, J.C.G. Esteves da Silva

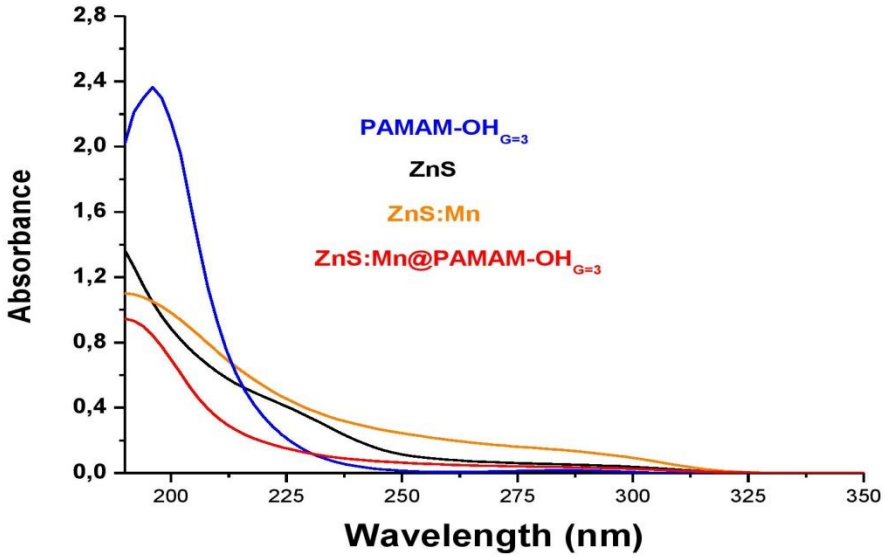

Figure SI 1. UV spectra of the different system obtained of the different synthesized nanoparticles. Using a UV-Vis spectrophotometer (Hewlett-Packard HP8452A diode array) was used to obtain the spectrum.

Optimization of the fluorescence intensity of ZnS when excited at 405 nm:

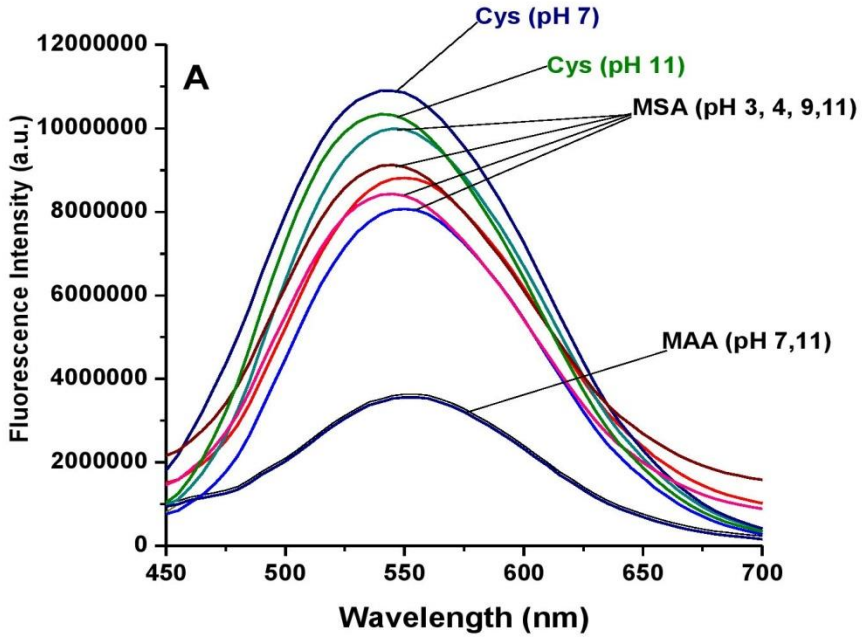

Figure SI2A. When used Cys, MSA and MAA as stabilizer agents and different pH

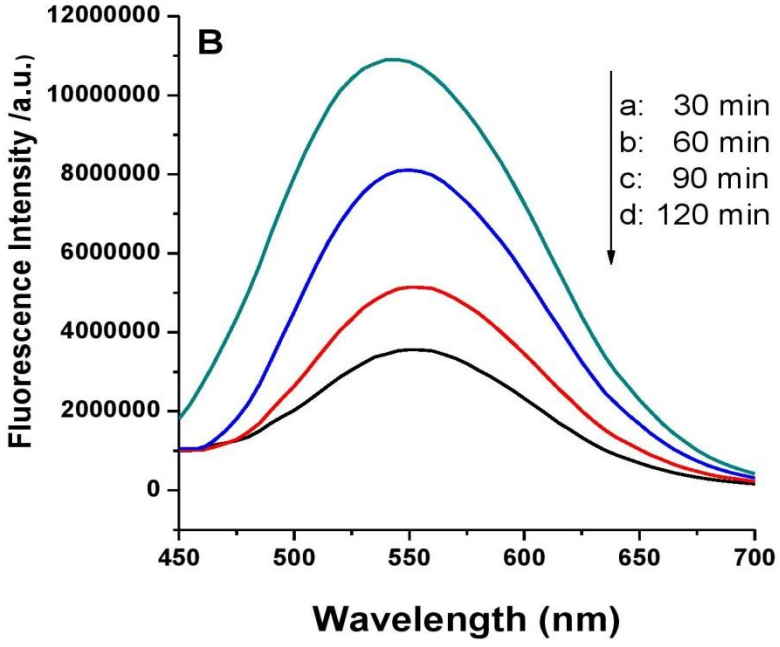

Figure SI2B: At different heating time with Cys (pH 11)

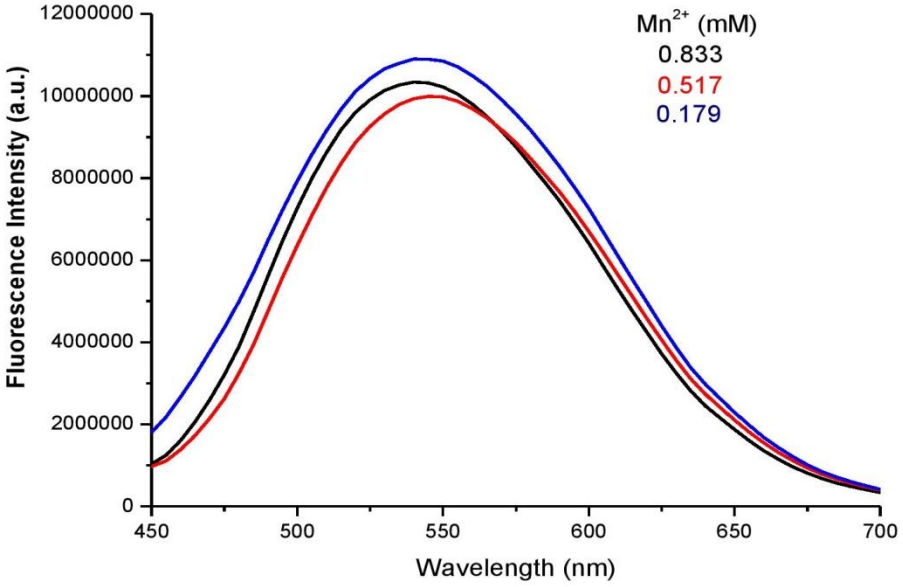

Figure SI 2C. Influence of the Mn^{2+} concentration on ZnSMn.

CHARACTERIZATION

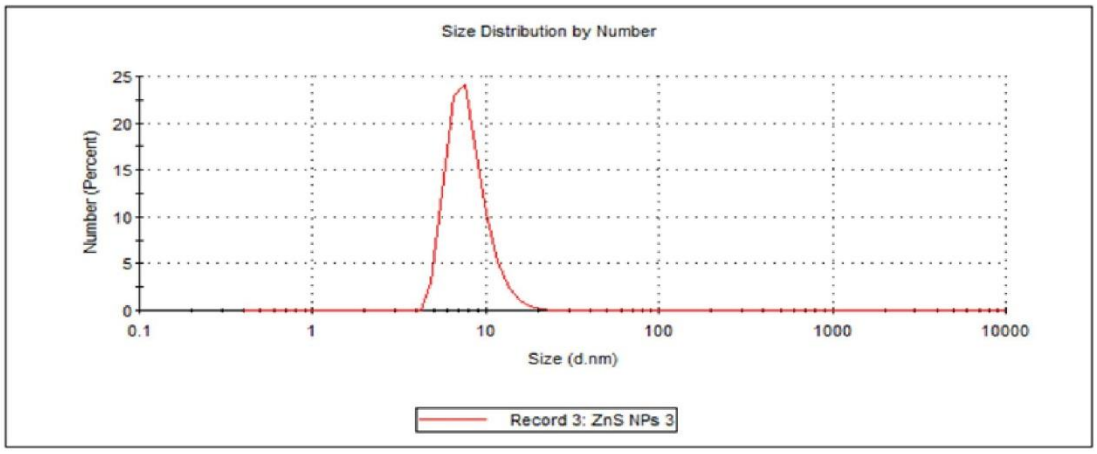

Figure SI 3. Size analysis by DLS of ZnSMn in aqueous solution

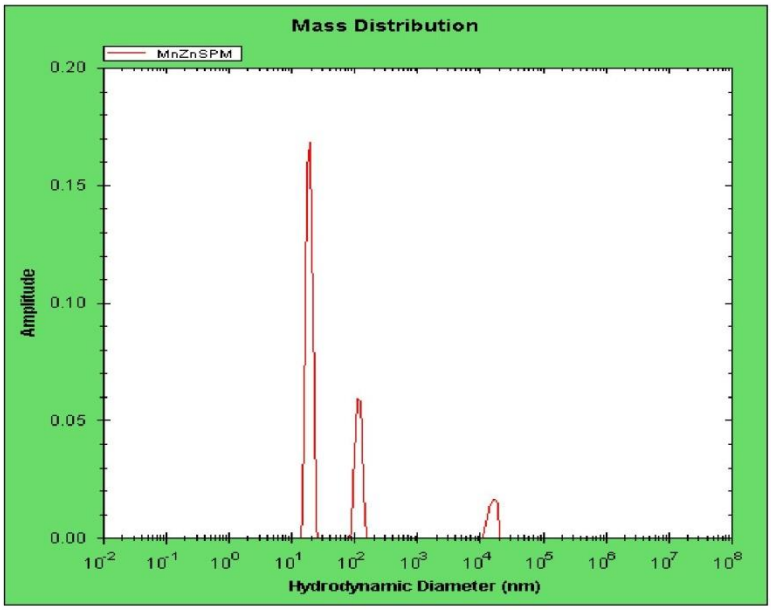

Figure SI 3 cont... Size analysis by DLS of ZnS:Mn@PAMAM-$OH_{G=3}$in aqueous solution

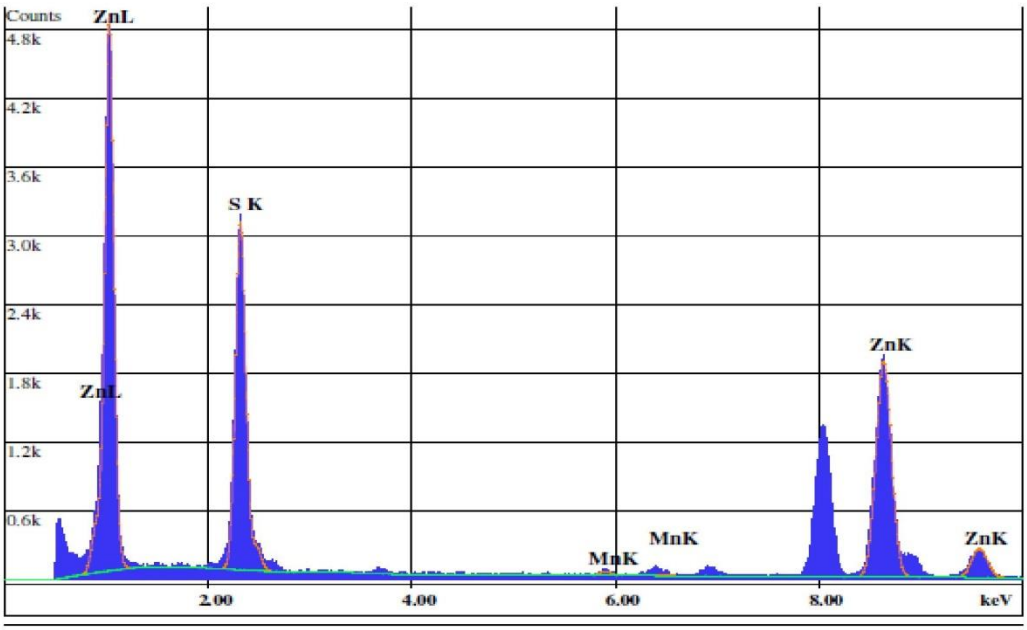

Figure SI 4 EDX spectrum collected for as-prepared ZnS:Mn.

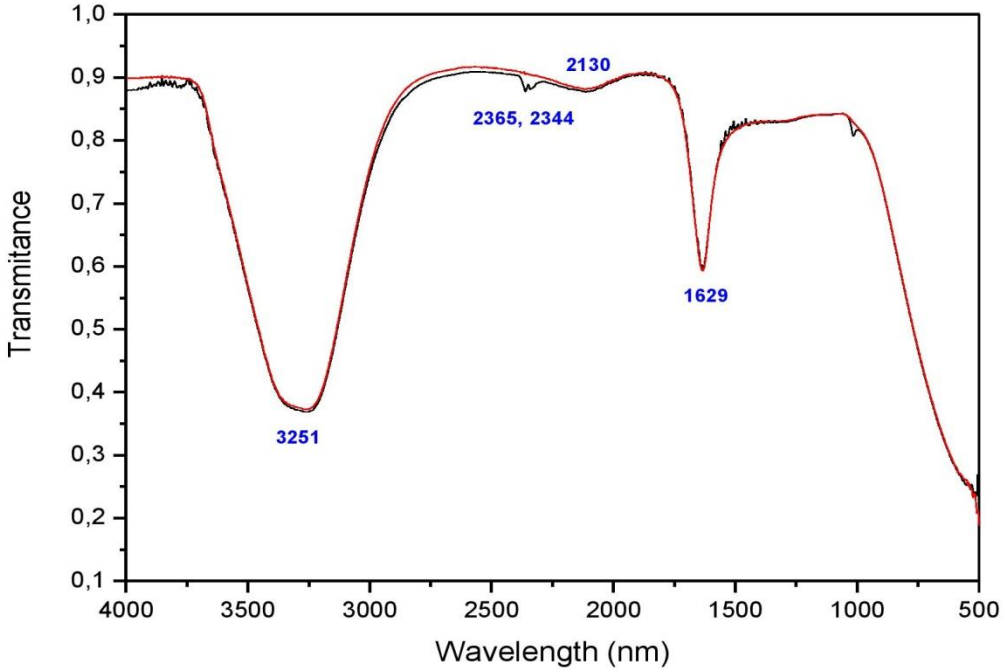

Figure SI 5. ATR-FTIR Spectra of ZnSMn and coated by PAMAM-OH in aqueous solution, which is stabilized by L-Cysteine**.** ATR-FTIR measurements were made with a Bruker Equinox 55 FT-IR spectrometer fitted with a Golden Gate single reflection ATR accessory kit from Specac. All spectra were collected using a resolution of 2 cm^{-1}, 50 scans were collected.

XPS Analyis

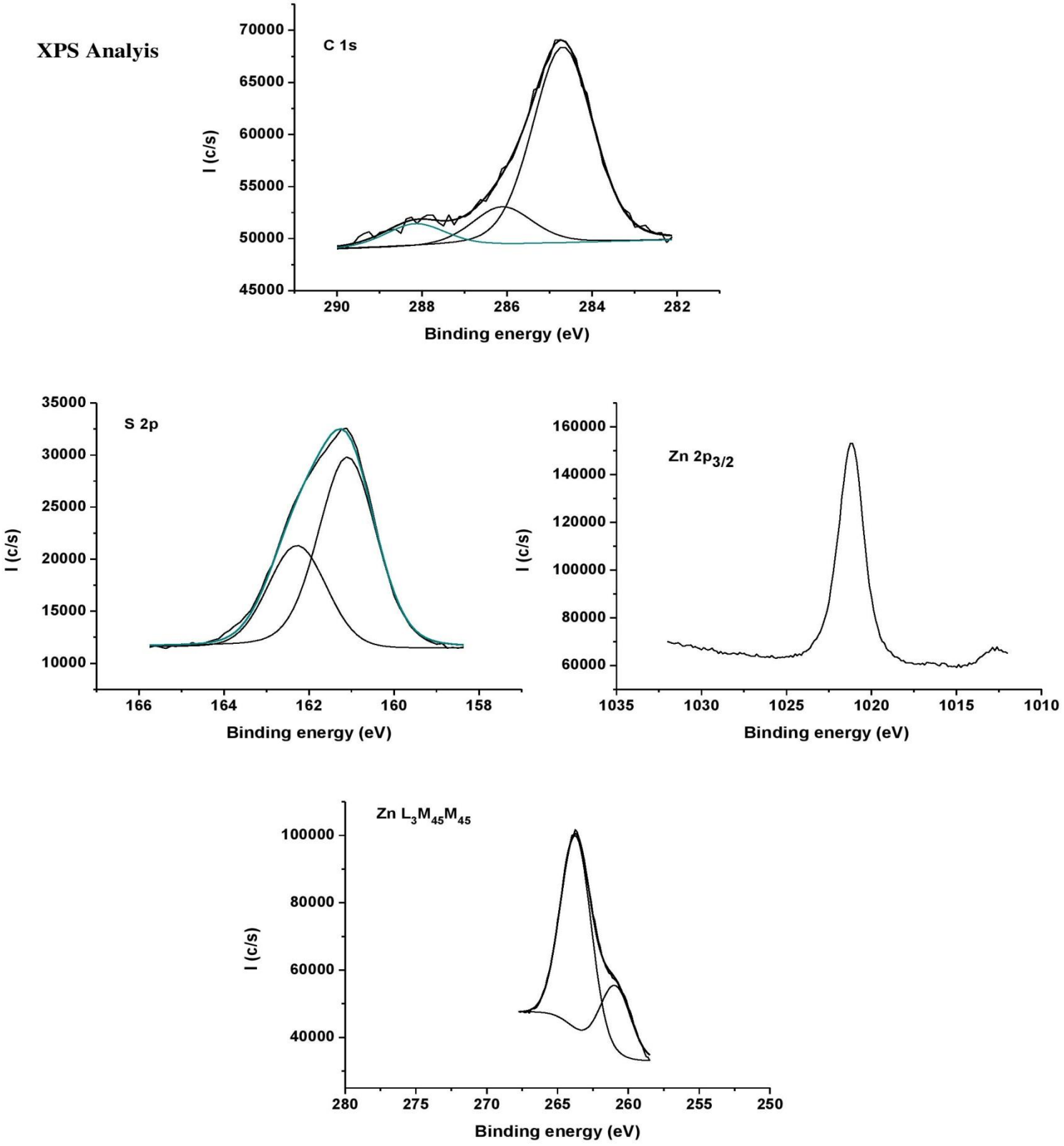

Figure SI 6A. **A**) C 1s, **B**) S 2p **C**) Zn $2p_{3/2}$ core level spectra and **D**) Zn $L_3M_{45}M_{45}$ spectrum for ZnS:Mn nanoparticles stabilized with L-cysteine.

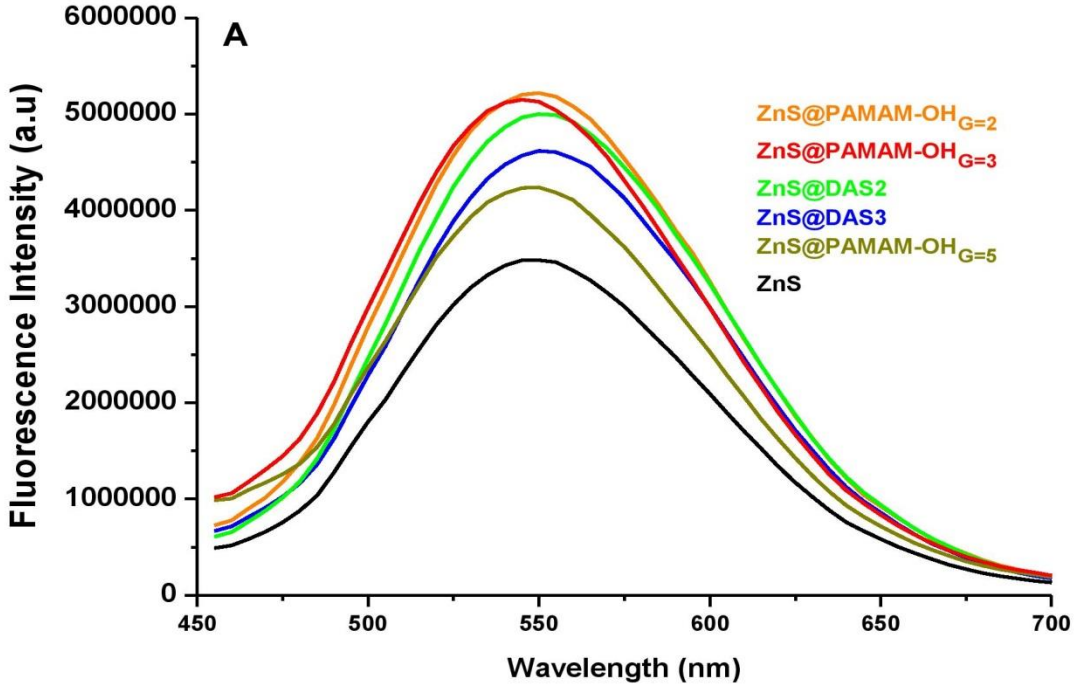

Figure SI 7. Fluorescence spectra of the different dendrimers studied

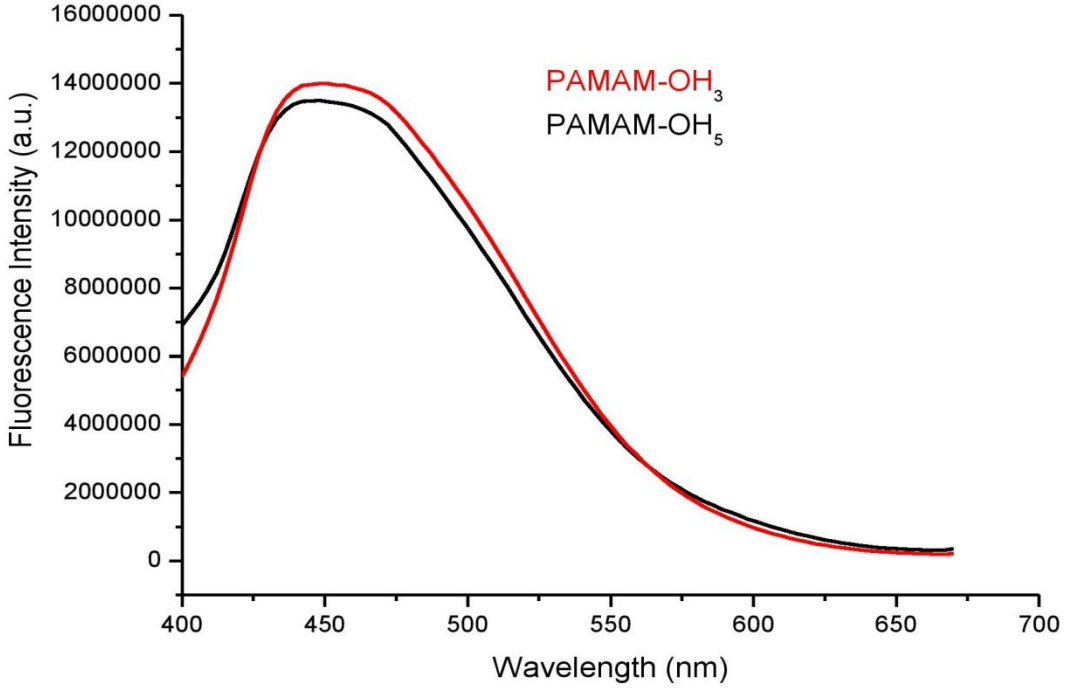

Figure SI 8. Fluorescence spectra of hydroxyl terminated PAMAM dendrimers of fifth and third generation

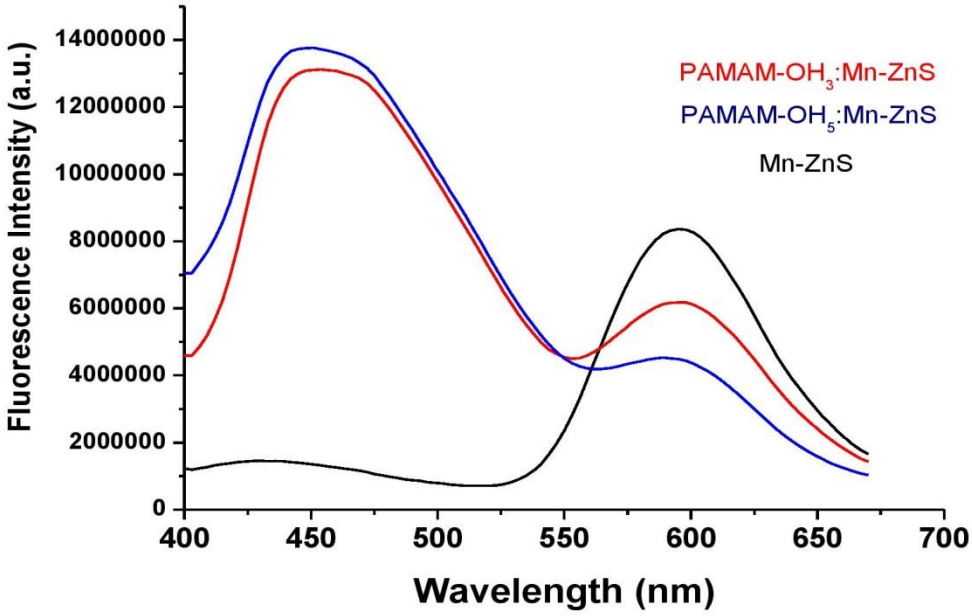

Figure SI 9. Comparation with PAMAM-$OH_{G=3 \text{ and } G=5}$ with raw ZnS:Mn.

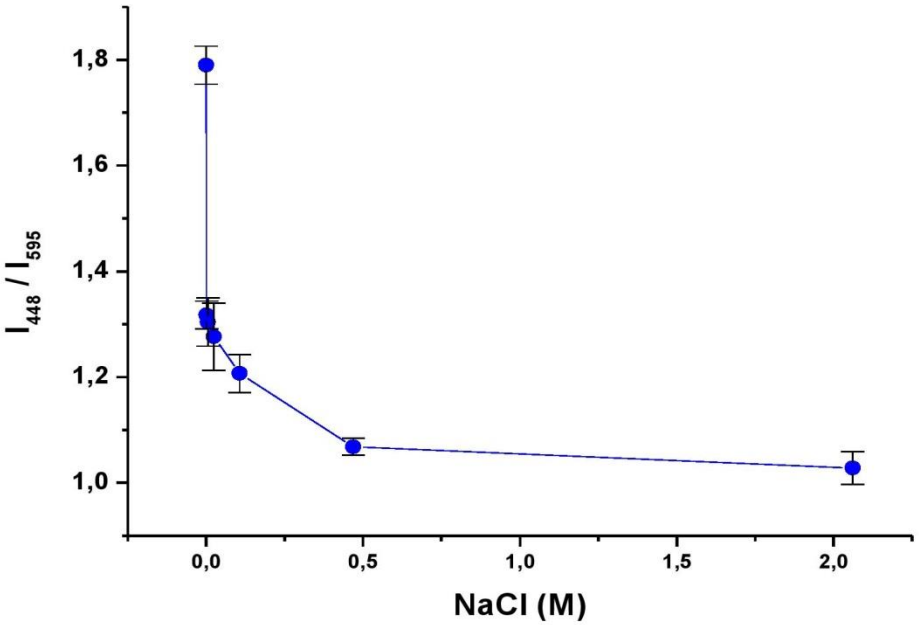

Figure SI10. Influence of the Ionic Strength on the fluorescence Intensity of ZnS:Mn@PAMAM-$OH_{G=3}$

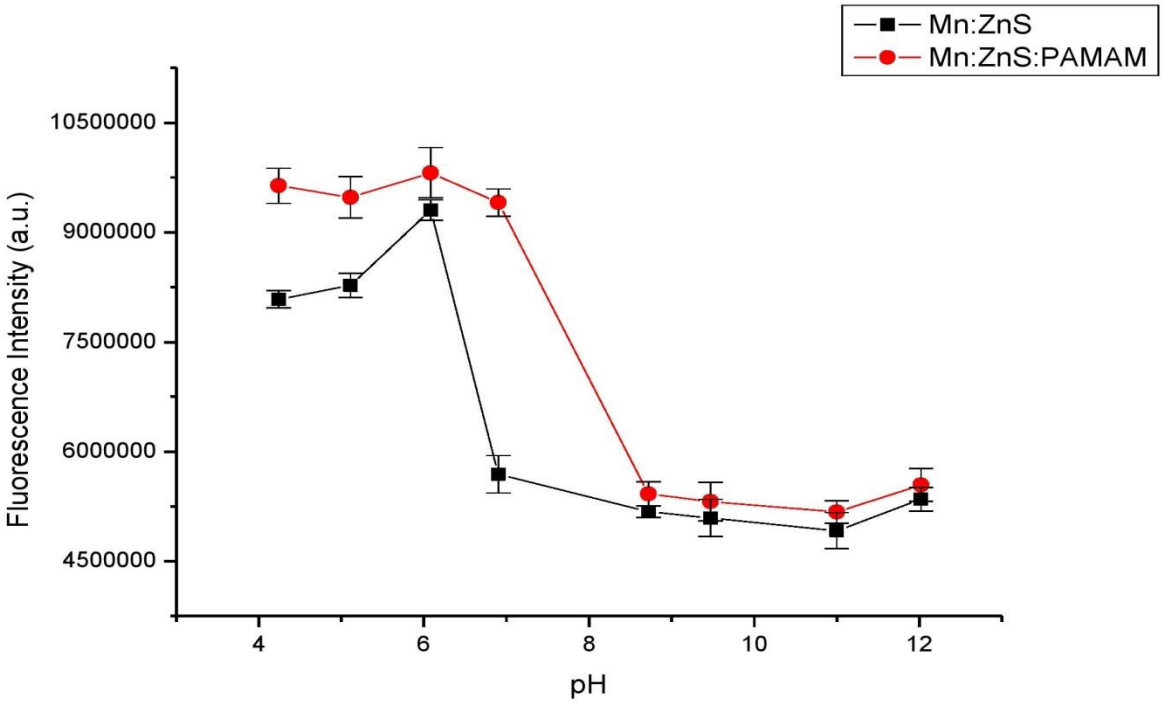

Figure SI11. Influence of the pH on the fluorescence Intensity of ZnSMn and ZnS:Mn@PAMAM-$OH_{G=3}$

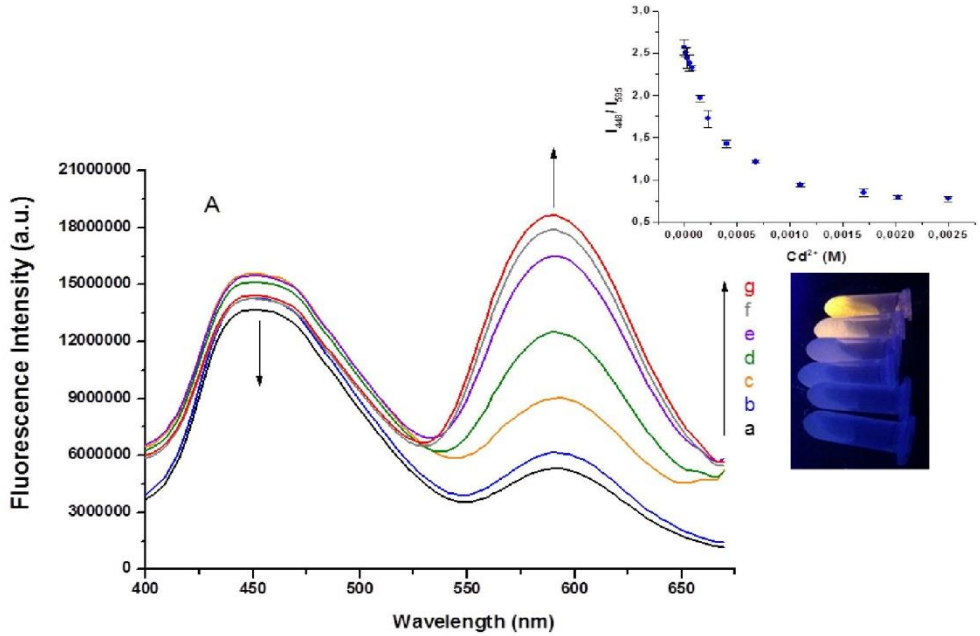

Figure SI12A. Fluorescence spectra of ZnS:Mn@PAMAM-$OH_{G=3}$ upon incremental addition of Cd^{2+} (inset: Changes in the fluorescence intensity ratio (I_{450}/I_{595}) with incremental addition of Cd^{2+}; **a**) 0 **b**) 1.5×10^{-5}, **c**) 2.5×10^{-5}, **d**) 7.5×10^{-5}, **e**) 2.25×10^{-4}, **f**) 6.75×10^{-4} and **g**) 2.3×10^{-3} M.

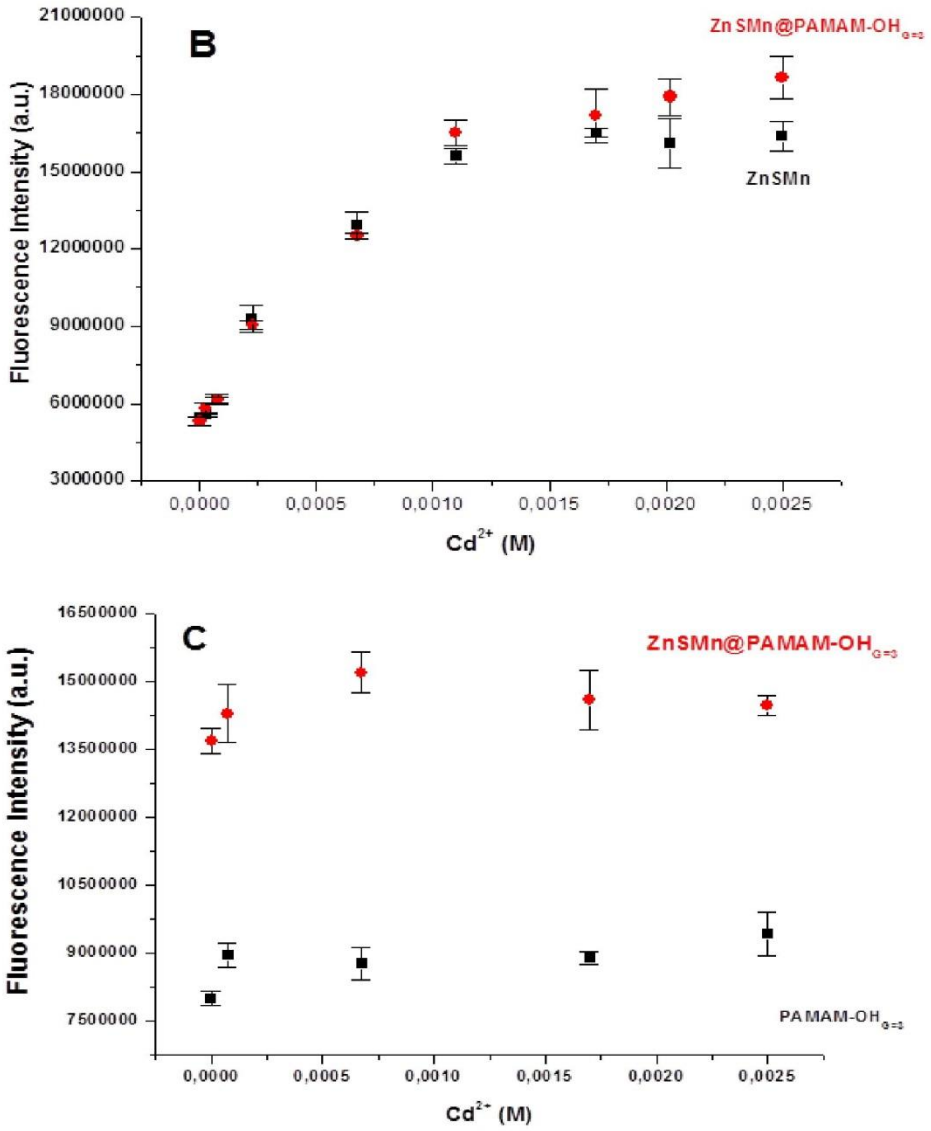

Figure SI12. B) Influence of PAMAM-$OH_{G=3}$ when is compared its addition to ZnSMn and **C**) Comparation of the fluorescence intensity between PAMAM-$OH_{G=3}$ and when coated ZnS:Mn.

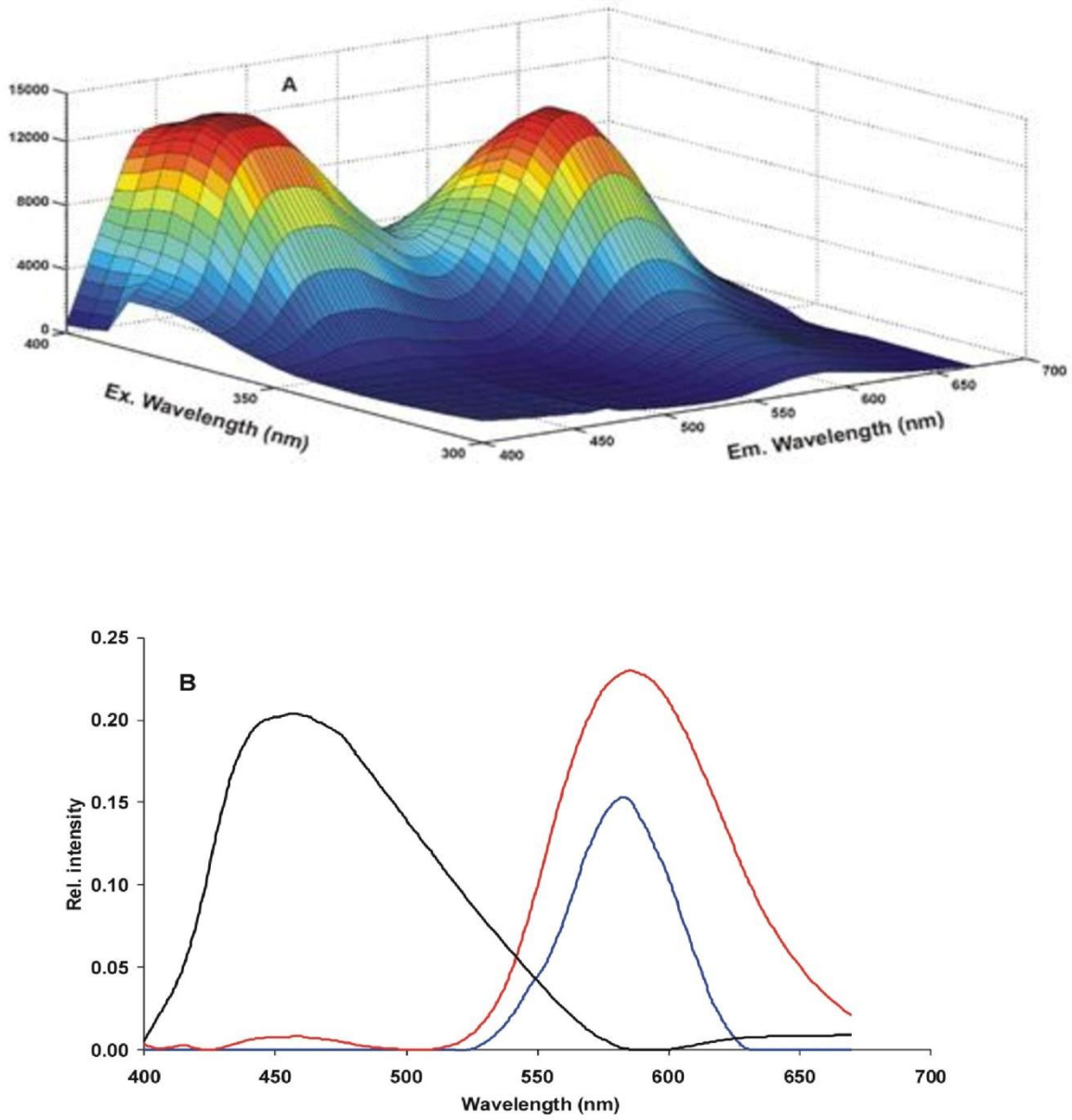

Figure SI13. Excitation-emission matrix for the raw spectra of ZnS:Mn@PAMAM-$OH_{G=3}$ complex in presence of Cd^{2+} (**A**), and corresponding estimated emission profiles (**B**).

Chapter 3

Luminescent carbon nanoparticles: effects of chemical functionalization, and evaluation of Ag^{+} sensing properties

3.1 Contribution to this Paper

My contribution to this paper included the bibliographic research and writing about carbon QDs, passivating agents and then the experimental planning. The synthesis, purification and functionalization with passivating agents were performed, even all the complementary studies including the effect of some parameters such as pH, ionic strength and the tolerance to some ions on the excitation/emission matrix. The data obtained by the characterization methods was analyzed and interpreted. The determination of analytical parameters and the application to silver nanoparticles dissolution was also performed and assayed with the fluorescent nanosensor. This paper was submitted as a scientific article and until the acceptation it passes through some adjustments required by the reviewers and under supervision of my advisor Professor Joaquim Esteves da Silva and co-advisor Doutor Manuel Algarra.

Journal of Materials Chemistry A

PAPER

View Article Online
View Journal

Luminescent carbon nanoparticles: effects of chemical functionalization, and evaluation of Ag^+ sensing properties†

Cite this: DOI: 10.1039/c4ta00264d

Manuel Algarra,*[a] Bruno B. Campos,[b] Ksenija Radotić,[c] Dragosav Mutavdžić,[c] Teresa Bandosz,[d] J. Jiménez-Jiménez,[a] E. Rodriguez-Castellón[a] and Joaquim C. G. Esteves da Silva[b]

Received 16th January 2014
Accepted 10th March 2014

DOI: 10.1039/c4ta00264d

www.rsc.org/MaterialsA

Luminescent carbon-based nanoparticles, addressed as carbon dots (CDs), were synthesized at relatively low temperature from lactose following an easy and inexpensive procedure. Modification of their surface was done by functionalization with mercaptosuccinic acid (MSA) (CDs–MSA). Transmission electron microscopy images showed regular spherical nanoparticles of 5 nm diameter. Raw and functionalized (CDs–MSA) CDs were highly fluorescent at 448 and 472 nm, with relative high quantum yield (Φ = 0.21 and 0.46 respectively). At the maximum fluorescence of CDs–MSA the intensity was quenched by addition of Ag^+ ions by a static mechanism with a Stern–Volmer constant of 3.7×10^3 M^{-1}. The analysis of the emission spectra showed that the CD–MSA complex was stable after this process. The quenching profiles showed that only 44% of the CD–MSA fluorophores are accessible to Ag^+. The main figures of merit were detection and quantification limits of 385.8 nM and 1.2 μM respectively, and the precision as relative standard deviation was 1.76%. No interference was observed when other metal ions were present indicating a high selectivity for Ag^+ detection. The results showed that CDs–MSA can be used for efficient quantification of Ag^+ in silver nanoparticle dissolution.

Introduction

Carbon dots (CDs) have emerged recently as one of the most striking discoveries in the quest for new nanomaterials. They are light emitting nanoparticles, less toxic than similar alternatives such as quantum dots (QDs). Even though these features make them suitable for use in living systems, they still need optimization.[1–5] Compared to QDs and organic dyes, photoluminescent CDs are superior in terms of high aqueous solubility, robust chemical inertness, easy functionalization, high resistance to photo-bleaching, low toxicity and good biocompatibility.[6–9] Particularly, much attention has also been paid to potential applications of CDs in biological labeling, bioimaging and drug delivery.[10–16]

The light emission of CDs can be quenched efficiently by either electron acceptor or electron donor molecules in solution. These interesting photo-induced electron transfer properties of CDs should offer exciting opportunities for light energy conversion, photovoltaic devices and related applications.[17–20] Particularly, CDs can be used as nanoprobes for sensitive ion detection; however, few functionalized CDs have been obtained for this purpose.[21–24]

One of the first proposed routes to prepare CDs was laser ablation. In this method the as-obtained carbon raw nanomaterial was treated with nitric acid and further modified.[1,23] Thereafter, other methods were established to synthesize CDs from soot-based carbon sources by refluxing in strong acid media (HNO_3) followed by a separation process.[25–28] In another method an organic acid is used as a carbon source and then ammonium is used as a modifier to produce oxygenated/nitrogenized functional groups on the surface of CDs.[9–29] In a laser irradiation approach carbon nanoparticles (<50 nm) are dispersed in ordinary organic solvents after ultra-sonication.[30,31] Electrochemical oxidation of graphite,[32,33] carbonization of suitable molecular precursors,[34] alkali/acid assistance of carbohydrates method[35–37] or assisted by microwave treatment[38,39] have also been used.

The objective of this paper is to introduce a rapid and low cost method to synthesize fluorescent nanoparticles, carbon dots (CDs), from lactose, using sulfuric acid treatment. The CDs

[a]Departamento de Química Inorgánica, Facultad de Ciencias, Universidad de Málaga, Campus de Teatinos s/n, 29071 Málaga, Spain. E-mail: malgarra67@gmail.com; Tel: +34 952 132021

[b]Centro de Investigação em Química, Departamento de Química e Bioquímica, Faculdade de Ciências da Universidade do Porto, Porto, Portugal

[c]Institute for Multidisciplinary Research, University of Belgrade, Kneza Višeslava 1, 11000, Beograd, Serbia

[d]Department of Chemistry, The City College of New York, 160 Convent Ave, New York, NY 10031, USA

† Electronic supplementary information (ESI) available. See DOI: 10.1039/c4ta00264d

obtained are extensively characterized by various physical and chemical methods and used as an effective fluorescent sensing platform for Ag^+ ion detection. The performance and selectivity of the detection process are linked to the surface chemistry of these materials, whereby esterification binds mercaptosuccinic acid, forming a stable complex with Ag^+ due to the affinity of their free thiol groups.

Experimental section

Chemicals

Lactose and the assayed thiol compounds as functionalized agents for CDs: L-cysteine (>97%), glutathione, *N*-acetyl cysteine (>99.0%, NAC), mercaptosuccinic acid (>99.0%, MSA), mercaptoacetic acid (>99.0%, MAA), and 3-mercaptopropanoic acid (>99.0%, MPA) were purchased from Sigma-Aldrich Química S.A. (Spain). In all experiments deionized water was used.

Synthesis, purification and functionalization of CDs

To obtain CDs, 100 mL of lactose 1 M were treated with 50 mL of H_2SO_4 using 1 h sonication. The resulting light yellow suspension was heated at 80 °C for 24 h. Then it was centrifuged, filtered, neutralized to pH 7 and centrifuged again. Finally, the CD solution was concentrated by using a rotary evaporator, until a third of the initial volume. The purification of CDs was carried out by a dialysis process. Further functionalization was carried out with MSA (CDs–MSA) and MPA, MAA, NAC, cysteine and glutathione. 1 mL of these chemicals were added to 2 mL of CD raw solutions and stirred for 1 h.

Characterization methods: data analysis

Transmission Electron Microscopy (TEM) analysis was carried out with a Philips CM-200. A UV-vis spectrophotometer (Hewlett–Packard HP8452A diode array) and a photoluminescence spectrophotometer (Horiba JovinYvon Fluoromax 4 TCSPC) were used to characterize CD optical performance. The UV-vis absorption spectrum of CDs was scanned in the wavelength range of 180–400 nm. The fluorescence of the nanoparticles was measured in the wavelength range of 300–740 nm. The spectra were obtained with an integration time of 0.1 s and 1 nm slits for excitation and emission. All measurements were performed at room temperature. For each compound a series of emission spectra were collected, by excitation at different wavelengths, in the range of 280–380 nm with a 5 nm step. The emission spectra were recorded in the 400–550 nm range. Infrared measurements were carried out using a Bruker Equinox 55 FT-IR spectrometer fitted with a Golden Gate single reflection ATR accessory kit from Specac. All spectra were collected using a resolution of 2 cm^{-1}, 50 scans were collected. The size and zeta potential (ζ) of CDs were determined using a Zetasizer Nano ZS (Malvern Instruments, UK) equipped with a 4 mW HeNe laser operating at $\lambda = 633$ nm. Size measurements were recorded using dynamic light scattering (DLS), at 25 °C in a polystyrene cell (ZEN0040) at a scattering angle of 173° and the results were the average of three tests. The ζ measurements were also performed at 25 °C in polycarbonate folded capillary cells, incorporated with gold plated electrodes (DTS1061) and deionized H_2O was used as the dispersion medium. Both size and ζ were automatically obtained by the software, using the Stokes–Einstein and the Henry equations, with the Smoluchowski approximation. X-ray photoelectron spectra (XPS) were obtained using a Physical Electronics PHI 5700 spectrometer with non-monochromatic Mg K_α radiation (300 W, 15 kV, and $h\nu = 1256.3$ eV) as the excitation source. Spectra were recorded at 45° take-off angles by a concentric hemispherical analyser operating in the constant pass energy mode at 25.9 eV, using a 720 μm diameter analysis area. Under these conditions the Au $4f_{7/2}$ line was recorded with 1.16 eV FWHM at a binding energy of 84.0 eV. The spectrometer energy scale was calibrated using Cu $2p_{3/2}$, Ag $3d_{5/2}$ and Au $4f_{7/2}$ photoelectron lines at 932.7, 368.3 and 84.0 eV, respectively. Charge referencing was done against adventitious carbon (C 1s 284.8 eV). The C 1s signal of some samples was studied using Al K_α radiation due to the presence of sodium to avoid the overlapping of the NaKLL Auger signal at 290.3 eV. Solid surfaces were mounted on a sample holder without adhesive tape and kept overnight in high vacuum in the preparation chamber before they were transferred to the analysis chamber of the spectrometer. Each region was scanned with several sweeps until a good signal-to-noise ratio was observed. The pressure in the analysis chamber was maintained lower than 10^{-9} Torr. A Shirley-type background was subtracted from the signals. Recorded spectra were always fitted using Gaussian–Lorentzian curves in order to determine more accurately the binding energy of the different element core levels. The accuracy of binding energy (BE) values was within ±0.1 eV.

Fluorescence data analysis

For each sample, 21 spectra were recorded. In the analysis we used 4 matrices, corresponding to the pure CDs, pure MSA, the CD–MSA complex and the CD–MSA@Ag^+ complex. Each matrix was analysed by using the Multivariate Curve Resolution-Alternating Least Squares (MCR-ALS) method,[40] which extracted the number of components, as well as their emission and excitation profiles. All analyses were performed using The Unscramble software package (Camo ASA).

Quantum yield and quenching, interference measurements and Ag^+ determination

The quantum yields (QY) of CDs and CDs–MSA were obtained using Rhodamine 6G ($\Phi = 0.93$ in methanol, $n = 1.329$ and $\lambda_{ex} =$ 535 nm) as the standard; CDs and CD–MSA were dissolved in deionized water ($n = 1.33$). Use of eqn (1) leads to obtain the QY of CDs and CDs–MSA with Rhodamine 6G as the reference. Fig. S1† shows the UV spectra.

$$QY_{CDs} = QY_{st}\left[\frac{(dI/dA)_{CDs}}{(dI/dA)_{st}}\right]\left(\frac{{n_{CDs}}^2}{{n_{st}}^2}\right) \quad (1)$$

where I is the area under the fluorescence curves and A is the corresponding absorbance.[41,42] The quenching by Ag^+ ions was described using the Stern–Volmer formalism. The collisional quenching of the fluorescence of CDs–MSA by Ag^+ was

described using the Stern–Volmer equation (eqn (2)); where I_0 is the fluorescence intensity without Ag^+; I is the fluorescence intensity observed in the presence of Ag^+ and K_{S-V} is the Stern–Volmer constant. The quenching was also described by a modified Stern–Volmer equation accounting for a fractional accessibility to quenchers (eqn (3)):

$$I_0/I = 1 + K_{S-V}[Ag^+] \quad (2)$$

$$I_0/\Delta I = 1/(f_a K_a [Ag^+]) + 1/f_a \quad (3)$$

where $\Delta I = (I_0 - I)$, f_a is the fraction of initial fluorescence that is accessible to the quencher and K_a is the Stern–Volmer quenching constant of the accessible fraction.[43] The effects of metal ions were studied by addition of Ag^+ from a stock solution (10^{-2} M) to CDs–MSA to the desired concentration levels. The solution mixture was then incubated at room temperature for 5 min and stirred. The fluorescence intensity was measured at 472 nm after addition of Ag^+. The same procedure was carried out to study the interference caused by other metal species (Hg^{2+}, Cd^{2+}, Pb^{2+}, Cu^{2+}, Co^{2+}, Ni^{2+}, K^+, Tl^+, Mn^{2+} and Zn^{2+}) at different Ag^+ (1.60×10^{-4} M)/metal ratio concentrations.

Determination of Ag^+ in AgNP dissolutions

Silver nanoparticles (AgNPs), purchased from Dept. Organic Chemistry (Univ. Málaga, Spain), were diluted to an appropriate range of concentration.[34] 10 mL was added to 500 μL of CDs–MSA, 100 μL of AgNP dissolution and buffered by acetic–acetate (100 mM) to adjust the pH to 4.5. Then, a standard calibration curve was built by addition of 1 mM Ag^+, the mixture was stirred at room temperature for 5 min before fluorescence measurements, following a previously published procedure,[44] obtaining the Ag^+ concentration in the AgNP dissolution.

Fluorescence lifetime data analysis

Fluorescence lifetime analysis was done using Decay Analysis Software version 6.4.1 (Horiba Jobin Yvon). Fluorescence decays were interpreted in terms of a multi-exponential: $I(t) = A + \sum B_i \exp^{-t/\tau_i}$, where A and B_i are the pre-exponential factors and τ_i the decay times.

Results and discussion

TEM, ATR and XPS analysis

A representative TEM micrograph (Fig. 1) shows a good dispersion of our CDs in water. The particles mostly exhibit regular globular shapes with sizes of about 5–6 nm; a typical amorphous carbonaceous structure with no discernible lattice was observed, similar to the results published in the literature.[45] The CDs irradiated under UV light show a blue/slightly greenish fluorescence (Fig. 1). These results show that the synthesised CDs exhibit excellent nanoparticle properties important for the fabrication of a metal ion sensor.

The results of XPS analysis are presented in Fig. 2. The content (in at%) of C, O and S on the surface of CDs is 23.4, 43.94 and 11.06%, respectively. For the CDs–MSA these values

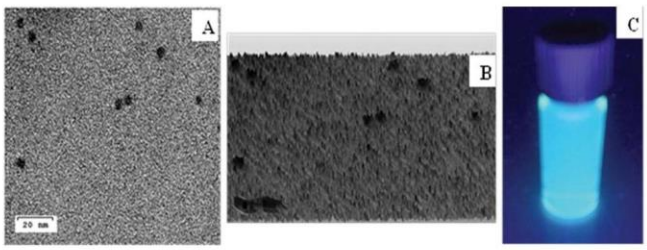

Fig. 1 (A) TEM image of CDs synthesized from sacarose with diameter around 6 nm; (B) TEM 3D representation of CDs; and (C) fluorescence from fresh CDs obtained when exposed to UV light at 365 nm.

are 14.21, 53.11 and 16.01%. As seen in the figure, the relative content of oxygen and sulfur significantly increased upon addition of the surface modifier. These values suggest that our CDs are very rich in chemical functionalities. The C 1s core level spectrum (Fig. 2A) of CDs can be decomposed into two contributions at 284.8 (82%) and 286.2 (18%). The more intense contribution at 284.8 eV is assigned to adventitious and graphitic carbon. The contribution at 286.2 eV presents a relatively high intensity and is mainly assigned to the presence of surface C–OH and C–O–C groups. Although the C 1s core level signal of the CD–MSA sample (Fig. 2B) can be also decomposed into two contributions at 284.8 eV (67%) and 287.9 eV (33%), the contribution at high binding energy is shifted by 1.8 eV due to the presence of the carboxylic group of the mercaptosuccinic acid. The relative amount of carbon bound to oxygen increased almost twice after modification owing to the oxygen rich formula of MSA. The presence of the mercaptosuccinic acid on the surface of the carbon dots is clearly observed in the corresponding S 2p core level spectrum (Fig. 2C). The S 2p signals of samples CDs and CDs–MSA show a strong signal at 168.3 eV due to the presence of sulphate groups, which must be linked to the sulphur acid treatment. Nevertheless, in the case of the CD–MSA sample additional contributions from S $2p_{3/2}$ at 161.3 and 163.6 eV are observed and these are assigned to the presence of sulphide and thiol groups, respectively (Fig. 2D).

ATR-FTIR spectra of CDs reveal a band (Fig. 3) at 1639 cm^{-1} representing the existence of carbonyls (C=O) on the surface. The band centered at 1077 cm^{-1} is ascribed to the C–H deformations and stretching vibrations of C–O (ether) and C–C, pertaining to carbohydrates. A very broad strong band at 3398 cm^{-1} and the band centered at 1077 cm^{-1} represent the stretching vibrations and in-plane bending vibration of –OH. After modification with MSA the band representing OH groups disappears suggesting their involvement in surface reactions with MSA. Taking into account the chemistry of the initial CDs it is possible that the esterification reactions took place. The two bands between 1301 and 1416 cm^{-1} have their origin from the MSA molecule and represent the stretching of –C–O and $-CH_2$ bending respectively, a small broadness centered at 2580 cm^{-1} is assigned to the –SH stretching. Both strong bands appearing at 600 cm^{-1} are assigned to C–H deformation. The –C=O stretching centered at 1689 cm^{-1} beside that mentioned at 1300 cm^{-1} justifies the presence of these functional groups on the surface of CD–MSA. The strong band centered at 1091 cm^{-1} can

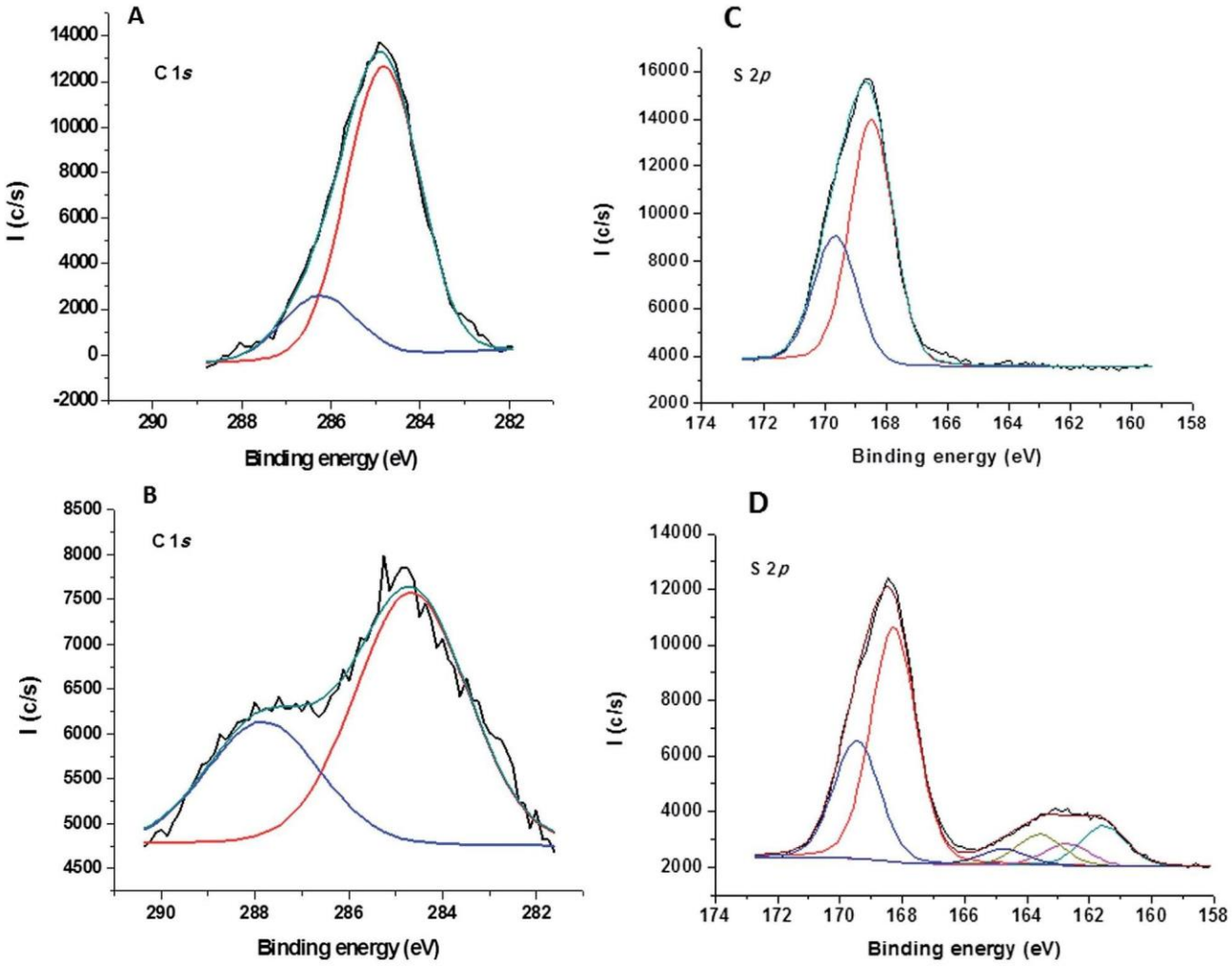

Fig. 2 XPS of C 1s core level for (A) CDs and (B) CD–MSA. XPS of the S 2p core level for (C) CDs and (D) CD–MSA.

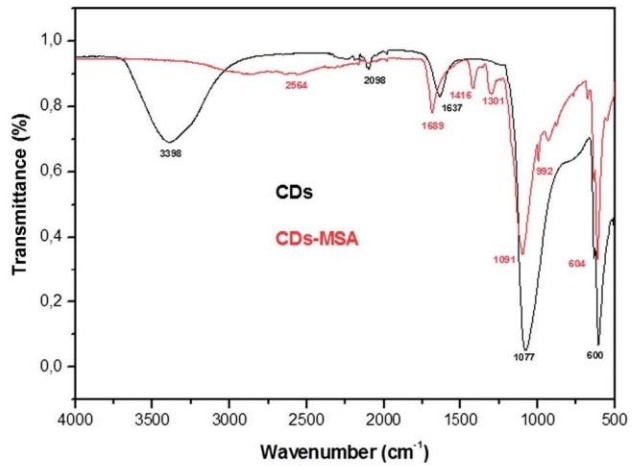

Fig. 3 ATR spectra of CDs and CDs functionalized with MSA (CD–MSA).

be attributed to the –C–O stretching of the free alcohols obtained after the esterification process in the MSA molecule. Based on the XPS and FTIR analyses, Scheme 1 proposes the surface chemistry of CDs and their MSA modified counterpart. This chemistry might be of paramount importance for the fluorescence/sensing behavior of these materials.

The zeta potential (ζ) of CDs is negative (−4.336 mV). This value can be explained by the presence of surface –COOH groups which can be deprotonated at the measured pH (pH 5). The existence of these functional groups imparts excellent solubility in water without further chemical modification.

Fluorescence properties of CDs and CDs–MSA

Steady state fluorescence. Fig. 4A shows the fluorescence spectra of raw CDs with a maximum of emission at 448 nm (λ_{exc} = 387 nm). The intensity increased about 45% when MSA is used as a functionalizing agent (compared with the raw CDs and the other coating agents used, MPA, MAA, NAC, cysteine and glutathione (Fig. 4B)). As is shown the fluorescence enhancement effect was only observed in the cases of MSA, glutathione and cysteine modifications. In contrast, modifications with NAC, MAA and MPA caused a decrease in the fluorescence of the CDs. MSA molecules probably act as modifying agents, after the chemical reaction in the CD surface forming a

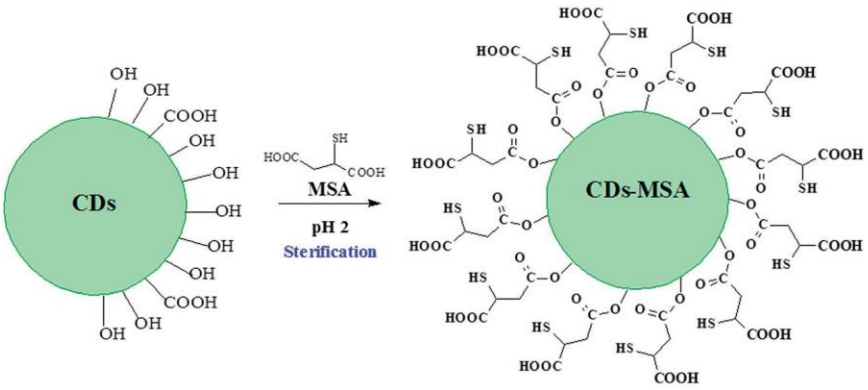

Scheme 1 Chemical representation of formation of CDs–MSA for the Ag^+ sensor.

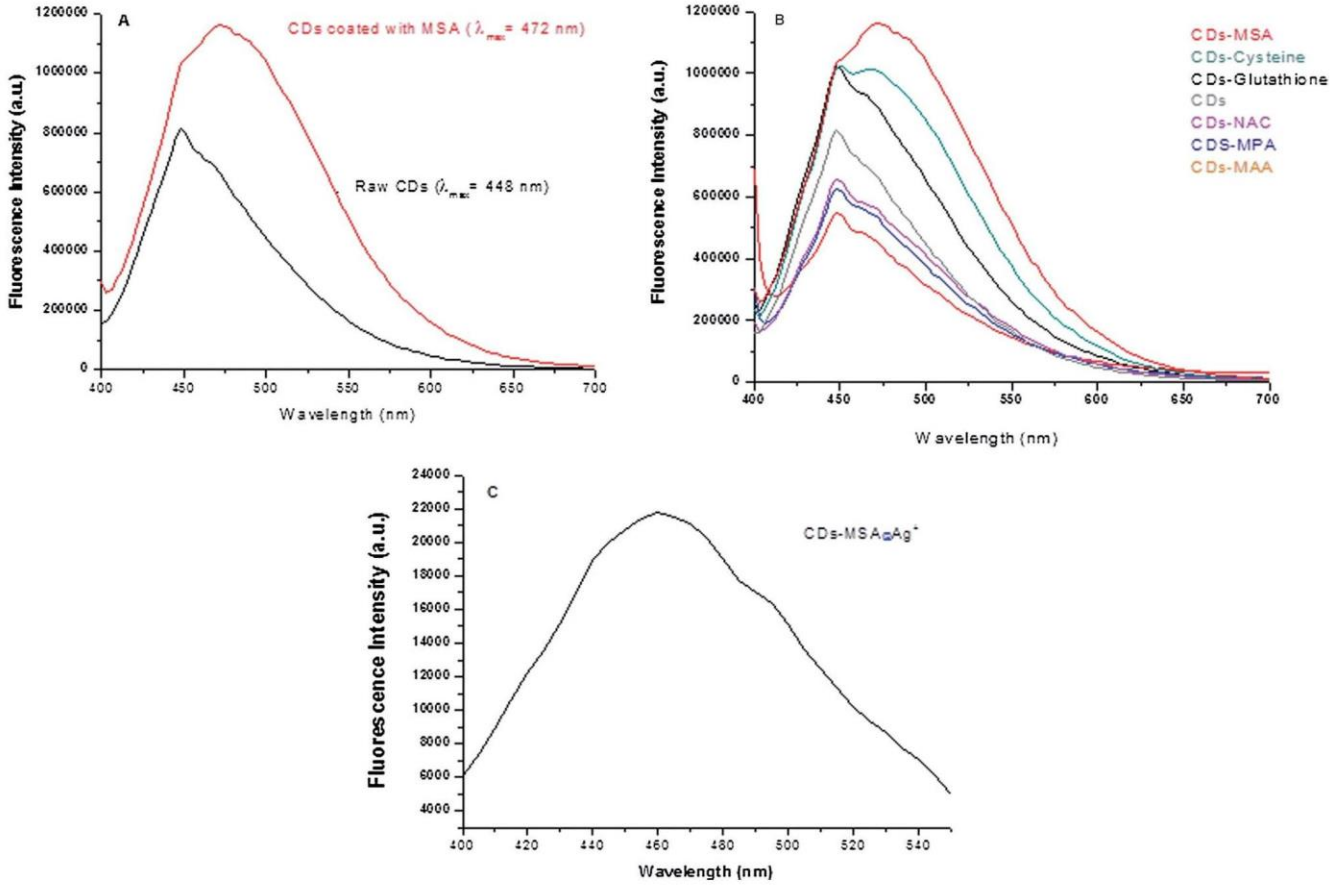

Fig. 4 (A) Fluorescence spectra of raw CDs (black); functionalized with MSA (blue), MAA (brown) and MPA (red). (B) Influence of MSA concentration: (a) 0; (b) 0.02 M; (c) 0.05 M, (d) 0.01 M; (e) 0.2 M; (f) 0.4 M and (g) 0.6 M.

new fluorophore, increasing the fluorescence efficiency compared with the raw CDs. A paramount importance for the measured fluorescence must be the presence of the –SH moiety and longer/much more complex surface organic molecules formed in the esterification reactions. In such molecules the electronic transitions upon excitation are expected to be more pronounced. The full width at half maximum (FWHM) is 112 nm for CDs–MSA and 86 nm for raw CDs; the relatively high FWHM suggests that the CD–MSA sample shows a heterogeneity of fluorescence effects, probably owing to the complexity of surface chemistry.[46] The relatively narrow FWHM of CDs suggests a narrow size distribution of the particles, which is consistent with the TEM results.

Various concentrations of MSA were used for the modification of CDs to evaluate the modifier effects on the fluorescence intensity. The results indicated that 0.4 M solution is an optimum one. The corresponding spectrum and the observed red shift are shown in Fig. S2.† Fig. 4C shows the examples of

the emission spectra of pure MSA and CD–MSA@Ag^+. The QYs of CDs and CDs–MSA show $\Phi = 0.21$ and 0.46, when excited at 228 and 235 nm, respectively in methanol solution.

Fluorescence analysis of CDs and CDs–MSA

The results of MCR-ALS analysis of the emission profiles for the CDs, MSA and the CDs–MSA and CDs–MSA@Ag^+ complexes are shown in Fig. 5A. The emission spectrum of pure CDs consists of two components, with the emission maxima positions at 430 nm and 463 nm. We linked it to the presence of various oxygen based fluorophores. As shown by XPS and FITR analysis the surface of CDs is rich in oxygen containing groups. The spectrum of pure MSA consists of three components with the maxima at 409 nm, 454 nm and 496 nm which can be related to an increase in surface heterogeneity owing to the esterification reactions and presence of thiol groups. The spectra of the CDs functionalized with MSA and MSA@Ag^+ also consist of three components, with similar maxima positions for both materials, at 424 nm, 457 nm and 514 nm. The positions of these maxima slightly differ from those in both CD and MSA spectra. The reason for this difference can be attributed to a new chemistry formed as a result of functionalization (esterification) and the presence of the carbon matrix in CDs which can affect the process of relaxation/electron transfer.

The corresponding loadings (excitation profiles) of the components distinguished in Fig. 5A are shown in Fig. 5B. The loadings of the individual components, for the pure MSA and for CDs–MSA and CDs–MSA@Ag^+, change in a similar way with changing excitation wavelength as well as they have similar maxima positions. These results are different from those for CDs. The results show that the modification of CDs with MSA leads to the change of the emission spectrum. The first and third components of the CD–MSA spectrum could be linked to the new/modified entities attached to the surface of QDs. The second component indicates its origin in MSA and may be related to the effect of SH groups on the fluorescence emission. The unchanged positions of all components in the CD–MSA@Ag^+ spectrum compared with the component positions for the CD–MSA spectrum indicate that binding of Ag^+ ions does

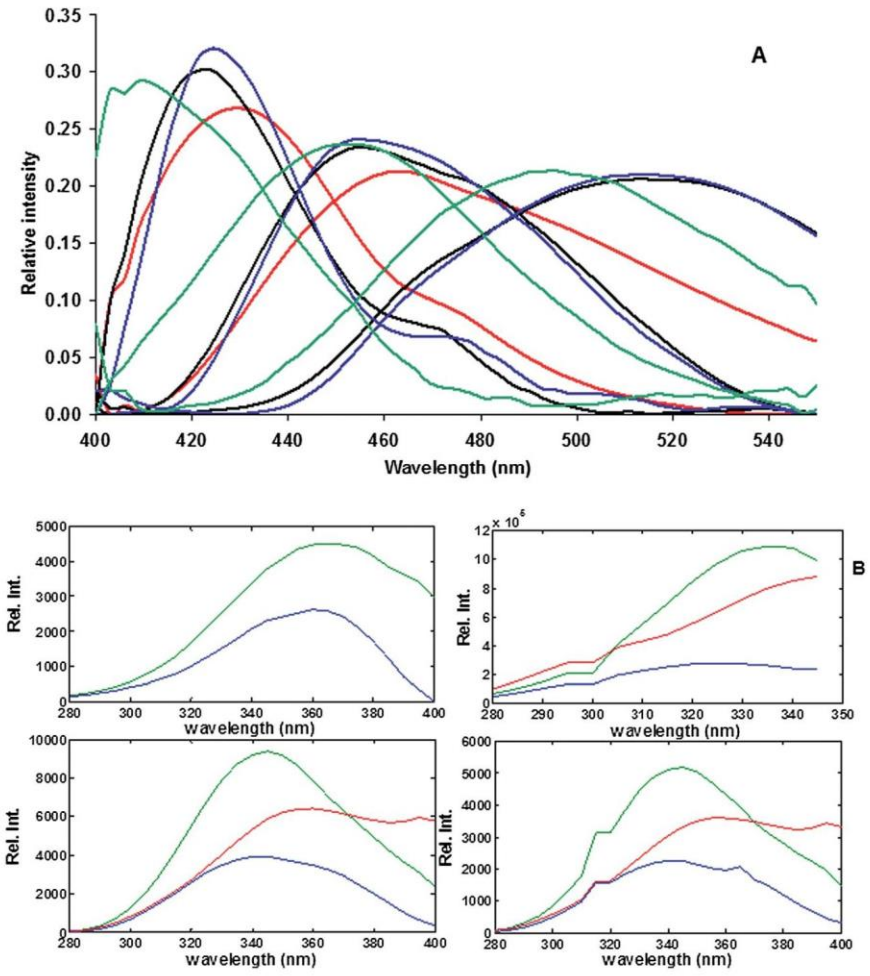

Fig. 5 (A) Emission spectra of the pure components obtained by applying the MCR-ALS method to the analysis of the emission spectra of pure CDs (red), pure MSA (green), CDs–MSA complex (blue) and CDs–MSA@Ag^+ complex (black). The examples of the spectra of pure CDs and MSA, as well as of the two complexes are shown in Figure 4. (B) The excitation spectra profiles (loadings) corresponding to the spectral components from the Figure 5A, obtained by the MCR-ALS method. Upper panel: CD (left) and MSA (right), lower panel: CDs–MSA (left) and CD–MSA–Ag^+ (right).

not induce any significant change in the fluorophores of CDs–MSA. This indicates the stability of our material, which is an important quality for the application of these modified CDs in metal ion detection. The additional confirmation of the stability is the similarity of the loadings of the individual components for the CD–MSA and CD–MSA@Ag^+ complexes. The analysis of the fluorescence decays shows that the lifetimes of the components (Table S1 in the ESI†), calculated with a three-component decay time model for CDs, CDs–MSA and CDs–MSA@Ag^+, are not particularly sensitive to the presence of the quencher. They do not depend on the Ag^+ concentration, demonstrating the static quenching effect over CDs–MSA linked to the formation of a stable complex between the fluorophore and Ag^+.

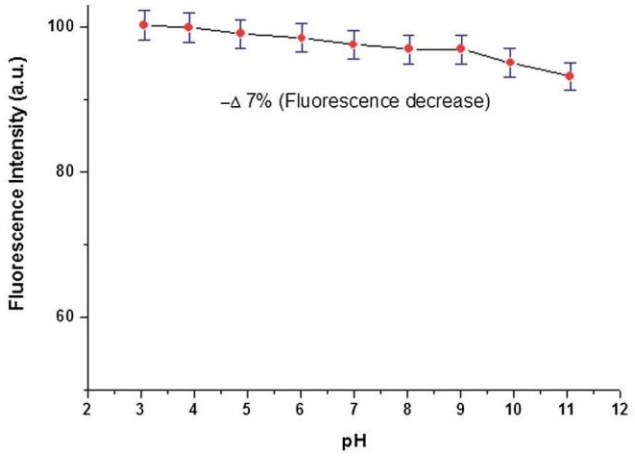

Fig. 6 Effect of pH on the fluorescence intensity of CDs–MSA.

Effect of pH and ionic strength on the fluorescence of CDs–MSA

Fig. 6 shows the effect of pH (3–11) on the fluorescence intensity of the aqueous solutions of CDs–MSA. The experiments were carried out by adding 0.1 M NaOH to achieve the desired pH. A small decrease in the fluorescent intensity, by around 7%, when the pH increases from 3 to 11, is observed. This small variation can be a consequence of the small change of the quantum confinement due to the functionalization by MSA. Another reason can be the high pK_a value of –SH groups of MSA (pK_a = 13) and their existence in undissociated form. These result in that the CD–MSA sample does not exhibit any shift in the maxima of fluorescence and maintains the same spectral shape. Apparently under these experimental conditions the CD–MSA sample is monodispersed and the fluorescence emission remains stable (Fig. S3†). To investigate the effect of ionic strength on fluorescence, various solutions of increasing concentrations of NaCl (between 0 and 1 M) were used. As seen from the fluorescence spectra (Fig. S4†) a moderate increase in the intensity is found when the NaCl concentration increases, indicating the high salt tolerance of CDs.

Sensing of Ag^+

Preliminary experiments demonstrated that no fluorescence changes occurred on the initial CDs tested for metal sensing.

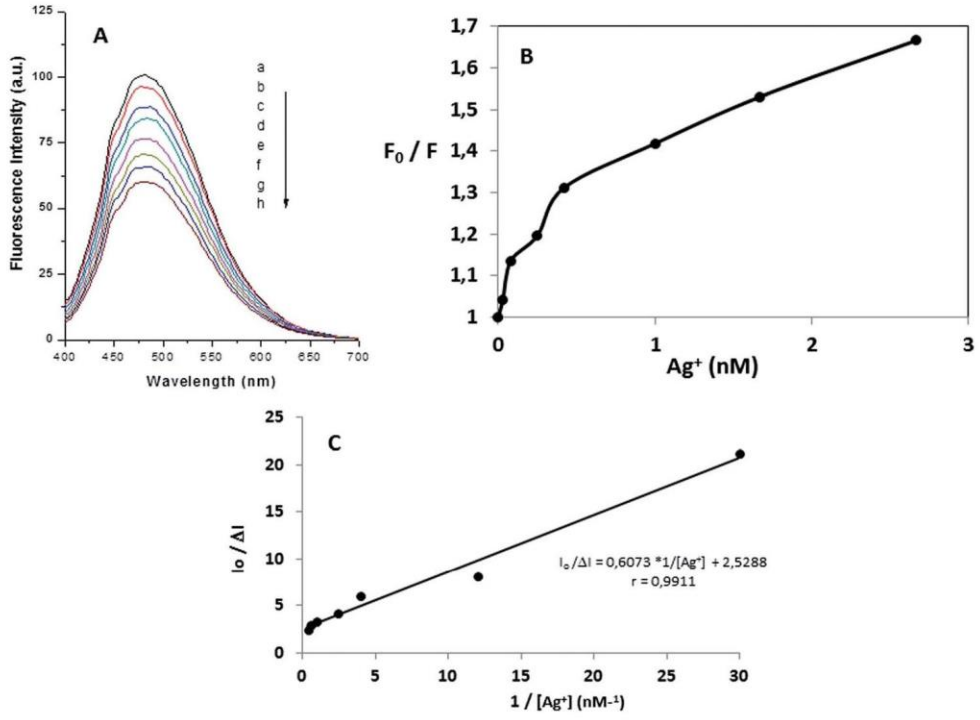

Fig. 7 (A) Fluorescence spectra of CDs–MSA with different Ag^+ ion concentrations: (a) 0 M; (b) 3.33×10^{-5} M; (c) 8.33×10^{-5} M; (d) 2.25×10^{-4} M; (e) 4.1×10^{-4} M; (f) 1×10^{-3} M; (g) 1.16×10^{-3} M and (h) 2.66×10^{-3} M. (B) Stern–Volmer representation of CD–MSA after the Ag^+ effect.

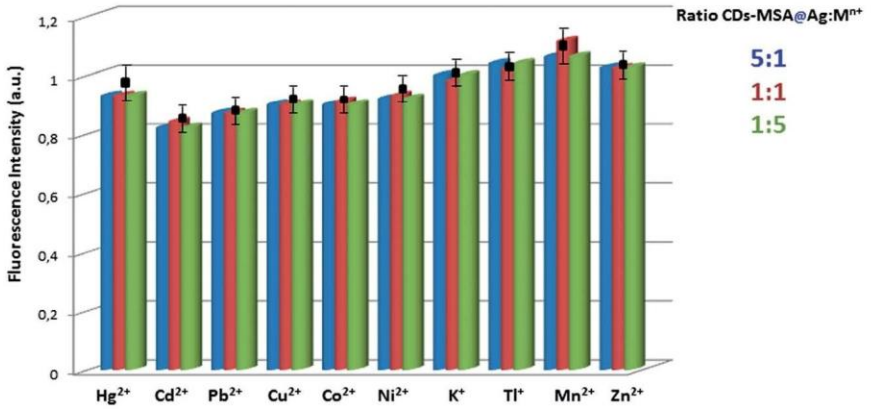

Fig. 8 Different fluorescence intensities before addition of metal (CD–MSA); after addition of Ag^+ (1.60×10^{-4} M); and CDs–MSA@Ag^+: Hg^{2+}, Cd^{2+}, Zn^{2+} and Pb^{2+} ($M^{++} = 1.60 \times 10^{-4}$ M).

After functionalization with MSA (CDs–MSA) the presence of Ag^+ ions causes a visible quenching of the fluorescence (Fig. 7A). Thus the presence of MSA, attached on the surface of CDs, is a key factor for their sensing applications. Based on the chemistry of MSA modified QDs we hypothesize that thiols are the active species sensitive to the presence of silver ions. The quenching was analyzed using Stern–Volmer plots (Fig. 7B and C). Even though Ag^+ ions cause quenching of fluorescence they do not affect the structure of CDs–MSA. That quenching is linked to the non-radiative transfer of the CD excited electrons to the ions resulting in their reduction to atomic Ag(s). The standard Stern–Volmer plot (Fig. 7B) shows the existence of a downward curvature. This type of curvature suggests that the fluorophores present in the CDs–MSA are not all equally accessible to the metal ions and only a fraction of of them is affected by Ag^+ and exhibits quenching of the fluorescence. In order to assess whether this effect results in the curvature of the standard Stern–Volmer plot, a modified Stern–Volmer model was used (Fig. 7C). It shows a linear trend indicating the existence of fluorophores in the CDs not accessible to Ag^+. From the plot it was evaluated that 44% of the fluorophores are accessible to Ag^+ with a static Stern–Volmer constant of 3.7×10^3 M^{-1}. This analysis shows that the functionalization of CDs with MSA allows the stable binding of Ag^+. Based on the results discussed above, the –SH groups are the sites which bind silver and the ratio of these groups to carboxylic acids in the MSA molecule (assuming that another carboxylic acid group of the MSA molecule was involved in the esterification reaction) is in fact 1 : 1. Moreover, the results suggest that MSA is evenly distributed around CDs because there are areas in the surface that are not sensitive (or accessible) towards Ag^+.

The proposed sensor was optimized to obtain the best sensitivity. The limit of detection (LOD) and limit of quantification (LOQ) were also evaluated to demonstrate its limitation. The LOD was calculated taking the fluorescence intensity equal to 3 times the SD of the blank ($n = 10$) divided by the slope of the calibration graph; while the LOQ was determined as 3 times the LOD. The LOD and LOQ of the proposed sensor were 385.8 nM and 1.2 μM, respectively. The precision was determined by analysing 10 samples containing 1.60×10^{-4} M of Ag^+ and it was 1.76%, as relative standard deviation (RSD).

Tolerance of foreign metals in the analysis of Ag^+ by CDs–MSA

In order to assess the possibility of analytical application of our approach, the effects of different metal ions present in the solution – Hg^{2+}, Cd^{2+}, Pb^{2+}, Cu^{2+}, Co^{2+}, K^+, Ni^{2+}, Mn^{2+}, Tl^+ and Zn^{2+} on the fluorescence intensity of CDs–MSA with Ag^+ (2.5×10^{-4} M) were tested. The summary of the results obtained is presented in Fig. 8. The fluorescence intensities of CDs–MSA@Ag^+, at different concentration ratios of CDs–MSA@Ag^+ to M^{n+} (5 : 1; 1 : 1 and 1 : 5), were measured in separate sets of experiments. When a high ratio of the CD–MSA@Ag^+ concentration was used (5 : 1), the interference was ±5%.

It can be seen that the fluorescence intensity of CDs–MSA@Ag^+ in the presence of the different tested metals ions did not show any significant change from the original intensity resulted from CDs–MSA@Ag^+ with the exception of Cd^{2+} and Pb^{2+}. These ions have a moderate quenching effect which probably results from their interaction with the capping ligands. In general for all the results obtained, using different concentration ratios (5 : 1; 1 : 1 and 1 : 5), it can be confirmed that Ag^+ could be determined by CDs–MSA in the presence of different metal ions. These results confirmed that the concentration of Ag^+ can be estimated in the presence of relatively small amounts of other metals using the proposed sensor system. The selectivity to Ag^+ can be explained by its soft acid nature and affinity to the soft base thiol groups of MSA attached to the surface of QDs. At higher concentration of CDs the bivalent metals can become involved in reactions with thiols or even with carboxylic acids acid which must be accompanied by the CD aggregation (linkages *via* bivalent metal).

Determinations of Ag^+ in AgNP dissolution

As an application, the feasibility of the proposed method was tested for the determination of free Ag^+ ions present in AgNP dissolution. As shown in Fig. 6, due to the low influence of the pH in the fluorescence intensity of CDs–MSA, the pH was

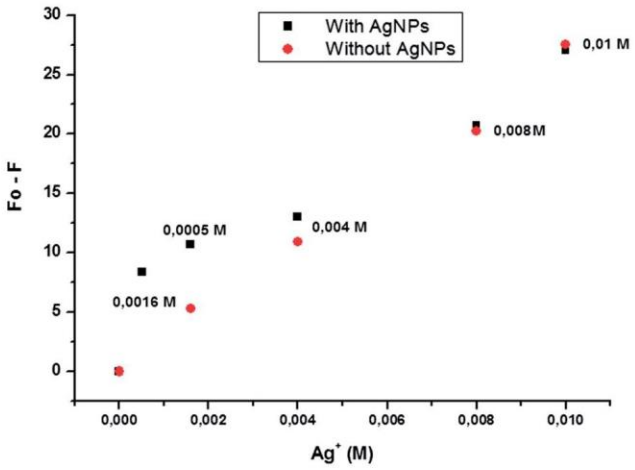

Fig. 9 Results obtained when comparing the analysis of Ag^+ by CDs–MSA in AgNPs presence (■) and absence (●).

Table 1 Determination of Ag^+ in AgNP dissolution by CD–MSA[a]

Added Ag^+ (M)	Found Ag^+ (M)	% Recovery	% RSD
0.005	0.0048 ± 0.0011	96	2.2
0.006	0.0061 ± 0.0015	101	1.9
0.007	0.0069 ± 0.0021	98	1.3
0.009	0.0092 ± 0.0019	102	1.6

[a] Means of three determinations.

adjusted to 4.5 with acetic–acetate buffer dissolution. A standard addition method was chosen and the AgNPs were dissolved to obtain the signal of the remaining Ag^+ ions in the valid range of the measurements. Fig. S7A and B† show the fluorescence spectra presenting the effect of the increase of the concentrations of Ag^+ in the presence of AgNPs and without them on the fluorescence intensity. The results show that the presence of remaining Ag^+ ions quenches the emission from CDs–MSA (Fig. 9). The presence of AgNP is negligible at high concentrations of Ag^+, for that to determine the concentration can be used the calibration curve obtained without AgNPs.

The concentrations of Ag^+ for different spiked samples are summarized in Table 1, which showed recoveries between 96 and 102% and a moderate accuracy as % RSD (1.3–2.2), demonstrating the feasibility of the CD–MSA system to be used as the Ag^+ sensor.

Conclusions

Summarizing, we have developed a fluorescent sensor for Ag^+ detection based on the decrease of the fluorescence intensity of carbon dots modified with thiols. This material is obtained from lactose by its acidic treatment which is followed by binding MSA to its surface. The oxygen and sulfur functional groups are suggested to function as fluorophores attached to the QD surface. Under the optimum conditions, fluorescence intensity was linearly proportional to the Ag^+ concentration in a wide range of values. The detection limit is in the range of nM. The probe had remarkably high selectivity and moderate sensitivity. The reaction of silver with thiols is proposed as a quenching/sensing mechanism. The results obtained show the promising application of CD–MSA in Ag^+ chemical sensing.

Acknowledgements

The authors would like to thank the Andalucia Tech program and the Ministry of Science and Technology of the Republic of Serbia which supported this study with Grant 173017.

References

1 Y. P. Sun, B. Zhou, Y. Lin, W. Wang, K. A. S. Fernando, P. Pathak, M. J. Meziani, B. A. Harruf, X. Wang, H. Wang, P. G. Luo, H. Yang, M. E. Kose, B. Chen, L. M. Veca and S. Y. Xie, *J. Am. Chem. Soc.*, 2006, **128**, 7756–7757.
2 S. N. Baker and G. A. Baker, *Angew. Chem., Int. Ed.*, 2010, **49**, 6726–6744.
3 J. C. G. Esteves da Silva and H. Gonçalves, *TrAC, Trends Anal. Chem.*, 2011, **30**, 1327–1336.
4 Q. L. Zhao, Z. L. Zhang, B. H. Huang, J. Peng, M. Zhang and D. W. Pang, *Chem. Commun.*, 2008, 5116–5118.
5 X. Wang, L. Cao, F. Lu, M. J. Meziani, H. Li, G. Qi, B. Zhou, B. A. Harruff, F. Kermarrec and Y. P. Sun, *Chem. Commun.*, 2009, 3774–3776.
6 S. C. Ray, A. Saha, N. R. Jana and R. Sarkar, *J. Phys. Chem. C*, 2009, **113**, 18546–18551.
7 H. T. Li, X. D. He, Y. Liu, H. Huang, S. Y. Lian, S. T. Lee and Z. H. Kang, *Carbon*, 2011, **49**, 605–609.
8 L. B. Tang, R. B. Ji, X. K. Cao, J. Y. Lin, H. X. Jiang, X. M. Li, K. S. Teng, C. M. Luk, S. J. Zeng, J. H. Hao and S. P. Lau, *ACS Nano*, 2012, **6**, 5102–5110.
9 A. B. Bourlinos, A. Stassinopoulos, D. Anglos, R. Zboril, M. Karakassides and E. P. Giannelis, *Small*, 2008, **4**, 455–458.
10 S. Chandra, S. Mitra, D. Laha, S. Bag, P. Das, A. Goswami and P. Pramanik, *Chem. Commun.*, 2011, **47**, 8587–8589.
11 S. Zhu, Q. Meng, L. Wang, J. Zhamg, Y. Song, H. Jin, K. Zhang, H. Sun, H. Wang and B. Yang, *Angew. Chem., Int. Ed.*, 2013, **52**, 3953–3957.
12 S. T. Yang, L. Cao, P. G. Luo, F. Lu, X. Wang, H. Wang, M. J. Meziani, Y. Liu, G. Qi and Y. P. Sun, *J. Am. Chem. Soc.*, 2009, **131**, 11308–11309.
13 X. Hou, F. Zheng, F. Du and S. Wu, *Nanotechnology*, 2013, **24**, 335502.
14 Q. Li, T. Y. Ohulchanskyy, R. L. Liu, K. Koynov, D. Q. Wu, A. Best, R. Kumar, A. Bonoiu and P. N. Prasad, *J. Phys. Chem. C*, 2010, **114**, 12062–12068.
15 D. Y. Pan, L. Guo, J. C. Zhang, C. Xi, Q. Xue, H. Huang, J. H. Li, Z. W. Zhang, W. J. Yu, Z. W. Chen, Z. Li and M. Wu, *J. Mater. Chem.*, 2012, **22**, 3314–3318.
16 Q. Wang, X. Huang, Y. Long, X. Wang, H. Zhang, R. Zhu, L. Liang, P. Teng and H. Zheng, *Carbon*, 2013, **59**, 192–199.

17 J. Xu, S. Sahu, L. Cao, C. E. Bunker, G. Peng, Y. Liu, K. A. Fernando, P. Wang, E. A. Guliants, M. J. Meziani, H. Qian and Y. P. Sun, *Langmuir*, 2012, **28**, 16141–16147.
18 F. Lin, D. Pei, W. He, Z. Huang, Y. Huang and X. Gui, *J. Mater. Chem.*, 2012, **22**, 11801–11807.
19 E. Morales-Narváez, B. Pérez-López, L. B. Pires and A. Merkoçi, *Carbon*, 2012, **50**, 2987–2993.
20 J. Shen, Y. Zhu, X. Yang and C. Li, *Chem. Commun.*, 2012, **48**, 3686–3699.
21 Y. Dong, R. Wang, H. Li, J. Shao, Y. Chi, X. Lin and G. Chen, *Carbon*, 2012, **50**, 2810–2815.
22 H. Li, Z. Kang, Y. Liu and S. T. Lee, *J. Mater. Chem.*, 2012, **22**, 24230–24253.
23 H. Gonçalves, P. A. S. Jorge, J. R. A. Fernandes and J. C. G. Esteves da Silva, *Sens. Actuators, B*, 2010, **145**, 702–707.
24 R. Liu, H. Li, W. Kong, J. Liu, Y. Liu, C. Tong, X. Zhang and Z. Kang, *Mater. Res. Bull.*, 2013, **48**, 2529–2534.
25 H. Liu, T. Ye and C. Mao, *Angew. Chem., Int. Ed.*, 2007, **46**, 6473–6475.
26 R. S. Cay, A. Saha, N. R. Jana and R. Sarkar, *J. Phys. Chem. C*, 2009, **113**, 18546–18551.
27 L. Tian, D. Ghosh, W. Chen, S. Pradhan, X. Chang and S. Chen, *Chem. Mater.*, 2009, **21**, 2803–2809.
28 X. J. Mao, H. Z. Zheng, Y. J. Long, J. Du, J. Y. Hao, L. L. Wang and D. B. Zhou, *Spectrochim. Acta, Part A*, 2010, **75**, 553–557.
29 A. B. Bourlinos, A. Stassinopoulos, D. Anglos, R. Zboril, V. Georgakilas and E. P. Giannelis, *Chem. Mater.*, 2008, **20**, 4539–4541.
30 Z. Ma, H. Ming, H. Huang, Y. Liu and Z. Kang, *New J. Chem.*, 2012, **36**, 861–864.
31 L. Hua, X. H. Shan, J. Chen, Y. H. Jiang, J. Q. Chen and Z. Y. Yan, *Carbon*, 2013, **64**, 559.
32 Q. L. Zhao, Z. L. Zhang, B. H. Huang, J. Peng, M. Zhang and D. W. Pang, *Chem. Commun.*, 2008, 5116–5118.
33 L. Y. Zheng, Y. W. Chi, Y. Q. Dong, J. P. Lin and B. B. Wang, *J. Am. Chem. Soc.*, 2009, **131**, 4564–4565.
34 P. G. Luo, S. Sahu, S. T. Yang, S. K. Sonkar, J. Wang, H. Wang, G. E. LeCroy, L. Cao and Y. P. Sun, *J. Mater. Chem. B*, 2013, **1**, 2116–2127.
35 H. Li, X. He, Y. Liu, H. Huang, S. Lian, S. T. Lee and Z. Kang, *Carbon*, 2011, **49**, 605–609.
36 R. L. Liu, D. Q. Wu, S. H. Liu, K. Koynov, W. Knoll and Q. Li, *Angew. Chem., Int. Ed.*, 2009, **48**, 4598–4601.
37 H. T. Li, X. D. He, Z. H. Kang, H. Huang, Y. Liu and J. L. Liu, *Angew. Chem., Int. Ed.*, 2010, **49**, 4430–4434.
38 X. Wang, K. Qu, B. Xu, J. Ren and X. Qu, *J. Mater. Chem.*, 2011, **21**, 2445–2450.
39 A. Salinas-Castillo, M. Ariza-Avidad, C. Pritz, M. Camprubí-Robles, B. Fernández, M. J. Ruedas-Rama, A. Megia-Fernández, A. Lapresta-Fernández, F. Santoyo-Gonzalez, A. Schrott-Fischer and L. F. Capitan-Vallvey, *Chem. Commun.*, 2013, **49**, 1103–1105.
40 J. Mendieta, M. S. Diaz-Cruz, M. Esteban and R. Tauler, *Biophys. J.*, 1998, **74**, 2876–2888.
41 A. M. Brouwer, *Pure Appl. Chem.*, 2011, **83**, 2213–2228.
42 G. Weber and F. W. J. Teale, *Trans. Faraday Soc.*, 1957, **53**, 646–655.
43 J. R. Lackowiz, *Principles of Fluorescence Spectroscopy*, Springer, New York, 2nd edn, 1999.
44 T. Khantawa, C. Boonmeea, T. Tuntulani and W. Ngeontae, *Talanta*, 2013, **115**, 849–856.
45 M. L. Shen, L. P. Zhang, M. L. Chen, X. W. Chen and J. H. Wang, *Carbon*, 2013, **55**, 343–349.
46 M. Algarra, B. B. Campos, B. Alonso, M. S. Miranda, A. M. Martínez, C. M. Casado and J. C. G. Esteves da Silva, *Talanta*, 2012, **88**, 403–407.

3.2 Supplementary Data

Supporting Information

Luminescent Carbon Nanoparticles: Effects of chemical Functionalization, and evaluation of Ag^+ Sensing properties

Manuel Algarra, Bruno B. Campos, Ksenija Radotić, Dragosav Mutavdžić, Teresa Bandosz, J. Jiménez-Jiménez , E. Rodriguez-Castellón , Joaquim CG Esteves da Silva.

Fig. SI.1. UV spectrum of CDs, MSA and the complex between CDs-MSA

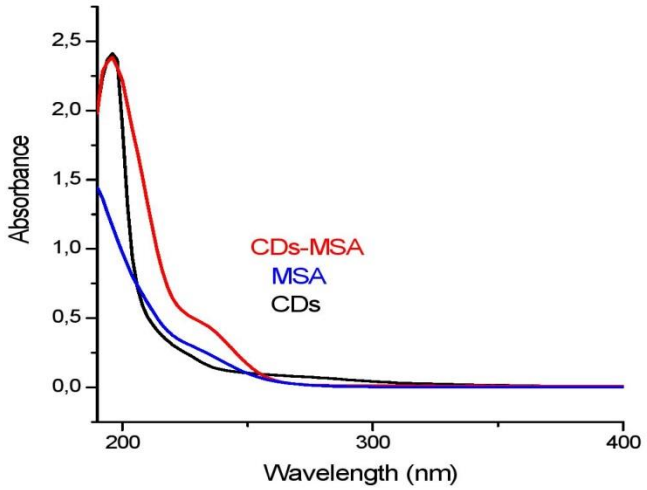

Fig. SI.2. Optimization of MSA concentration on the Fluorescence Intensity

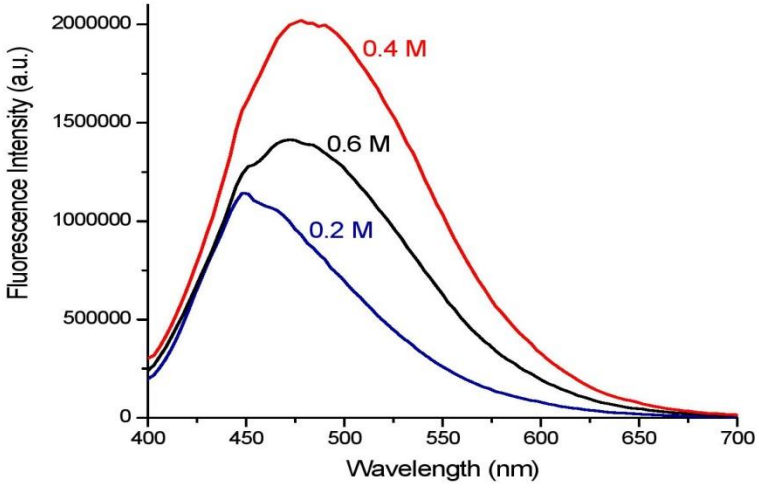

Fig. SI.3. Effect of pH on the Fluorescence Intensity of CDs-MSA sensor

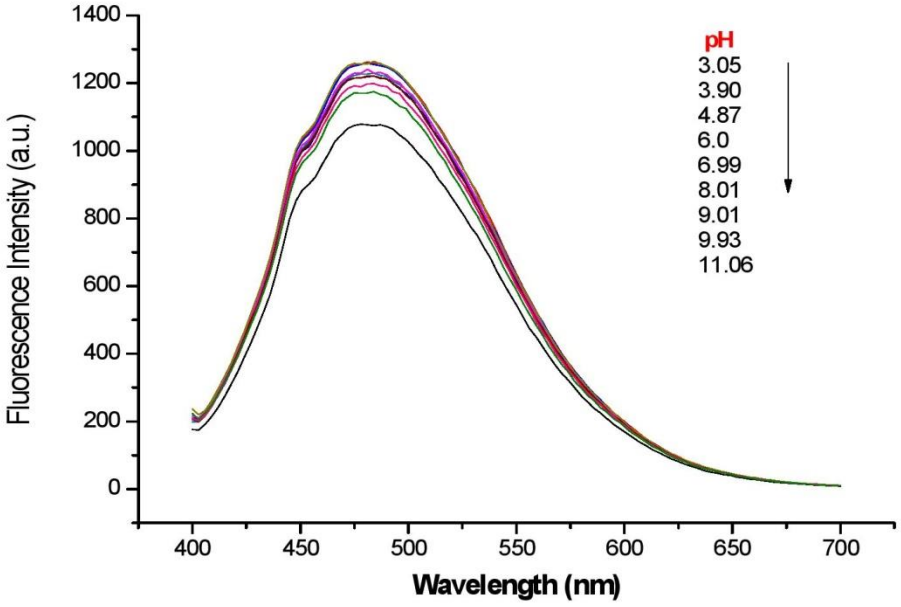

Fig. SI.4. Effect of Ionic Strength on the Fluorescence Intensity of CDs-MSA sensor

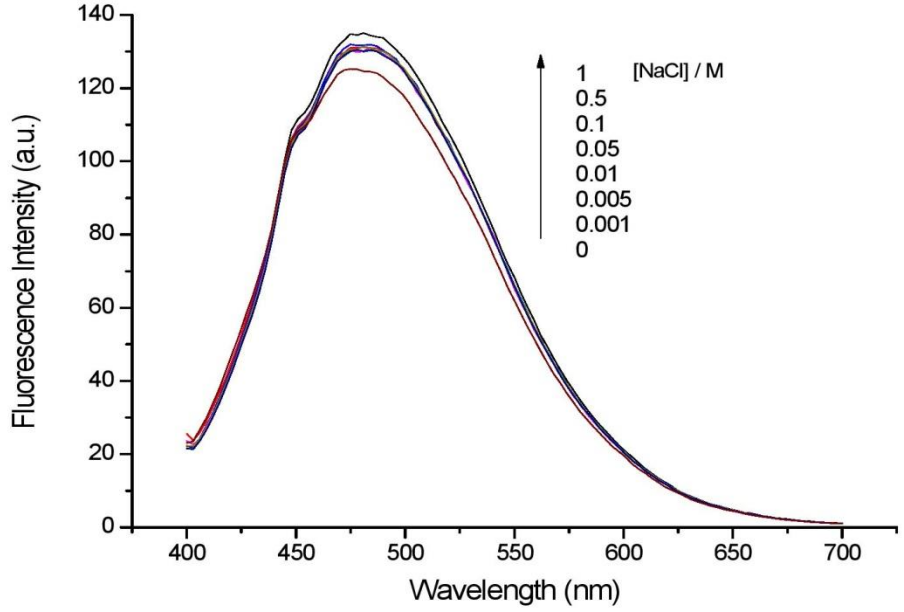

Fig. SI. 5

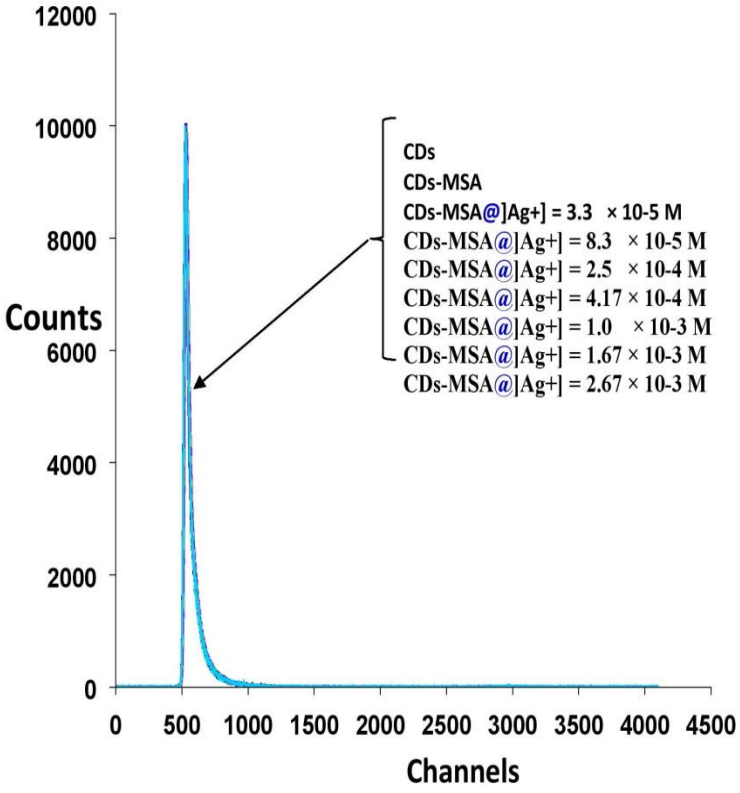
12000
10000
8000
6000
4000
2000
0
Counts
0
500
1000
1500
2000
2500
3000
3500
4000
4500
Channels
CDs
CDs-MSA
CDs-MSA@]Ag+] = 3.3 × 10-5 M
CDs-MSA@]Ag+] = 8.3 × 10-5 M
CDs-MSA@]Ag+] = 2.5 × 10-4 M
CDs-MSA@]Ag+] = 4.17 × 10-4 M
CDs-MSA@]Ag+] = 1.0 × 10-3 M
CDs-MSA@]Ag+] = 1.67 × 10-3 M
CDs-MSA@]Ag+] = 2.67 × 10-3 M

Table S1. Lifetime intensity decays of CDs, CDs-MSAin water without and in the presence of Ag^+

	τ_I (ns)	B_i	A	χ^2
CDs	2.56 (0.08) 0.450 (0.012) 6.33 (0.08)	0.0216 (0.0001) 0.0873 (0.0004) 0.00493 (0.00003)	9.98 (0.23)	1.1627
CDs-MSA	2.43 (0.08) 0.506 (0.015) 6.37 (0.06)	0.0235 (0.0001) 0.0700 (0.0004) 0.00622 (0.00003)	4.71 (0.18)	1.249645
CDs-MSA@[Ag^+] = 3.33×10^{-5} M	2.53 (0.07) 0.502 (0.013) 6.78 (0.06)	0.0236 (0.0001) 0.0738 (0.0004) 0.00509 (0.00003)	4.22 (0.17)	1.132022
CDs-MSA@[Ag^+] = 8.33×10^{-5} M	2.52 (0.08) 0.527 (0.013) 6.71 (0.07)	0.0213 (0.0001) 0.0772 (0.0004) 0.00446 (0.00003	4.31 (0.18)	1.253027
CDs-MSA@[Ag^+] = 0.00025 M	2.48 (0.08) 0.495 (0.014) 6.57 (0.06)	0.0235 (0.0001) 0.0737 (0.0004) 0.00554 (0.00003)	5.44 (0.19)	1.070406
CDs-MSA@[Ag^+] = 0.0004 M	2.55 (0.07) 0.506 (0.015) 6.79 (0.07)	0.0240 (0.0001) 0.0697 (0.0004) 0.00517 (0.00003)	4.86 (0.20)	1.16096
CDs-MSA@[Ag^+] = 0.001 M	2.52 (0.08) 0.505 (0.014) 6.59 (0.07	0.0238 (0.0001) 0.0729 (0.0004) 0.00550 (0.00003)	7.79 (0.23)	1.078386
CDs-MSA@[Ag^+] = 0.002 M	2.52 (0.08) 0.521 (0.014) 6.56 (0.07)	0.0237 (0.0001) 0.0706 (0.0004) 0.00553 (0.00003)	8.76 (0.24)	1.176244

Fig. SI. 6. TEM analysis of CDs nanoparticles

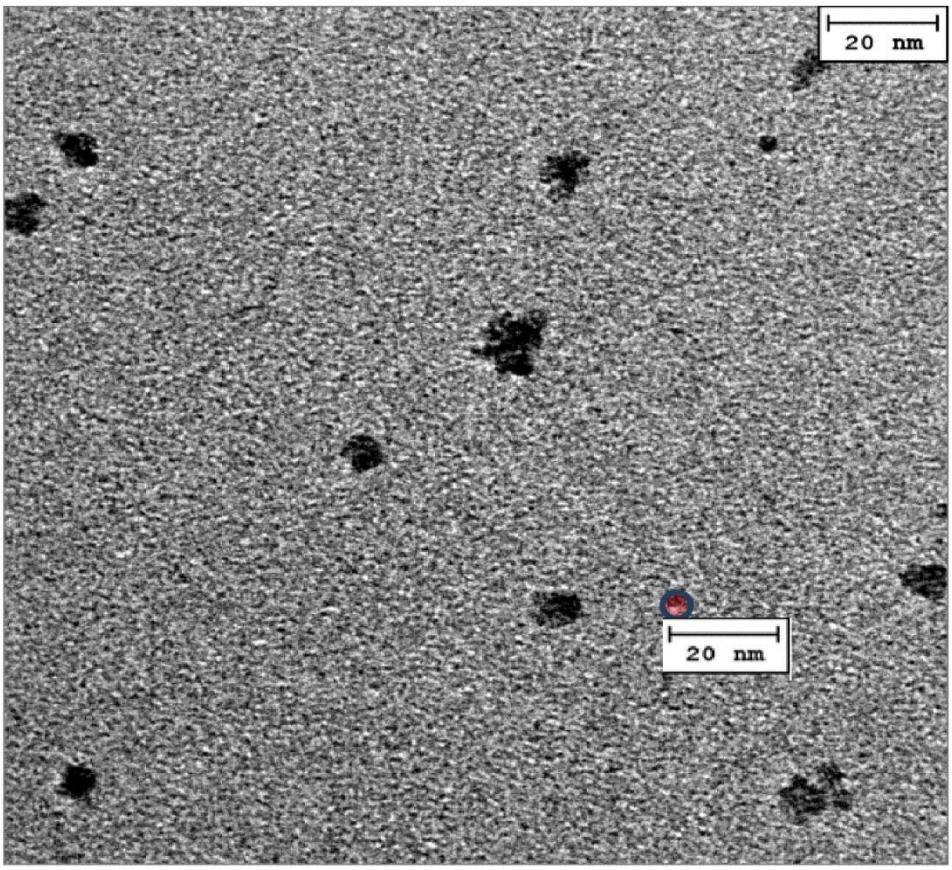

In the picture is picked up one of the nanoparticles and was measured and can be obtained a size

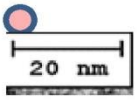

The size of the nanoparticles in this case is around 5.70 nm.

Fig. SI. 7.

A

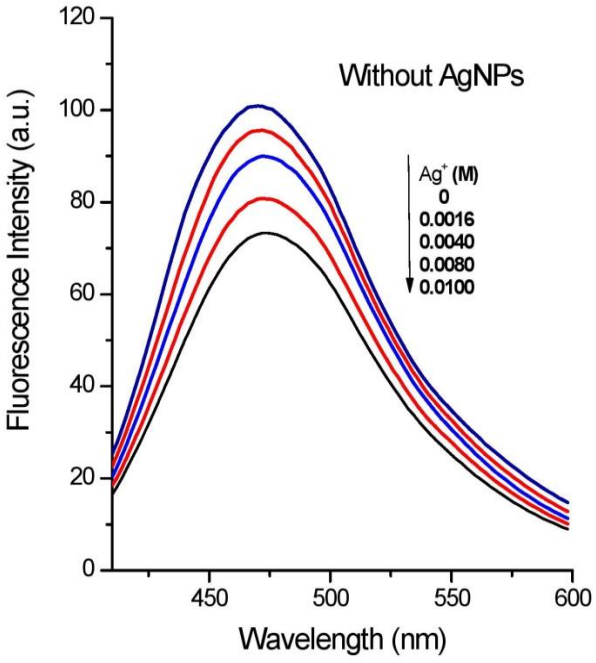
Without AgNPs
Fluorescence Intensity (a.u.)
Wavelength (nm)
Ag+ (M)
0
0.0016
0.0040
0.0080
0.0100
0
20
40
60
80
100
120
450
500
550
600

B

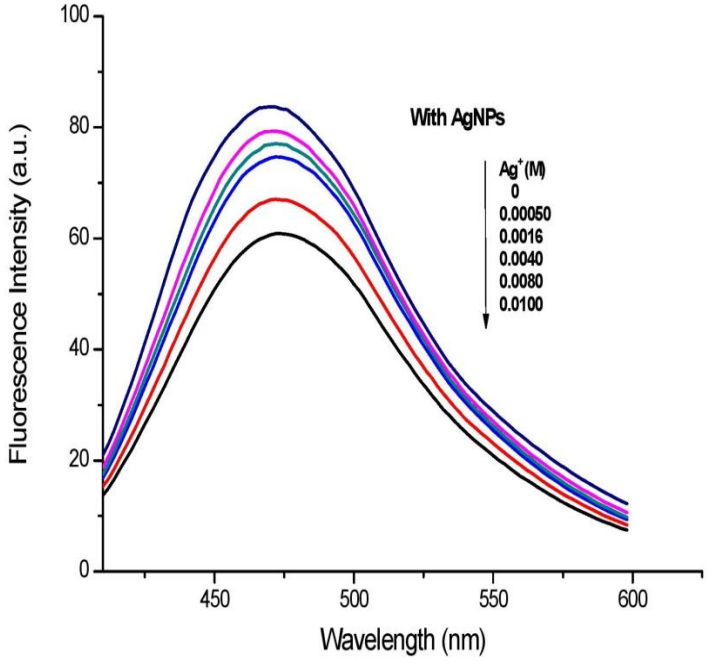
With AgNPs
Fluorescence Intensity (a.u.)
Wavelength (nm)
Ag+(M)
0
0.00050
0.0016
0.0040
0.0080
0.0100
0
20
40
60
80
100
450
500
550
600

Calibration Curves obtained for the analysis of Ag^{+} in presence of AgNPs and without

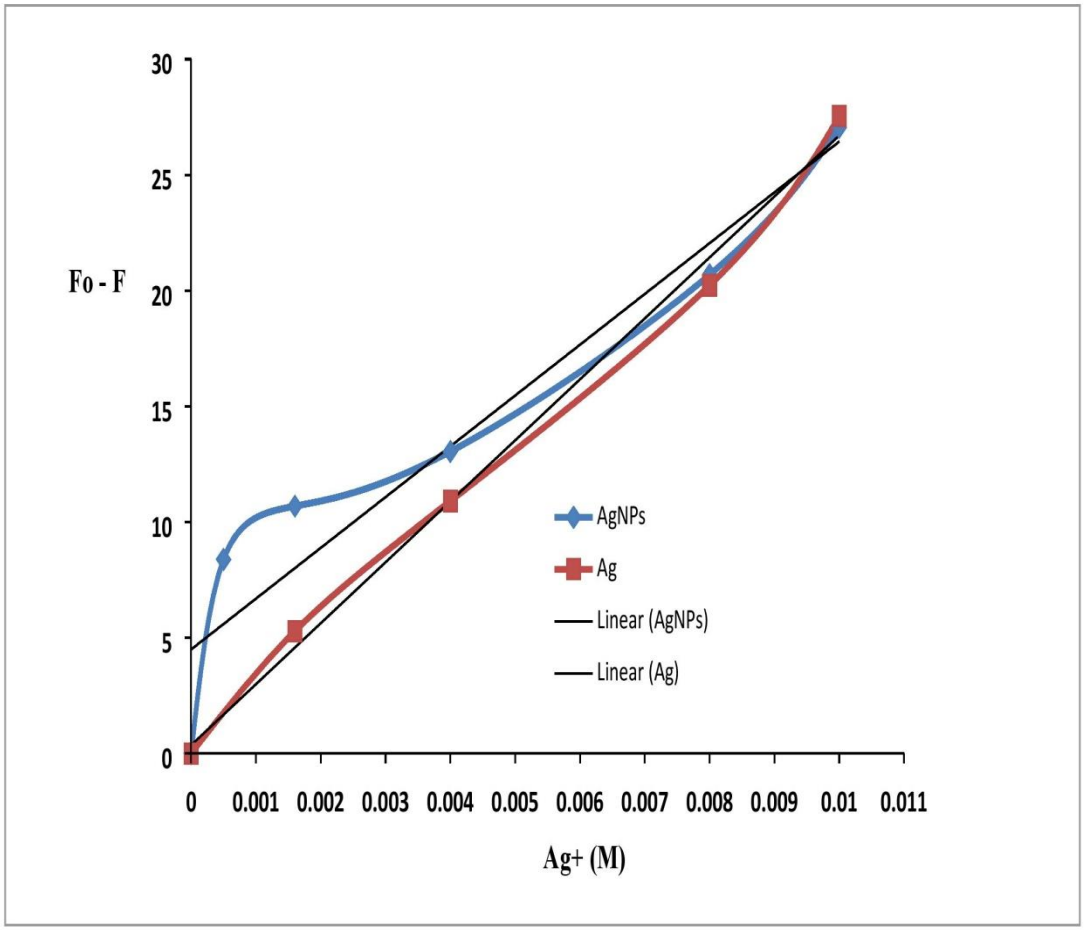

Chapter 4

Fluorescent Chemosensor for Pyridine Based on N-Doped Carbon Dots

4.1 Contribution to this Paper

My contribution to this paper included the bibliographic research and writing about carbon QDs, doping agents and then the experimental planning. The synthesis, purification and doping were performed, including the effect of pH on the excitation/emission matrix. The data obtained by the characterization methods and thermal analysis was analyzed and interpreted. The determination of analytical parameters and the sensing of pyridine was also performed and assayed with the fluorescent nanosensor. This paper was submitted as a scientific article and until the acceptation it passes through some adjustments required by the reviewers and under supervision of my advisor Professor Joaquim Esteves da Silva and co-advisor Doutor Manuel Algarra.

Journal of Colloid and Interface Science 458 (2015) 209–216

Contents lists available at ScienceDirect

Journal of Colloid and Interface Science

journal homepage: www.elsevier.com/locate/jcis

Fluorescent chemosensor for pyridine based on N-doped carbon dots

B.B. Campos [a], C. Abellán [b,c], M. Zougagh [c,d], J. Jimenez-Jimenez [e], E. Rodríguez-Castellón [e], J.C.G. Esteves da Silva [a], A. Ríos [b,c], M. Algarra [e,*]

[a] Centro de Investigação em Química, Departamento de Química, Faculdade de Ciências da Universidade do Porto, 4169-007 Porto, Portugal
[b] Department of Analytical Chemistry and Food Technology Department, University of Castilla-La Mancha, Ciudad Real, Spain
[c] Regional Institute for Applied Chemistry Research (IRICA), 13004 Ciudad Real, Spain
[d] Castilla-La Mancha Science and Technology Park, 20006 Albacete, Spain
[e] Departamento de Química Inorgánica, Facultad de Ciencias, Universidad de Málaga, Campus de Teatinos s/n, 29071 Málaga, Spain

GRAPHICAL ABSTRACT

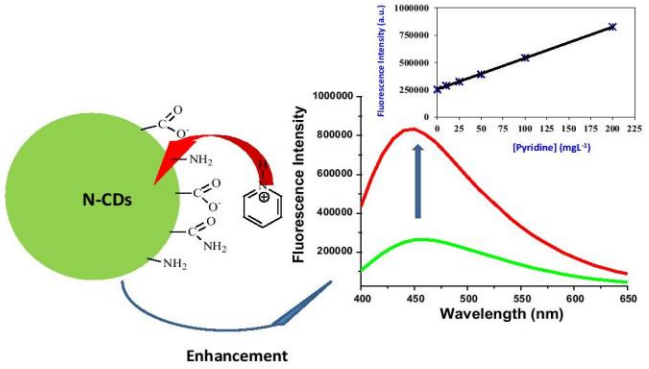

ARTICLE INFO

Article history:
Received 20 February 2015
Revised 17 July 2015
Accepted 23 July 2015

Keywords:
Carbon nanomaterial
Nanoparticle
N-doped carbon dots
Pyridine sensor

ABSTRACT

Fluorescent carbon dots (CDs) and its nitrogen doped (N-CDs) nanoparticles have been synthesized from lactose as precursor using a bottom-up hydrothermal methodology. The synthesized nanoparticles have been characterized by elemental analysis, FTIR, Raman, TEM, DLS, XPS, and steady-state and life-time fluorescence. The synthesized carbon nanoparticles, CDs and N-CDs, have a size at about 7.7 ± 2.4 and 50 ± 15 nm, respectively, and quantum yields of 8% (CDs) and 11% (N-CDs). These techniques demonstrated the effectiveness of the synthesis procedure and the functionalization of the CDs surface with amine and amide groups in the presence of NH_3 in aqueous media. The effect of excitation wavelength and pH on the luminescent properties was studied. Under the optimal conditions, the nitrogen doped nanoparticles can be used as pyridine sensor in aqueous media because they show an enhancement of its fluorescence with a good linear relationship. The analytical method is simple, reproducible and very sensitive for pyridine determination.

1. Introduction

Among the recent advances of novel materials, carbon quantum dots nanoparticles (in short carbon dots, CDs), are a new class of carbonaceous nanomaterials with potential advantages to the toxic

* Corresponding author.
E-mail address: malgarra67@gmail.com (M. Algarra).

http://dx.doi.org/10.1016/j.jcis.2015.07.053
0021-9797/

metal based quantum dots (QDs). Both nanoparticles share traditional nanosized semiconductors properties, namely: size and wavelength luminescence emission dependence, resistance to photobleaching, biocompatibility associated with their nanoscale structures in conjunction with chemical functionality, among others. CDs are easily functionalized and they present some advantageous properties when they are compared to QDs [1–5].

CDs can be obtained either by chemical bottom up and/or top down synthesis methods, using different procedures. Thus, electrochemical, combustion, thermal, hydrothermal, acidic oxidation, microwave and ultrasonic, laser ablation, have been reported as techniques used for these purposes [6–19]. Although fluorescent CDs have easily been obtained by these strategies, emission features (in terms of sensitivity, meanly) and quantum yield (QY) of CDs are still scarce and highly desirable to be improved.

Doping heteroatoms into CDs has been demonstrated an effective approach to improve QY and for incorporating a surface passivation, which has showed good results [14,20]. Different strategies have been used to obtain doped CDs with nitrogen, such as those obtained by heating carbon tetrachloride and 1,2-ethylendiamine [21], by pyrolyzing ethanolamine [22], from citric acid and L-cysteine [23], glutamic [24], and folic acid [25]. The effect of different doping atoms such as N, P or B was deeply studied, as well as their influence on the photo-physical properties [26], showing that N-CDs are the most efficient [27–30].

Pyridine is an organic liquid very soluble in water [31]. It is released to the environment from industrial sources, as fugitive emissions from facilities such as coal gasification and oil shale processing [32,33]. It is used for synthesis of drugs, insecticides and herbicides [34–36]. In this way, inhalation, ingestion or skin absorption induced in humans many symptoms like headaches, infertility, respiratory distress or puke [37]. This is the reason why the determination of pyridine is very important in environmental, food and clinic fields. Some methods have been reported in the literature for the detection and quantification of pyridine, including electrostatic precipitation [38], GC [39,40], liquid chromatography–mass spectrometry (LC–MS) [41], and GC–MS [42,43].

In this article, lactose was used as precursor to develop a new method of preparing fluorescent nitrogen doped carbon dots (N-CDs) via a facile hydrothermal (solvothermal) methodology [44]. By this method, the surface of the CDs is populated by C—N organic functionalities, such as amine and amide. After exploring its chemical and physical properties, the detection capabilities of prepared N-CDs for pyridine was further exploited, revealing an enhancement of their luminescent signal, this can be used for analytical purposes.

2. Experimental

2.1. Chemicals

D-Lactose monohydrate (99%), aqueous ammonia (37%) and hydrochloric acid (37%) were purchased from Panreac SAU (Barcelona, Spain). Pyridine, anhydrous (98.8%) was purchased from Sigma–Aldrich (St. Louis, USA). Ultrapure water, used throughout all experiments, was purified through a Millipore system. All reagents were used as received without further purification.

2.2. Synthesis of doped CD nanoparticles

Raw CDs were obtained by addition of 50 mL of concentrated HCl (37%) to 50 mL of a lactose solution (1 M), followed by hydrothermally heating at 100 °C in a Teflon-equipped stainless-steel for 3 h. Finally, the remained solution was neutralized with NaOH (1 M), filtered and dialyzed against water for 24 h. The N doped CDs (N-CDs) were synthesised by following the same procedure as stated for CDs: 50 mL of aqueous NH_3 (25%) were added to 50 mL of a lactose solution (1 M), hydrothermally heated at 100 °C in a Teflon-equipped stainless-steel at 100 °C for 3 h. Finally, the remained solution was neutralised with HCl (1 M), filtered and dialyzed against water for 24 h.

2.3. Characterization methods and data analysis

The morphology was analyzed by transmission electron microscopy (TEM) and examined under a Philips CM-200 (SCAI-UMA). To obtain the size distribution histograms of CDs and N-CDs nanoparticles, it was used the Image Tool Software v_3 (UTHSCSA, USA). The zeta potential (ζ) of CDs and N-CDs were determined using a Zetasizer Nano ZS (Malvern Instruments, U.K.) equipped with a 4 mW HeNe laser operating at $\lambda = 633$ nm. The ζ measurements were also performed at 25 °C in polycarbonate folded capillary cells, incorporated with Au plated electrodes (DTS1061) and deionized H_2O was the dispersion medium. The different ζ were automatically obtained by the software, using the Stokes-Einstein and the Henry equation, with the Smoluchowski approximation. Equinox 55 FT-IR spectrometer fitted with a Golden Gate single reflection ATR accessory kit from Specac. All spectra were recorded using a resolution of 2 cm^{-1}; 50 scans were collected. The fluorescence measurements were performed with a Jovin Yvon Fluoromax 4 TCSPC (Horiba), and measured between 400 and 700 nm using an integration time of 0.1 s and 5 nm slits for excitation and emission. Resonance FT-Raman spectra, with excitation at 532 nm, were recorded on a Senterra Raman Microscope from Bruker. Fluorescence lifetime analysis was carried out using an Edinburgh Instruments FLS920, equipped with a Xe lamp (450 W) as excitation source for steady state fluorescence measurements and monochromatic LEDs (PicoQuant PLS), controlled by a PDL 880-B system. Fluorescence decays were interpreted in terms of a multi-exponential function:

$$I(t) = A + \Sigma B_i \exp^{-t/\tau_i} \quad (1)$$

where A and B_i are the pre-exponential factors and τ_i the decay times. QY of CDs and N-CDs were obtained using Rhodamine 6G as reference ($\Phi = 0.93$) in methanol ($n = 1.329$, $\lambda_{ex} = 535$ nm). The nanoparticles were dissolved in deionized H_2O_2 ($n = 1.33$) and, by using Eq. (2), QY values were obtained for both nanoparticles.

$$QY_{CDs} = QY_{st}\left[\frac{(dI/dA)_{CDs}}{(dI/dA)_{st}}\right]\left(\frac{n^2_{CDs}}{n^2_{st}}\right) \quad (2)$$

In this equation, I is the area under the fluorescence curves and A is the corresponding absorbance [45].

X-ray photoelectron spectroscopic (XPS) studies were performed by a Physical Electronic PHI 5700 spectrometer using non-monochromatic Mg Ka radiation (300 W, 15 kV, 1253.6 eV) for analyzing the core-level signals of the elements of interest with a hemispherical multichannel detector. The spectra of powdered samples were recorded with a constant pass energy value at 29.35 eV, using a 720 μm diameter circular analysis area. The X-ray photoelectron spectra obtained were analyzed using PHI ACESS ESCA-V6.0F software and processed using Multipak 8.2B package. The binding energy values were referenced to adventitious carbon C 1*s* signal (284.8 eV). Shirley-type background and Gauss–Lorentz curves were used to determine the binding energies.

2.4. DSC–TG analysis

Thermo-gravimetric analysis (TG) and differential scanning calorimetric (DSC) were performed through a TG/DSC 1 Star System (Mettler-Toledo) coupled with MS-Thermostar GSD320 (Pfeiffer Vacuum) Mass Spectrometer. TG/DSC curves were measured in Pt crucibles, in N_2 flow (20 mL/min) and using a heating rate of 5 °C min^{-1} in the range of 25–1600 °C by a HT1600 oven connected to a MX5 microbalance (thermostatic at 22 °C). The process was controlled by a STARe software v.10.0 (Mettler Toledo STARe system). All the samples were air dried in an oven at a temperature of 60 °C for one week, in order to remove the excess of water, particularly for the samples subjected to high humidity conditions.

2.5. Detection of pyridine

For the detection of pyridine by N-CDs, 5 mL of the aqueous solution of N-CDs was poured into four test tubes, which were then mixed with different volumes (50 μL, 125 μL, 250 μL, 500 μL and 1000 μL) of aqueous solution of pyridine (12.6 mM), separately. The as-produced materials were finally sonicated for 30 min and their emission fluorescence spectra were recorded (λ_{ex} = 350 nm). The concentration of pyridine was in the 0.13–2.53 mM range, where linear emission intensity – concentration relationship was found.

3. Results and discussion

3.1. Synthesis and analysis of CDs and N-CDs nanoparticles

The raw material (lactose) was selected due to its low cost and, as previously reported, because it is a source of CDs showing an excellent fluorescence signal, and presenting good surface functionalization capabilities [14,46]. Solvothermal process was chosen because allowed us to obtain a precise control over the size and shape distribution of nanoparticles [47]. Fig. 1A shows the TEM image of raw CDs, which revealed that these spherical nanoparticles were well dispersed from each other, showing a regular mean size of CDs (7.7 ± 2.4 nm). Additional TEM images are available in Fig. S1 (Supplementary information). To obtain N-CDs, the direct presence of NH_3 in the raw aqueous media was selected, instead of release it from precursors for incorporating N in the carbon matrix. N-CDs show similar spherical morphology as the CDs but with high dimensions (average diameters of 50 ± 15 nm). Also, a local nano-environment was observed around each nanoparticle, probably ascribed to the inhomogeneous thermal process (Fig. 1B).

The zeta potential of CDs and N-CDs were −7.22 and −7.58 mV, respectively, which did not change significantly after the doped process with N, and it revealed the presence of carboxylate as prominent organic groups at pH 7, as it is shown in the FTIR spectra (Fig. 2). The elemental analysis demonstrated the incorporation of N, with a N-CDs/CDs ratio of 3.9.

The FTIR spectra of CDs and N-CDs (Fig. 2) are strongly affected by the presence of H_2O, which is IR active at about 3400 and 1630 cm^{-1}, assigned to the asymmetric stretching and bending modes of O—H. Weak bands at 1431 cm^{-1} and the small shift centered at 3249 cm^{-1}, can be assigned to the presence of the stretching modes of C—N and N—H respectively, suggesting the existence of amino-containing functional groups. Apparently, N mainly exists as doping element in the core of the N-CDs, contributing to increase its QY. The absorption of the carbonyl group (C=O) at 1630 cm^{-1} is weak, due to the minor oxidation of the N-CDs in the outer surface [48], which explains the presence of the band at 1070–1030 cm^{-1}, attributed to the C—O—C stretching mode in N-CDs [49].

The 532 nm laser wavelength Raman spectra of N-CDs (Fig. 3), compared to CDs, shows a weak band at 1647 cm^{-1}, related to the vibration of sp^2 bonded carbon atoms in a two dimensional

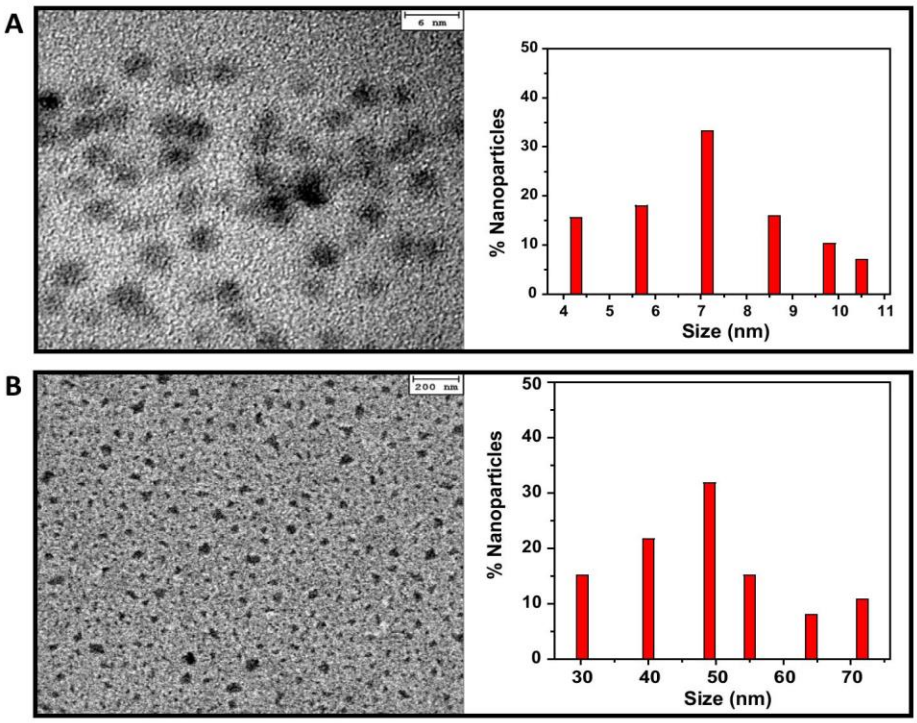

Fig. 1. TEM images of (A) CDs and (B) N-CDs nanoparticles obtained from aqueous ammonia aqueous solution (37%), showing their respective size distribution bar plots. For size distribution, 189 and 277 nanoparticles of CDs and N-CDs were analyzed, respectively.

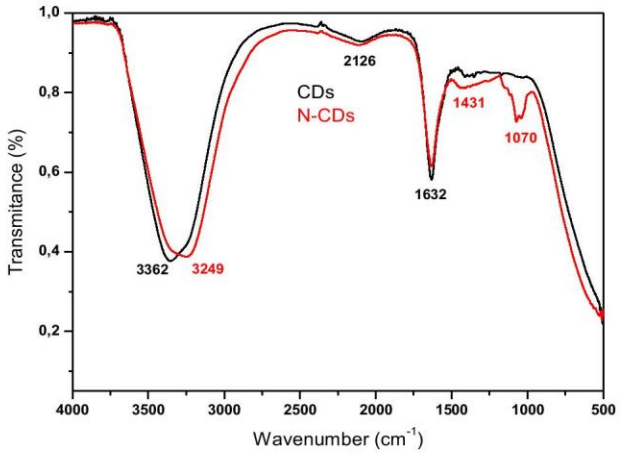

Fig. 2. FTIR spectrum of raw CDs (black) and doped N-CDs (red) nanoparticles. (For interpretation of the references to colour in this figure legend, the reader is referred to the web version of this article.)

hexagonal lattice, graphite structure. The small peak at 1350 cm^{-1} can be associated to the vibrations of carbon atoms with dangling bonds in the termination plane of disordered graphite or glassy carbon [50–52]. It is common the presence of G (1600 cm^{-1}) and D (1300–1350 cm^{-1}) bands in carbon graphitic materials; however, here a small intensity signal ascribable to the D band is detected [53]. These spectroscopic fingerprints suggest that the hydrothermal treatment reduces an important fraction of the oxygen groups of the lactose precursor, but it does not lead to a full reduction to unsaturated sp^2 species [54]. A band at 2950 cm^{-1}, observed only on disordered carbons, is suggested to be a defect-induced mode [55]. The bands centered at 3300 cm^{-1} was associated to the N—H stretch [56].

3.2. XPS analysis

The surface of the CDs and N-CDs materials were characterized by XPS. The C 1*s* core level spectrum of CDs (Fig. 4A) can be decomposed in three contributions at 284.8 eV (75%), 287.5 eV (18%) and 289.3 eV (7%). The contribution at low binding energy (284.8 eV) is the most intense and is assigned to the graphitic carbon and to adventitious carbon [51,52]. The contribution at 287.5 eV is mainly derived from the presence of carbonyl groups [52,53]; and finally,

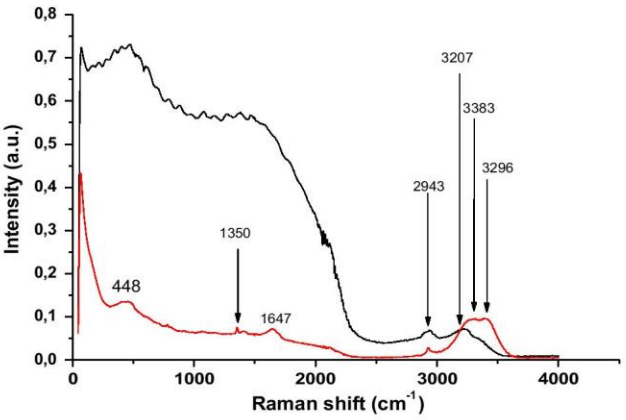

Fig. 3. Room temperature 532 FT-Raman spectrum of CDs (black) and N-CDs (red) nanoparticles. (For interpretation of the references to colour in this figure legend, the reader is referred to the web version of this article.)

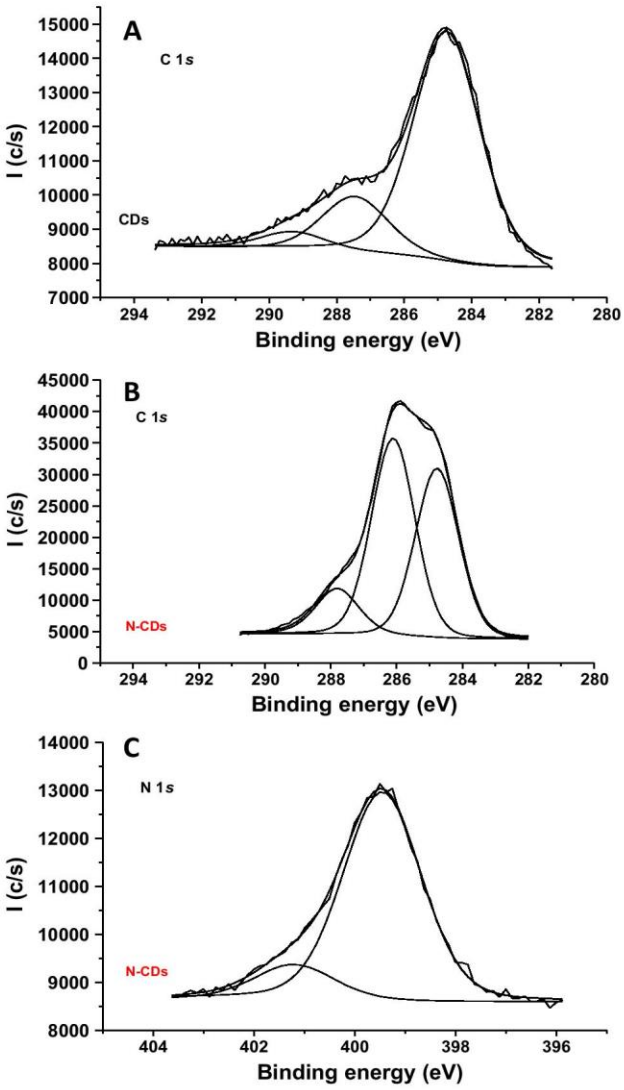

Fig. 4. (A) C 1*s* core level spectrum for sample CDs; and (B) C 1*s* and (C) N 1*s* core level spectra for sample N-CDs.

the weak contribution at 289.3 eV is due to carboxylic and carboxylate groups [51,54]. The C 1*s* core level spectrum of N-CDs can be also decomposed in three contributions at 284.8 eV (41%), 286.1 eV (47%) and 287.8 eV (12%), but showing marked differences with respect to that of CDs (Fig. 4B). Now, the contribution due to the presence of carboxylic or carboxylate groups disappears and a new contribution at 286.1 eV is more intense. This contribution is due to the presence of C—OH and C—N groups [53,54]. The N 1*s* core level spectrum is asymmetric due to the existence of two contributions at 399.5 eV (86%) and 401.2 eV (14%) (Fig. 4C). The high intensity is due to the presence of amino groups, while the contribution at high binding energy is due to the presence of NH_4^+ or alkyl ammonium groups [51,54] The atomic surface concentrations for CDs and N-CDs were C (48.05%), O (9.71%), N (0.67%), Na (21.89%), Cl (19.68%) for CDs; and C (65.72%), O (30.09%), N (3.63%) for N-CDs. The elemental analysis of the surface of N by XPS of CDs and N-CDs were 3.85% and 0.48% (in wt%), respectively. The surface mass N-CDs/CDs ratio was 7.56. This value is much higher than that observed by bulk elemental analysis (3.9), indicating that most of the N is mainly at the surface forming part of the surface nitrogen containing functionalities. The high

surface contamination with NaCl of CDs is due to the treatment with HCl and NaOH. However, N-CDs present negligible amounts of Cl and Na. In summary, XPS data show a lower atomic concentration of carbon and a higher atomic concentration of O on the surface of N-CDs, together to the appearance of N containing species mainly as amino groups, indicating that the nature of the functional groups at the surface of CDs and N-CDs are markedly different.

3.3. DTA–TG analysis

A study of the thermal stability of CDs and N-CDs was carried out in order to determine the effect of N (Fig. 5). In both cases an intense endothermic effect, associated with an important weight loss, occurs at about 100 °C, which is due to the evaporation of the water solution. In the case of pure CDs, it overlapped with other endothermic effect centered at 130 °C, both gives a weigh loss of 76% (Fig. 5A). In the case of N-CDs a weigh loss of 84% was observed until 140 °C (Fig. 5B), followed by other weigh loss of 5.20% between 300 and 500 °C, which was associated with an exothermic effect due to the combustion of the organic matter containing N. This exothermic effect was not observed in the case of CDs. These results are in agreement with those obtained by XPS and elemental analysis, demonstrating the incorporation of N containing functionalities is N-CDs. The next change is an exothermic effect which is presents in both materials, but whereas for doped N-CDs occurs at 560 °C (a weight loss of 3%), for pure CDs the exothermic effect was produced at 611 °C with a weight loss of 1%. Finally, for pure CDs a light endothermic effect, centered at 760 °C, was observed (Fig. 5A). The original files can be seen in Fig. S2 (Supplementary information).

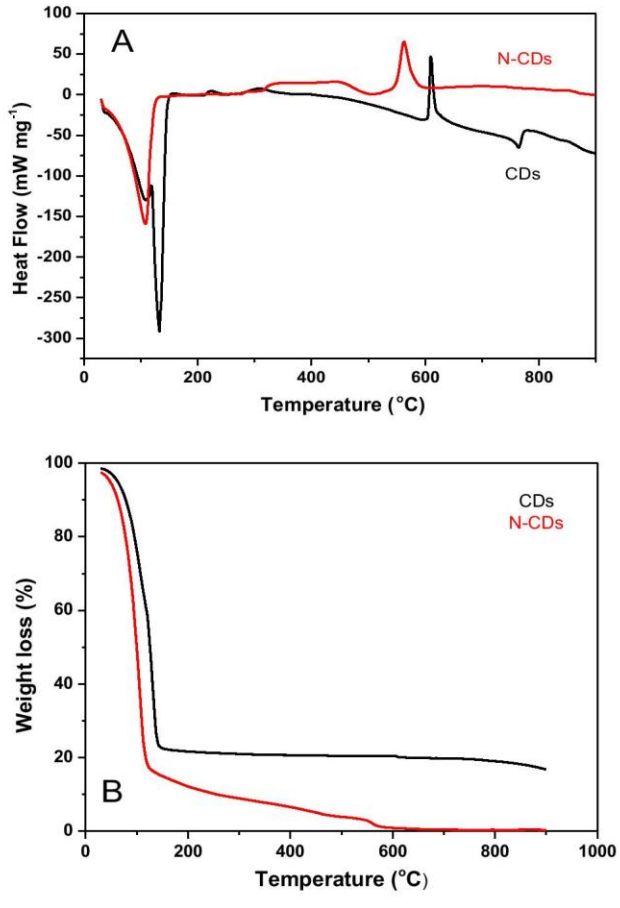

Fig. 5. (A) TG and (B) DSC curves of CDs (black) and N-CDs (red). (For interpretation of the references to colour in this figure legend, the reader is referred to the web version of this article.)

3.4. Fluorescence analysis

In order to explore the luminescent properties of N-CDs, the detailed fluorescence spectra were studied under different excitation wavelengths. As it is shown in Fig. 6, in concordance with the reported CDs and N-CDs references [46,47,55,56], the as-prepared N-CDs also exhibit a distinctive dependent fluorescent behavior. When the N-CDs were excited from 300 to 350 nm, the corresponding emission bands shifted from 440 to 460 nm. Moreover, the intensity of this emission bands were increased when the excitation wavelengths increased, showing a width at half maximum (FWHM) of 139 nm. This value indicated their size distribution dependence [57].

The highest blue emission intensity, with a QY as high as ca. 10.75%, was obtained when N-CDs were excited at 350 nm; somewhat higher compared to the raw CDs (8.10%). The observed distinctive luminescence emissions should be closely related to the N doping. The excitation-dependent fluorescent behavior of CDs can be related not only with the different sizes of N-CDs, but also from the inhomogeneous distribution of emissive sites due to the N doping [58].

The influence of pH on the fluorescence of N-CDs, in presence of pyridine, has been studied in the 1–10 pH range (Fig. 7). The presence of the N of pyridine molecule induces a change about the different signal between the signal produced by N-CDs and those produced by N-CDs in the presence of pyridine. The highest difference was observed in the pH 8–9 range, which can be explained by the presence of carboxylate ions and pyridine molecules ($pK_a = 5.16$). Therefore, in this range of pH, the interaction between N-CDs and pyridine is produced when the $>N^+$—H group of pyridine interacts with the carboxylate ($—COO^-$) in the surface of N-CDs. This fact is corroborated with the values obtained of ζ, showing the negative charge susceptible of electrostatic interactions.

The measured fluorescent lifetime values for CDs and N-CDs were obtained through a two components decay time model, showing a good fit (χ^2). Although these values were expected to be sensitive to the two types of treatment, a small difference was found (Table 1). Fluorescence lifetimes for N-CDs are 2-folds than raw CDs, explained by the low excitation density, but the QY are still low. This suggests the existence of efficient non-radiative pathways involving only a single exciton. A small increase in the

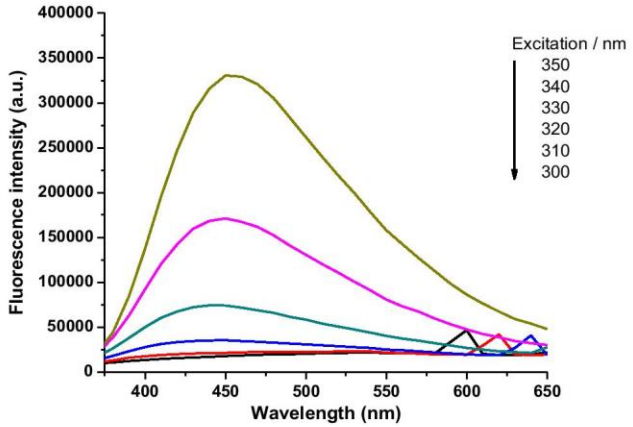

Fig. 6. Fluorescence emission spectra of N-CDs at different excitation wavelengths with at $\lambda_{em} = 450$ nm).

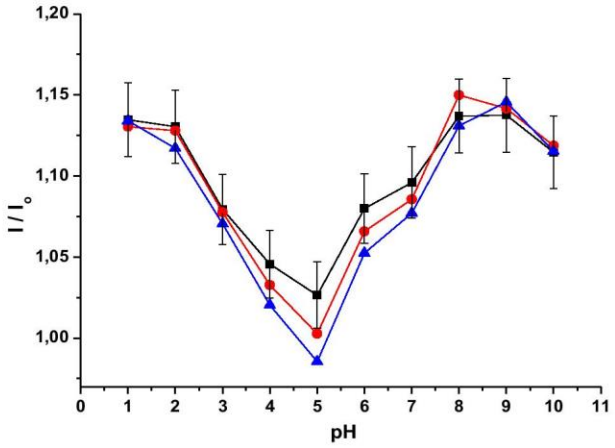

Fig. 7. Influence of pH on fluorescence intensity of N-CDs with pyridine (2×10^{-3} M) (λ_{ex} = 350; λ_{em} = 450 nm).

weight of τ_1 was observed (from 46.3% to 52.6%) in N-CDs. This is a typical behavior of a mono-exponential fitting of Eq. (1) [59].

The dilution of the N-CDs affects its fluorescence intensity. Five dilutions of N-CDs in proportions 1:25, 1:33, 1:50, 1:100, 1:200 and 1:500 with ultrapure water and PBS solution were investigated. In both cases, a 50-fold dilution was the optimum value for N-CDs. This experimental condition was considered as the stock solutions of this material because its higher fluorescence intensity. The study of the interaction of different chemical species with the surface of N-CDs is widely reported in the literature [14,15]. It has revealed that the luminescence properties of these nanomaterials strongly depend on their surface atoms and their environment [60].

3.5. Pyridine detection

In order to exploit the potential applications of the produced N-CDs, this material was directly applied in the detection of pyridine without any further functionalization. In literature, the main detection system used are based on spectrophotometric methods [61–63], where the level of detection for pyridine is at a concentration level of 0.5 mg L^{-1}. A potentiometric method was also reported for pyridine, presenting a limit of detection level of 0.28 mg L^{-1} [64]. At the same level of concentration pyridine was determined based on the quenching effect of ZnS nanoparticles coated with thioglycerol [65], or by using chitosan-CdS nano-composites films [66]. Additionally, a review of the detection systems for vapor of pyridine and related hazards can be found in the literature [67].

Therefore, the as-prepared N-CDs were evaluated as potential fluorescence probe nanosensor for pyridine. Different concentrations of an aqueous solution of pyridine were injected into the N-CDs solution and the mixture was treated under ultrasounds for 30 min before the fluorescence measurements. Fig. 8 show that the presence of pyridine induces an enhancement on the fluorescence of N-CDs, obtaining a broadness and blue shift when the concentration of pyridine increased. These modifications on the photo-physical properties on the N-CDs were produced by modifications on the surface, due to the chemical/physical sorption of pyridine molecules. The explanation of this fact can be associated to the formation of a complex, based on electrostatic interactions, when pyridine was added to the solution of N-CDs. The aggregation of nanoparticles was induced, and an energy transfer process is involved [68]. In contrast, the behavior of raw CDs when mixed with pyridine only showed small changes in the fluorescence emission spectra (see Fig. S3 in Supplementary information).

The dependence of the measured fluorescence intensity signal with increasing concentrations of pyridine was linear within the concentration range of 0.13–2.53 mM, showing a good regression

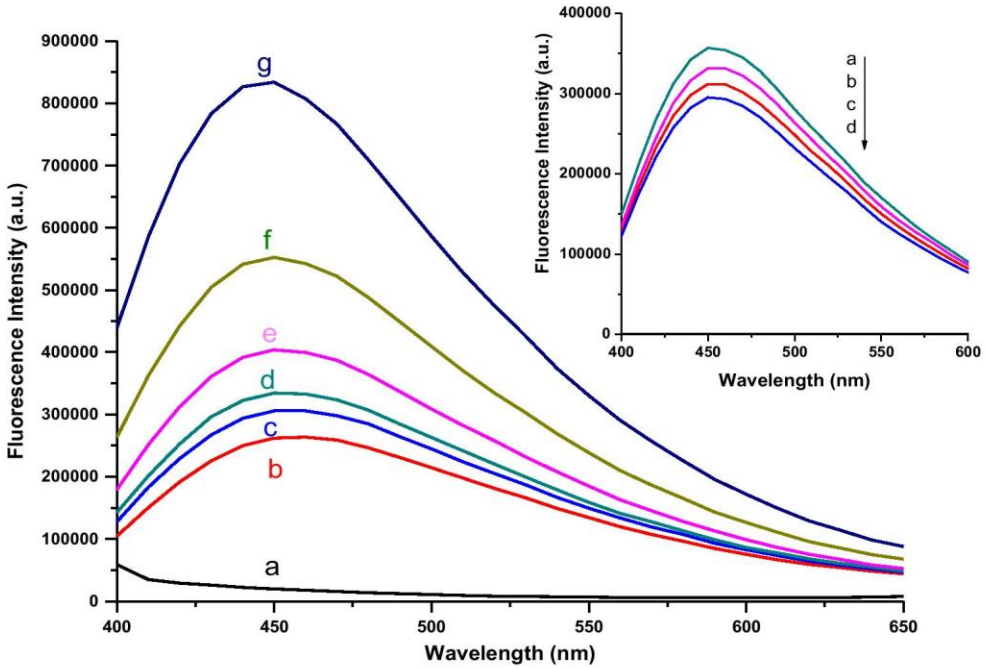

Fig. 8. Influence of pyridine concentration on fluorescence intensity of N-CDs (a) Pure pyridine; (b) Pure N-CDs; (c) 50; (d) 125; (e) 250; (f) 500 and (g) 1000 μL. Inset: Evolution of fluorescence intensity of N-CDs-pyridine (a) 5 days; (b) 3 days; (c) 3 h, and (d) Initial taken as reference (0 h); (λ_{ex} = 350; λ_{em} = 450 nm).

Table 1
Fluorescence lifetime CDs and N-CDs obtained from lactose.

	A	B_1	B_2	τ_1 (ns)	τ_2 (ns)	χ^2
CDs	16.914	0.0247	0.0068	1.045 (46.3%)	4.395 (53.7%)	1.089
N-CDs	49.401	0.0580	0.0134	2.265 (52.6%)	8.824 (47.4%)	1.084

A and B_i are the pre-exponential factor.
τ_i the lifetimes.

Table 2
Calibration data and validation parameters obtained for pyridine determination by using the proposed fluorescence chemosensor.

Linear range (mM)	0.13–2.53
Intercept $(a \pm S_a) \times 10^4$	2505.6 ± 0.1
Slope $(b \pm S_b) \times 10^4$	22.8 ± 0.1
R^2	0.9999
$S_{y/x}$	2.6×10^3
LOD (mM)	0.03
LOQ (mM)	0.11
RSD	0.25

a: Intercept; S_a: SD of the intercept; b: slope; S_b: SD of the slope; R: regression coefficient; $S_{y/x}$: SD of residuals; RSD: relative standard deviation ($n = 10$).

coefficient ($R^2 = 0.999$). The figures of merit of the method are summarized in Table 2. The LOD obtained was 0.03 mM, which presents advantages with respect to the previous value using other similar fluorescent sensor for detection of pyridine, for which a LOD of 0.068 mM was reported [69]. Moreover, in addition to the good sensitivity, with the sensor proposed here, very reproducible results were obtained, involving a simple methodology at much reduced costs. The precision, expressed in terms of relative standard deviation (RSD), was 0.25% ($n = 10$), which are at the level order of concentration of the previous analytical methods described.

4. Conclusions

In conclusion, we have presented a facile and rapid method to obtain N-CDs by using lactose as the precursor under a solvothermal process, under the treatment with NH_3 at 100 °C. The as-prepared N-CDs, with spherical morphology and a distribution of nanoparticles with an 3×10^{-5} average diameter of 50 ± 15 nm (lager than the un-treated with NH_3, 7.7 ± 2.4 nm). N-CDs showed a moderate quantum yield (10.75%) and bright green fluorescence. By XPS and Raman spectroscopy it was elucidated the presence of surface carbonyl, amine and amide functional groups. Also, N-CDs showed sensitivity towards pyridine in aqueous media because it enhanced the fluorescence of N-CDs proportionally to the concentration, being its limit of detection of 0.03 mM with a precision of 0.25%, while raw CDs did not show outstanding change on the fluorescence intensity when mixed with pyridine. The method is simple, sensitive and a low cost is involved.

Acknowledgments

M. Algarra is gratefully to the PLASMON program from ESF for the Exchange Grant. B.B Campos is gratefully to Grant SFRH/BD/84318/2012 to FCT (Lisbon, Portugal) Financial support from the Spanish Ministry of Economy and Competitiveness (CTQ2013-48411-P) and Junta Comunidades Castilla-La Mancha (Project PEIC-2014-001-P) are gratefully acknowledged. The support given through an "INCRECYT" research contract to M. Zougagh is also acknowledged.

Appendix A. Supplementary material

Supplementary data associated with this article can be found, in the online version, at http://dx.doi.org/10.1016/j.jcis.2015.07.053.

References

[1] Y.P. Sun, B. Zhou, Y. Lin, W. Wang, K.A.S. Fernando, P. Pathak, M.J. Meziani, B.A. Harruff, X. Wang, H. Wang, P.G. Luo, H. Yang, M.E. Kose, B. Chen, L.M. Veca, S.Y. Xie, J. Am. Chem. Soc. 128 (2006) 7756.
[2] S.N. Baker, G.A. Baker, Angew. Chem. Int. Ed. 49 (2010) 6726.
[3] Q. Liang, W. Ma, Y. Shi, Z. Li, X. Yang, Carbon 60 (2013) 421.
[4] S. Zhu, Q. Meng, L. Wang, J. Zhang, Y. Song, H. Jin, K. Zhang, H. Sun, H. Wang, B. Yang, Angew. Chem. Int. Ed. 52 (2013) 3953.
[5] Y. Wang, A. Hu, J. Mater. Chem. C 2 (2014) 6921.
[6] H.T. Li, X.D. He, Z.H. Kang, H. Huang, Y. Liu, J.L. Liu, S.Y. Lian, C.H.A. Tsang, X.B. Yang, S.T. Lee, Angew. Chem. Int. Ed. 49 (2010) 4430.
[7] H. Ming, Z. Ma, Y. Liu, K.M. Pan, H. Yu, F. Wang, Z.H. Kang, Dalton Trans. 41 (2012) 9526.
[8] J.G. Zhou, C. Booker, R.Y. Li, X.T. Zhou, T.K. Sham, X.L. Sun, Z.F. Ding, J. Am. Chem. Soc. 129 (2007) 744.
[9] Z.L. Wu, P. Zhang, M.X. Gao, C.F. Liu, W. Wang, F. Leng, C.Z. Huang, J. Mater. Chem. B 1 (2013) 2868.
[10] Z. Yang, Z. Li, M. Xu, Y. Ma, J. Zhang, Y. Su, F. Gao, H. Wei, L. Zhang, Nano-Micro Lett. 5 (2013) 247.
[11] C.Z. Zhu, J.F. Zhai, S.J. Dong, Chem. Commun. 48 (2012) 9367.
[12] X.Y. Qin, W.B. Lu, A.M. Asiri, A.O. Al-Youbi, X.P. Sun, Catal. Sci. Technol. 3 (2013) 1027.
[13] S. Sahu, B. Behera, T.K. Maiti, S. Mohapatra, Chem. Commun. 48 (2012) 8835.
[14] M. Algarra, B.B. Campos, K. Radotić, D. Mutavdžić, T.J. Bandosz, J. Jiménez-Jiménez, E. Rodriguez-Castellon, J.C.G. Esteves da Silva, J. Mater. Chem. A 2 (2014) 8342.
[15] M. Algarra, M. Pérez-Martín, M. Cifuentes-Rueda, J. Jiménez-Jiménez, J.C.G. Esteves da Silva, T.J. Bandosz, E. Rodríguez-Castellón, J.T. López-Navarrete, J. Casado, Nanoscale 6 (2014) 9071.
[16] H. Li, X. He, Y. Liu, H. Huang, S. Lian, S.T. Lee, Z. Kang, Carbon 49 (2011) 605.
[17] X. Wang, L. Cao, F.S. Lu, M.J. Meziani, H. Li, G. Qi, B. Zhou, B.A. Harruff, F. Kermarrec, Y.P. Sun, Chem. Commun. (2009) 3774.
[18] G.X. Chen, M.H. Hong, T.C. Chong, H.I. Elim, G.H. Ma, W. Ji, J. Appl. Phys. 95 (2004) 1455.
[19] H. Gonçalves, P.A.S. Jorge, J.R.A. Fernandes, J.C.G. Esteves da Silva, Sens. Act. B Chem. 145 (2010) 702.
[20] A. Sachev, I. Matai, P. Gopinath, RSC Adv. 4 (2014) 20915.
[21] S. Liu, J. Tian, L. Wang, Y. Luo, J. Zhai, X. Sun, J. Mat. Chem. 21 (2011) 11726.
[22] X. Dong, Y. Su, H. Geng, Z. Li, C. Yang, X. Li, Y. Zhang, J. Mater. Chem. C 2 (2014) 7477.
[23] Y. Dong, H. Pang, H.B. Yang, C. Guo, J. Shao, Y. Chi, C.M. Li, T. Yu, Angew. Chem. Int. Ed. 52 (2013) 7800.
[24] J. Niu, H. Gao, J. Luminescence 149 (2014) 159–162.
[25] M.K. Barman, B. Jana, S. Bhattacharyya, A. Patra, J. Phys. Chem. C. 118 (2014) 20034.
[26] W. Guan, W. Gu, L. Ye, C. Gui, s. Su, P. Xu, M. Xue, Int. J. Nanomedicine 9 (2014) 5071.
[27] G. Xu, G. He, Z. Li, F. He, F. Gao, Y. Su, L. Zhang, Z. Yang, Y. Zhang, Nanoscale 6 (2014) 10307.
[28] G. Jiang, T. Jiang, X. Li, Z. Wei, X. Du, X. Wan, Mater. Res. Express 1 (2014) 025708.
[29] Y.Q. Zhang, D.K. Ma, Y. Zhuang, X. Zhang, W. Chen, L.L. Hong, Q.X. Yan, K. Yu, S.M. Huang, J. Mater. Chem. 22 (2012) 16714.
[30] Y.Q. Zhang, D.K. Ma, Y.G. Zhang, W. Chen, S.M. Huang, Nano Energy 2 (2013) 545.
[31] D.R. Lide (Ed.), Handbook of Chemistry and Physics (nineteenth ed.), Boca Raton, CRC Press, 2009.
[32] G.K. Sims, E.J. O'Loughlin, R.L. Crawford, Crit. Rev. Environ. Contr. 19 (1989) 309.
[33] D.H. Stuermer, D.J. Ng, C.J. Morris, Environ. Sci. Tech. 16 (1982) 582.
[34] J.A. Joule, K. Mills, Heterocyclic Chemistry, fifth ed., Blackwell Publishing, Chichester, 2010.
[35] S. Shimizu, N. Watanabe, T. Kataoka, T. Shoji, N. Abe, S. Morishita, H. Ichimura, Pyridine and Pyridine Derivatives, Ullmann's Encyclopedia of Industrial Chemistry, 2002.
[36] E.A. Bakhite, A.A. Abd-Ella, m.E. El-Sayed, S.A. Abdel-Raheem, J. Agric. Food Chem. 62 (2014) 9982.
[37] International Agency for Research on Cancer (IARC), "Pyridine Summary & Evaluation", IARC Summaries & Evaluations, IPCS INCHEM, 2007.
[38] E.L. White, M.S. Uhrig, T.J. Johnson, B.M. Gordon, R.D. Hicks, M.F. Borgerding, W.M. Coleman III, J.F. Elder Jr., J. Chromatogr. Sci. 28 (1990) 393.
[39] H. Tang, G. Richards, K. Gunter, J. Crawford, M.L. Lee, E.A. Lewis, D.J. Eatough, J. High Resolut. Chromatogr. Chromatogr. Commun. 11 (1988) 775.
[40] K.D. Brunnemann, G. Stahnke, D. Hoffmann, Anal. Lett. 11 (1978) 545.
[41] S. Saha, R. Mistri, B.C. Ray, J. Chromatogr. A 1217 (2010) 307.
[42] S. Vainiotalo, R. Vaaranrinta, J. Tornaeus, N. Aremo, T. Hase, K. Peltonen, Environ. Sci. Technol. 35 (2001) 1818.

[43] G. Pieraccini, S. Furlanetto, S. Orlandini, G. Bartolucci, I. Giannini, S. Pinzauti, G. Moneti, J. Chromatogr. A 1180 (2008) 138.
[44] M. Choucair, P. Thordarson, J.A. Stride, Nat. Nanotech. 4 (2008).
[45] A.M. Brouwer, Pure Appl. Chem. 83 (2011) 2228.
[46] C. López, M. Zougagh, M. Algarra, E. Rodríguez-Castellón, B.B. Campos, Joaquim C.G. Esteves da Silva, J. Jiménez-Jiménez, A. Ríos, Talanta 132 (2015) 845.
[47] S.L. Hu, K.Y. Niu, J. Sun, J. Yang, N.Q. Zhao, X.W. Du, J. Mater. Chem. 19 (2009) 484.
[48] R. Vikneswaran, S. Ramesh, R. Yahya, Mat. Lett. 136 (2014) 179.
[49] B. Wang, Y. Zhang, Z. Guo, J. Cheng, Z. Fang, J. Polym. Res. 18 (2011) 187.
[50] S. Iijima, Nature 354 (1991) 56.
[51] Z.H. Kang, E.B. Wang, S.Y. Lian, L. Gao, M. Jiang, C.W. Hu, L. Xu, Nanotechnology 15 (2004) 490.
[52] M.S. Dresselhaus, G. Dresselhaus, M.A. Pimenta, P.C. Eklund, in: M. J. Pelletier (Ed.), Analytical Applications of Raman Spectroscopy, Blackwell Science, Oxford, 1999, (Chap. 9).
[53] G. Gouadec, P. Colomban, Prog. Cryst. Growth Charact. Mater. 56 (2007) 1.
[54] M. Bose, S. Gayen, S.N. Behera, Phys. Rev. B 72 (2005) 153402.
[55] Y. Sato, M. Kamo, N. Setaka, Carbon 16 (1978) 279.
[56] D.W. Mayo, F.A. Miller, R.W. Hannah, Courses on the Interpretation of Infrared and Raman Spectra, Wiley-Interscience, Hoboken, NJ, 2003.
[57] J.F. Moulder, W.F. Stickle, P.E. Sobol, K.D. Bomben, in: Jill Chastain (Ed.), Handbook of X-ray Photoelectron Spectroscopy, Minnesota, 1992.
[58] S.D. Gardner, C.SK. Singamsetty, G.L. Booth, G.R. He, Carbon 33 (1995) 587.
[59] M. Seredych, E. Rodríguez-Castellón, M.J. Biggs, W. Skinner, T.J. Bandosz, Carbon 78 (2014) 540–548.
[60] N. Travlou, M. Seredych, E. Rodriguez-Castellón, T.J. Bandosz, J. Mater Chem. A 3 (2015) 3821.
[61] A. Cayuela, M.L. Soriano, M. Valcárcel, Anal. Chim. Acta 804 (2013) 246.
[62] Y. Liu, C.Y. Liu, Z.Y. Zhang, Appl. Surf. Sci. 263 (2012) 481.
[63] S.C. Hill, R.G. Pinnick, S. Niles, N.F. Fell, Y.L. Pan, J. Bottiger, B.V. Bronk, S. Holler, R.K. Chang, Appl. Opt. 40 (2001) 3005.
[64] B.K. An, S.-K. Kwon, S.-D. Jung, S. Park, J. Am. Chem. Soc. 124 (2002) 14410.
[65] U.R. Genger, M. Grabolle, S.C. Jaricot, R. Nitschke, T. Nann, Nat. Methods 5 (2008) 763.
[66] M. Jones, C. Engtrakul, W.K. Metzger, R.J. Ellingson, A.J. Nozik, M.J. Heben, G. Rumbles, Phys. Rev. B 71 (2005) 15426.
[67] K.N. Ramachandran, V.K. Gupta, Microchem. J. 44 (1991) 272.
[68] S. Amlathe, S. Upadhyay, V.K. Gupta, Microchem. J. 37 (1998) 225.
[69] Z. Li, J. Ma, Y. Zong, Y. Men, J. Alloys Comp. 559 (2013) 39.

4.2 Supplementary Data

Supplementary Information

Fluorescent Chemosensor for Pyridine Based on N-Doped Carbon Dots

B.B. Campos, C. Abellán, M. Zougagh, J. Jimenez-Jimenez,
E. Rodríguez-Castellón J.C.G. Esteves da Silva, A. Ríos, M. Algarra

Figure S1. TEM Images

A) CDs

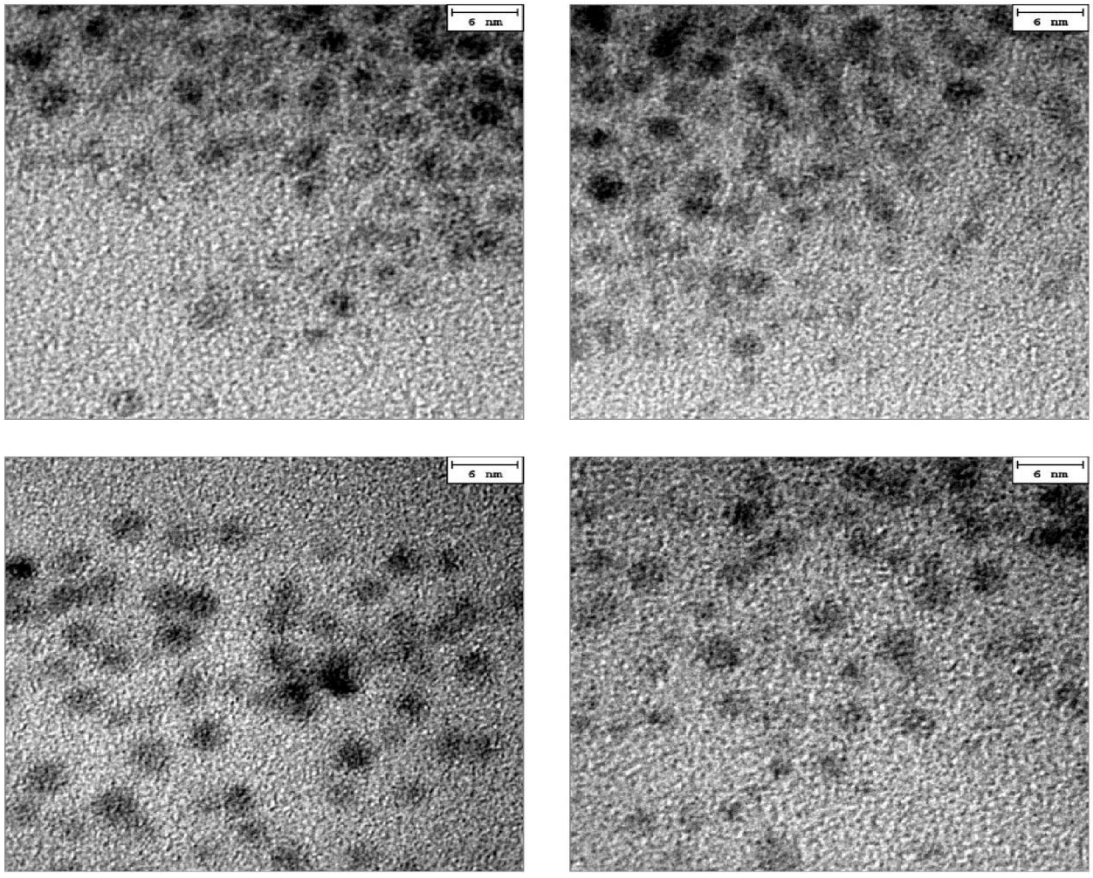

B) N-CDs (It has been obtained 25 Nanoparticles)

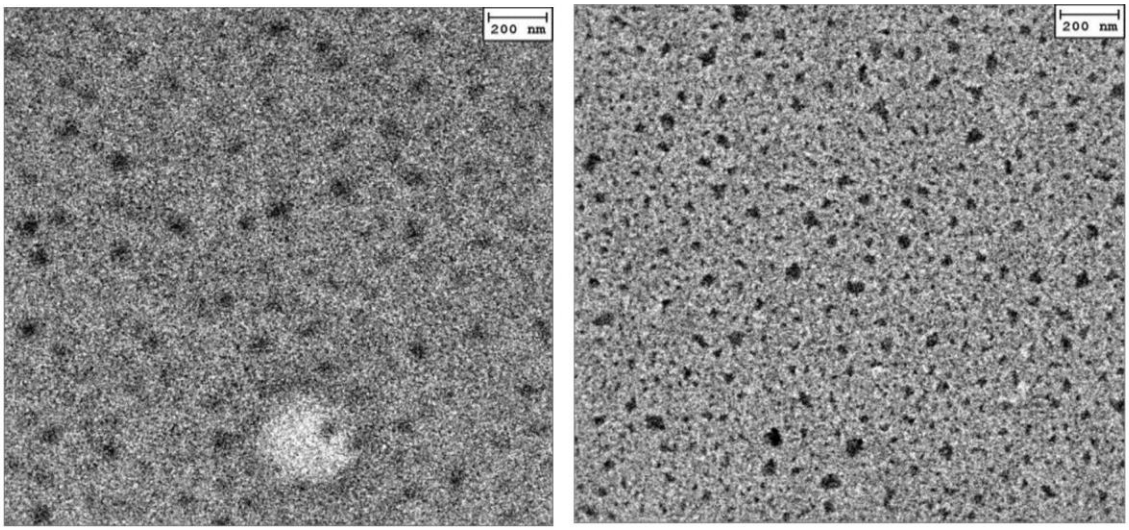

Figure S2. Original TGA-DSC curves of **A)** CDs and **B**) N-CDs Nanoparticles

A)

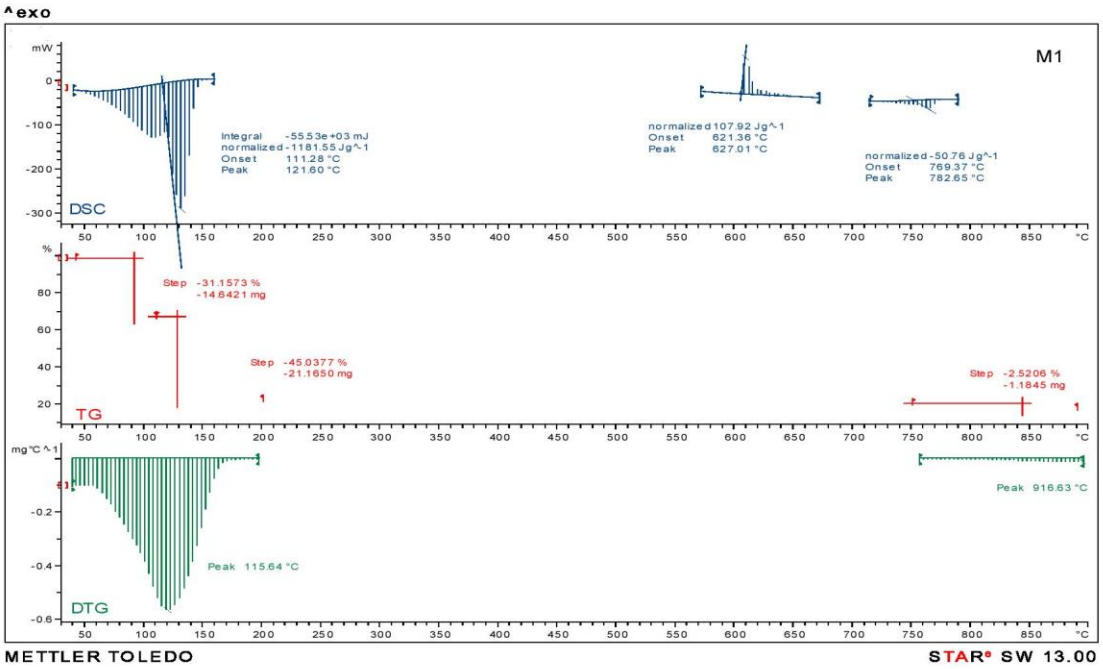

B)

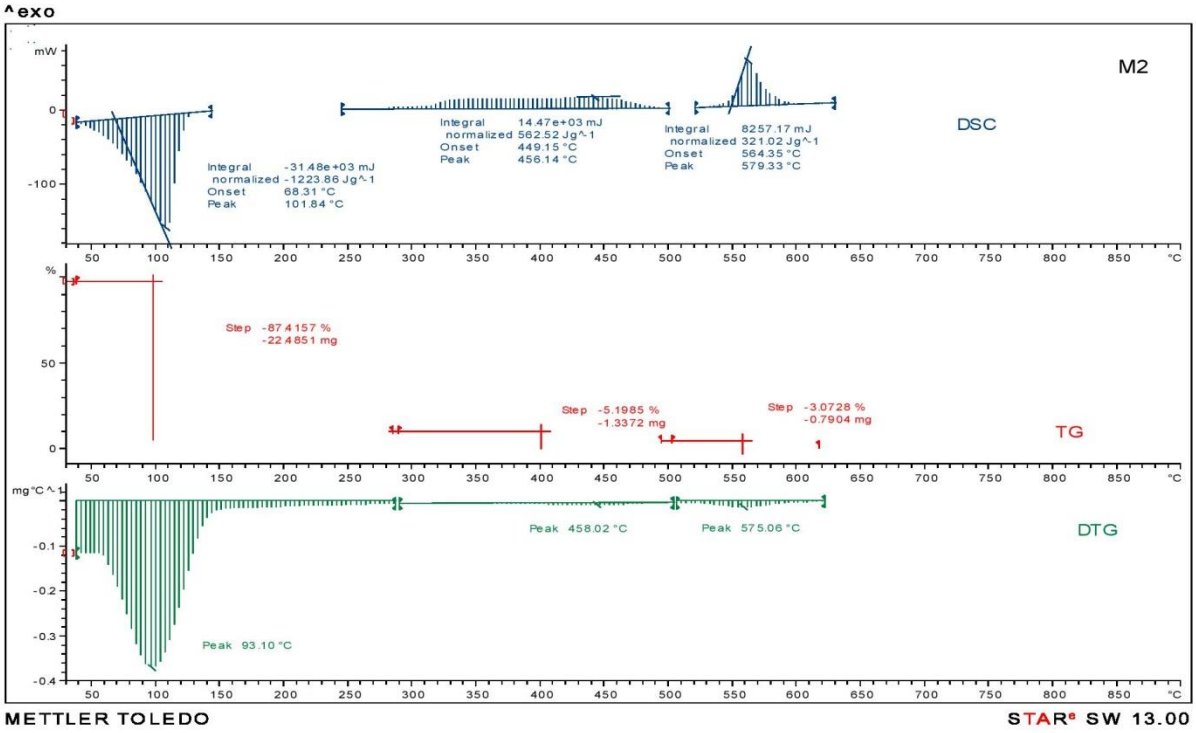
^exo
mW
M2
Integral -31.48e+03 mJ
normalized -1223.86 Jg^-1
Onset 68.31 °C
Peak 101.84 °C
Integral 14.47e+03 mJ
normalized 562.52 Jg^-1
Onset 449.15 °C
Peak 456.14 °C
Integral 8257.17 mJ
normalized 321.02 Jg^-1
Onset 564.35 °C
Peak 579.33 °C
DSC
%
Step -87.4157 %
-22.4851 mg
Step -5.1985 %
-1.3372 mg
Step -3.0728 %
-0.7904 mg
TG
mg/°C^-1
Peak 458.02 °C
Peak 575.06 °C
DTG
Peak 93.10 °C
°C
METTLER TOLEDO
STARe SW 13.00

Figure S3. Effect of Pyridine on the fluorescence intensity of un-doped CDs

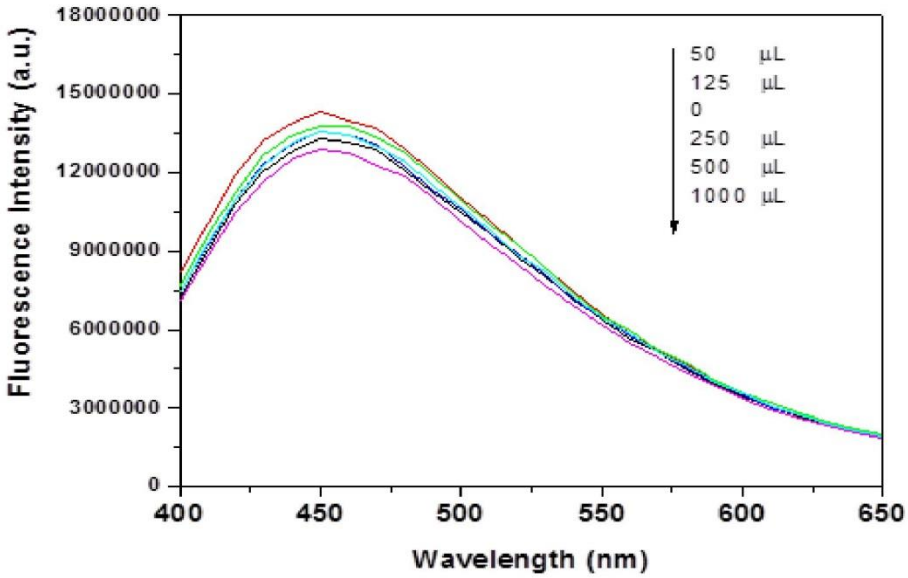

Chapter 5

Carbon Dots Coated with Vitamin B_{12} as Selective Ratiometric Nanosensor for Phenolic Carbofuran

5.1 Contribution to this Paper

My contribution to this paper included the bibliographic research and writing about carbon QDs, FRET phenomenon and then the experimental planning. The synthesis, purification and functionalization with Vitamin B_{12} were performed, even all the complementary studies including the influence of carbon source, dehydrating agents, temperature and time of reaction and the tolerance to some metabolites carbofuran on the excitation/emission matrix. The data obtained by the characterization methods was analyzed and interpreted. The determination of analytical parameters and the sensing of carbofuran phenol 3-Keto in solution and real samples, as soy sauce, were also performed and assayed with the fluorescent nanosensor. This paper was submitted as a scientific article and until the acceptation it passes through some adjustments required by the reviewers and under supervision of my advisor Professor Joaquim Esteves da Silva and co-advisor Doutor Manuel Algarra.

Sensors and Actuators B 239 (2017) 553–561

Contents lists available at ScienceDirect

Sensors and Actuators B: Chemical

journal homepage: www.elsevier.com/locate/snb

Carbon dots coated with vitamin B_{12} as selective ratiometric nanosensor for phenolic carbofuran

Bruno B. Campos[a], Rafael Contreras-Cáceres[b], Teresa J. Bandosz[c], José Jiménez-Jiménez[d], Enrique Rodríguez-Castellón[d], Joaquim C.G. Esteves da Silva[a], Manuel Algarra[d,*]

[a] Centro de Investigação em Química, Departamento de Química e Bioquímica, Faculdade de Ciências da Universidade do Porto, Porto, Portugal
[b] Departamento de Química Orgánica, Facultad de Ciencias, Universidad de Málaga, Campus de Teatinos s/n, 29071 Málaga, Spain
[c] Department of Chemistry and Biochemistry, The City College of New York, 160 Convent Ave., New York, NY 10031, USA
[d] Departamento de Química Inorgánica, Facultad de Ciencias, Universidad de Málaga, Campus de Teatinos s/n, 29071 Málaga, Spain

ARTICLE INFO

Article history:
Received 21 April 2016
Received in revised form 23 July 2016
Accepted 10 August 2016

Keywords:
Carbon quantum dots
Ratiometric sensor
Energy transfer
Phenolic carbamates
Soy sauce

ABSTRACT

A carbon quantum dots (CQDs) based ratiometric nanosensor exhibiting dual emission fluorescence was developed. The spherical fluorescent carbon nanoparticles were obtained from lactose using a hydrothermal method. Under a single excitation at 355 nm they showed the typical blue emission at 417 nm and a red emission at 550 nm attributed to the coating effect of vitamin B_{12}. The latter is explained by the fluorescence resonance energy transfer (FRET) and it consists of 61% of total emission. Upon the presence of carbofuran phenol 3-Keto, a phenolic metabolite of carbofuran, the red emission was quenched, resulting in a ratiometric fluorescence response in the blue range. This ratiometric nanosensor exhibited a good selectivity to carbofuran phenol 3-Keto. The ratio of I_{417}/I_{550} linearly decreased with an increasing carbofuran phenol 3-Keto concentration in the range 9.8 μM–1.40×10^{-4} M. A detection limit for carbofuran phenol 3-Keto pesticide was 12.2 μM. The pesticide tested was extracted from soy sauce. Recovery values ranged from 98% to 114% with RSD values from 1.50% to 6.50%.

1. Introduction

Nowadays pesticides are widely used chemicals in agriculture. Specifically N-methyl carbamate insecticide derivatives are applied to main field crops of Europe and USA including wheat, corn, grapes, alfalfa and soybeans. Therefore their control in the environment is essential to prevent the toxic effects of their exposure on humans [1].

N-methyl carbamates are highly toxic for vertebrates and possess one of the highest severe toxicities to humans when compared to any other insecticides used on field crops. Carbofuran is considered by FAO (Food Agriculture Organization) as a toxic pesticide and its ADI (acceptable diary intake) has been re-evaluated by this organization several times. Consequently, the development of methods and systems for the detection of these compounds is highly desirable [2].

Currently, the standard reference methods for the determination of carbamate pesticide residues in real samples are mainly based on gas chromatography or high performance liquid chromatography. These methods are highly efficient and they are able to separate and detect different types of carbamates and their metabolites [3,4]. However, for these analyses expensive instruments are required, apart from trained technician, as well as complicated sample pre-treatments. Moreover, these methods are time-consuming and they are not suitable for field applications where multiple samples need to be tested. Therefore, it is necessary to develop simple, rapid, low-cost and sensitive screening analytical techniques that need almost no sample pre-treatment for the identification and quantification of pesticide residues. This leads to extensive efforts focussing on the development of novel approaches involving nanomaterials for the optical/electronic sensing of pesticides. Besides low costs, easy operation, fast response, these methods also provide reproducibility and flexibility for in situ analysis [5–9].

Fluorescent analytical methods are based on increased/decreased emission when a fluorescent material is subjected to a variety of factors [10–15]. These factors are mainly related to the change of an analyte concentration and to the chemical environment in complex solutions. Ratiometric fluorescent sensors can be a good alternative to spectroscopic methods [16–19]. Dual fluorescent emission can happen as a result of the combination of two different emission fluorophores. Their two

* Corresponding author.
E-mail address: malgarra67@gmail.com (M. Algarra).

http://dx.doi.org/10.1016/j.snb.2016.08.055
0925-4005/

responses (bands) arise as a result of a reaction in excited state where a proton transfer or electronic charge transfer is involved. Because the change in the intensities of the two bands is an indication of perturbations at the interfaces with the analyte, these sensors offer many advantages over other categories of probes. Consequently, a demand for two-color ratiometric probes increases [20].

Following this line of research, the objective of this paper is the investigation of fluorescent nanoparticles, commonly denoted as carbon quantum dots (CQDs), obtained from lactose, as fluorescent sensors for pesticides [21]. CQDs are an exciting new class of carbonaceous nanoparticles with higher photo-activity and biocompatibility, lower toxicity and lower costs than heavy-metal based quantum dots [22,23]. They have been successfully used in optical imaging [24,25] and as photocatalysts [26,27]. Nevertheless, intense research efforts still focus on their new applications and on understanding an intrinsic photoluminescence mechanism [28,29]. Here we show that CQDs synthesized from lactose and coated with vitamin B_{12} (VB_{12}) offer a new gateway leading to a ratiometric detection system. Although VB_{12} is not highly fluorescent, when it is combined with CQDs it is possible to increase its emission by fluorescence resonance energy transfer (FRET) phenomenon. FRET is a process in which energy is transferred non-radiatively from an excited state donor to a proximal ground state acceptor via resonant dipole–dipole interactions [30]. Only few reports indicated that CQDs can act as a component of a FRET system [31,32]. This dual emission of CQDs modified with $VB_{12,}$ at 435 and 550 nm is used as a principle of a ratiometric fluorescence sensor for a detection of phenolic metabolite of carbofuran, carbofuran phenol 3-Keto. This species is a hydrolysis product of carbofuran applied to soy crops.

2. Experimental

2.1. Chemicals and materials

D-Lactose (≥98%) and phosphoric acid (85 wt%, 99.99%) were purchased from Sigma-Aldrich Química S.A. (Spain). Carbofuran 3-keto (7-(Methylcarbamoyloxy)-2,2-dimethylbenzofuran-3(2H)-one, **CBFK**), Carbofuran phenol 3-keto (2,3-dihydro-2,2-dimethylbenzofuran-7-yl methylcarbamate, **CBFP**), **Bendiocarb** ((2,2-Dimethyl-1,3-benzodioxol-4-yl) N-methylcarbamate), **Pirimicarb** ((2-Dimethylamino-5,6-dimethylpyrimidin-4-yl) *N,N*-dimethylcarbamate) and **Aldicarb** (2-Methyl-2-(methylthio)propanal O-(N methylcarbamoyl)oxime) were purchased from Riedel de Haen (AG, Seelze, FRG) as reference standard, at least 95% of purity. The water used throughout all experiments was purified through a Millipore system. SPEs were performed using LiChrolut RP-18 cartridges (Merck, Darmstadt, Germany) with 40–63 μm/500 mg/3 mL standard polypropylene tubes.

2.2. Preparation of CQDs coated by vitamin B_{12} ($CQDs@VB_{12}$)

The CQDs were synthesized as described in a previous work with some modifications [33]. A one-step hydrothermal method was used. The synthesis was done at 150 °C for 2 h, by dissolving lactose (12 mg) in 200 μL of water in the presence of vitamin B_{12} (10 mg) and H_3PO_4 (800 μL, 85%) in a Teflon lined stainless steel vessel. Then, the colloidal solution was dialyzed and purified with ethyl acetate. The final solution of CQDs was orange in color and showed a high fluorescent intensity under UV light.

2.3. Characterization methods

The morphology of CQDs was evaluated using transmission electron microscopy (TEM). The analysis was carried out on a Philips CM-200 microscope. Fluorescence between 400 and 700 nm (an integration time of 0.1 s and 5 nm slits for excitation and emission) was measured on a Jovin Yvon Fluoromax 4 TCSPC (Horiba). X-ray photoelectron spectroscopy (XPS) was performed on a Physical Electronic PHI 5700 spectrometer using non-monochromatic Mg-Kα radiation (300 W, 15 kV, 1253.6 eV) for analysing the core-level signals of the elements of interest with a hemispherical multi-channel detector. The spectra of powdered samples were recorded with a constant pass energy value at 29.35 eV, using a 720 μm diameter circular analysis area. The X-ray photoelectron spectra obtained were analysed using the PHI ACESS ESCA-V6.0F software and processed using Multipak 8.2 B package. The binding energy values were referenced to adventitious carbon C 1*s* signal (284.8 eV). Shirley-type background and Gauss-Lorentz curves were used to find the binding energies. The zeta potential (ζ) of $CQDs@VB_{12}$ was determined using a Zetasizer Nano ZS (Malvern Instruments, U.K.) equipped with a 4 mW HeNe laser operating at λ = 633 nm. The ζ measurements were also performed at 25 °C in polycarbonate folded capillary cells, incorporated to Au plated electrodes (DTS1061). Deionized H_2O was the dispersion medium. ζ were calculated using the Stokes-Einstein and the Henry equation with the Smoluchowski approximation.

2.4. Fluorescence detection of CBFP

The detection of carbofuran phenol 3-Keto based on fluorescence was performed as follows: 10 μL of $CQDs@VB_{12}$ were added to aliquots of CBFP (5×10^{-3} M) in ethyl acetate solution. Acetonitrile was added to give a final volume of 1000 μL. The samples were sonicated for 10 min and their fluorescence spectra were recorded with excitation at 355 nm.

2.5. Selectivity and interference tests

For the interference tests, the stock solutions of carbofuran-3-keto, aldicarb, bendiocarb, and pirimicarb were prepared in ethyl acetate at various concentrations ratio (1:1; 1:5 and 1:10) with respect to CBFP (7.81×10^{-5} M) were prepared. Stock solutions of the interference substances were mixed with $CQDs@VB_{12}$ nanoparticle solution (10 μL), and then the fluorescence spectra were recorded at 355 nm. The samples were homogenized by sonication (10 min) before at 355 nm were recorded. The following relationship was used to analyse the data:

$$Ratio = \frac{\left(I_{417}/I_{550}\right)_{CQDs@VitB_{12}-Interferen\ ce}}{\left(I_{417}/I_{550}\right)_{CQDs@VitB_{12}-\mathrm{CBFP}}} \quad (1)$$

2.6. Determination of carbofuran phenol 3-Keto in soy sauce

The soy sauces used for developing and validating the proposed method were purchased from local markets (Spain) and stored at 4 °C. Sauce (25 ± 0.05 g) was weighed and centrifuged (50 mL, 13000 rpm), filtered in 40/0.45 μm filters, spiked with the appropriate aliquots of CBFP stock solution (5×10^{-3} M) and stirred for homogenization. For the solid phase extraction, cartridges were preconditioned with acetonitrile (5 mL) and water (10 mL) and placed on the top of a vacuum block. The pretreated sauces were transferred to the cartridge to be eluted with acetonitrile at a flow rate of 0.5 mL/min and, concentrated to 1 mL with N_2. The samples were sonicated for 10 min, and its fluorescence intensity (excited at 355 nm) at 417 and 550 nm was recorded to obtain the ratio of I_{417}/I_{550}.

3. Results and discussions

3.1. Synthesis and fluorescence analysis

To test CQDs of highest fluorescence intensity, the materials were obtained by hydrothermal carbonization of various inexpensive carbon sources (i.e.: lactose, cellulose, stearic acid, saccharin, chitosan, alginate and citric acid) [33] at 150 °C. Then they were mixed with VB_{12} in aqueous acidic media (H_2SO_4, H_3PO_4, HCl and HNO_3).

It was found that the most promising properties had CQDs obtained from lactose and treated with phosphoric acid. Therefore they were chosen for further studies

(Fig. SI1A, B). Various parameters were studied including changes in a H_2O/H_3PO_4 ratio, temperature, and reaction time (Fig. SI1C-E). The highest fluorescent intensity was obtained for 1:4 H_2O:H_3PO_4 ratio, and a 2 h process at 150 °C. The CQDs obtained from lactose (12 mg, Fig SI1F) and coated with VB_{12} (CQDs@VB_{12}) showed a well-defined fluorescence spectrum with dual emission at 417 and 550 nm when excited at 355 nm. The presence of VB_{12} as a coating agent results in a new band at 550 nm. This may the applications of this kind of materials for sensing.

The approach used not only simplifies the CQDs@VB_{12} synthesis but it also provides the spectroscopic improvements. VB_{12} by itself shows low fluorescence intensity at 550 nm when excited at 355 nm (Fig. SI2). On the other hand, when coated on the surface of CQDs. the intensity of emission increases and dual signal can be used for the detection purpose. Fig. 1A shows the fluorescence spectra of CQDs@VB_{12} at various excitation wavelengths (in the range 355–395 nm). The fluorescence intensity at 550 nm increases when excited at 355 nm in comparison with that for pure VB_{12}. This can be explained by a favorable energy transfer from CQDs to CQDs@VB_{12}, as observed in the UV spectra. This energy transfer can take place only when the participating molecules are in a close proximity. This provides an indirect evidence for the occurrence of FRET phenomenon between two light sensitive molecules. The ratio of the absorbances at the maximum of the spectra (264 nm) allow us to estimate the increase of the specific absorptivities (absorption cross sections) when the nanoparticle is coated with VB_{12}. This increase was found to be 4.6. In our case the donors are CQDs and the acceptors-VB_{12} (Fig. 1B). The efficiency (ϕ_{CQDs}@VB_{12}/ϕ_{CQDs}) [34] of the FRET process calculated using steady state fluorescence data is 61%. It indicates the parallel disposition of the transition dipole of the donor and acceptor. The efficiency of FRET was calculated by the measurements QYs for CQDs and CQDs@VB_{12} using quinine sulphate as a reference (see SI). The corresponding QYs were 8.10% and 5%, respectively.

The fluorescence lifetime of CQDs@VB_{12} was analyzed using a bi-exponential equation (goodness of the fit (χ^2 = 1.122), and τ_1 = 1.539 ns and τ_2 = 3.683 ns). The results indicate the presence of two different emissive sites: at short time, this represents 81.75% of the total fluorescence and at longer time, which represents 18.25% of the total fluorescence. Such a short lifetime is similar to that of QDs, and reveals the radiative recombination nature of excitations [35]. The average fluorescence lifetimes of the CQDs@VB_{12} in the nanosecond regime suggest the suitable behavior of these materials for sensing applications. Moreover, the lifetime of CQDs decreases when the donor molecule is engaged in the energy transfer process, which supports the existence of the FRET phenomena. Hence, fluorescence lifetime measurement can provide a strong and direct evidence for the presence of the excited state energy transfer process. Data obtained from pristine CQDs showed an average lifetime of 5.2 ns (bi-exponential fitting), which is much longer than the average lifetime of 2.7 ns found for CQDs@VB_{12}. Thus the substantial decrease in the lifetime of the donor (CQDs) after the addition of VB_{12} supports the presence of an excited state energy transfer process.

3.2. Characterization analysis of CQDs@VB_{12}

A representative TEM image (Fig. 1C) for purified CQDs@VB_{12} shows a narrow dispersion of spherical nanoparticle sizes. They mostly exhibit regular globular shapes in the range of nanometers with a very low level of agglomeration.

The inset in Fig. 1B shows the results of the size analysis of 130 particles. The average measured size was 53 ± 8.4 nm and a typical amorphous carbonaceous structure with no discernible lattice was found, similar to the results published in the literature [29]. The surface charge density of CQDs coated with VB_{12} evaluated by ζ measurements showed a high negative charge (−68.3 ± 0.3 mV). This suggests a high concentration of carboxylic surface groups, which can be deprotonated at pH 7 ($-COO^-$). These functional groups contribute to an excellent solubility of CQDs in water without further chemical modifications.

The functional groups of CQDs@VB_{12} were analyzed and compared with the raw CQDs by ATR-FTIR (Fig. 2). The spectrum of CQDs showed a prominent band at 3425 cm^{-1} which can be assigned to the stretching vibration of O—H groups, stemming from the lactose content. This mode decreases drastically for CQDs@VB_{12}, which indicates an involvement of these groups in reactions with vitamin B_{12}. The O—H stretch of a carboxylic acid is also broadened as a result of surface interactions. The spectra show typical absorption bands at 2986 cm^{-1} associated to stretching vibration of methyl or methylene. They are more intense after coating with VB_{12}. At 1456 cm^{-1} the band related to the C—H vibration of CH_2/CH_3 can be found. The intensity of a band at 1407 cm^{-1} mode, assigned to the CH_2 bending vibration, increases for CQDs@VB_{12} due to the high content of these entities. A band at 1743 cm^{-1} in the spectrum of CQDs@VB_{12} suggests the change of the polarity of the carbonyl groups (C═O) assigned to the presence of amide groups in VB_{12}. The presence of the latter is supported by a prominent band at 1047 cm^{-1}. A band at 1366 cm^{-1} corresponds to phenolic hydroxyl groups from the VB_{12}. Bands at 1235 and 1101 cm^{-1} are assigned to the stretching mode of C—N from VB_{12}. These features can be responsible for a low QY caused by the complexity and heterogeneity of the surface of CQDs with attached VB_{12}

CQDs@VB_{12} nanoparticles were also analyzed by XPS. The surface chemical composition in atomic% is: C: 47.98%, N: 0.39%, O: 41.95%, P: 9.48% and Co: 0.20%. This clearly denotes that phosphate groups predominate on the surface. The P 2*p* core level spectrum is centered at 134.7 eV (Fig. 3A) and the O 1*s* core level spectrum can be decomposed in two contributions at 533.4 eV (65%) and 532.1 eV, which can be assigned to the bridging oxygen of the phosphate [36], and the oxygen bonded to phosphorus (P = O) and/or to the organic part of VB_{12} (C═O) [37], respectively (Fig. 3B). The N 1*s* core level spectrum is noisy and of a low intensity. Nevertheless, it can be deconvoluted in two contributions at 402.1 eV (64%) and 400.5 eV (36%) assigned to protonated amino groups and pyrrolic nitrogen, respectively (Fig. 3C) [38,39].

The Co 2*p* signal is very weak and noisy and it is not possible to analyze it in detail. Finally, the C 1*s* signal is deconvoluted to three contributions at 284.8 eV (84%), 286.6 eV (12%) and 289.0 eV (4%). The main contribution at a low binding energy is linked to sp^2 configurations in carbon dots, the contribution at 286.6 eV represents C═O and C═N, and the contribution at 289.0 eV – the surface carboxylic groups (Fig. 3D) [40].

3.3. Sensing to carbofuran phenol 3-keto

As it was mentioned above, our objective is to use the synthesized CQDs@VB_{12} as a fluorescent sensor of specific pesticides.

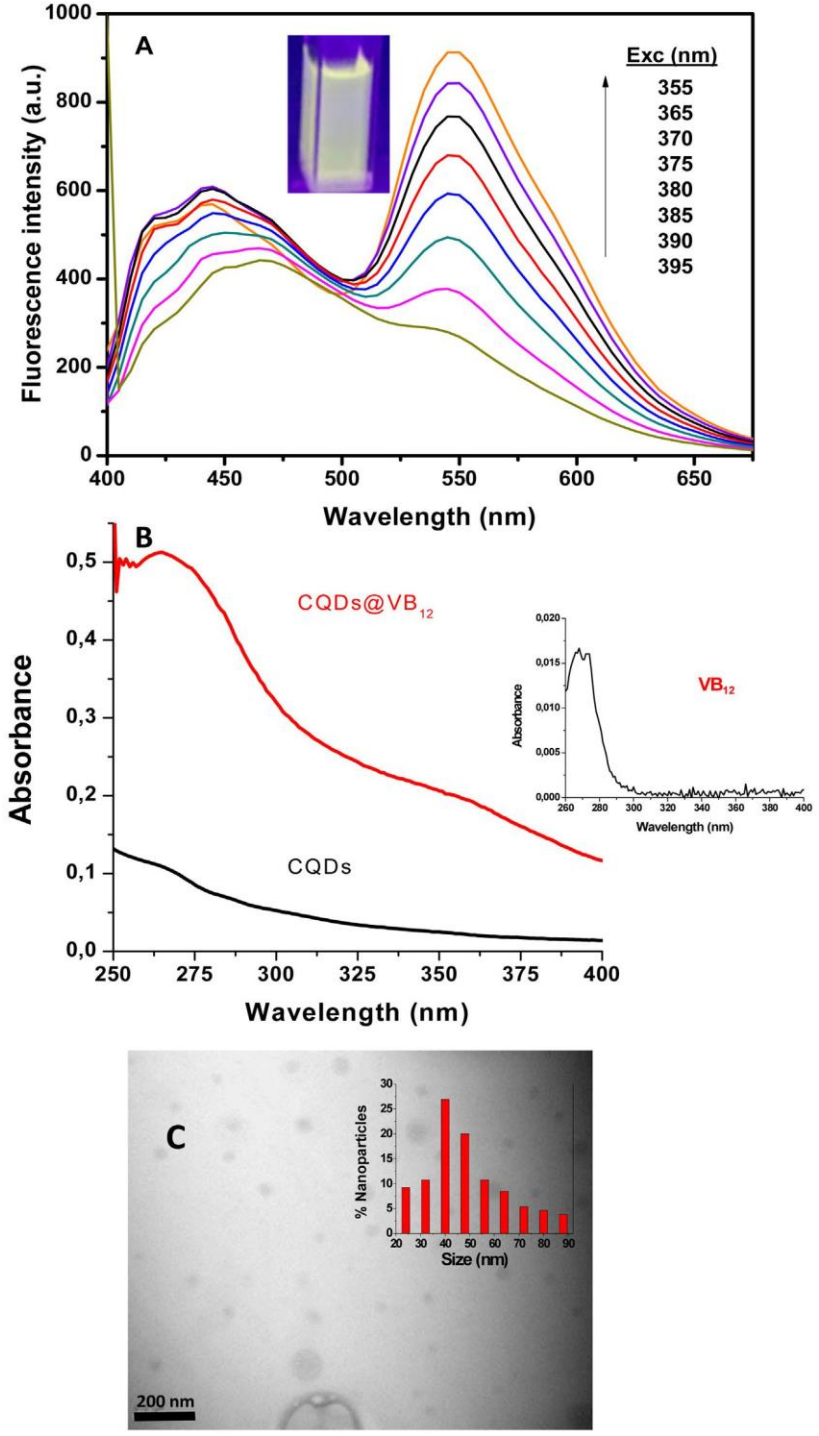

Fig. 1. A) Fluorescence spectra at different excitation wavelength, inset the emission under UV light of CQDs@VB_{12}. B) UV spectra of raw CQDs and CQDs@VB_{12}, inset the UV spectra of VB_{12}. C) Representative TEM image CQDs@VB_{12} (For size distribution, 130 nanoparticles of CQDs@VB_{12} from various collected images were analyzed).

Therefore, the fluorescence titration of different pesticides (Fig. 4) was carried out. A quenching effect was observed when carbamate derivate pesticides were added to the colloidal dispersion of CQDs@VB_{12} [41]. The addition of pirimicarb, bendiocarb and aldicarb at 0.25 mM resulted in no or little effect on the emission of CQDs. However, remarkable fluorescence changes were detected upon the addition of either carbofuran 3-keto or carbofuran phenol 3-keto (CBFP). The effect was especially pronounced in the case of CBFP where around 50% fluorescence intensity quenching was found (Fig. SI3). Previously triazine derivates were tested and no influence on the fluorescence signal was noticed (Fig. SI4).

In order to analyze the quenching mechanism imposed by CBFP molecule, Stern-Volmer analysis was carried out (Fig. 5). The plot showed a linear trend ($r > 0.99$). The

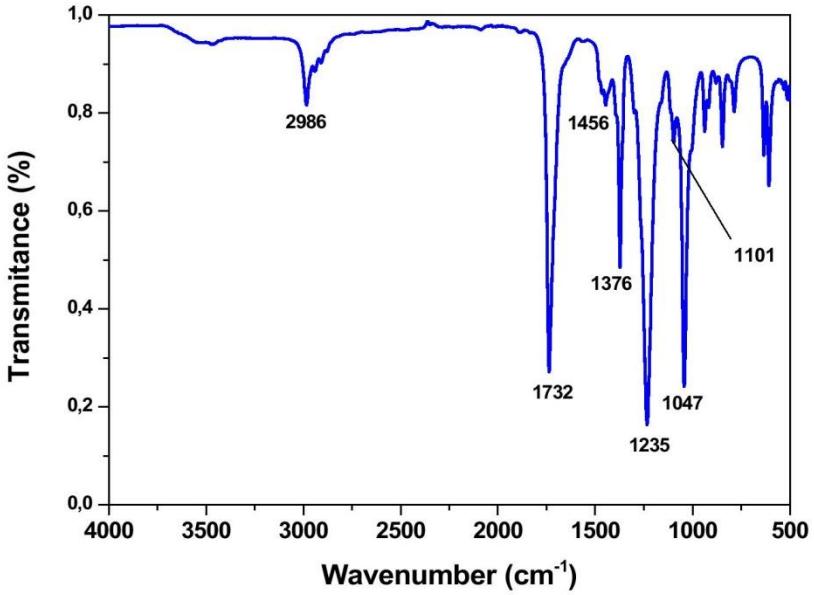

Fig. 2. ATR-FTIR spectra of the obtained CQDs@VB_{12} after purification in ethyl acetate, compared with the raw CQDs.

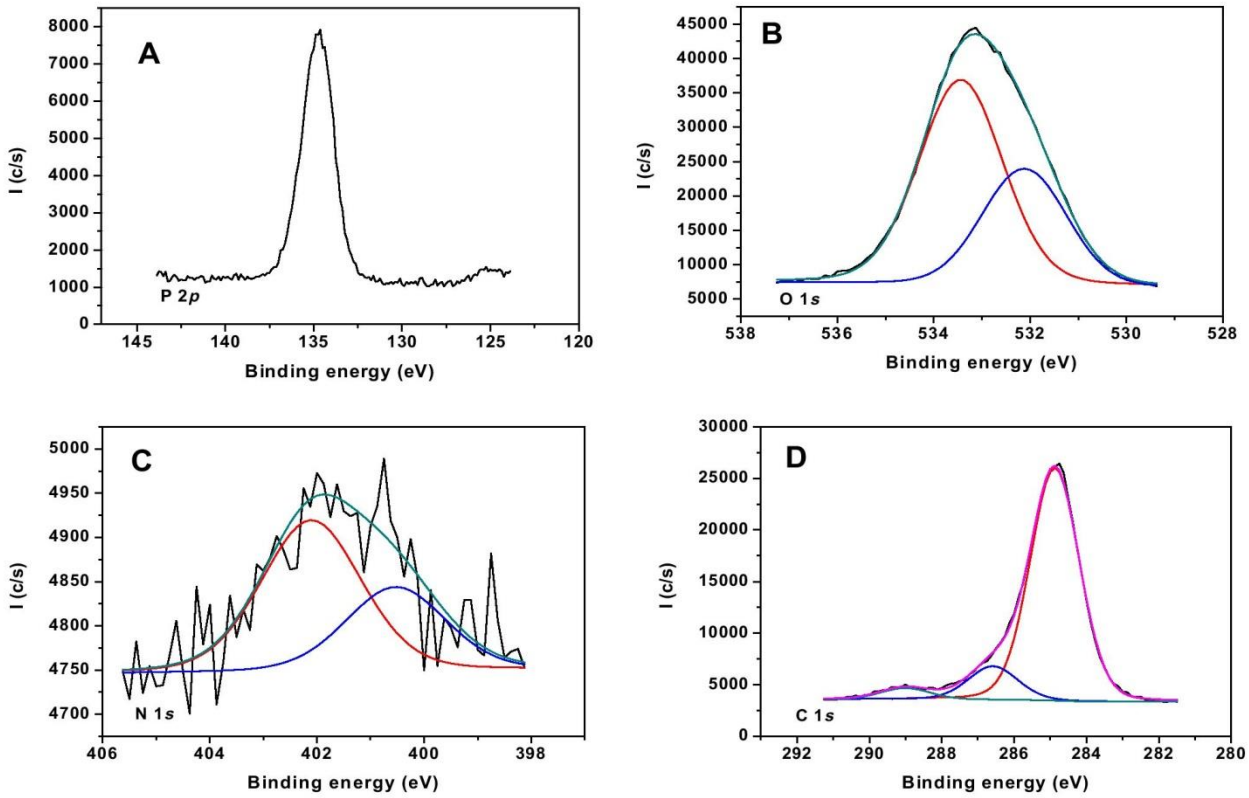

Fig. 3. XPS spectra of CQDs@VB_{12} A) P 2*p*; B) O 1*s*; C) N 1*s* core and D) C 1*s*.

reproducibility of the sensor was good as shown in the error bars (inset in Fig. 5). The Stern-Volmer constant for CBFP was 2186.6 M^{-1}. This order of magnitude is compatible with the formation of a stable complex (static quenching) between the CQDs@VB_{12} and the CBFP molecule. A quenching mechanism has been proposed to explain the decrease in the fluorescence intensity of CQDs@VB_{12} when CBFP molecules are present. Complexation of CBFP molecules by surface ligands of CQDs@VB_{12} generates a charge transfer process on the surface of CQDs. Extended surface area facilitates this phenomenon [42]. This can be seen in a constant lifetime listed in Table 1. The most interesting trend derived from Fig. 5 is in the ratio of the maximum of fluorescence corresponding to the first peak

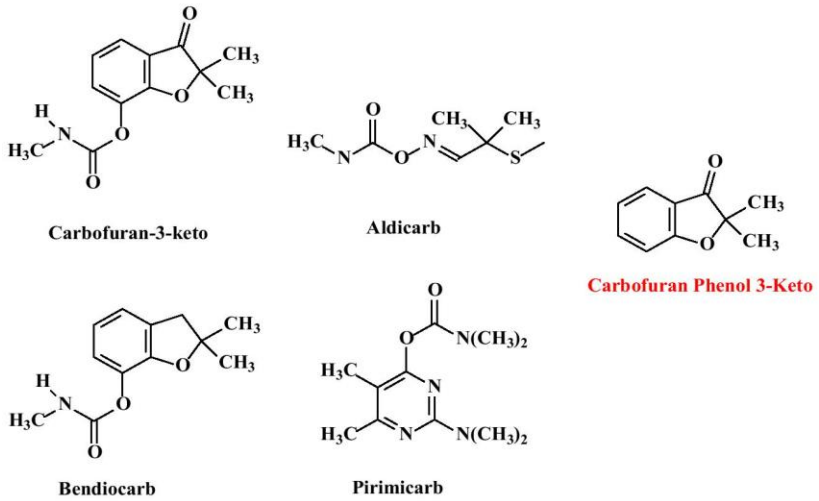

Fig. 4. Molecular structure of the pesticides studied.

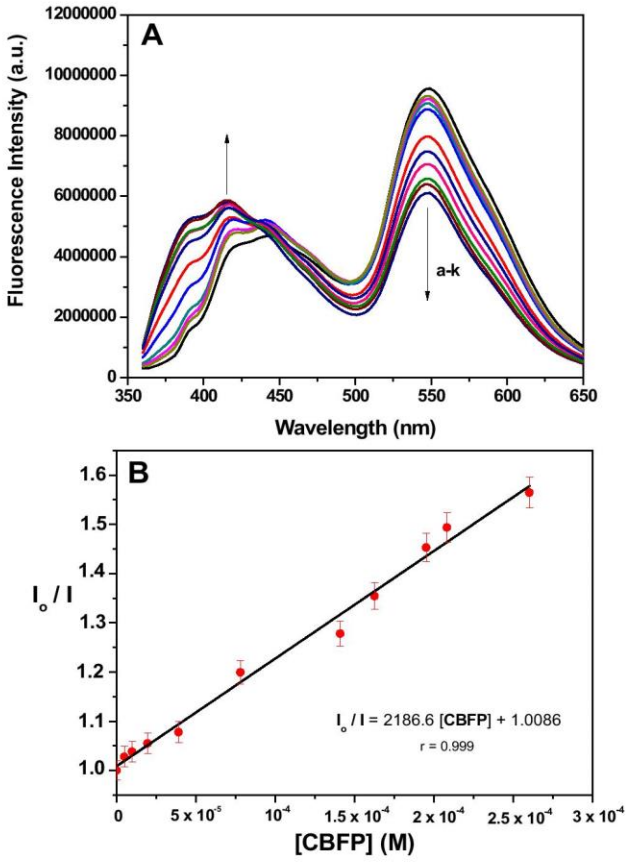

Fig. 5. (A) Fluorescence spectra of CQDs@VB_{12} under increasing concentrations of CBFP: a) 0, b) 9.77×10^{-6}, c) 7.81×10^{-6}, d) 4.88×10^{-6}, e) 3.91×10^{-6}, f) 2.60×10^{-5}, g) 1.95×10^{-5}, h) 2.08×10^{-4}, i) 1.95×10^{-4}, j) 1.63×10^{-4} and k) 1.41×10^{-4} M. (B) Stern-Volmer plot of CQDs based on fluorescence change with various amounts of CBFP.

and the maximum of the second peak. While for CBFP this ratio is 1.26, for the others compounds it remains almost constant (control (0.56); carbofuran-3-keto (0.53); aldicarb (0.55); bendiocarb (0.56) and pirimicarb (0.62)).

Table 1
Fluorescence decay lifetime measurements* of CQDs@$VitB_{12}$ in the presence of different CBFP concentrations.

[CBFP] (M)	τ_1 (ns)	τ_2 (ns)
0	$9.46 \pm 0.84 \times 10^{-10}$	$3.63 \pm 0.01 \times 10^{-9}$
4.88×10^{-6}	$7.66 \pm 0.68 \times 10^{-10}$	$3.60 \pm 0.01 \times 10^{-9}$
9.77×10^{-6}	$1.13 \pm 0.10 \times 10^{-9}$	$3.66 \pm 0.01 \times 10^{-9}$
1.95×10^{-5}	$1.07 \pm 0.09 \times 10^{-9}$	$3.64 \pm 0.01 \times 10^{-9}$
3.91×10^{-5}	$1.65 \pm 0.02 \times 10^{-9}$	$3.70 \pm 0.01 \times 10^{-9}$
7.81×10^{-5}	$1.66 \pm 0.03 \times 10^{-9}$	$3.72 \pm 0.01 \times 10^{-9}$

* Averages and standard deviation (in parentheses) of three independent experiences.

Table 2
Recovery values (%)* for CBFP determined by CQDs@$VitB_{12}$ in the presence of other related pesticides.

	1:01	1:05	1:10
CBFP	98.1 ± 2.0	97.7 ± 2.9	93.5 ± 3.7
Aldicarb	102.0 ± 3.1	102.7 ± 3.6	101.8 ± 2.0
Bendiocarb	101.0 ± 4.0	103.3 ± 2.1	103.3 ± 2.1
Pirimicarb	103.6 ± 2.6	115.3 ± 4.0	115.3 ± 4.0

* Averages and standard deviation (in parentheses) of three independent experiences.

The data collected demonstrate the selectivity of the ratiometric response defined as I_{417}/I_{550}. Under these optimum conditions we also found the linear dependence of the fluorescence intensity of both peaks ($r > 0.99$) on the concentration of CBFP in the range of 15.2×10^{-5}–2.5×10^{-3} M (Fig. SI6). All processes discussed are illustrated in Scheme 1.

In order to assess the possibility of analytical applications of our sensor, the effect of different pesticides present along with CBFP in the solution tested on the selectivity of the detection was evaluated. The fluorescence ratiometric determination of CBFP at the 7.81×10^{-5} M level was examined over a wide range of concentrations of carbamates.

3.4. The fluorescence intensities of CQDs@VB_{12}

CBFP, at various concentration ratios with respect to other pesticides (1:1, 1:5, and 1:10, respectively) were measured in separate sets of experiments. The recoveries of CBFP when analysed in mixtures are collected in Table 2. The results show low interferences of CBFK, aldicarb and bendiocarb and a moderate one of pirimi-

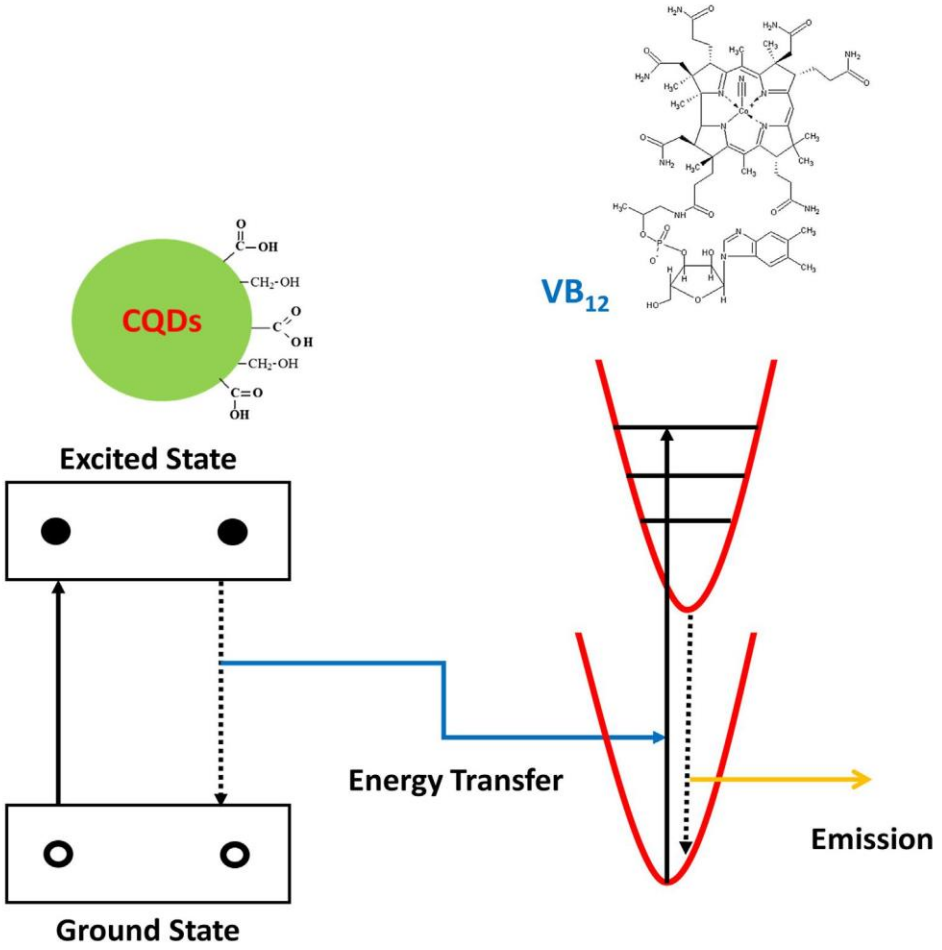

Scheme 1. Representation of the FRET process involved when CQDs transfers energy to VB_{12} molecules. The signal of CQDS@VB_{12} is quenched after sensing with CBPF.

carb (>110%). The proposed sensor was optimized to obtain the best sensitivity. The limit of detection (LOD) and quantification ($L_{OQ} = 3 \times L_{OD}$) were 12.2 and 40.7 μM, respectively, with an accuracy of 1.13% expressed as a relative standard deviation (RSD, n = 10). The cartridges used for a solid phase extraction (SPE) of CBPF showed the best extraction efficiency when acetonitrile was used *Application in sauce soy*.

To determine the extraction efficiency, soy sauce was spiked with different concentrations of CBFP; the mean recoveries ranged from 98% to 114% with RSD values of 1.50% to 6.50% (Table 3, Fig. 6). All results are expressed as mean values of five replicates. The obtained recovery values using the proposed method are almost 100% and demonstrate the feasibility of the CQDs@VB_{12} application for the analysis of CBPF presence in soy sauce. The UE legislation establishes the maximum residue limits (MRL) for the sum of carbofuran and its metabolites in foods as 0.01 mg/kg [43]. Thus, the precision and accuracy obtained using our sensor is considered as adequate for the validation of the method following the established criteria.

A few analytical methods based on complex nano-systems are addressed in the literature for the detection of carbofuran. From those, the most used are amperometric acetylcholinesterase biosensors based on Pt nanoparticles. Even though they show low detection limits (ng), their application is complex due the maintenance of the sensor activity [44–46]. Another important aspect is the cost of those noble metal based sensors. A non-enzymatic sensor based on Co(II) oxide (CoO) decorated reduced graphene oxide

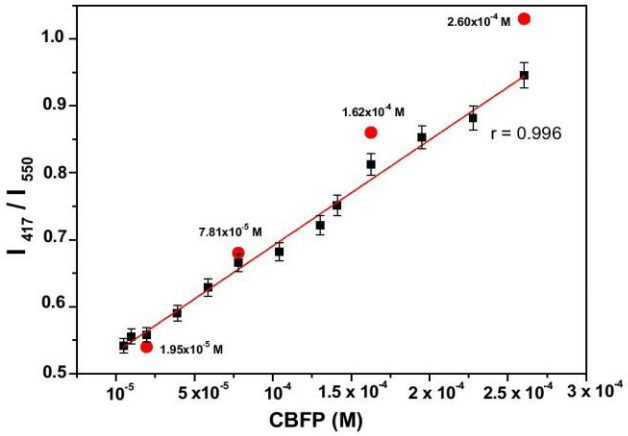

Fig. 6. Results obtained when comparing the analysis of CBPF by CQDs@VB_{12} in soy (●) using the calibration graph and the recoveries when used real samples of soy souce (■).

(rGO) was developed for the detection of carbofuran over a wide concentration range of

0.2–70 μM in fruits [47]. To detect specifically the phenolic carbofuran metabolites the chromatographic techniques need to be applied and the detection limits are at ppm levels in food matrices [48–50]. In our case spiked carbofuran phenol 3-Keto was extracted

from soy sauce by a solid phase extraction and the recovery values ranged from 98% to 114% with RSD values of 1.50% to 6.50%. We consider these results as important characteristics of a good sensor.

4. Conclusions

The CQDs nanoparticles synthesized from lactose and modified with VB_{12} showed blue emission characteristic of CQDs and an intense red emission at 550 nm. They can be used as a fluorescent sensor based in the FRET phenomena. The latter is justified by the energy transfer between the CQDs, as donor and $VB_{12,}$ as an acceptor. This results in an increased its fluorescence intensity. which is an important asset of a fluorescence based sensor. These VB_{12} modified CQDs were successfully used for the selective determination of CBFP, by a ratiometric fluorescence method, in a concentration range of $12.2 \times 10^{-5} - 2.5 \times 10^{-3}$ M in the presence of other pesticides. LOD and LOQ were 12.2 and 40.7 μM respectively.

Acknowledgments

Authors are gratefully to Grant SFRH/BD/84318/2012 to Faculdade de Ciências e Tecnologia (FCT, Lisbon, Portugal). This work was supported by the projects P12-RNM-1565 (Junta de Andalucía, Spain).

Appendix A. Supplementary data

Supplementary data associated with this article can be found, in the online version, at http://dx.doi.org/10.1016/j.snb.2016.08.055.

References

[1] U.S. Environmental Protection Agency, Carbofuran: Receipt of Application for Emergency Exemption. Solicitation of Public Comment, Docket ID #OPP-2002-0124.
[2] J. Bachman, H.H. Patterson, Photodecomposition of the carbamate pesticide carbofuran: kinetics and the influence of dissolved organic matter, Environ. Sci. Technol. 33 (1999) 874–881.
[3] X. Song, H.M. McNair, Fast gas chromatography analysis of *N*-carbamates with cold on-column injection, J. Chromatogr. Sci. 40 (2002) 321–325.
[4] Method 531.2 Measurement of *N*-methylcarbamoyloximes and *N*-methylcarbamates in water by direct aqueous injection HPLC with post column derivatization U.S. EPA Revision 1.0, Cincinnati, OH, 2001.
[5] J.M. Nogueira, T. Sandra, P. Sandra, Considerations on ultra-trace analysis of carbamates in water samples, J. Chromatogr. A 996 (2003) 133–140.
[6] Q. Chen, Y. Fung, Capillary electrophoresis with immobilized quantum dot fluorescence detection for rapid determination of organophosphorus pesticides in vegetables, Electrophoresis 31 (2010) 3107–3114.
[7] Y. Zho, Q. Xia, M. Ding, H. Kageruka, H. Jiang, Y. Jiang, H. Jing, X. Xiao, H. Zhong, Magnetic nanoparticles of nitrogen enriched carbon (mnNEC) for analysis of pesticides and metabolites in zebrafish by gas chromatography–mass spectrometry, J. Chromatogr. B 915–916 (2013) 46–51.
[8] R. Kaur, A. Hasan, N. Iqbal, S. Alam, M.K. Saini, S.K. Raza, Synthesis and surface engineering of magnetic nanoparticles for environmental clean-up and pesticide residue analysis: a review, J. Sep. Sci. 37 (2014) 1805–1825.
[9] Z. Li, Y. Wang, Y. Ni, S. Kokot, Unmodified silver nanoparticles for rapid analysis of the organophosphorus pesticide dipterex, often found in different waters, Sens. Actuators B: Chem. 193 (2014) 205–211.
[10] D. Liu, W. Chen, J. Wei, X. Li, Z. Wang, X. Jiang, A highly sensitive, dual-readout assay based on gold nanoparticles for organophosphorus and carbamate pesticides, Anal. Chem. 84 (2012) 4185–4191.
[11] S. Peng, J. Xiao, J. Cheng, M. Zhang, X. Li, M. Cheng, Ionic liquid magnetic bar microextraction and HPLC determination of carbamate pesticides in real water samples, Microchim. Acta 179 (2012) 193–199.
[12] J. Guo, Y. Luo, H. Li, X. Liu, J. Bie, M. Zhang, X. Cao, F. Shen, C. Sun, J. Liu, Sensitive fluorescent detection of carbamate pesticides represented by methomyl based on the inner filter effect of Au nanoparticles on the fluorescence of CdTe quantum dots, Anal. Methods 5 (2013) 6830–6838.
[13] D.D. Thiaré, A. Khonté, A. Diop, A. Mendy, A. Coly, F. Delattre, M.D. Gaye-Seye, A. Tine, Spectrofluorimetric Analysis of the fungicide carbendazim and its metabolite 2-aminobenzimidazole in natural water, Am. J. Anal. Chem. 6 (2015) 767–775.
[14] X. Wang, T. Hou, S. Dong, X. Liu, F. Li, Fluorescence bio-sensing strategy based on mercury ion-mediated DNA conformational switch and nicking enzyme-assisted cycling amplification for highly sensitive detection of carbamate pesticide, Biosens. Bioelectron. 77 (2016) 644–649.
[15] L. Rubio, L.A. Sarabia, M.C. Ortiz, Standard addition method based on four-way PARAFAC decomposition to solve the mATR-FTIRix interferences in the determination of carbamate pesticides in lettuce using excitation emission fluorescence data, Talanta 138 (2015) 86–89.
[16] C. Yu, X. Li, F. Zeng, F. Zheng, S. Wu, Carbon-dot based ratiometric fluorescent sensor for detecting hydrogen sulfide in aqueous media and inside live cells, Chem. Commun. 49 (2013) 403–405.
[17] B.B. Campos, M. Algarra, K. Radotić, D. Mutavdžić, E. Rodríguez-Castellón, J. Jiménez-Jiménez, B. Alonso, C. Casado, J.C.G. Esteves da Silva, ZnS:Mn nanoparticles functionalized by PAMAM-OH dendrimer based fluorescence ratiometric probe for cadmium, Talanta 134 (2015) 317–324.
[18] X. Liu, N. Zhang, T. Bing, D. Shangguan, Carbon dots based dual-emission silica nanoparticles as a ratiometric nanosensor for Cu^{2+}, Anal. Chem. 86 (2014) 2289–2296.
[19] M. Lan, J. Zhang, Y.S. Chui, P. Wang, X. Chen, C.S. Lee, H.L. Kwong, W. Zhang, Carbon nanoparticle-based ratiometric fluorescent sensor for detecting mercury ions in aqueous media and living cells, ACS Appl. Mater. Interfaces 6 (2009) 21270–21278.
[20] A.P. Demchenko, A.S. Klymchenko, V.G. Pivovarenko, S. Ercelen, Ratiometric probes: design and application in fluorescence spectroscopy, imaging and probes-new tools, in: R. Kraayenhof, A.J.W.G. Visser, H.C. Gerritsen (Eds.), Chemical, Physical and Life Sciences, Springer-Verlag, Heidelberg, 2002, pp. 101–110.
[21] Y. Wang, A. Hu, Carbon quantum dots: synthesis, properties and applications, J. Mater. Chem. C 2 (2014) 6921–6939.
[22] M.H. Lee, Y.C. Chen, M.H. Ho, H.Y. Lin, Optical recognition of salivary proteins by use of molecularly imprinted poly(ethylene-*co*-vinyl alcohol)/quantum dot composite nanoparticles, Anal. Bioanal. Chem. 397 (2010) 1457–1466.
[23] K. Hola, Y. Zhang, Y. Wang, E.P. Giannelis, R. Zboril, A.L. Rogach, Carbon dots-emerging light emitters for bioimaging, cancer therapy and optoelectronics, Nano Today 9 (2014) 590–603.
[24] S.N. Baker, G.A. Baker, 1 Luminescent carbon nanodots: emergent nanolights, Angew. Chem. Int. Ed. 49 (2010) 6726–6744.
[25] M. Algarra, M. Pérez-Martín, M. Cifuentes-Rueda, J. Jiménez-Jiménez, J.C.G. Esteves da Silva, T.J. Bandosz, E. Rodríguez-Castellón, J.T. López-Navarrete, J. Casado, Carbon dots obtained using hydrothermal treatment of formaldehyde. Cell imaging in vitro, Nanoscale 6 (2014) 9071–9077.
[26] Q. Li, T.Y. Ohulchanskyy, R. Liu, K. Koynov, D. Wu, A. Best, R. Kumar, A. Bonoiu, P.N. Prasad, Photoluminescent carbo dots as biocompatible nanoprobes for targeting cancer cells in vitro, J. Phys. Chem. B 114 (2010) 12062–12068.
[27] X. Qin, W. Lu, G. Chang, Y. Luo, A.M. Asiri, A.O. Al-Youbi, X. Sun, Novel synthesis of Au nanoparticles using fluorescent carbon nitride dots as Photocatalyst, Gold Bull. 45 (2012) 61–67.
[28] Z. Ma, H. Ming, H. Huang, Y. Liu, Z. Kang, One step ultrasonic synthesis of fluorescent N-doped carbon dots from glucose and their visible-light sensitive photocatalytic ability, New J. Chem. 36 (2012) 861–864.
[29] S. Zhu, Y. Song, X. Zhao, J. Shao, J. Zhang, B. Yang, The photoluminescence mechanism in carbon dots (graphene quantum dots carbon nanodots, and polymer dots): current state and future perspective, Nano Res. 8 (2015) 355–381.
[30] B. Valeur, M. Berbera-Santos, Excitation Energy Transfer. Molecular Fluorescence: Principles and Applications, 2nd ed., Wiley-VCH, Weinheim, 2012, pp. 213–261.
[31] S. Hu, Q. Zhao, Q. Chang, Y. Yang, J. Liu, Enhanced performance of Fe^{3+} detection via fluorescence resonance energy transfer between carbon quantum dots and Rhodamine B, RSC Adv. 4 (2014) 41069–41075.
[32] M. Ganiga, J. Cyriac, FRET based ammonia sensor using carbon dots, Sens. Actuators B: Chem. 225 (2016) 522–528.
[33] M. Algarra, B.B. Campos, K. Radotić, D. Mutavdžić, T.J. Bandosz, J. Jiménez-Jiménez, E. Rodríguez-Castellón, J.C.G. Esteves da Silva, Luminescent carbon nanoparticles: effects of chemical functionalization, and evaluation of Ag^{+} sensing properties, J. Mater. Chem. A 2 (2014) 8342–8351.
[34] D.C. Harris, Applications of Spectrophotometry Quantitative Chemical Analysis, 8th ed., W. H. Freeman and Co., New York, 2010, pp. 419–444.
[35] H. Zhu, H. Wang, Y. Li, Z. Wang, F. Yang, X. Yang, Microwave synthesis of fluorescent carbon nanoparticles with electrochemiluminescence properties, Chem. Commun. (2009) 5118–5120.
[36] R. Brückner, H.U. Chun, H. Goretzki, M. Sammet, XPS measurements and structural aspects of silicate and phosphate glasses, J. Non Cryst. Solids 163 (1993) 268–273.
[37] G. Beamson, D. Briggs, High Resolution XPS of Organic Polymers. Chichester : The Scienta ESCA300 Database, John Wiley and Son, 1992.
[38] F. Lupo, C. Capici, G. Gattuso, A. Notti, M.F. Parisi, A. Pappalardo, S. Pappalardo, A. Gulino, Optical recognition of *n*-butylammonium and 1,5-pentanediammonium picrates by a calix[5] arene monolayer covalently assembled on silica substrates, Chem. Mater. 22 (2010) 2829–2834.
[39] G. de Ruiter, M. Lahav, G. Evmenenko, P. Dutta, D.A. Cristaldi, A. Gulino, M.E. Van der Boo, Composite molecular assemblies: nanoscale structural control and spectroelectrochemical diversity, J. Am. Chem. Soc. 132 (2010) 14554.
[40] A. Gulino, Structural and electronic characterization of self-assembled molecular nanoarchitectures by X-ray photoelectron spectroscopy, Anal. Bioanal. Chem. 405 (2013) 1479–1495.
[41] J. Bachman, H.H. Patterson, Photodecomposition of the carbamate pesticide carbofuran: kinetics and the influence of dissolved organic matter, Environ. Sci. Technol. 33 (1999) 874–881.

[42] H. Sun, L. Wu, W. Wei, X. Qu, Recent advances in graphene quantum dots for sensing, Mater. Today 16 (2013) 433–442.
[43] Regulation EC 396/2005 and amendments. Pesticides MRLs in/on food and feed of plant and animal origin and Commission implementing rules, 2005.
[44] L. Yang, G. Wang, Y. Liu, An acetylcholinesterase biosensor based on platinum nanoparticles-carboxylic graphene-nafion-modified electrode for detection of pesticides, Anal. Biochem. 437 (2013) 144–149.
[45] Y. Zhu, Y. Cao, X. Sun, X. Wang, Amperometric immunosensor for carbofuran detection based on MWCNTs/GS-PEI-Au and AuNPs-antibody conjugate, Sensors 13 (2013) 5286–5301.
[46] J. Seo, S.D. Kim, S. Kang, J. Han, H.G. Hur, Fungal biodegradation of carbofuran and carbofuran phenol by the fungus Mucor ramannianus: identification of metabolites, Water Sci. Technol. 55 (2007) 163–167.
[47] M.Y. Wang, J. Huang, M. Wang, D. Zhang, J. Che, Electrochemical nonenzymatic sensor based on CoO decorated reduced graphene oxide for the simultaneous determination of carbofuran and carbaryl in fruits and vegetables, Food Chem. 152 (2014) 191–197.
[48] R.D. Inman, U. Kiigemagi, D.A. Griffin, M.L. Deinzer, Determination of the phenolic metabolites of carbofuran in peppermint hay and peppermint oil by multiple ion detection mass spectrometry, J. Agric. Food Chem. 31 (1983) 722–726.
[49] T.R. Nelsen, R.F. Cook, M.H. Gruenauer, M.D. Gilbert, S. Witkonton, Determination of the phenolic metabolites of carbofuran in plants by gas chromatography/mass spectrometry, J. Agric. Food Chem. 31 (1983) 1147–1150.
[50] R.F. Cook, J.E. Jackson, J.M. Shuttleworth, O.H. Fullmer, G.H. Fujie, Determination of the phenolic metabolites of carbofuran in plant and animal matrices by gas chromatography of their 2,4-dinitrophenyl ether derivatives, J. Agric. Food Chem. 25 (1977) 1013–1017.

Biographies

Bruno B. Campos finished her B.Sc. and M. Sc. in Chemistry in the University of Porto. His master degree research work was based in the development of analytical sensing systems based in the incorporation of dendrimers to Quantum Dots. Currently he is a PhD student in the third year of his doctoral programme at the Faculty of Sciences of the University of Porto, Portugal (FCUP). The focus of his research programme is the development of optical fluorescent carbon nanoparticles sensors for the quantification of a great variety of analytical systems.

Rafael Contreras-Cáceres obtained his PhD degree in 2011 from the University Almeria (Spain). He worked as postdoctoral researcher in the Leibniz-Institut für Polymerforschung in Dresden (Germany) from 2011 to 2012, under the supervision of Prof. Manfred Stamm. Then, he obtained a Marie Curie fellowship COFUND under the programme "U-mobility" co-financed by the University of Malaga and the European Community's Seventh Framework Program. He spent 2 years at the University of Houston (US) under the supervision of Prof. Chengzhi Cai, and from 2014 he is a postdoctoral researcher at the Department of Organic Chemistry in the University of Malaga (Spain).

Teresa J. Bandosz holds Ph.D. in Chemical Engineering and D.Sc. in Physical Chemistry. She is a full professor of Chemistry and Chemical Engineering at the City College of New York. Dr. Bandosz has a broad experience in the field of materials preparation, and their applications to environmental problems related to development of adsorbents for gas separation. For three years she was associated with Dalian University of Technology in China as a sky scholar/guest professor of Chemical Engineering. Dr. Bandosz is a Fulbright Senior Scholar (2016/2017). She edited the book "Activated carbon surface in environmental remediation," published by Elsevier (2006). Her work during last 30 years has resulted in 6 US patents and over 400 publications in peer-reviewed journals. Her recent research interests include synthesis of Graphene/MOF, Graphene/hydroxide composites for separation and energy harvesting applications, visible light photoactivity of carbonaceous materials, energy storage, and CO_2 sequestration and reduction. Since 2014 she is coeditor of Journal of Colloid and Interface Science. She was on the Advisory Board of American Carbon Society (2011–2016). Dr. Bandosz serves on the Board of Directors of International Adsorption Society and on the Editorial Boards of Carbon, C, Adsorption Science and Technology, and Applied Surface Science. She was selected as a Graffin Lecturer for 2016/2017 by American Carbon Society.

José Jiménez-Jiménez obtained his B. Sc and Ph. D in Chemistry from the University of Málaga (UMA, Spain). He has participated in a great variety of projects financed by UE since 1996, based in the development of materials for environmental applications. Currently he works as Full Professor in the Inorganic Chemistry Department (UMA) in the synthesis and development of systems to improve the quality of the water. He is author of more than 100 papers in ISI journals.

Enrique Rodríguez-Castellón obtained his B. Sc in Chemistry from the Autonoma University of Madrid (Spain), Ms. Sc. in Chemistry at the University of Puerto Rico, Mayagüez campus and obtained his Ph. D. in the University of Málaga. He is Full Professor in Inorganic Chemistry of the University of Málaga. Currently his research developments are based in the synthesis of new catalyst materials for environmental applications. He is the scientific leader of the XPS technique in UMA. He has participated as principal investigator in numerous international cooperation projects with the participation of the Autonomous University of Puebla (Mexico), Havana (Cuba), Nacional de La Plata (Argentina), Technical Cordoba (Argentina), Nacional San Luis (Argentina), Federal do Ceará (Brazil), Federal do Rio Grande do Norte (Brazil), Montevideo (Uruguay), Central de Caracas (Venezuela), Concepción (Chile), among others. He is the author of 5 patents and more than 400 research scientific papers with a h index of 45. He has participated in 6 European projects since 1986, collaborating with the University of Montpellier 2, Bologna, Ca 'Foscari of Venice, Genoa, Exeter, Consiglio Nazionale delle Richerca, and companies REPSOL-YPF, UOP; ENI, SNAMPROGETTI, IKO, VIANA, as well as numerous national projects and the Government of Andalusia.

Joaquim C.G. Esteves da Silva obtained his B.Sc., M.Sc. and Ph.D. in chemistry from the Faculty of Sciences of the University of Porto (FCUP), Portugal, where he worked on chemometric methodologies to environmental inorganic systems. Currently, he is a full professor in the Geoscience department of the FCUP where he teaches inorganic, environment, forensic, bioanalytical and chemometric courses. Current main research interests are the development of fluorescent nanomaterials and experimental and theoretical studies of chemiluminescent and bioluminescent systems. Also is focusing his R&D efforts on the development of biomedical, environmental and industrial innovative products.

Manuel Algarra obtained his B. Sc and Ph. D in Chemistry from the University of Málaga (UMA, Spain), which was shared with the University of Bordeaux in the LPTC, CNRS). He has been Assistant Research in the University of Porto (2008–2013). Currently he works as Senior Research in the Inorganic Chemistry Department (UMA) for the development of sensor systems based in fluorescent carbon nanoparticles, since 2013 under the frame of Andalucía Tech fellowship. He has collaboration with different groups such the University of Belgrade (Serbia), CCNY in NY (USA), University of Porto (Portugal), University of Castilla La Mancha and Autonoma de Madrid (Spain), among others.

5.2 Supplementary Data

Carbon dots coated with Vitamin B_{12} as selective Ratiometric Nanosensor for Phenolic Carbofuran

Supplementary Information

B. B. Campos, R. Contreras-Cáceres, Teresa J. Bandosz, E. Rodríguez-Castellón,
J.C.G. Esteves da Silva, M. Algarra

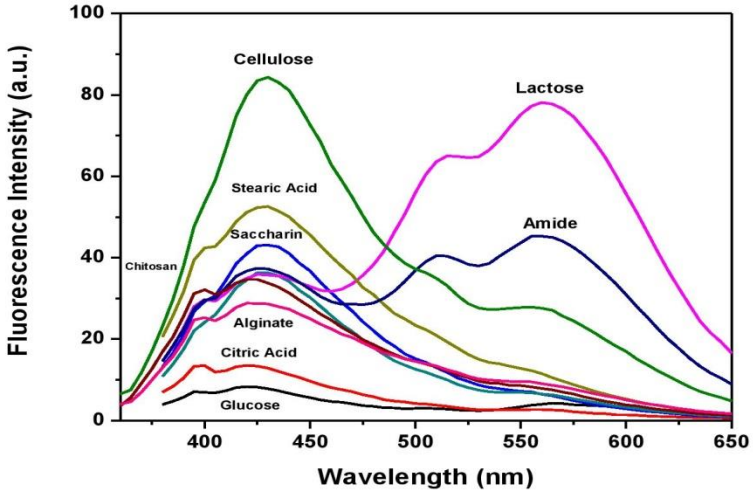

Figure SI1A. Fluorescence spectra of CQDs obtained using various carbon sources

.

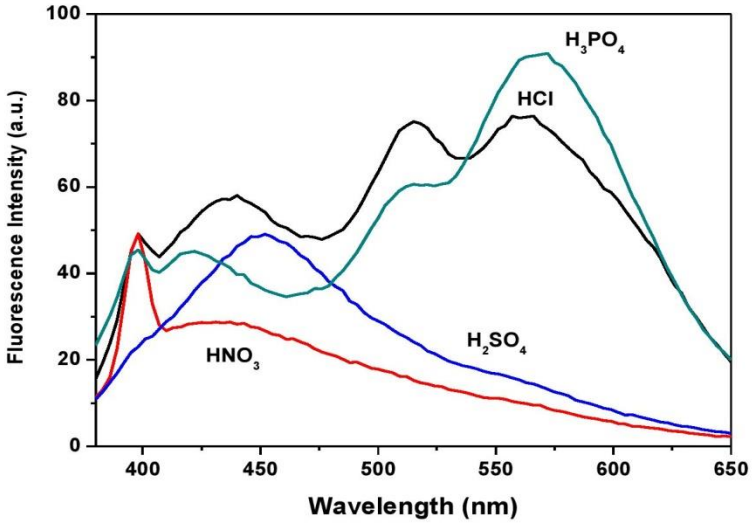

Figure SI1B. Fluorescence spectra of CQDs@VitB_{12} obtained from lactose treated with different mineral acids.

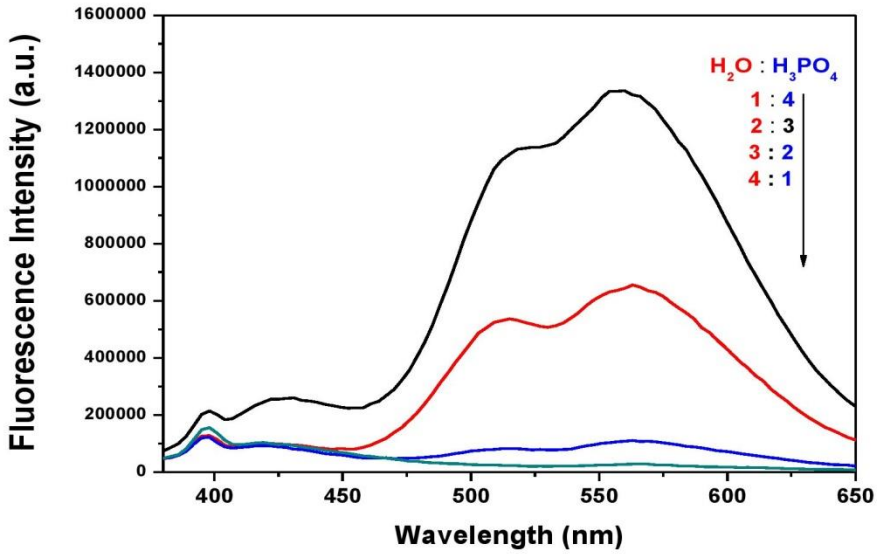

Figure SI1C. Fluorescence spectra of CQDs@VitB$_{12}$ obtained from lactose treated with with H_2O / H_3PO_4 of various ratios.

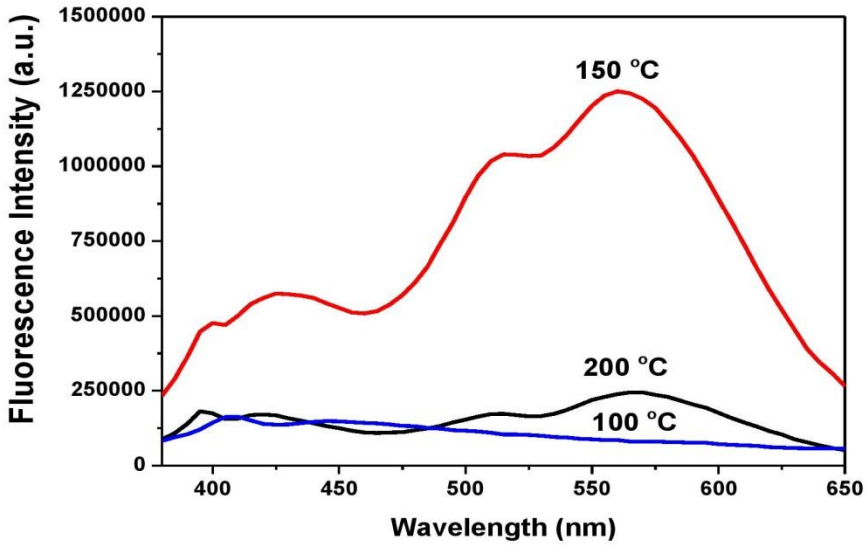

Figure SI1D. Fluorescence spectra of CQDs@VitB$_{12}$ obtained at various temperatures.

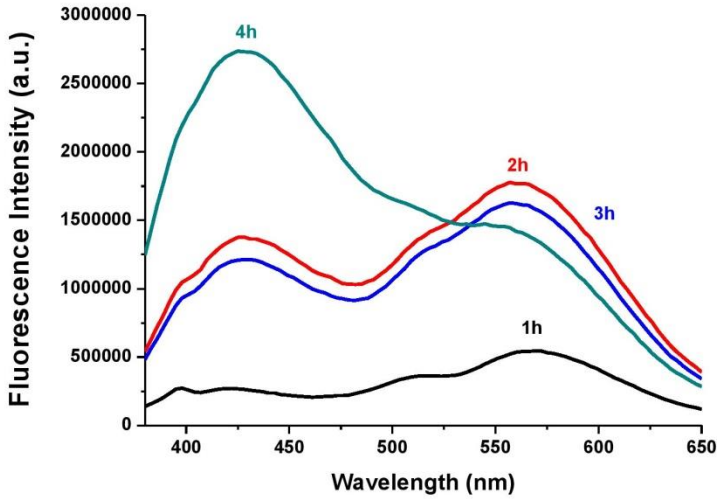

Figure SI1E. Fluorescence spectra of CQDs@VitB$_{12}$ obtained at different synthesis times.

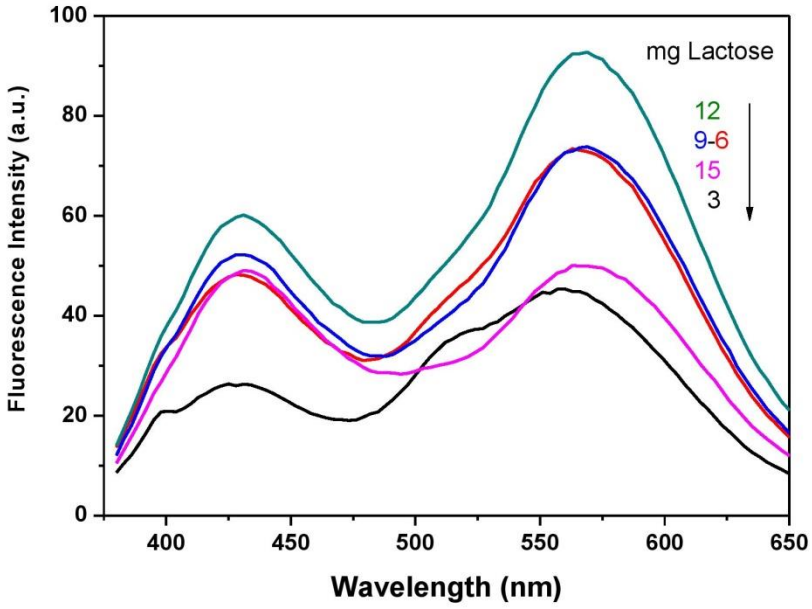

Figure SI1F. Fluorescence spectra of CQDs@VitB$_{12}$ obtained at different lactose concentrations

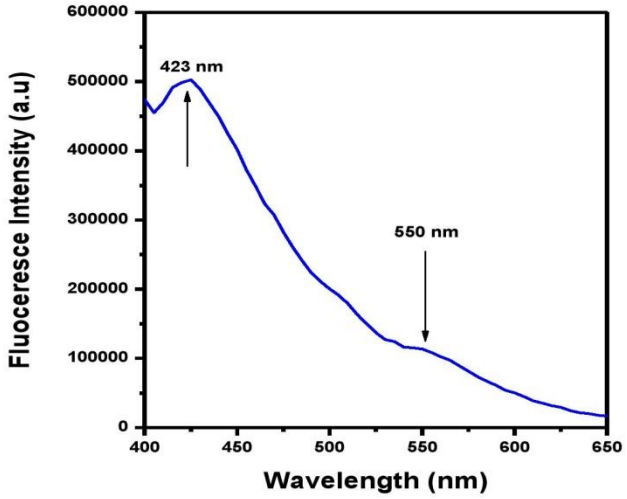

Figure SI2. Fluorescence spectra of pure Vitamin B_{12} after excitation at 355 nm.

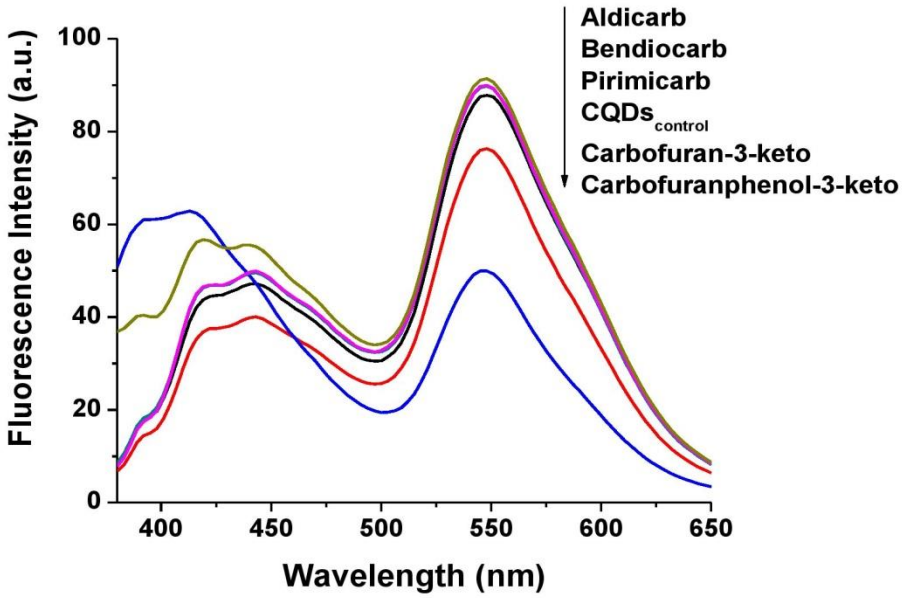

Figure SI 3. Fluorescence spectra of CQDs@VitB_{12} exposed to various pesticides (0.25 mM); Excitation at 355 nm.

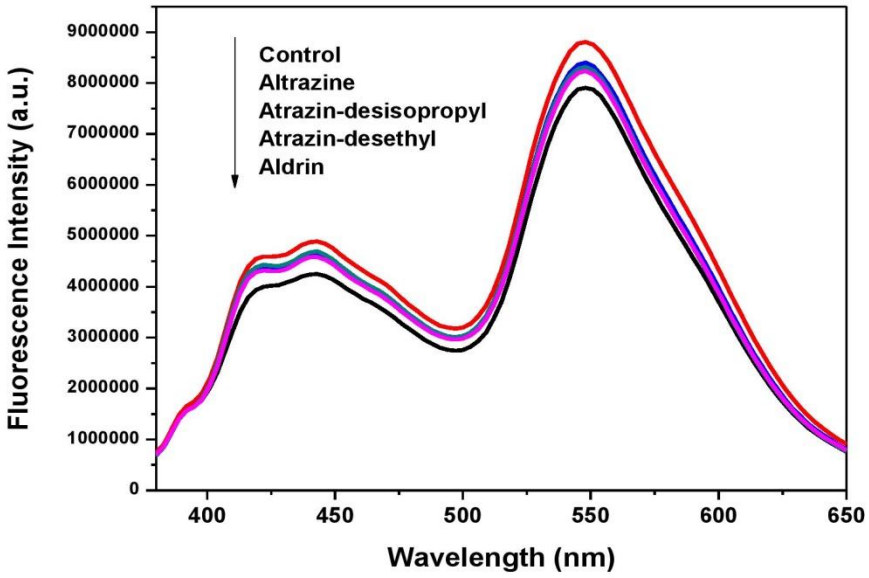

Figure SI4. Influence of triazine derivates on the fluorescence intensity of CQDs@VitB$_{12}$. Excitation at 355 nm.

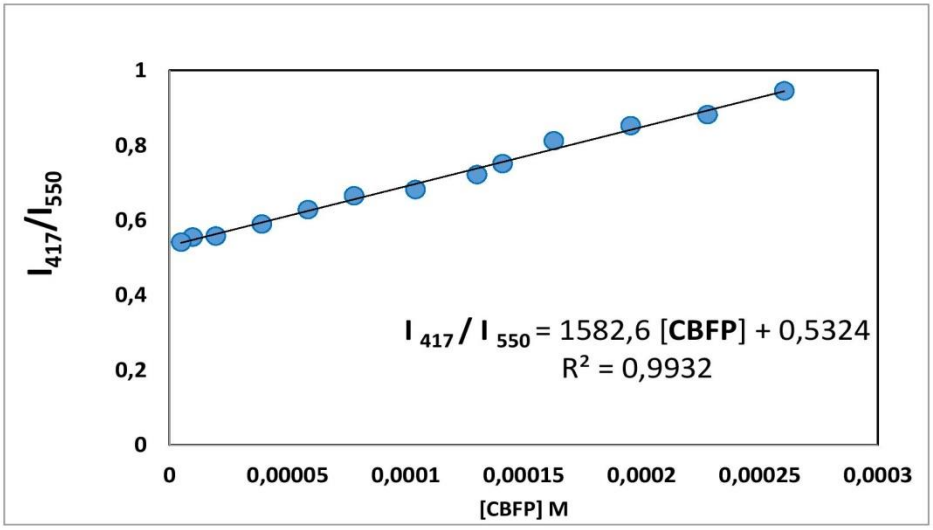

Figure SI5. Calibration graph of the specific fluorescence peak intensity ratios for CQDs@VitB$_{12}$ exposed to CBFP. Excitation at 355 nm.

Chapter 6

Carbon Dots on Based Folic Acid Coated with PAMAM Dendrimer as Platform for Pt(IV) detection

6.1 Contribution to this Paper

My contribution to this paper included the bibliographic research and writing about carbon QDs, dendrimers and then the experimental planning. The synthesis, purification and functionalization with dendrimers were performed, even all the complementary studies including the effect of some parameters such as pH, ionic strength and the tolerance to some ions on the excitation/emission matrix. The data obtained by the characterization methods was analyzed and interpreted. The determination of analytical parameters and the sensing of chloroplatinate ions in platinum nanoparticles dissolutions was also performed and assayed with the fluorescent nanosensor. This paper was submitted as a scientific article and until the acceptation it passes through some adjustments required by the reviewers and under supervision of my advisor Professor Joaquim Esteves da Silva and co-advisor Doutor Manuel Algarra.

Journal of Colloid and Interface Science 465 (2016) 165–173

Contents lists available at ScienceDirect

Journal of Colloid and Interface Science

journal homepage: www.elsevier.com/locate/jcis

Carbon dots on based folic acid coated with PAMAM dendrimer as platform for Pt(IV) detection

Bruno B. Campos [a], María Moreno Oliva [b], Rafael Contreras-Cáceres [c], Enrique Rodriguez-Castellón [d], José Jiménez-Jiménez [d], Joaquim C.G. Esteves da Silva [a], Manuel Algarra [d,*]

[a] Centro de Investigação em Química, Departamento de Geociencias, ambiente e ordenamento do territorio, Faculdade de Ciências da, Universidade do Porto, Porto, Portugal
[b] Departamento de Química Física, Facultad de Ciencias, Universidad de Málaga, Campus de Teatinos s/n, 29071 Málaga, Spain
[c] Departamento de Química Orgánica, Facultad de Ciencias, Universidad de Málaga, Campus de Teatinos s/n, 29071 Málaga, Spain
[d] Departamento de Química Inorgánica, Universidad de Málaga, Campus de Teatinos s/n, 29071 Málaga, Spain

HIGHLIGHTS

- Fluorescent Carbon dots coated with PAMAM-NH_2 (CQDs@PAMAM-NH_2) based on folic acid.
- Characterized by DLS, TEM, XPS, ATR, Raman and fluorescence techniques.
- Quenching by the unreacted Pt(IV) as $(PtCl_6)^{2-}$ proposed an analytical method.
- The static mechanism was demonstrated by fluorescence lifetime analysis.
- A wide range of interferences studied make suitable for a sensitivity of 78 nM.

GRAPHICAL ABSTRACT

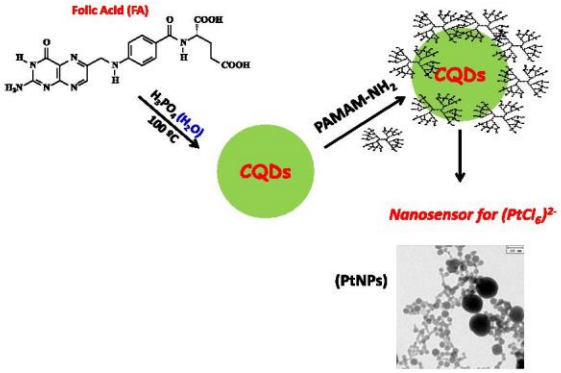

ARTICLE INFO

Article history:
Received 12 October 2015
Revised 19 November 2015
Accepted 23 November 2015
Available online 24 November 2015

Keywords:
Carbon quantum dots
Chloroplatinate ion
Dendrimer
Sensor
Doped nanoparticles

ABSTRACT

Carbon quantum dots (CQDs) coated with poly(amidoamine) (PAMAM-NH_2) dendrimer are prepared from folic acid and phosphoric acid under a hydrothermal procedure. The obtained nanoparticles are successfully used as fluorescent sensor for Pt(IV) (in the form of chloroplatinate ion). CQDs possess many attractive features including uniform dispersion with average size about 13 nm for unmodified particles and, ~30 nm when they are coated with PAMAM-NH_2 dendrimer. The synthesized nanoparticles have been characterized by elemental analysis, attenuated total reflectance (ATR), X-ray photoelectron (XPS) and Raman spectroscopies, transmission electron microscopy (TEM), dynamic light scattering (DLS), and steady-state and life-time fluorescence. CQDs are used as fluorescent sensor of Pt(IV) ion in aqueous media showing linear quenching effect of their fluorescence. The results obtained demonstrated a limit of detection of 657 nM with an accuracy of the method of 0.13% (as RSD, $n = 10$) and sensitivity of 78 nM. Moreover, with the presence of other interference species, good results are obtained when applied in real samples from platinum nanoparticles synthesis. The dissolved platinum ions can be quantified in the range 6–96 μM with an accuracy of 2.5%.

* Corresponding author.
E-mail address: malgarra67@gmail.com (M. Algarra).

http://dx.doi.org/10.1016/j.jcis.2015.11.059
0021-9797/

1. Introduction

Carbon quantum dots (CQDs) are a new class of fluorescent metal free nanomaterials with only a few nanometers of size with an inner graphitic core [1–3]. Recently, they have become in an attractive field, if they are compared to Quantum Dots and organic dyes, due to their high solubility, chemical stability and easy to be functionalized in order to communicates a high resistance to photo-bleaching and tunable emission [4–8]. Due to their non-toxic and biocompatible properties, *in vivo* applications are increasing, as cell imaging [9–14]; drug delivery [15–17]; biosensors [18–23]. Apart from that high quantum yield and tunable photoluminescence have made CQDs potential components in energy related applications [24–31].

Synthesis procedures to obtain CQDs can be classified into two main groups: (i) top-down approaches, where larger carbon structures are broken off to smaller CQDs including arc discharge [32,33], electrochemical oxidation [34,35] and laser ablation [36,37] technique, and (ii) bottom-up methods, which include combustion, thermal and hydrothermal, supported synthesis, microwave/ultrasonic, solution chemistry which CQDs are formed from molecular precursors [38–44]. To date, fluorescent CQDs have been easily obtained through the above mentioned strategies. However, efficient means for tuning the emission wavelength and quantum yields of CQDs are stills care and highly desirable.

Currently, intensive research has been focused on the synthesis of multifunctional systems based on CQDs to improve their quantum yield, by doping with inorganic salts [45–47] or by functionalization/passivation their large surface to achieve red-shifted emissions and rendering them as attractive fluorescent nanomaterials [20,48–50]. Alternatively, the substitutions of carbon atoms with heteroatoms such as N, S, P and Si enhance their fluorescence efficiency [51–57]. It is theorized that fluorescence emissions of CQDs are associated to radiative recombination in the passivated surface defects of the CQDs core. So the surface passivation plays an important role in the surface stability and more effective radiative recombination with the introduction of new energy trapping sites [58,59]. For instance, the N dopants promote a high yield of radiative recombination while S surface states suppress excitation-dependent photoluminescence [44]. Even without the addition of some dopant/passivation agents to carbon materials, the precursors which possess in their framework functional groups with the atoms reported above, and a suitable bottom-up method, are able to produce reliable doped and passivated CQDs with improved optical properties, as the examples of the CQDs synthesized from L-cysteine and glutathione, both with thiol, carboxyl and amino functional groups [60,61].

In this work, due to the higher content, we have employed folic acid, treated with phosphoric acid as source materials for the preparation of enriched fluorescent nitrogen and phosphorous doped carbon nanoparticles through one-pot aqueous phase synthesis. Previously, folic acid has been used for this purpose, where was approached the presence of N atoms as mentioned using microwave, hydrothermal [62–65], for a wide field of applications. Moreover to increase their affinity, were further coated by PAMAM-NH_2 dendrimer. In the literature, a similar amino passivation strategy using 1,2-ethylenediamine [3,66,67], and branched polyethylenimine/poly(amino amine) are found [49,68–70].

The obtained CQDs were characterized by various physical methods and used as an effective fluorescent sensing system for Pt(IV) in the chloroplatinate ion ($[PtCl_6]^{2-}$) form. Indeed, CQDs have been shown to be excellent electron donors which make these nanomaterials particularly suitable sensor platforms for easily reducible chemical species, like the Pt(IV) [58]. Here is proposed an alternative and potential analytical method to the conventional found in the literature such as the anodic stripping voltammetry [71,72], polarography [73], electrophoresis [74], small-angle X-ray scattering (SAXS) and X-ray absorption near-edge structure techniques [75,76], chemiluminescence previous flow injection method [77] and atomic absorption [78]. However, to improve the performance and selectivity of the nanosensor the surface chemistry of these nanomaterials will be coated by PAMAM-NH_2 dendrimer. It is expected that the negative surface charge of raw CQDs become positive after PAMAM-NH_2 capping allowing close interaction with the $[PtCl_6]^{2-}$ ion. The sensor present the novelty to be the first assay, which CQDs are used, in the analysis of the excess of Pt(IV) as $[PtCl_6]^{2-}$ ion during a platinum nanoparticles (PtNPs) synthesis, by a simple and low cost analytical method.

2. Experimental

2.1. Chemicals and materials

Folic acid (⩾97%, FA), hexachloroplatinic (IV) acid hexahydrate ($H_2PtCl_6{\cdot}6H_2O$) from Merck (Darmstadt, Germany), polyamidoamine dendrimer-1,12-diaminododecane core generation 4 $(PAMAM\text{-}NH_2)_{G=4}$ solution in methanol 10%, sodium borohydride ($NaBH_4$, ⩾96%), sodium citrate dehydrate (>99%), phosphoric acid (85 wt%, 99.99%) and cellulose membrane for dialysis were supplied from Sigma–Aldrich Química S.A. (Spain). All reagents were used as received without further purification. Ultrapure Millipore water and further reagents of analysis quality were used throughout all experiments.

2.2. Synthesis of CQDs coated with PAMAM dendrimer from FA

CQDs were obtained by adding 10 mg of FA to 5 mL phosphoric acid solution (7.31 M) and heated under reflux at 100 °C for 1 h. Then, 500 μL of the previous solution were diluted with deionized water and capped with 30 μL of PAMAM-NH_2 in a Teflon-equipped stainless-steel, assisted by an autoclave reactor, at 200 °C for 1 h. Finally, the obtained highly green fluorescent solution (CQDs@PAMAM-NH_2) was dialyzed *vs* water for 1 h.

2.3. Characterization methods and data analysis

Photoluminescence spectrophotometer (Horiba Jovin Yvon Fluoromax 4 TCSPC) was used to characterize CQDs@PAMAM-NH_2 optical performance. The fluorescence was measured in the wavelength range of 300–650 nm. The spectra were obtained with an integration time of 0.1 s and 1 nm slits for excitation and emission. All measurements were performed at room temperature. Fluorescence lifetime analysis was done using an Edinburgh Instruments FLS920, equipped with a Xe lamp (450 W) as excitation source for steady state fluorescence measurements and monochromatics LEDs (PicoQuant PLS), controlled by a PDL 880-B system. Fluorescence decays were interpreted in terms of a multi-exponential: $I(t) = A + \Sigma B_i e^{-\tau i}$, where A and B_i are the pre-exponential factors and τ_i the decay times. Transmission electron microscopy (TEM) analysis was carried out with a JEOL JEM1010 (100 kV) microscope (Tokyo, Japan), where the images were recorded with a camera Gatan SC200 (Pleasanton, CA). The zeta potential (ζ) of CQDs were determined using a Zetasizer Nano ZS (Malvern Instruments, U.K.) equipped with a 4 mW HeNe laser operating at $\lambda = 633$ nm. ζ were also performed at 25 °C in polycarbonate folded capillary cells, incorporated with gold plated electrodes (DTS1061) and deionized H_2O was the dispersion medium. ζ were automatically obtained by the software, using the

Stokes–Einstein and the Henry equation, with the Smoluchowski approximation. X-ray photoelectron spectroscopy (XPS) studies were performed on a Physical Electronic PHI 5700 spectrometer using non-monochromatic Mg K_α radiation (300 W, 15 kV, 1253.6 eV) for analyzing the core-level signals of the elements of interest with a hemispherical multichannel detector. The spectra of powdered samples were recorded with a constant pass energy value at 29.35 eV, using a 720 μm diameter circular analysis area. The X-ray photoelectron spectra obtained were analyzed using the PHI ACESS ESCA-V6.0F software and processed using Multipak 8.2B package. The binding energy values were referenced to adventitious carbon C 1*s* signal (284.8 eV). Shirley-type background and Gauss-Lorentz curves were used to determine the binding energies. Infrared absorption spectroscopic measurements were performed by means of a Specac Golden Gate single reflection diamond ATR (attenuated total reflectance) accessory coupled to a Bruker VERTEX 70 Fourier transform infrared spectrometer. ATR spectra were recorded with a 4 cm^{-1} resolution in the spectral range between 4000 and 500 cm^{-1}. Raman measurements were carried out with a Senterra dispersive Raman spectrometer from Bruker with 785 nm as excitation, with collection of the Raman scattering in back-scattering configuration with a standard spectral resolution of 3 cm^{-1}, spatial resolution of 0.5 μm, and spot size of about 3 μm.

2.4. Metal ions study

1 mL of 0.25 mM aqueous solutions of the following species were equilibrated at room temperature for 15 min with 10 μL of CQDs@PAMAM-NH_2: Ag(I), Al(III), As(III), Cd(II), CN^-, Co(II), Cr (III), Au (III), Cu(II), Fe(II), Fe(III), Hg(II), Ni(II), Pb(II), $[PtCl_6]^{2-}$, Sb (II), and Zn(II). The fluorescence of these mixtures was measured.

2.5. Platinum nanoparticles (PtNPs)

PtNPs were prepared by the following procedure: 20 μL of a sodium citrate solution (25 mM) were added to 1.98 mL of $H_2PtCl_6{\cdot}H_2O$ aqueous solution (0.25 mM) and kept under agitation for 3 min. Then 60 μL of a freshly $NaBH_4$ solution (0.1 M), diluted with sodium citrate solution (25 mM) were added, followed instantly by a reddish changing color, indicating the formation of PtNPs. The solution was stirred for 15 min more and dialyzed *vs* water.

3. Results and discussion

3.1. Analysis of the nanocomposites CQDs@PAMAM-NH_2

Our Preliminary work are focused on the effect of the different concentrated mineral acids, as HCl, HNO_3, H_2SO_4 and H_3PO_4, on the fluorescence intensity of the obtained CQDs (with 4.53 mM of FA refluxed for 1 h at 100 °C). As shown in Fig. 1, the use of H_3PO_4 results in CD with the highest fluorescence intensity, with a maximum emission at 486 nm. The wavelengths of the maximum emission for the other three acids were: 499 nm (HNO_3); 487 nm (HCl); and 475 nm (H_2SO_4).

Accordingly to the results obtained, CQDs treated with H_3PO_4 were chosen for further experiments and for PAMAM-NH_2 dendrimer coating. Fig. 2 shows the influence of the ratio (v/v) of H_3PO_4 as dehydrating reagent and as coating molecule on the fluorescence intensity of the obtained nanocomposites. A control sample was obtained without PAMAM-NH_2 but subjected to the hydrothermal heating process. This sample was settled a control sample, which was obtained by means of the remaining CQDs synthesized by reflux, where the main difference was the blue shift (9 nm). The addition of PAMAM-NH_2 to CQDs leads the wavelength

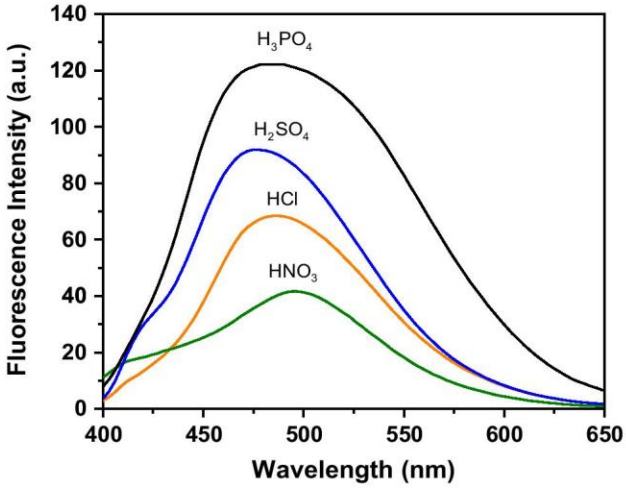

Fig. 1. Fluorescence intensity of CQDs obtained with different dehydrating agents when exited at 360 nm.

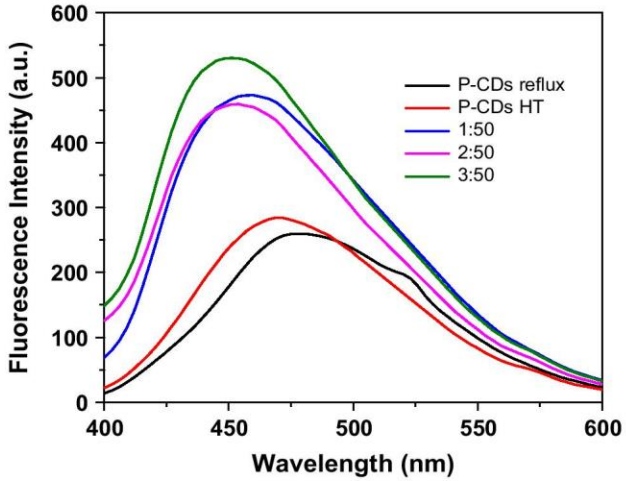

Fig. 2. Study of PAMAM-NH_2:P-CQDs volume ratio ($\lambda_{exc.}$ = 360 nm). It showed the effect when compared the hydrothermal (HT) and reflux procedure to obtain CQDs.

to blue-shifted emission from 469 nm (control) to 451 nm (3:50 ratio), a blue-shift of 18 nm and an increasing in the fluorescence intensity of 86%, thus contributing to achieve a quantum yield of 0.27.

Fig. 3 shows the TEM images of control samples CQDs (A) and CQDs@PAMAM-NH_2 (B). Raw CQDs showed a regular average diameter size (13.2 ± 1.6 nm, inset Fig. 3A) and with a good dispersion in H_2O, while CQDs@PAMAM-NH_2 showed an aggregation process (30 ± 5 nm, inset Fig. 3B), probably influenced by the dendrimer coating. Contrary to the strategies of CQDs functionalization with polyamines, the PAMAM-NH_2 has a high content not only in amine groups but also in amide groups. It has been observed that functionalization only with amine groups leads to a red-shifted emission, but in this case the dendrimer used is composed by both amine and carboxyl groups [79]. An increasing of PAMAM-NH_2 also leads to an increase of amine and carboxyl groups but seems that the optical properties of CQDs@PAMAM-NH_2 are mainly affected by the increasing of carboxyl groups, since the amine and carboxyl group ratio is constant. The ζ of the as-prepared CQDs was determined to be 14.0 ± 0.8 mV while the as-prepared with PAMAM-NH_2 was 20.2 ± 1.7 mV. These

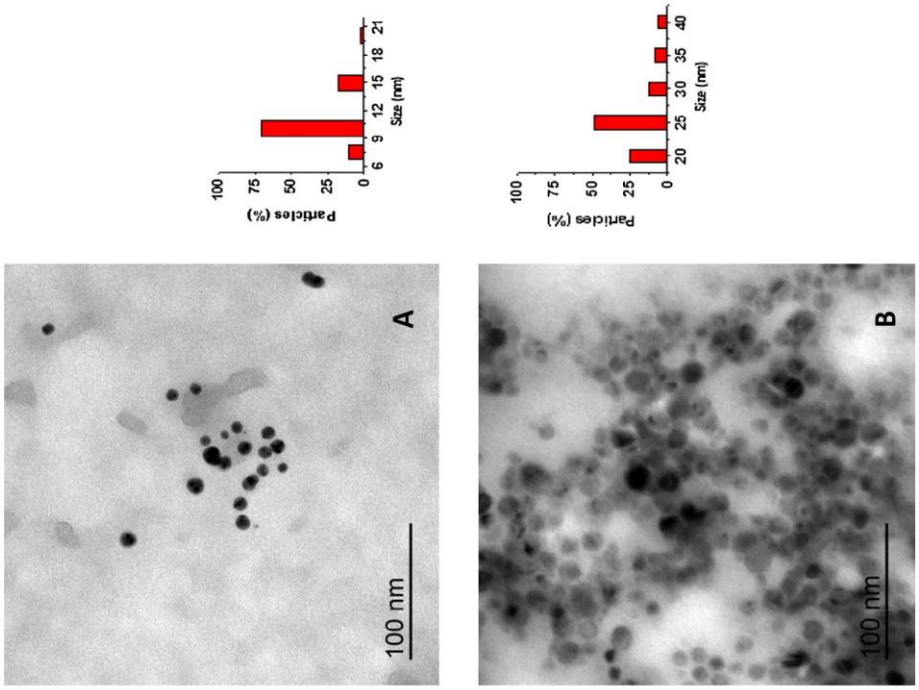

Fig. 3. TEM images of (A) CQDs (NPs = 70 nanoparticles) and (B) CQDs@PAMAM-NH_2 (NPs = 102 nanoparticles) obtained from folic acid treated with H_3PO_4 at 100 °C. (In Supplementary information is provided more TEM images, Fig. SI.1.)

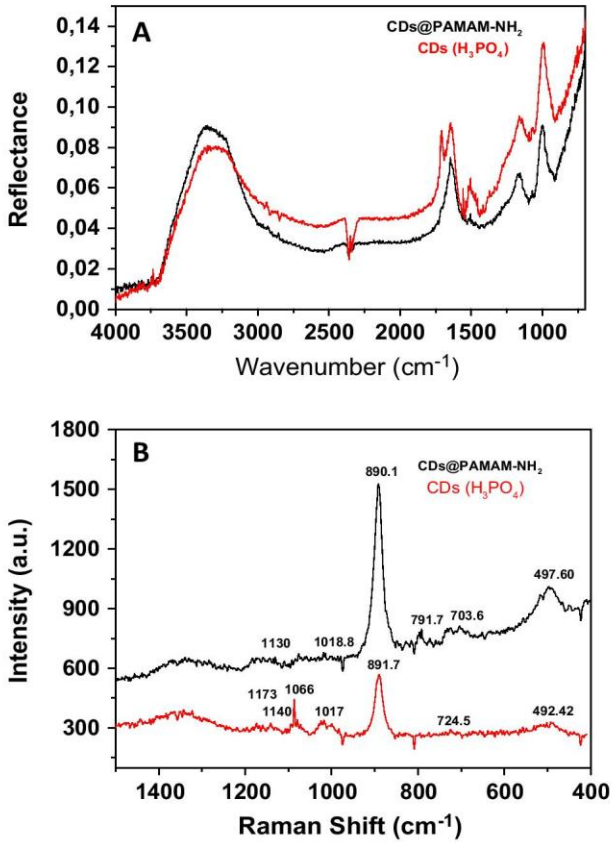

Fig. 4. (A) ATR and (B) FT-Raman spectra of CQDs and CQDs@PAMAM-NH_2.

results of positive charge indicated a favorable dispersibility of CQDs and their complex in aqueous solution. To further elucidate the surface features of the CQDs, various spectroscopic analyses were carried out. As was previously mentioned, the surface composition and elemental analysis for the resultant CQDs were characterized by ATR, Raman and XPS spectroscopies.

ATR spectra (Fig. 4A) revealed chemical information regarding the capping dendrimer; furthermore Raman spectra (Fig. 4B) gave insights into the surface functionalization. In both ATR spectra, the broad band centered at 3315 cm^{-1} was ascribed to the stretching vibration of —OH. [79] In the case of CQDs, a band at 1709 cm^{-1} was ascribed to the carbonyl groups (—C=O), that is not present after the dendrimer capping (Fig. 4A). The observed bands in CQDs at 1163 cm^{-1} due to the C—O and C—C stretching modes, and at 991 cm^{-1} due to the C—H bending mode, shifted to higher frequencies in CQDs@PAMAM-NH_2, 1172 cm^{-1} and 997 cm^{-1}, respectively, as a result of the chemical transformation, and showing more effective conjugation in functionalized CQDs. However, the intense band at 1647 cm^{-1} was assigned to vibration modes of the amide group with a larger contribution from the C=O stretching and smaller contributions from the C—N stretching and the N—H bending, remaining at same frequencies in both samples. The asymmetrical stretch of CO_2 gives a strong band in the IR at 2350 cm^{-1}, impossible to remove in both spectra due to the environmental conditions, although not interfering in the bands of interest. Raman spectra (Fig. 4B) of both CQDs samples were very similar, indicating no important changes on the surface functionalization. The Raman signals around 891 cm^{-1} was associated with the C—H bending mode, increasing the intensity after the dendrimer inclusion. The spectrum of CQDs@PAMAM-NH_2 revealed a broad feature at 497 cm^{-1}, due to PO_4^{3-} bending mode. We do not observe any typical Raman signal of the carbon graphitic materials, i.e. G and D bands [80].

The surface chemical composition (in atomic concentration %) of the CQDs determined by XPS reveals the presence of C (17.25%), N (0.52%), O (64.73%) and P (17.50%). The C 1*s* core level signal (Fig. 5) is composed of three contributions at 284.8 eV (75%), 286.7 eV (16%) and 289.2 eV (8%). The contribution at high binding energy is assigned to the presence of carboxylic group from folic acid and that at 286.7 eV to carbonyls from amide groups [81]. The N 1*s* core level signal is asymmetric (Fig. 5) and can be deconvoluted into two contributions at 400.8 eV (80%) and 402.3 eV (20%) assigned to amide and protonated amine groups, respectively [82]. The P 2*p* signal at 134.7 eV comes from the phosphate group. The O 1*s* signal is asymmetric (Fig. 5) and can be decomposed in two contributions at 532.3 and 533.4 eV. The main contribution is assigned to the O of the phosphate group. After the incorporation of the dendrimer, the surface chemical composition is modified: C (28.54%), N (0.37%), O (55.74%), P (15.35%). As expected, a clear increase of the % of C is observed due to the incorporation of the dendrimer. The C 1*s*, P 2*p* and O 1*s* core level signals hardly varied, but the N 1*s* signal (Fig. 5) is modified with a much higher relative intensity of the contribution assigned to the protonated amine.

The influence of ionic strength was assessed, and it was observed that NaCl concentrations above 5.5×10^{-3} M led to major fluorescence quenching, reaching less 80% intensity at 2.06 M (Fig. SI2). At the same time the influence of pH in the intensity of the proposed nano-sensor was analyzed and the data set presented a sigmoidal behavior (Fig. SI3). The CQDs@PAMAM-NH_2 solution has a pH of 1.25 and was not subsequently neutralized in order to facilitate the solubility and stability of metals ions in the presence of the nano-sensor.

3.2. Fluorescent response of CQDs@PAMAM-NH_2 in the presence of metal ions

Under the optimal analytical conditions, the influence of metal ions in the fluorescent signal of CQDs@PAMAM-NH_2 solution (pH = 1.25) was analyzed. It observed a slight enhancement for the ions (enhancement percentages under parenthesis) As(III) (0.1%) and Pb(II) (0.2%) and quenching (quenching percentages under parenthesis) for Ag(I) (0.5%), Al(III) (9.4%), Cd(II) (1.8%), Au(III) (0.8%), CN^- (0.8%), Co(II) (0.2%), Cr(III) (9.7%), Cu(II) (6.4%), Fe(II) (5.6%), Fe(III) (51.6%), Hg(II) (60.7%), Ni(II) (0.4%), $[PtCl_6]^{2-}$ (91.5%), Sb(II) (6.7%), and Zn(II) (3.9%), Fig. 6.

As expected, the fluorescence of the nanocomposites is highly sensible to $[PtCl_6]^{2-}$ ion by comparing with the other species. Fe (III) and Hg(II) ions showed a moderated quenching effect [58]. Similar surface modification strategies use folic acid and PAMAM-NH_2, separately, to conjugate with Pt nanoparticles for chemotherapy applications [83–85] In the case of CQDs@PAMAM-NH_2 nano-sensor, the precursors folic acid and the PAMAM-NH_2 had both contributed with amine and carboxylic groups to bind with $[PtCl_6]^{2-}$ decreasing markedly the fluorescence intensity of CQDs@PAMAM-NH_2, which can be explained their affinity due to their moderate high ζ (20.2 mV).

3.3. Calibration curve of CQDs@PAMAM-NH_2 with $[PtCl_6]^{2-}$ ion

The effect of $[PtCl_6]^{2-}$ ion on the CQDs@PAMAM-NH_2 fluorescence intensity was evaluated between the ranges of 1.6 μM up to 96 μM and a linear correlation was obtained with an equation of, $I_F = 2.94 \times 10^{11}\ [PtCl_6]^{2-} - 5.23 \times 10^7$ ($r = 0.997$) (Fig. 7). The

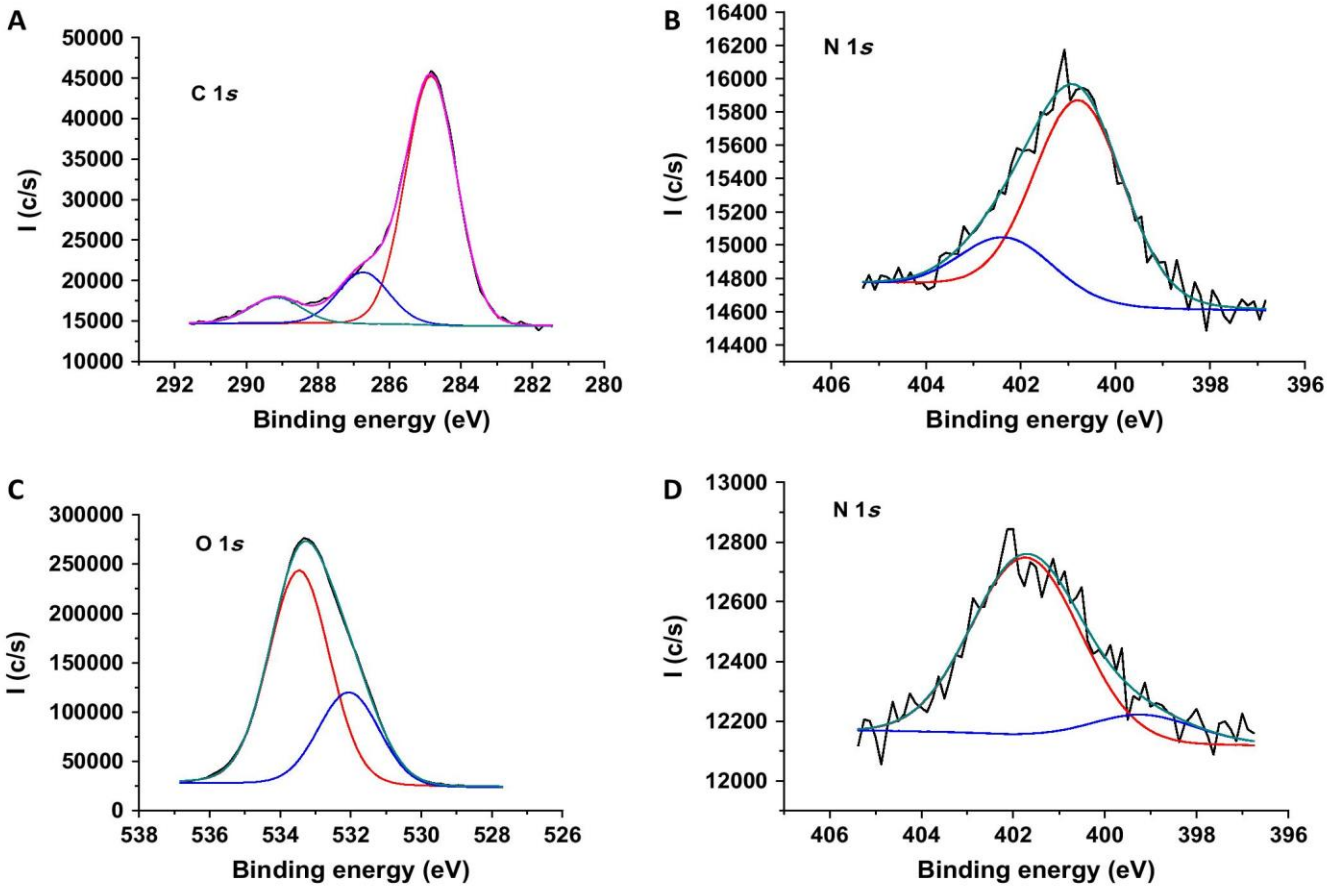

Fig. 5. C 1*s*, N 1*s* and O 1*s* core level spectra of CQDs and N 1*s* of CQDs@PAMAM-NH_2.

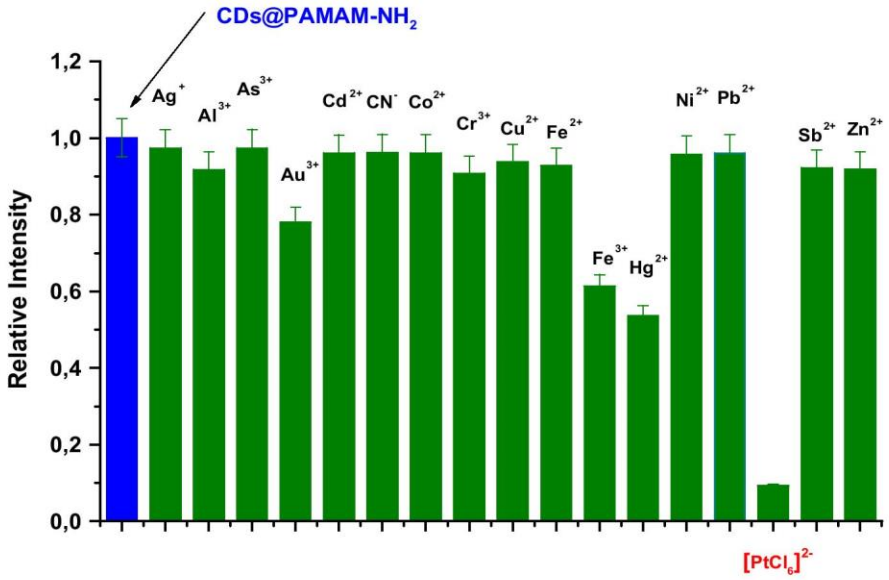

Fig. 6. Influence on the fluorescence intensity at 465 nm of CQDs@PAMAM-NH_2 by 5×10^{-3} M of different ions in dissolution with λ_{ex} = 360 nm.

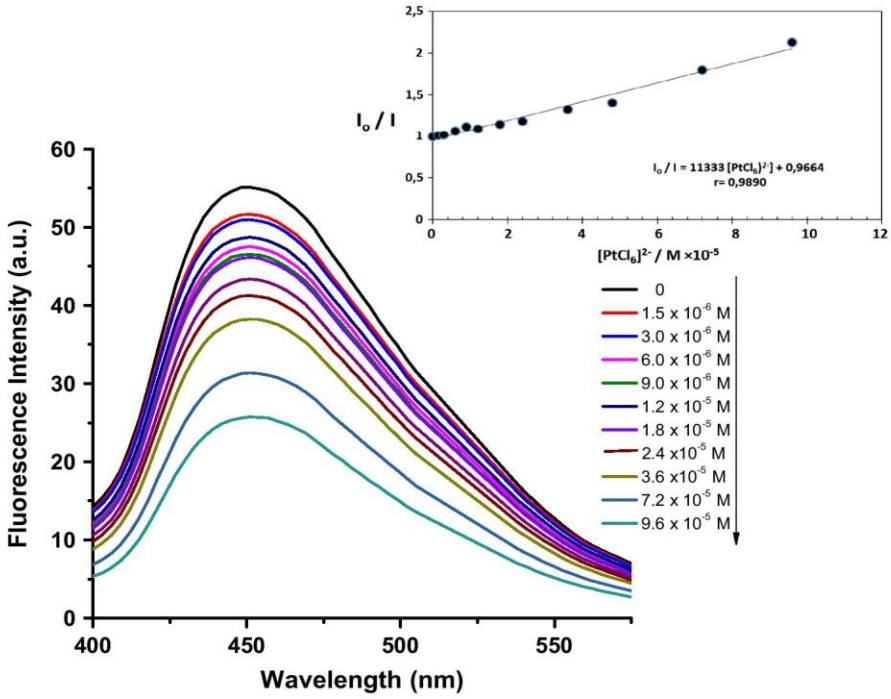

Fig. 7. Fluorescence intensity of CQDs@PAMAM-NH_2 in function of $[PtCl_6]^{2-}$ ion with λ_{ex} = 360 nm.

fluorescence quenching can be modeled by a Stern–Volmer equation (r = 0.989), with a K_{SV} = 8381 M^{-1} (inset Fig. 7). The relatively high magnitude of the Stern–Volmer constant and the fluorescence lifetimes presented in Table 1 suggest that a static mechanism is predominant in the quenching of the fluorescence intensity of CQDs@PAMAM-NH_2 by $[PtCl_6]^{2-}$ ion. This order of magnitude is compatible with the formation of a quite stable complex (static quenching) between CQDs@PAMAM-NH_2 and $[PtCl_6]^{2-}$ ions, which can be justified by the complexation of metal ions by surface ligands of the CQDs@PAMAM-NH_2 provoking a charge transfer process on its surface. Moreover, the fluorescence lifetime (the two main components, see τ_1 and τ_2) do not change or do not decrease since those CQDs@PAMAM-NH_2 which are not complexed – and hence are able to emit after excitation – will have normal excited state properties. The fluorescence of the sample is reduced since the quencher is essentially reducing the number of fluorophores which can emit [86].

The proposed sensor was optimized to obtain the best sensitivity, limit of detection (LOD) and limit of quantification (LOQ). The LOD was calculated by measuring the fluorescence intensity equal to 3 times the SD of the blank (n = 10) divided by the slope of the calibration graph, while the LOQ was determined as 3 times the

Table 1
Components of lifetime decay ($1.14 < \chi < 1.19$).[a]

$(PtCl_6)^{2-}$] (M)	A	τ_1 (ns)	B_1	τ_2 (ns)	B_1	τ_3 (ns)	B_1
0	5.84	2.06 (0.06)	2.30×10^{-2}	6.70 (0.03)	1.78×10^{-2}	0.24 (0.02)	9.18×10^{-2}
6.0×10^{-6}	2.47	3.32 (0.23)	1.79×10^{-2}	7.00 (0.05)	2.09×10^{-2}	7.68 (0.03)	3.01×10^{-2}
1.2×10^{-5}	4.86	2.19 (0.14)	2.10×10^{-2}	6.68 (0.03)	2.20×10^{-2}	5.70 (0.04)	2.81×10^{-2}
2.4×10^{-5}	5.10	2.03 (0.07)	2.38×10^{-2}	6.68 (0.02)	2.10×10^{-2}	3.72 (0.04)	3.70×10^{-2}
4.8×10^{-5}	6.22	1.96 (0.06)	2.40×10^{-2}	6.62 (0.02)	2.01×10^{-2}	2.31 (0.03)	7.25×10^{-2}
9.6×10^{-5}	5.59	1.89 (0.06)	2.20×10^{-2}	6.61 (0.02)	0.02×10^{-2}	1.72 (0.02)	0.12×10^{-2}

[a] Averages and standard deviation (in parentheses) of three independent experiences.

Table 2
Recovery (%) values for CQDs@PAMAM-NH_2 in the presence of $(PtCl_6)^{2-}$ (1.25×10^{-5} M) and different concentration ratios of interfering species.[a]

	1:5	1:1	5:1
Al(III)	96.75 (3.10)	98.89 (4.45)	94.96 (4.08)
Cr(III)	92.92 (1.95)	98.95 (5.34)	96.95 (3.10)
Cu(II)	99.77 (4.49)	101.48 (3.45)	97.30 (5.35)
Fe(III)	83.02 (2.82)	95.83 (4.98)	94.61 (4.35)
Hg(II)	81.11 (4.54)	98.47 (2.26)	90.29 (3.88)
Au(III)	97.15 (0.36)	92.10 (1.23)	80.14 (3.33)

[a] Averages and standard deviation (in parentheses) of three independent experiences.

LOD. The LOD and LOQ of the proposed nano-sensor were 657.4 nM and 2.2 mM, respectively, with a relative standard deviation of 0.13% (as RSD, $n = 10$), and a sensitivity of 77.9 nM.

3.4. Tolerance to interfering species

Besides of the metal screening represented above, the tolerance of the nano-sensor was evaluated in the presence of the metals which caused the highest changing in the fluorescence intensity, i.e. Al(III), Cr(III), Cu(II), Fe(III) and Hg(II) with different concentration ratios of 1:5, 1:1 and 5:1 ($[PtCl_6]^{2-}$:[Interference]) in relation to a fixed concentration of $[PtCl_6]^{2-}$ (1.25×10^{-5} M) (Table 2). As seen in Table 2, when the concentration of the interference is superior to the $[PtCl_6]^{2-}$ the values of recovery are very satisfactory for Al(III), Cr(III) and Cu(II), increasing the interference for Fe(III) and Hg(II) with recovery values between 80% and 85%. For ratios were the $[PtCl_6]^{2-}$ is in equality and superiority the recovery values are upper 90%. The reported range of ratios of the nano-sensor still showed high affinity for $[PtCl_6]^{2-}$ even in competition with other interfering species demonstrating the high selectivity of the nano-sensor for $[PtCl_6]^{2-}$ determination.

3.5. Application to real samples

To assess the applicability of CQDs@PAMAM-NH_2, PtNPs were synthesized and the unreacted $[PtCl_6]^{2-}$ ion were quantified by the standard addition method (Fig. 8). As previously demonstrated, the quenching of the fluorescence intensity of CQDs@PAMAM-NH_2 is described by the following calibration curve, $\mathbf{I_F} = -3.30 \times 10^{-11}$ $\{\mathbf{[PtCl_6]^{2-}}\} + 5.20 \times 10^7$ ($r = 0.996$) in the range of 6.0–96 μM. The accuracy of the results is between 2.5% and 5.6%, validating the CQDs@PAMAM-NH_2 as a fluorescent nano-sensor $[PtCl_6]^{2-}$. The results obtained for these experiments are shown in Table 3. In the literature it has been recently described the use of quantum dots to establish a qualitative determination of Pt, which is used extensively in chemotherapy, and explained by fluorescence quenching [87], but no quantitative determinations was achieved.

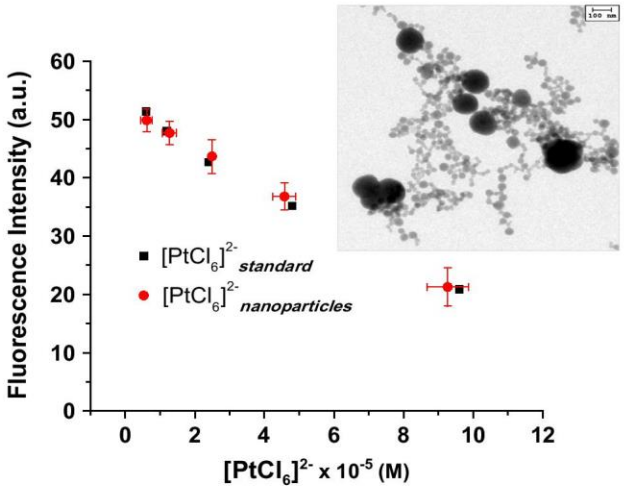

Fig. 8. Results obtained when comparing the analysis of $[PtCl_6]^{2-}$ by CQDs@PAMAM-NH_2 using a standard solution (■) and a real solution of PtNPs (■). Inset shows the TEM images of the quality of the PtNPs obtained by the procedure described in 2.5 at $\lambda_{em} = 465$ nm with $\lambda_{ex} = 360$ nm.

Table 3
Determination of $\mathbf{(PtCl_6)^{2-}}$ for PtNP solutions.[a]

$[(PtCl_6)^{2-}]_{st}$ (μM)	$[(PtCl_6)^{2-}]_{nano}$ (μM)	Accuracy %
6.0	6.2 (1.6)	2.50
12.0	12.7 (2.1)	5.64
24.0	24.9 (0.3)	3.74
48.0	45.8 (3.3)	4.85
96.0	92.7 (6.0)	3.58

[a] Averages and standard deviation (in parentheses) of three independent experiences.

4. Conclusions

In summary, a fluorescent sensor for detection of chloroplatinate ion in solution of platinum nanoparticles, based on the quenching effect of the intensity of the synthesized carbon dots by the acid treatment of folic acid with H_3PO_4, was reported. Folic acid showed an attractive source of CQDs due to inherent doped effect in nitrogen composition, and its further surface coating with PAMAM-NH_2, demonstrated its successfully use as fluorescent sensor for free platinum in solutions of their nanoparticles. The detection limit is in the range of nM. The probe had remarkably high selectivity and moderate sensitivity (77.9 nM). The reaction with CQDs coated with dendrimer is proposed as a sensor based in its quenching mechanism with a good accuracy (RSD = 0.13%) and moderate free of interference.

Acknowledgments

BB Campos is acknowledged to SFRH/BD/84318/2012 scholarship and PTDC/QEQ-QAN/5955/2014 (FCT, Portugal). Authors

thank to projects P12-RNM-1565 (Junta de Andalucía, Spain) and CTQ2012-37925-C03-03 (MINECO, Spain). MMO & RCC acknowledge to M Curie COFUND "U-Mobility" program co-financed by UMA and EC FP7 (Grant Agreement 246550). MMO thanks Juan de la Cierva contract (MINECO).

Appendix A. Supplementary material

Supplementary data associated with this article can be found, in the online version, at http://dx.doi.org/10.1016/j.jcis.2015.11.059.

References

[1] S.N. Baker, G.A. Baker, Luminescent carbon nanodots: emergent nanolights, Angew. Chem., Int. Ed. 49 (2010) 6726–6744.
[2] F. Wang, Z. Xie, H. Zhang, C.Y. Liu, Y.G. Zhang, Highly luminescent organosilane-functionalized carbon dots, Adv. Funct. Mater. 21 (2011) 1027–1031.
[3] Y. Dong, R. Wang, H. Li, J. Shao, Y. Chi, X. Lin, G. Chen, Polyamine-functionalized carbon quantum dots for chemical sensing, Carbon 50 (2012) 2810–2815.
[4] C. Wang, Z. Xu, H. Chen, H. Li, A hydrothermal route to water-stable luminescent carbon dots as nanosensors for pH and temperature, Carbon 82 (2015) 87–93.
[5] J.C.G. Esteves da Silva, H.M.R. Gonçalves, Analytical and bioanalytical applications of carbon dots, Trends Anal. Chem. 30 (2011) 1327–1336.
[6] W. Wang, Z. Gao, G. Gao, Y. Wo, Y. Wang, G. Shen, D. Cui, Systematic safety evaluation on photoluminescent carbon dots, Nanoscale Res. Lett. 8 (2013) 122–129.
[7] A.B. Bourlinos, A. Atassinopoulos, D. Anglos, R. Zboril, M. Karakassides, Surface functionalized carbogenic quantum dots, Small 4 (2008) 455–458.
[8] S.C. Ray, A. Saha, N.R. Jana, R. Sarkar, Fluorescent carbon nanoparticles: synthesis, characterization, and bioimaging application, J. Phys. Chem. C 113 (2009) 18546–18551.
[9] Q. Li, T.Y. Ohulchanskyy, R. Liu, K. Koynov, D. Wu, A. Best, R. Kumar, A. Bonoiu, P.N. Prasad, Photoluminescent carbon dots as biocompatible nanoprobes for targeting cancer cells in vitro, J. Phys. Chem. C 114 (2010) 12062–12068.
[10] B. Han, W. Wang, H. Wu, F. Fang, N. Wang, S. Xu, Polyethyleneimine modified fluorescent carbon dots and their application in cell labeling, Colloids Surf., B 100 (2012) 209–214.
[11] K. Hola, Y. Zhang, Y. Wang, E.P. Giannelis, R. Zboril, A.L. Rogach, K. Hola, Y. Zhang, Y. Wang, E.P. Giannelis, R. Zboril, A.L. Rogach, Carbon dots-emerging light emitters for bioimaging, cancer therapy and optoelectronics, Nano Today 9 (2014) 590–603.
[12] S.K. Bhunia, A. Saha, A. Maity, S.C. Ray, N.R. Jana, Carbon nanoparticle-based fluorescent bioimaging probes, Sci. Rep. 3 (2013) 1473.
[13] J.H. Liu, S.T. Yang, X. Wang, H. Wang, Y. Liu, P.G. Luo, Y. Liu, Y.P. Sun, Carbon nanoparticles trapped in vivo-similar to carbon nanotubes in time-dependent biodistribution, Appl. Mater. Interf. 6 (2014) 14672–14678.
[14] C. Ding, A. Zhu, Y. Tian, Functional surface engineering of C-dots for fluorescent biosensing and in vivo bioimaging, Acc. Chem. Res. 47 (2014) 20–30.
[15] H. Wang, J. Shen, Y. Li, Z. Wei, G. Cao, Z. Gai, K. Hong, P. Baneriee, S. Zhou, Magnetic iron oxide–fluorescent carbon dots integrated nanoparticles for dual-modal imaging, near-infrared light-responsive drug carrier and photothermal therapy, Biomater. Sci. 2 (2014) 915–923.
[16] Q. Wang, X. Huang, Y. Long, X. Wang, H. Zhang, R. Zhu, L. Liang, P. Teng, H. Zheng, Hollow luminescent carbon dots for drug delivery, Carbon 59 (2013) 192–199.
[17] S. Karthik, B. Saha, S.K. Ghosh, N.D.P. Singh, Photoresponsive quinoline tethered fluorescent carbon dots for regulated anticancer drug delivery, Chem. Commun. 49 (2013) 10471–10473.
[18] J. Zhao, G. Chen, L. Zhu, G. Li, Graphene quantum dots-based platform for the fabrication of electrochemical biosensors, Electrochem. Commun. 13 (2011) 31–33.
[19] W. Bai, H. Zheng, Y. Long, X. Mao, M. Gao, L.V. Zhang, A carbon dots-based fluorescence turn-on method for DNA determination, Anal. Sci. 27 (2011) 243–246.
[20] M. Algarra, B.B. Campos, K. Radotić, D. Mutavdžić, T.J. Bandosz, J. Jiménez-Jiménez, E. Rodriguez-Castellon, J.C.G. Esteves da Silva, Luminescent carbon nanoparticles: effects of chemical functionalization, and evaluation of Ag^{+} sensing properties, J. Mater. Chem. A 2 (2014) 8342–8351.
[21] C. López, M. Zougagh, M. Algarra, E. Rodríguez-Castellón, B.B. Campos, Joaquim C.G. Esteves da Silva, J. Jiménez-Jiménez, A. Ríos, Microwave-assisted synthesis of carbon dots and its potential as analysis of four heterocyclic aromatic amines, Talanta 132 (2015) 845–850.
[22] Z. Lin, W. Xue, H. Chen, J.M. Lin, Peroxynitrous-acid-induced chemiluminescence of fluorescent carbon dots for nitrite sensing, Anal. Chem. 83 (2011) 8245–8251.
[23] L. Zhou, Y. Lin, Z. Huang, J. Ren, X. Qu, Carbon nanodots as fluorescence probes for rapid, sensitive, and label-free detection of Hg^{2+} and biothiols in complex matrices, Chem. Commun. 48 (2012) 1147–1149.
[24] H. Li, X. He, Z. Kang, H. Huang, Y. Liu, J. Liu, S. Lian, C.H.A. Tsang, X. Yang, S.T. Lee, Water-soluble fluorescent carbon quantum dots and photocatalyst design, Angew. Chem., Int. Ed. 49 (2010) 4430–4434.
[25] Z. Ma, H. Ming, H. Huang, Y. Liu, Z. Kang, One-step ultrasonic synthesis of fluorescent N-doped carbon dots from glucose and their visible-light sensitive photocatalytic ability, New J. Chem. 36 (2012) 861–864.
[26] Q. Wu, W. Li, Y. Wu, Z. Huang, S. Liu, Pentosan-derived water-soluble carbon nano dots with substantial fluorescence: properties and application as a photosensitizer, Appl. Surf. Sci. 315 (2014) 66–71.
[27] K.A.S. Fernando, S. Sahu, Y. Liu, W.K. Lewis, E.A. Guliants, A. Jafariyan, P. Wang, C.E. Bunker, Y.P. Sun, Carbon quantum dots and applications in photocatalytic energy conversion, Appl. Mater. Interf. 7 (2015) 8363–8376.
[28] S. Liu, N. Zhao, C. Cheng, H. Liu, Amino-functionalized green fluorescent carbon dots as surface energy transfer biosensors for hyaluronidase, Nanoscale 7 (2015) 6836–6842.
[29] M. Rinzan, G. Jenkins, H.D. Drew, S. Shafranjuk, P. Barbara, Carbon nanotube quantum dots as highly sensitive terahertz-cooled spectrometers, Nano Lett. 12 (2012) 3097–3100.
[30] Y. Han, H. Huang, H. Zhang, Y. Liu, X. Han, R. Liu, H. Li, Z. Kang, Review on recent progress in nitrogen-doped graphene: synthesis, characterization, and its potential applications, ACS Catal. 4 (2014) 781–794.
[31] R. Narayanan, M. Deepa, A.K. Srivastava, Förster resonance energy transfer and carbon dots enhance light harvesting in a solid-state quantum dot solar cell, J. Mater. Chem. A 1 (2013) 3907–3918.
[32] X.Y. Xu, R. Ray, Y.L. Gu, H.J. Ploehn, L. Gearheart, K. Raker, W.A. Scrivens, Electrophoretic analysis and purification of fluorescent single-walled carbon nanotube fragments, J. Am. Chem. Soc. 126 (2004) 12736–12737.
[33] M. Bottini, C. Balasubramanian, M.I. Dawson, A. Bergamaschi, S. Bellucci, T. Mustelin, Isolation and characterization of fluorescent nanoparticles from pristine and oxidized electric arc-produced single-walled carbon nanotubes, J. Phys. Chem. B 110 (2006) 831–836.
[34] L. Zheng, Y. Chi, Y. Dong, J. Lin, B. Wang, Electrochemiluminescence of water-soluble carbon nanocrystals released electrochemically from graphite, J. Am. Chem. Soc. 131 (2009) 4564–4565.
[35] Q.L. Zhao, Z.L. Zhang, B.H. Huang, J. Peng, M. Zhang, D.W. Pang, Facile preparation of low cytotoxicity fluorescent carbon nanocrystals by electrooxidation of graphite, Chem. Commun. (2008) 5116–5118.
[36] Y.P. Sun, B. Zhou, Y. Lin, W. Wang, K.A.S. Fernando, P. Pathak, M.J. Meziani, B.A. Harruff, X. Wang, H.F. Wang, P.J.G. Luo, H. Yang, M.E. Kose, B.L. Chen, L.M. Veca, S.Y. Xie, Quantum-sized carbon dots for bright and colorful photoluminescence, J. Am. Chem. Soc. 128 (2006) 7756–7757.
[37] H. Gonçalves, P.A.S. Jorge, J.R.A. Fernandes, J.C.G. Esteves da Silva, Hg(II) sensing based on functionalized carbon dots obtained by direct laser ablation, Sens. Actuators, B 145 (2010) 702–707.
[38] M. Algarra, M. Pérez-Martín, M. Cifuentes-Rueda, J. Jiménez-Jiménez, J.C.G. Esteves da Silva, T.J. Bandosz, E. Rodríguez-Castellón, J.T. López-Navarrete, J. Casado, Carbon dots obtained using hydrothermal treatment of formaldehyde. Cell imaging in vitro, Nanoscale 6 (2014) 9071–9077.
[39] H. Li, X. He, Y. Liu, H. Huang, S. Lian, S.T. Lee, Z. Kang, One-step ultrasonic synthesis of water-soluble carbon nanoparticles with excellent photoluminescent properties, Carbon 49 (2011) 605–609.
[40] H. Zhu, X.L. Wang, Y.L. Li, Z.J. Wang, F. Yang, X.R. Yang, Microwave synthesis of fluorescent carbon nanoparticles with electrochemiluminescence properties, Chem. Commun. (2009) 5118–5120.
[41] Y. Bae, N. Myung, A.J. Bard, Electrochemistry and electrogenerated chemiluminescence of CdTe nanoparticles, Nano Lett. 4 (2004) 1153–1161.
[42] Z.F. Ding, B.M. Quinn, S.K. Haram, L.E. Pell, B.A. Korgel, A.J. Bard, Electrochemistry and electrogenerated chemiluminescence from silicon nanocrystals quantum dots, Science 296 (2002) 1293–1297.
[43] H. Jiang, H.X. Ju, Electrochemiluminescence sensors for scavengers of hydroxyl radical based on its annihilation in CQDs quantum dots film/peroxide system, Anal. Chem. 79 (2007) 6690–6696.
[44] L. Cao, S.T. Yang, X. Wang, P.G. Luo, J.H. Liu, S. Sahu, Y. Liu, Y.P. Sun, Competitive performance of carbon "quantum" dots in optical bioimaging, Theranostics 2 (2012) 295–301.
[45] X. Qin, W. Lu, G. Chang, Y. Luo, A.M. Asiri, A.O. Al-Youbi, X. Sun, Novel synthesis of Au nanoparticles using fluorescent carbon nitride dots as photocatalyst, Gold Bull. 45 (2012) 61–67.
[46] P. Anilkumar, X. Wang, L. Cao, S. Sahu, J.H. Lui, P. Wang, K. Korch, K.N. Tackett, A. Parezen, Y.P. Sun, Toward quantitatively fluorescent carbon-based "quantum" dots, Nanoscale 3 (2011) 2023–2027.
[47] A. Sachdev, I. Matai, S.U. Matai, S.U. Kumar, B. Bhushan, P. Dubey, P. Gopinath, A novel one-step synthesis of PEG passivated multicolour fluorescent carbon dots for potential biolabeling application, RSC Adv. 3 (2013) 16958–16961.
[48] G. Tong, J. Wang, R. Wang, X. Guo, L. He, F. Qiu, Ge Wang, B. Zhu, X. Zhu, T. Liu, Amorphous carbon dots with high two-photon fluorescence for cellular imaging passivated by hyperbranched poly(amino amine), J. Mater. Chem. B 3 (2015) 700–706.
[49] Q. Wang, X. Liu, L. Zhang, Y. Lv, Microwave-assisted synthesis of carbon nanodots through an eggshell membrane and their fluorescent application, Analyst 137 (2012) 5392–5397.
[50] S.A. Wohlgermuth, R.J. White, M.G. Willinger, M.M. Titirici, M. Antonietti, A one-pot hydrothermal synthesis of sulfur and nitrogen doped carbon aerogels with enhanced electrocatalytic activity in the oxygen reduction reaction, Green Chem. 14 (2012) 1515–1523.

[51] Q. Li, S. Zhang, L. Dai, L.S. Li, Nitrogen-doped colloidal graphene quantum dots and their size-dependent electrocatalytic activity for the oxygen reduction reaction, J. Am. Chem. Soc. 134 (2012) 18932–18935.
[52] Z. Qian, X. Shan, L. Chai, J. Ma, J. Chen, H. Feng, Si-doped carbon quantum dots: a facile and general preparation strategy, bioimaging application, and multifunctional sensor, Appl. Mater. Interf. 6 (2014) 6797–6805.
[53] S. Chandra, P. Patra, S.H. Pathan, S. Roy, S. Mitra, A. Layek, R. Bhar, P. Pramanik, A. Goswami, Luminescent S-doped carbon dots: an emergent architecture for multimodal applications, J. Phys. Chem. B 1 (2013) 2375–2382.
[54] J. Deng, Q. Lu, Y. Hou, M. Liu, H. Li, Y. Zhang, S. Yao, Nanosensor composed of nitrogen-doped carbon dots and gold nanoparticles for highly selective detection of cysteine with multiple signals, Anal. Chem. 87 (2015) 2195–2203.
[55] H. Ding, J.S. Wei, H.M. Xiong, Nitrogen and sulfur co-doped carbon dots with strong blue luminescence, Nanoscale 6 (2014) 13817–13823.
[56] P. Shen, Y. Xia, Synthesis-modification integration: one-step fabrication of boronic acid functionalized carbon dots for fluorescent blood sugar sensing, Anal. Chem. 86 (2014) 5323–5329.
[57] Y. Xu, M. Wu, Y. Liu, X.Z. Feng, X.B. Yin, X.W. He, Y.K. Zhang, Nitrogen-doped carbon dots: a facile and general preparation method, photoluminescence investigation, and imaging applications, Chem. Eur. J. 19 (2013) 2276–2283.
[58] J. Xu, S. Sahu, L. Cao, C.E. Bunker, G. Peng, Y. Liu, K.A. Fernando, P. Wang, E.A. Guliants, M.J. Meziani, H. Qian, Y.P. Sun, Efficient fluorescence quenching in carbon dots by surface-doped metals-disruption of excited state redox processes and mechanistic implications, Langmuir 28 (2012) 16141–16147.
[59] Y. Dong, H. Pang, H.B. Yang, J. Shao, Y. Chi, C.M. Li, T. Yu, Carbon-based dots co-doped with nitrogen and sulfur for high quantum yield and excitation-independent emission, Angew. Chem., Int. Ed. 52 (2013) 7800–7804.
[60] I. Odriozola, I. Loinaz, J. Pomposo, H.J. Grande, Gold–glutathione supramolecular hydrogels, J. Mater. Chem. 17 (2007) 4843–4845.
[61] X. Zhai, P. Zhang, C. Liu, Highly luminescent carbon nanodots by microwave-assisted pyrolysis, Chem. Commun. 48 (2012) 7955–7957.
[62] W. Guan, W. Gu, L. Ye, C. Guo, S. Su, P. Xu, M. Xue, Microwave-assisted polyol synthesis of carbon nitride dots from folic acid for cell imaging, Int. J. Nanomedicine 9 (2014) 5071–5078.
[63] Li Wang †, Y. Yin, A. Jain, H.S. Zhou, Aqueous phase synthesis of highly luminescent, nitrogen-doped carbon dots and their application as bioimaging agents, Langmuir 30 (2014) 14270–14275.
[64] Y. Zheng, D. Yang, X. Wu, H. Yan, Y. Zhao, B. Feng, K. Duan, J. Weng, J. Wang, A facile approach for the synthesis of highly luminescent carbon dots using vitamin-based small organic molecules with benzene ring structure as precursors, RSC Adv. 5 (2015) 90245–90254.
[65] R. Zhang, W. Chen, Nitrogen-doped carbon quantum dots: facile synthesis and application as a "turn-off" fluorescent probe for detection of Hg^{2+} ions, Biosens. Bioelectron. 55 (2014) 83–90.
[66] W. Wang, Y. Li, L. Cheng, Z. Cao, W. Liu, Water-soluble and phosphorus-containing carbon dots with strong green fluorescence for cell labeling, J. Mater. Chem. B 2 (2014) 46–48.
[67] C. Liu, P. Zhang, X. Zhai, F. Tian, W. Li, J. Yang, H. Wang, W. Wang, W. Liu, Nano-carrier for gene delivery and bioimaging based on carbon dots with PEI-passivation enhanced fluorescence, Biomaterials 33 (2012) 3604–3613.
[68] Y. Liu, J. Hu, Y. Li, H.P. Wei, X.S. Li, X.H. Zhang, S.M. Chen, X.Q. Chen, Synthesis of polyethyleneimine capped carbon dots for preconcentration and slurry sampling analysis of trace chromium in environmental water samples, Talanta 134 (2015) 16–23.
[69] Y. Dong, R. Wang, G. Li, C. Chen, Y. Chi, G. Chen, Polyamine-functionalized carbon quantum dots as fluorescent probes for selective and sensitive detection of copper ions, Anal. Chem. 84 (2012) 6220–6224.
[70] K. Sato, J.I. Anzai, Dendrimers in layer-by-layer assemblies: synthesis and applications, Molecules 18 (2013) 8440–8460.
[71] E.M. Ustinova, N.A. Kolpakova, Anodic stripping determination of Pt(IV) based on the anodic oxidation of Cu from the intermetallic phase of Cu_3Pt, Proc. Chem. 10 (2014) 271–274.
[72] E.M. Ustinova, E.V. Gorchakov, N.A. Kolpakova, Anodic stripping determination of Pt(IV) based on the anodic oxidation of In from electrochemically deposited Pt–In alloy phases, J. Solid State Electrochem. 16 (2012) 2455–2458.
[73] I.G. Dominova, N.A. Kolpakova, A.G. Stromberg, Determination of platinum in the presence of mercury film by polarography with accumulation, J. Anal. Chem. 10 (1977) 1980–1983.
[74] L.N. Moskvin, N.M. Yakimova, Determination of trace amounts of Pd(II), Pt(IV), and Ir(IV) chlorocomplexes by capillary electrophoresis with extraction-chromatographic preconcentration, J. Anal. Chem. 70 (2015) 765–769.
[75] N. Steinfeldt, In situ monitoring of Pt nanoparticle formation in ethylene glycol solution by SAXS-Influence of the NaOH to Pt ratio, Langmuir 28 (2012) 13072–13079.
[76] M.D. Hall, G.J. Foran, M.Z.P.J. Beale, T.W. Hambley, XANES determination of the platinum oxidation state distribution in cancer cells treated with platinum(IV) anticancer agents, J. Am. Chem. Soc. 125 (2003) 7524–7525.
[77] J. Malejko, B. Godlewska-Zyłkiewicz, A. Kojło, A novel flow-injection method for the determination of Pt(IV) in environmental samples based on chemiluminescence reaction of lucigenin and biosorption, Talanta 81 (2010) 1719–1724.
[78] W.I. Mortada, M.H. Hassanien, A.A. El-Asmy, Cloud point extraction for the determination of trace amounts of Pt(IV) by graphite furnace atomic absorption spectrometry, Anal. Methods 5 (2013) 530–535.
[79] N.P.G. Roeges, A Guide to the Complete Interpretation of Infrared Spectra of Organic Structures, John Wiley & Sons, England, 1994.
[80] M.S. Dresselhaus, G. Dresselhaus, R. Saito, A. Jorio, Raman spectroscopy of carbon nanotubes, Phys. Rep. 409 (2005) 47–99.
[81] J.F. Moulder, W.F. Stickle, P.E. Sobol, K.D. Bomben, in: Jill Chastain (Ed.), Handbook of X-ray Photoelectron Spectroscopy, Perkin Elmer, Eden Prairie, Minnesota, 1992.
[82] J.M. Lázaro-Martínez, E. Rodriguez-Castellon, D. Vega, G. Monti, A. Chattah, Solid-state studies of the crystalline/amorphous character in linear poly (ethyleneimine hydrochloride) (PEI:HCl) polymers and their copper complexes, Macromolecules 48 (2015) 1115–1125.
[83] E. Gabano, M. Ravera, C. Cassino, S. Bonetti, G. Palmisano, D. Osella, Stepwise assembly of platinum–folic acid conjugates, Inorganica Chim Acta 361 (2008) 1447–1455.
[84] Y. Teow, S. Valiyaveettil, Active targeting of cancer cells using folic acid-conjugated platinum nanoparticles, Nanoscale 2 (2010) 2607–2613.
[85] T. Kapp, A. Dullin, R. Gust, Platinum(II)-dendrimer conjugates: synthesis and investigations on cytotoxicity, cellular distribution, platinum release, DNA, and protein binding, Bioconjug. Chem. 21 (2010) 328–337.
[86] J.R. Lakowicz, Principles of Fluorescence Spectroscopy, third ed., Springer, New York, 2006.
[87] D. Zhao, J. Li, T. Yang, Z. He, "Turn off-on" fluorescent sensor for platinum drugs–DNA interactions based on quantum dots, Biosens. Bioelectron. 15 (2014) 29–35.

6.2 Supplementary Data

Supplementary Information

P-doped Carbon Dots Functionalized with PAMAM Dendrimer for Pt(IV) Detection

Bruno B. Campos, María Moreno Oliva, Enrique Rodriguez-Castellón,
José Jiménez-Jiménez, Rafael Contreras-Cáceres,
Joaquim C.G. Esteves da Silva, Manuel Algarra

Figure ESI 1. TEM images of raw CDs obtained from FA treated with H_3PO_4 (A) and coated with PAMAM-NH_2 dendrimer

A

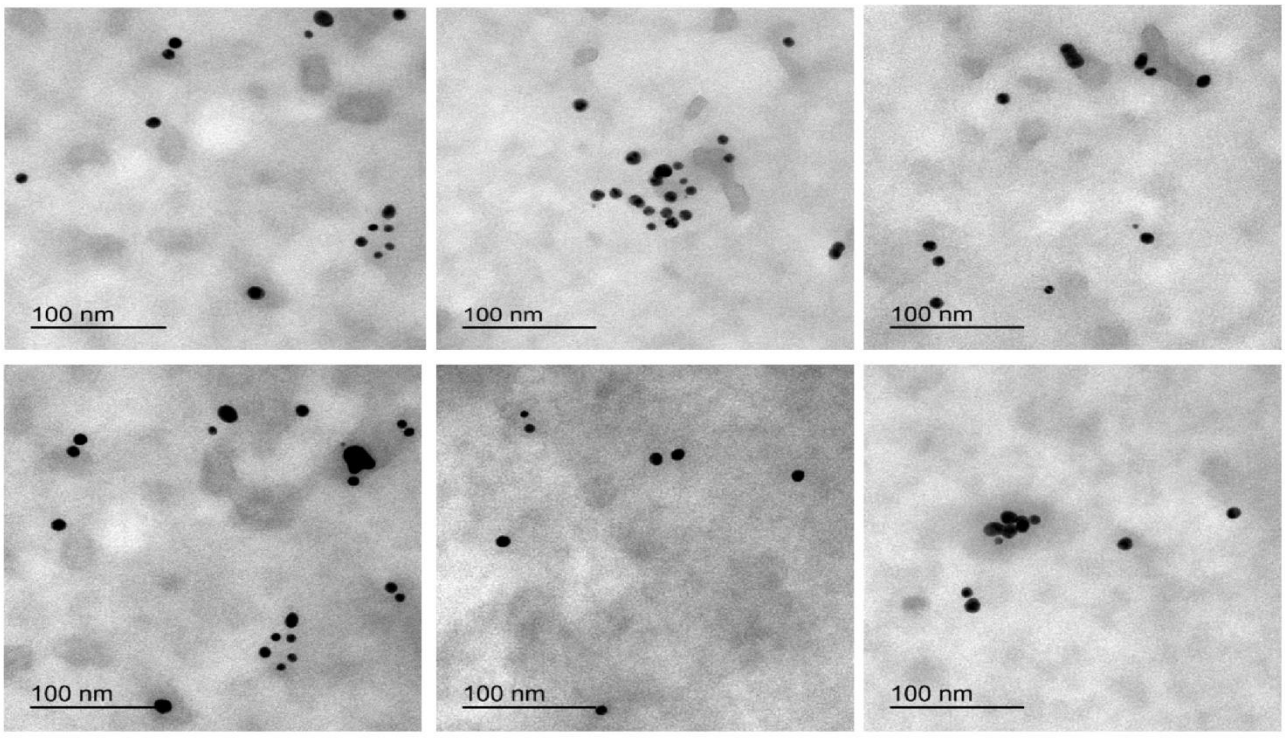

B

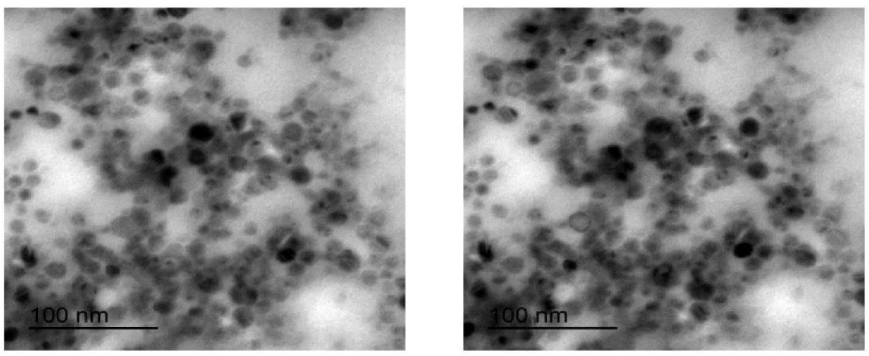

Figure ESI 2. Influence of the ionic strength on the fluorescence intensity of CDs@PAMAM-NH_2

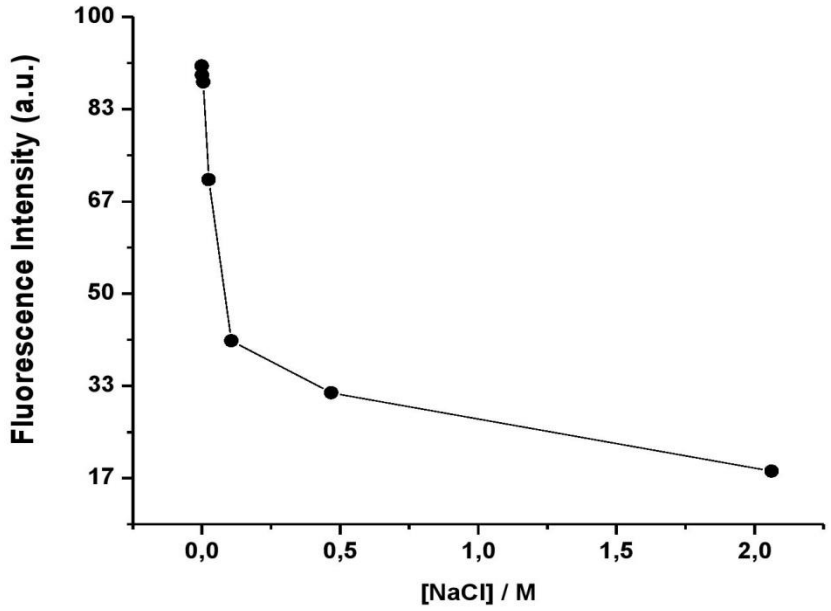

Figure ESI 3. Influence of the pH on the fluorescence intensity of CDs@PAMAM-NH_2. Error comprised of 5% at λ_{em}= 465 nm with λ_{ex}= 360 nm.

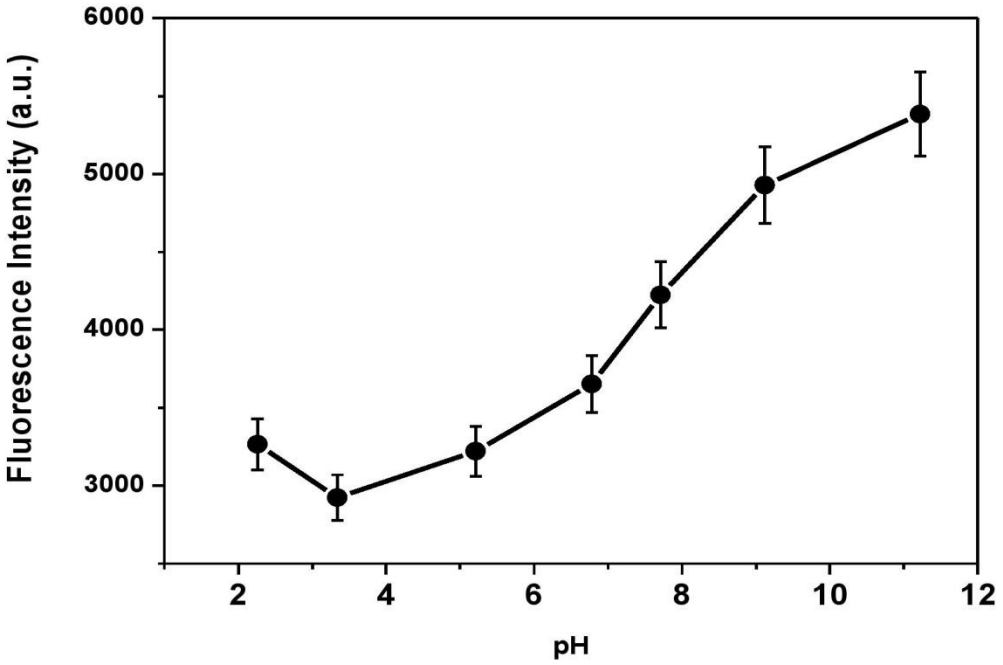

Figure ESI 4. UV Spectra of the different molecules involved in this research

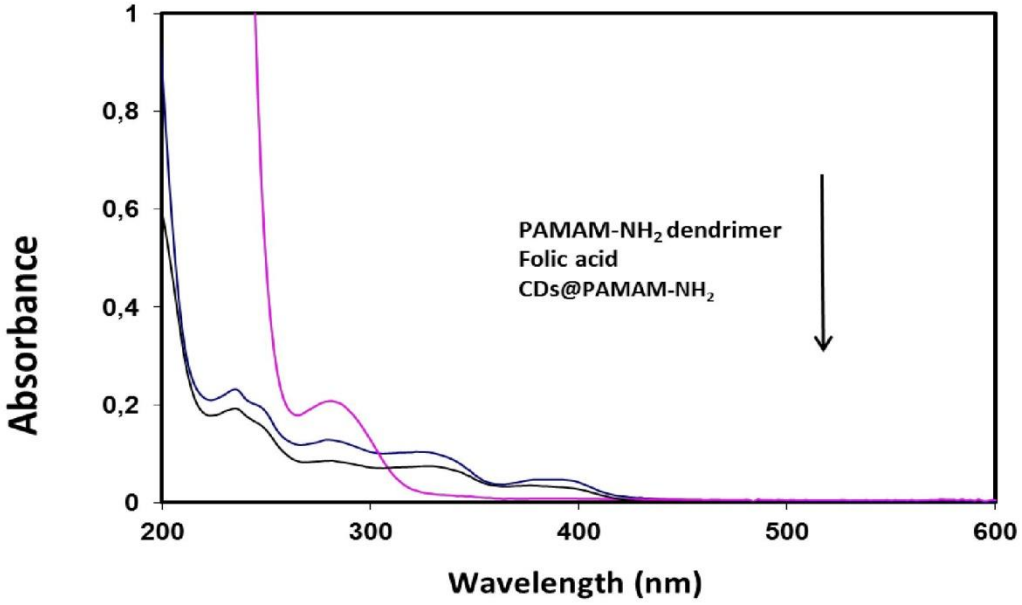

Figure ESI 5. Here is presented the fluorescence spectra at different excitation wavelength, and justified the selection of 360 nm as the best performance of the emission signal for the CDs@PAMAM-NH_2 obtained by this synthesis.

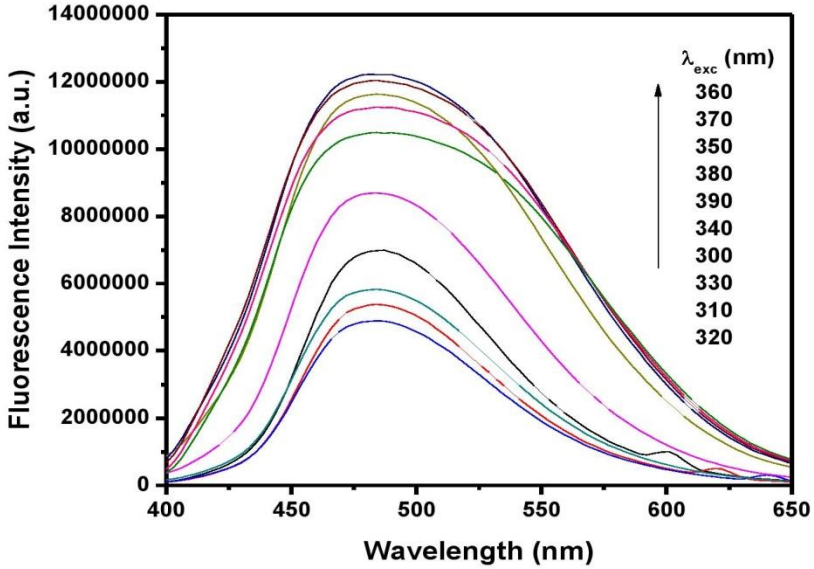

Figure ESI 6. Fluorescence decay of CDs@PAMAM-NH_2 at the different concentrations of metal:

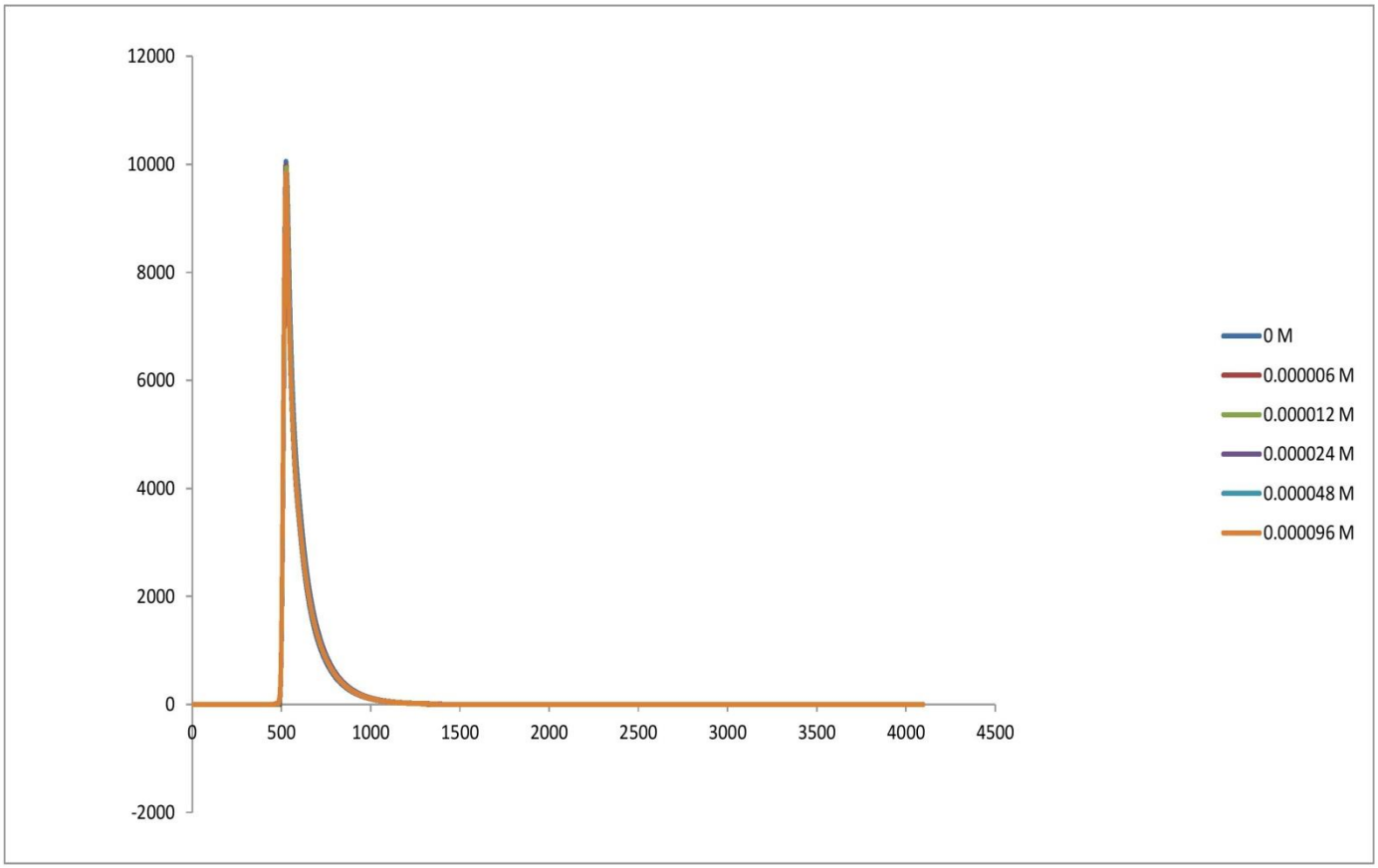

Chapter 7

Carbon Dots as Fluorescent Sensor for Detection of Explosive Nitrocompounds

7.1 Contribution to this Paper

My contribution to this paper included the bibliographic research and writing about carbon QDs, dendrimers and then the experimental planning. The synthesis, purification and functionalization with dendrimers were performed, even all the complementary studies including the effect of some parameters such as pH, ionic strength and the tolerance to explosive nitrocompounds on the excitation/emission matrix. The data obtained by the characterization methods was analyzed and interpreted. The determination of analytical parameters and the application to 4-chloro-2,6-dinitroaniline was also performed and assayed with the fluorescent nanosensor. This paper was submitted as a scientific article and until the acceptation it passes through some adjustments required by the reviewers and under supervision of my advisor Professor Joaquim Esteves da Silva and co-advisor Doutor Manuel Algarra.

Carbon 106 (2016) 171–178

Contents lists available at ScienceDirect

Carbon

journal homepage: www.elsevier.com/locate/carbon

Carbon dots as fluorescent sensor for detection of explosive nitrocompounds

Bruno B. Campos [a], Rafael Contreras-Cáceres [b], Teresa J. Bandosz [c], José Jiménez-Jiménez [d], Enrique Rodríguez-Castellón [d], Joaquim C.G. Esteves da Silva [a], Manuel Algarra [d, *]

[a] Centro de Investigação em Química, Departamento de Química, Faculdade de Ciências da Universidade do Porto, 4169-007, Porto, Portugal
[b] Departamento de Química Orgánica, Facultad de Ciencias, Universidad de Málaga, Campus de Teatinos s/n, 29071, Málaga, Spain
[c] Department of Chemistry and Biochemistry, The City College of New York, 160 Convent Ave, New York, NY, 10031, USA
[d] Departamento de Química Inorgánica, Facultad de Ciencias Universidad de Málaga, Campus de Teatinos s/n, 29071, Málaga, Spain

ARTICLE INFO

Article history:
Received 27 March 2016
Received in revised form
9 May 2016
Accepted 10 May 2016
Available online 11 May 2016

ABSTRACT

Highly and stable fluorescent carbon dots (CQDs), with $\lambda_{ex}/\lambda_{em}$ = 350/465 nm were obtained using a strong acid oxidation of activated carbon in aqueous suspension. The nanoparticles had a mean size of 12 nm and quantum yield of 3.94%. After functionalization with amine groups by PAMAM-NH_2 dendrimer (CQDs@PAMAM-NH_2), the size of particles increased and aggregates of 65 nm were formed. Quantum yield also increased to 6.33%. CQDs were characterized by various analytical techniques including ATR-FTIR, Raman, XPS and fluorescence spectroscopies. The prepared CQDs@PAMAM-NH_2 were used as fluorescent ratiometric nanosensor of 4-chloro-2,6-dinitroaniline, which is a constituent of explosives. As a result of interactions, the fluorescence at 465 nm was quenched. Moreover, a new band at 507 nm emerged and it is linked to a charge transfer and the formation of a Meisenheimer complex. A ratio of fluorescence intensities at 465 and 507 nm (I_{465}/I_{507}) is used for a ratiometric fluorescence sensing. A linear detection ranges from 1.0×10^{-5} to 6.0×10^{-4} M with a detection limit of 2 μM and accuracy of 0.85% as standard relative deviation (RSD, n = 10). The detection accuracy in the presence of other nitrocompounds was 2.80% as RSD.

1. Introduction

Inorganic quantum dots (QDs) have been widely used in various fields ranging from optoelectronics to biosensors because of their unique properties including photo-stability and brightness. Even though the advantages are in the stability and chemical coupling inherent to the colloidal state of QDs [1], the drawback of their applications are in an intrinsic cytotoxicity, mainly attributed to cadmium QDs [2–9]. Therefore, metal free QDs with luminescent properties comparable to those of QDs have received much attention recently [10,11].

Carbon quantum dots (CQDs) are a new class of carbon nanomaterials of 10 nm in diameter which are considered as being able to overcome the restrictions attributed to QDs. They exhibit high water solubility, bright photoluminescence in the visible spectrum, low toxicity, good biocompatibility, high stability and are easy to functionalize [12–14]. The unique properties of CQDs lead to their promising applications in bio-sensing, cellular imaging, drug delivery and catalysis [14]. Inspired by the variety of their usage, there is a growing interest in the synthesis of new carbon dots [15–18]. The photoluminescence of CQDs may be tunable by changing their size, depending on the synthesis method, and by introducing various functional groups at the graphitic sheet edges [19]. So far their photoluminescence mechanism has been explained based on the edge structure, surface defects, doping, and triple ground state of carbene like free zig-zag sites [20], quantum size, and electron-hole recombination [13]. Another interesting property observed in some CQDs is the multi-photon excitation or up-conversion, which is considered as an anti-Stokes transition [21,22].

Synthetic methods used to obtain CQDs are classified into two categories [23]: **i**) Top-down procedures in which graphite powder or multi-walled carbon nanotubes are exposed to harsh physical or chemical conditions such arch discharge, laser ablation, electrochemical methods [24–27] and **ii**) Bottom-up synthetic approaches, where small molecules such as carbohydrates are the

* Corresponding author.
E-mail address: malgarra67@gmail.com (M. Algarra).

http://dx.doi.org/10.1016/j.carbon.2016.05.030
0008-6223/

sources of CQDs by applying external energy as, for instance, ultrasonication, microwave pyrolysis, and heating [28–32]. This leads to materials of diverse properties that make it difficult to understand the mechanism of CQDs luminescence [33].

Strategies for tuning the surface chemistry include a heteroatom doping and functionalization. In the case of the latter approach the edge groups, like carboxyl and hydroxyl groups, are used as reactive sites [34,35]. While carboxyl groups induce non-radiative recombination of electron-hole pairs, the functionalization of CQDs with amine groups decreases surface defects and consequently diminishes the non-radiative recombination process, resulting in a fluorescence enhancement and a photoluminescence blue shift [36] Examples are passivation with polyethylenimine/poly(amino amine), 1,2-ethylenediamine, branched or PAMAM-NH_2 dendrimer [37–42].

The objective of this paper is to introduce a bottom-up synthesis of CQDs, using activated carbon as a precursor. These CQDs are functionalized with PAMAM-NH_2 and used for the detection of 4-chloro-2,6-dinitroaniline, a nitrocompound characteristic to explosives. The detection is based on ratiometric fluorescence method by using the ratio of fluorescence intensities at 465 and 507 nm I_{465}/I_{507}.

2. Experimental

2.1. Chemicals and materials

Activated carbon (100 mesh particle size, powder), polyamidoamine dendrimer-1,12-diaminododecane 4-chloro-2,6-dinitroaniline core generation 4 (PAMAM-$NH_{2,G4}$, solution in methanol 10%), 2,6-dichloro-4-nitroaniline (96%, 2,6DC-4NA), 2,5-dichloro-4-nitroaniline (97%, 2,5DC-4NA), 6-chloro-2,4-dinitroaniline (97%, 6C-2,4DNA) and (98%, 4C-2,6DNA) were purchased from Sigma-Aldrich Spain; sulfuric acid (H_2SO_4, 99.999%), potassium permanganate ($KMnO_4$, >99.0%) and hydrogen peroxide (H_2O_2, 30%, p/v) were purchased from Merck, Darmstadt (Germany). Deionized water with resistivity higher than 4MΩ/cm was used.

2.2. Synthesis, purification and functionalization of carbon dots

Ground activated carbon (200 mg) and $KMnO_4$ (1.2 g) were added to concentrated sulfuric acid (95%, 12 mL) and then the suspension obtained was stirred for 1 h. After this, deionized H_2O (25 mL) was added and the mixture was heated 90 °C for 30 min. This solution was left at room temperature until it reached 60 °C. Then H_2O_2 (2 mL) was added with continuous stirring for 30 min. After centrifugation, ethyl acetate (40 mL) was added to the water suspension of CQDs to purify them. Then the organic phase was evaporated under N_2 and CQDs were re-dissolved in water (20 mL). The pH of this solution was adjusted to 7 with NaOH 1 M. As a next step the dialysis of the solution was carried out versus water. To obtain CQDs@PAMAM-NH_2, same procedure was carried out. Briefly, to CQDs (500 μL) obtained previously, PAMAM-NH_2 dendrimer (10 μL) was added and the solution was stirred for 48 h. To control the functionalization, fluorescence measurements at 465 nm were recorded with excitation at 365 nm.

2.3. Methods

Absorbance was measured on a Hewlett-Packard HP8452A diode array spectrophotometer. Infrared measurements were carried out using a Bruker Equinox 55 FT-IR spectrometer fitted with a Golden Gate single reflection ATR accessory kit from Specac. All spectra were collected using a resolution of 2 cm^{-1} and 50 scans were collected. Raman measurements were carried out on a Senterra dispersive Raman spectrometer (Bruker with 785 nm as excitation. The back Raman scattering was collected with a standard spectral resolution of 3 cm^{-1}, spatial resolution of 0.5 μm, and spot size of about 3 μm. X-ray photoelectron spectroscopic (XPS) studies were performed on a Physical Electronic PHI 5700 spectrometer using non-monochromatic Mg-K_α radiation (300 W, 15 kV and 1253.6 eV) for analyzing the core-level signals of the elements of interest with a hemispherical multichannel detector. The spectra of powdered samples were recorded with a constant pass energy value at 29.35 eV, using a 720 μm diameter circular analysis area. The X-ray photoelectron spectra obtained were analyzed using PHI ACESS ESCA-V6.0F software and processed using MultiPak 8.2B package. The binding energy values were referenced to adventitious carbon C 1s signal (284.8 eV). Shirley-type background and Gauss-Lorentz curves were used to determine the binding energies. Zeta potential measurements (ζ). ζ of CQDs was determined using a Zetasizer Nano ZS (Malvern Instruments, U.K.) equipped with a 4 mW HeNe laser operating at λ = 633 nm ζ measurements were performed at 25 °C in polycarbonate folded capillary cells, with Au plated electrodes (DTS1061). Deionized H_2O was the dispersion medium. The different ζ were automatically obtained by the software, using the Stokes-Einstein and the Henry equation, with the Smoluchowski approximation. Photoluminescence spectrophotometer (Horiba Jovin Yvon Fluoromax 4 TCSPC) was used to characterize CQDs optical performance. The fluorescence was measured in the wavelength range of 300–650 nm. The spectra were obtained with an integration time of 0.1 s and 1 nm slits for excitation and emission. All measurements were performed at room temperature. Fluorescence lifetime analysis was done using an Edinburgh Instruments FLS920, equipped with a Xe lamp (450 W) as excitation source for steady state fluorescence measurements and mono-chromatics LEDs (PicoQuant PLS), controlled by a PDL 880-B system. Fluorescence decays were interpreted in terms of a multi-exponential: $I(t) = A + \Sigma B_i e^{-\tau i}$, where A and B_i are the pre-exponential factors and τ_i the decay times.

2.4. Fluorescence ratiometric determination of 4-chloro-2,6-dinitroaniline

Previous the study of the quenching effect of 4C-2,6DNA, the effects of this and other nitrocompounds were studied by addition of nitrocompounds stock solutions (8×10^{-5} M) to 10 μL of CQDs@PAMAM-NH_2 to the desired concentrations levels in 1 mL quartz cuvette. The mixture was then equilibrated at room temperature for 5 min before the spectral measurements at 465 and 507 nm. To assess the selectivity of this sensor was carried out with related nitrocompounds, such as 2,6DC-4NA, 2,5DC-4NA and 6C-2,4DNA at different 4C-2,6DNA/nitrocompound ratio concentrations (3:1; 1:1; 1:3). Data were obtained by the following relationship:

$$Ratio = \frac{(I_{465}/I_{507})_{GCQDs@PAMAM-NH_2:\ 4C-2,6DNA-Nitrocompound}}{(I_{465}/I_{507})_{GCQDs@PAMAM-NH_2\ :\ 4C-2,6DNA}}$$

where the quotient between the ratios of the fluorescence of the solutions of CQDs@PAMAM-NH_2 with 4C-2,6DNA interacts at I_{465}/I_{507} with the different selected nitrocompounds as interferences (dividend), and without the interference (divider). In other words, the fluorescence at different peaks was recorded and the ratio obtained with this equation.

QY was determined using quinine sulfate Rhodamine as standard, which according literature has a QY of 0.54 in 0.1 M H_2SO_4 (n = 1.38). Both nanoparticles were dissolved in distilled water

(n = 1.33). The integrated area under the fluorescence curves (excitation at 470 nm) was plotted versus the absorbance at 370 nm (after subtraction of the solvent absorbance) for different concentrations. The excitation intensity and slit width were held constant for all measurements. The QY of the CQDs was obtained from:

$$QY_{CQDs} = QY_{st}\left[\frac{(dI/dA)_{CQDs}}{(dI/dA)_{st}}\right]\left(\frac{n^2_{CQDs}}{n^2_{st}}\right)$$

where I is the area under the fluorescence curves and A is the corresponding absorbance [43].

3. Results and discussion

The synthetic route used for the preparation of CQDs from activated carbon is an exhausted oxidation process, which consists of the isolation of the nanostructures and oxidation of their edges. The CQDs obtained are well dispersed and have a uniform size distribution in water. Despite of the general affinity of CQDs to a solvent of a low polarity, the re-dissolution in water at neutral pH was used having in mind CQDs application as a sensor. CQDs exhibit green fluorescence when are irradiated with UV light (365 nm, see Fig S1, in Supplementary Information), however the colour of a purified solution is light brown. The source material, activated carbon was selected due to its low cost, little toxicity and easiness to oxidize [14].

3.1. Characterization of CQDs and CQDs@PAMAM-NH_2

The size and morphology of CQDs and CQDs@PAMAM-NH_2 nanoparticles were characterized by TEM (Fig. 1). TEM images (Fig. 1A, Fig. S2A) show a spherical morphology and narrow size distribution from 7 to 22 nm for CQDs, with a mean value of 12 ± 3.12 nm. The average particle size of the CQDs@PAMAM-NH_2 ranges from 25 to 110 nm due to the formation of spherical aggregates, which, according to the size distribution histogram, have a mean diameter of 65 ± 5.33 nm (Fig. 1B, Fig. S2B).

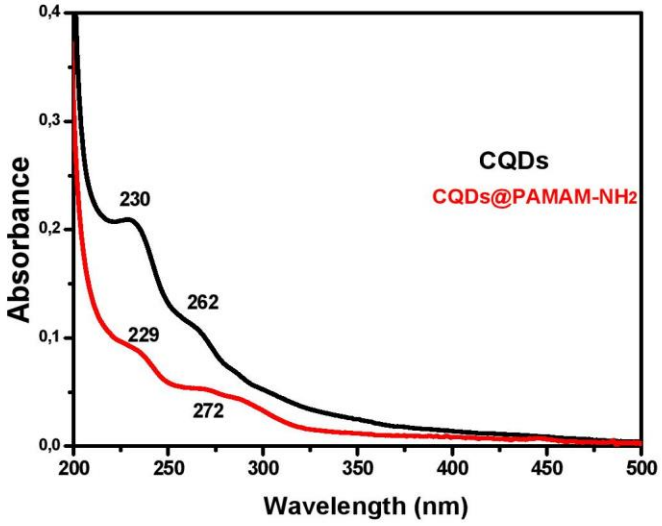

Fig. 2. UV–visible spectra of purified CQDs and functionalized with PAMAM dendrimer (CQDs@PAMAM-NH_2). (A colour version of this figure can be viewed online.)

The optical spectra of purified CQDs and CQDs@PAMAM-NH_2 displayed in Fig. 2 reveal two distinct peaks at 230/229 and 262/272 nm, respectively. They arise due to $\pi \rightarrow \pi^*$, $n \rightarrow \sigma^*$ and $n \rightarrow \pi^*$ transitions associated with C=C and carbonyl/hydroxyl groups, respectively [44]. In CQDs, there are no classical bandgap absorptions, so the surface defect states must be accessed directly from the ground state. Therefore, the trapping of excited state energy

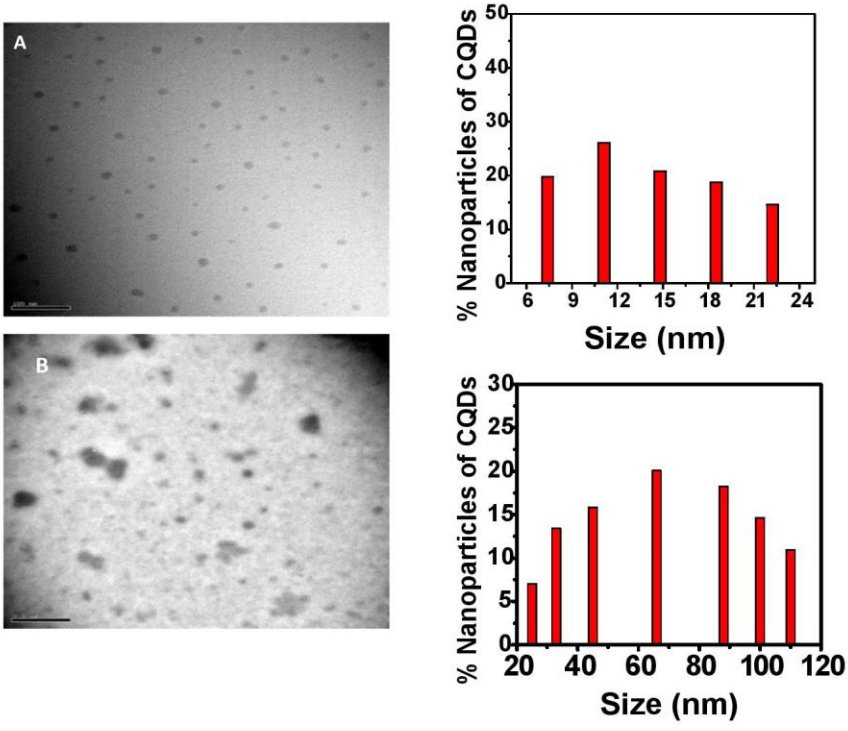

Fig. 1. TEM images of purified (**A**) CQDs and (**B**) functionalized with PAMAM dendrimer CQDs@PAMAM-NH_2. (A colour version of this figure can be viewed online.)

probably occurs between the defects responsible for absorptions and those for emission. One may thus expect a broad distribution of excitations, corresponding to mostly featureless absorption spectra, as those typically observed for CQDs [45].

ATR-FTIR spectra of CQDs and coated with PAMAM-NH_2 counterpart (Fig. S3) reveal bands at 1677 and 1743 cm^{-1}, respectively. They represent carbonyls (C═O) and their presence is supported by the bands ascribed to C–OH at 1211 cm^{-1} (CQDs), and the band at 1373 cm^{-1} observed only for CQDs@PAMAM-NH_2. The band centered at 1077 cm^{-1} is ascribed to the overlapping of C–H deformations and stretching vibrations of C–O (ether) and C–C. A very broad and intense band at 3327 cm^{-1} and the band centered at 1071 cm^{-1} represent the stretching vibrations and in-plane bending vibration of –OH, respectively. The N–H stretching vibrations occur near 3300–3500 cm^{-1} and they overlap with the –OH stretching band. The emerging band at 1633 cm^{-1} on the spectra for CQDs@PAMAM-NH_2 indicates the presence of amide from PAMAM-NH_2 dendrimer. The 785 nm laser wavelength Raman spectra of CQDs (Fig. S4), show a strong feature at 989 cm^{-1}, related to the vibration of sp^2 bonded carbon atoms in a two dimensional hexagonal lattice of graphite structure. It is interesting that on the Raman spectra G (1600 cm^{-1}) and D (1300-1350 cm^{-1}) bands typical for carbon materials do not appear.

The negative ζ of CQDs nanoparticles (−18.50 mV) is due to the presence of deprotonated carboxyl groups on the nanoparticles surface. The negative ζ value is linked to the oxidation effect of the sulfuric acid, which results in carboxylic acids as main functional groups.

The surface composition of CQDs obtained from activated carbon was evaluated using XPS (Fig. S5.) These results indicate that our CQDs are composed, of C, O, N, Na, Si, Cl and S, and their atomic concentrations % is shown in Table 1. The presence of Na, Si, Cl is likely related to the ash content in the parent carbon and the synthesis procedure.

The C 1*s* core level spectrum (Fig. 3A) can be decomposed into three contributions, corresponding to C–C at a binding energy of 284.8 eV (77%), O–C═O at 287.3 eV (5%) and π→π* at 291.0 eV (18%). The O 1*s* signal is decomposed into two contributions (Fig. 3B) with binding energy at 530.2 (C═O) and 531.7 (C–O) eV [46]. After the incorporation of the dendrimer, the same elements are found on the surface but the surface chemical composition changes (see Table 1). As expected, a clear increase of in the C and N content is visible due to the incorporation of the dendrimer molecules containing nitrogen in its functional groups. The C 1*s* core energy level spectrum of sample CQDs@PAMAM-NH_2 (Fig. 3C) is also deconvoluted into three components, corresponding to C–C at a binding energy of 284.8 eV, (72%), O–C═O at 287.0 eV (16%) and π→π* at 290.7 eV (12%). The contribution at 287.0 eV increases due to the presence of amide groups. The N 1*s* core energy level spectrum is asymmetric (Fig. 3D) and is deconvoluted into two contributions at 398.4 eV (81%) and 399.9. eV (19%) assigned to amide and amine groups, respectively [47].

Fig. 4A shows the room temperature fluorescence spectra of the CQDs and CQDs@PAMAM-NH_2, excited at 350 nm. As seen, the modification of CQDs with PAMAM-NH_2 dendrimer resulted in a significant increase (2 fold) in the fluorescence intensity. This indicates a protective effect of the dendrimer on the surface of the CQDs nanoparticles on the surroundings. It decreases the radiative effect from the excited state by increasing the fluorescence intensity. The fluorescence quantum yields (QY) of CQDs and CQDs@PAMAM-NH_2 were determined to be 3.94 and 6.93%, respectively. The N atoms in PAMAM dendrimer, and especially N-doping precursors and as surface passivating agents for CQDs. Their presence results in the enhanced fluorescence intensity and increases QY with an increase in N content [48].

Table 1
Surface chemical composition of CQDs and CQDs@PAMAM-NH_2 (in at. %).

	C	O	N	Na	S
CQDs	47.35	29.86	2.25	7.66	6.47
CQDs@PAMAM-NH_2	55.48	25.53	6.50	6.10	4.83

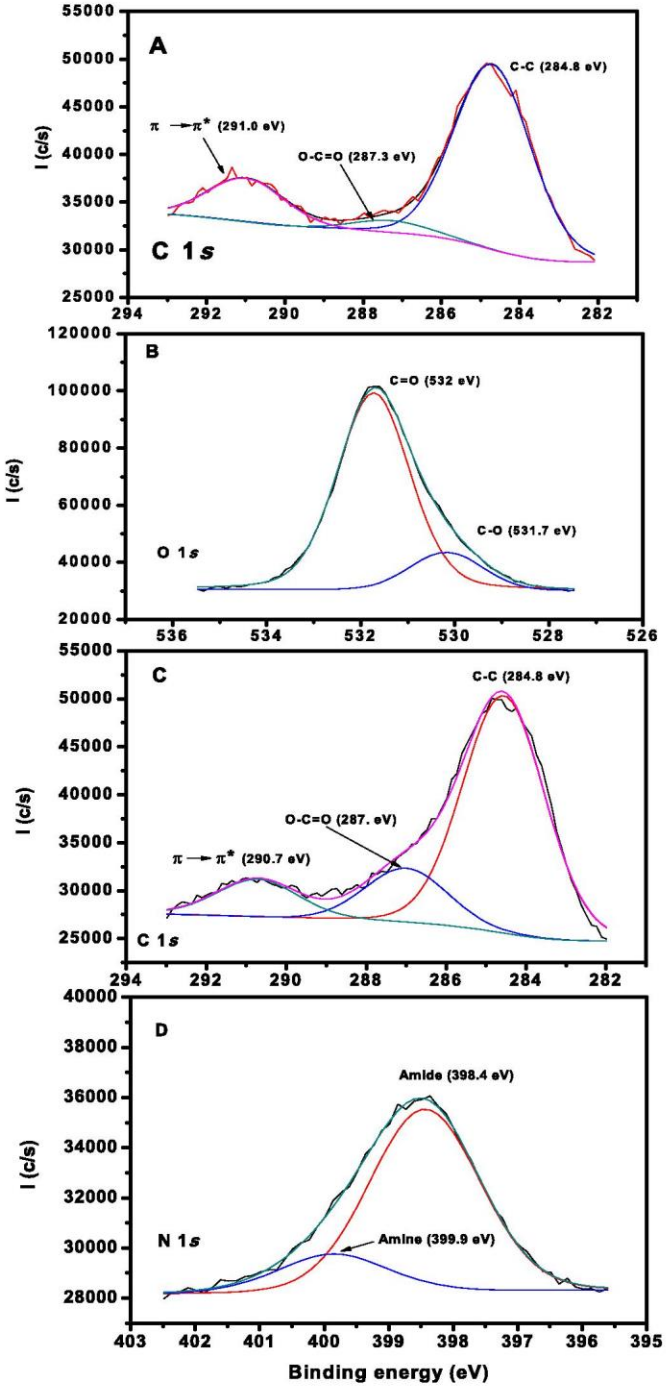

Fig. 3. **A**) and **B**) C 1*s*, and O 1*s* core level spectra of CQDs synthesized from activated carbon. **C**) and **D**) C 1*s* and N 1*s* core level spectra of CQDs@PAMAM-NH_2. (A colour version of this figure can be viewed online.)

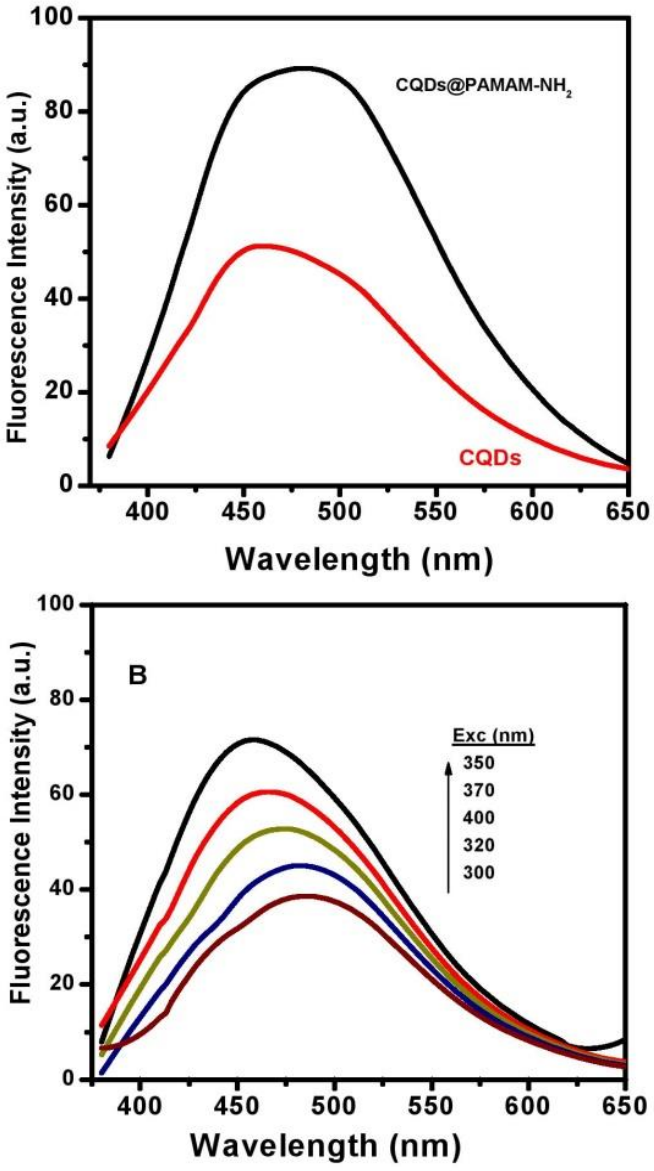

Fig. 4. A) Fluorescence spectra of CQDs and CQDs@PAMAM-NH_2 with excitation at 350 nm). **B)** Fluorescence spectra of CQDs@PAMAM-NH_2 when excited at different wavelength. (A colour version of this figure can be viewed online.)

To further explore the optical properties of CQDs@PAMAM-NH_2, a detailed fluorescence study was carried out under various excitation wavelengths. As shown in Fig. 4B, when the excitation wavelength increases from 300 to 400 nm, the emission peak gradually blue-shifts to shorter wavelengths. Its intensity increases, which indicates an existence of different surface energy traps of CQDs@PAMAM-NH_2 than those in CQDs. They emit at 465 nm when excited at 350 nm. Consequently, the fluorescence dependence on the excitation wavelength cannot be ascribed to CQDs@PAMAM-NH_2 of different sizes. Therefore, the presence of various functional groups (C═O, C—OH, and C—N) on the CQDs@PAMAM-NH_2 could be responsible for at least 2 different emissive sites with different energy levels, as justified by the study of the fluorescence decay. This overall complexity behavior of the emission spectra is apparently associated with the variety of emission centers present in CQDs@PAMAM-NH_2.

The fluorescent lifetimes for CQDs and CQDs@PAMAM-NH_2 were calculated. The fluorescent decay curve was fitted to two exponential decay models. Table 2 shows the fluorescence lifetime parameters (A, Bi and τ_i) and the fit (χ^2) values. A short fluorescence lifetime (1.17 ns/1.01 ns) is similar to that of QDs, and reveals the radiative recombination nature of excitations [49]. The average fluorescence lifetimes of CQDs and CQDs@PAMAM-NH_2 are in the nanosecond range and they indicate that both CQDs and CQDs@PAMAM-NH_2 are suitable for sensor applications, because they are not susceptible to changes in an excitation light intensity, to photo-bleaching, and to variations in light scattering and absorption by the sample [50]. The fluorescence spectra (peak at 465 nm and intensity) were considered as unchanged for 6 months, when stored at 4° C, within the experimental errors. The effect of pH (2.5–11) on the fluorescence intensity of CQDs@PAMAM-NH_2 was studied (Fig. 5). With an increasing pH starting from 2.25, the fluorescence intensity increases drastically (~60%) and become constant from pH 6. We linked this trend to the buffering effect of the surface groups (—COOH and —NH_2 mainly). This is another important feature indicating the suitability of these materials for sensing applications.

3.2. *CQDs@PAMAM-NH_2 as fluorescent sensors of nitroaromatic compounds*

To evaluate the feasibility of quenching-based nitro compound detection, and thus the application of our CQDs for sensing of explosives, the interactions of CQDs@PAMAM-NH_2 with target compounds were first evaluated. Fig. 6A shows the effect of the nitroaromatic compounds, 4C-2,6DNA, 6C-2,4DNA, 2,5DC-4NA and 2,6DC-4NA on the fluorescence spectra of CQDs@PAMAM-NH_2 nanoparticles. The results show that these species quench the fluorescence in a marked way. It is interesting that the addition of 4C-2,6DNA quenched the fluorescence of CQDs@PAMAM-NH_2 differently that did the other three compounds and on the spectra a unique emission band at 507 nm emerges at the expense of the decrease intensity of the band at 465 nm. On other hand, the two shoulders of the emission bands at 465 and 507 nm decreased at different ratios because of the presence of 4C-2,6DNA that quenches the emission. Fig. 6B presents the correlation between the intensity ratios of the emission at 465 nm to that at 507 nm (I_{465}/I_{507}). Based on the results collected, 4C-2,6DNA was selected as a detection target owing to its presence in explosives as a powerful initiator [51] and due to its highest toxicity among all four species tested.

The quenching of CQDs@PAMAM-NH_2 fluorescence by 4C-2,6DNA was rapid and sensitive to the presence of the target molecule, even at a very low concentration. After 1 h exposure the fluorescence intensity remained stable. A charge transfer process could be a possible mechanism for the CQDs@PAMAM-NH_2 fluorescence quenching by 4C-2,6DNA. Since the maximum absorption band of 4C-2,6DNA centers at 440 nm in aqueous media [52], it overlaps with the emission band of CQDs@PAMAM-NH_2, giving rise to an energy transfer process. These results in the formation of a

Table 2
Fluorescence lifetime for CQDs and CQDs@PAMAM-NH_2.

	CQDs	CQDs@PAMAM-NH_2
A	3.021	1.496
B_1	0.063	0.064
B_2	0.0087	0.0074
τ_1 (ns)	1.174 (60.95%)	1.011 (64.93%)
τ_2 (ns)	5.403 (39.1%)	4.758 (35.07%)
χ^2	1.294	1.093

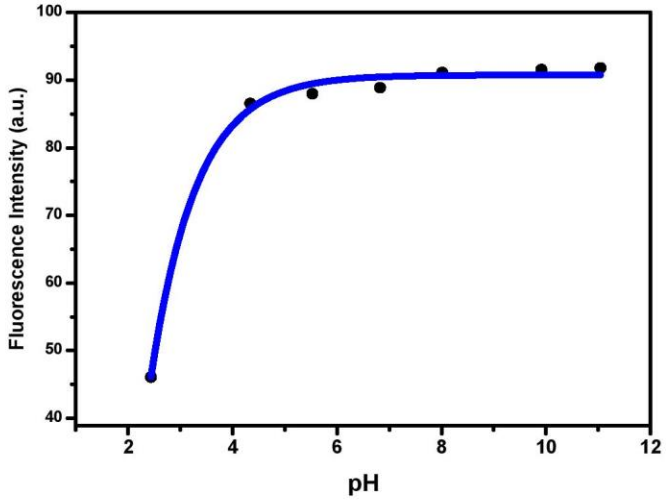

Fig. 5. Influence of the pH on the fluorescence intensity of CQDs@PAMAM-NH_2 with excitation at 350 nm. (A colour version of this figure can be viewed online.)

complex in which the negative charge is delocalized over the cyclohexadienine ring and the nitro group and the positive charge is distributed over an iminium group, known as Meisenheimer complex (Fig. 7) [53]. The formation of such complex with amino groups is typical for of nitroaromatic compounds. In our case, the amine groups of PAMAM-NH_2 dendrimer contribute to this complexation [54]. The two electron-withdrawing nitro groups in 4C-2,6DNA enable the aniline ring to be electron-poor donating, but enough to form a stable complex, which is observed at 507 nm.

Under the optimum conditions determined in our experimental procedure, the Stern-Volmer formalism indicates that there is a linear relationship between the change in the fluorescence intensity at 465 nm and the concentration of 4C-2,6DNA over the range 1.0×10^{-5}–6.0×10^{-4} M,($I_F = 1 + 23108$ [4C-2,6DNA] with $r = 0.994$) with a $K_{SV} = 23108\ M^{-1}$ (inset Fig. 6B). The results collected in Table 3 suggest that a static mechanism is predominant in the quenching of the fluorescence intensity of CQDs@PAMAM-NH_2 by 4C-2,6DNA. In the case of pure static quenching the lifetime is unaffected by the presence of quencher and a plot of $\tau 0/\tau$ versus [Q] is expected to give a linear relationship. Results collected in Table 3 follow this pattern [55].

Calculated detection (LOD) and sensitivity limits of 4C-2,6DNA are 2.57 and 111.6 μM, respectively. The repeatability, expressed as standard relative deviation (RSD, n = 10) was 0.85% at the concentration level of 10 μM of 4C-2,6DNA. When unmodified CQDs, without functionalization with PAMAM-NH_2 dendrimer, were used a LOD and sensitivity limits of 5.19 μM and 27.0 μM, respectively, were obtained with RSD = 1.65%. Thus the presence of the dendrimer in the system improves the analytical signal. These differences demonstrate the feasibility of the proposed functionalization of CQDs for the detection of explosives.

Systems based in fluorescence spectroscopy to detect TNT or DNT at 30 and 40.7 μM, using molecularly imprinting polymer, have been addressed in the literature [56]. For this purpose functionalized ZnS-Mn nanoparticles [57] or CdSe coated with PAMAM-NH_2 [58] were used. The detection sensitivity was 1 nM or 0.01 ppm, respectively, A hybrid capped mesoporous material, which was selectively opened in the presence of Tetryl and TNT, has been synthesized and used for the fluorogenic recognition at ppm range [59]. TNT has been also quantified electrochemically using CQDs as electrode on the level of nM. Nevertheless, when CQDs was used as

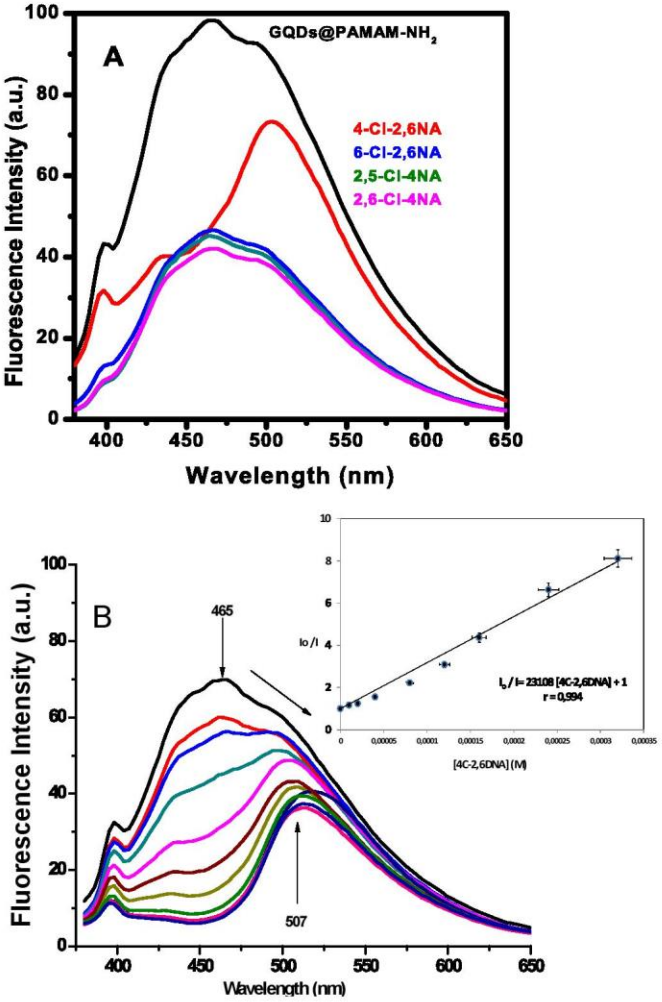

Fig. 6. A) Effect of nitroaromatic compounds (8×10^{-5} M) on the fluorescence spectrum of the CQDs@PAMAM-NH_2. **B**) Influence of the [4C-2,6DNA] on the fluorescence spectra of CQDs@PAMAM-NH_2 (10 mL in 1 final volume: **a**) 0 M, **b**) 1×10^{-5} M, **c**) 2×10^{-5} M, **d**) 4×10^{-5} M, **e**) 8×10^{-5} M, **f**) 1.2×10^{-4} M, **g**) 1.6×10^{-4} M, **h**) 2.4×10^{-4} M,**i**) 3.2×10^{-4} and **j**) 6×10^{-4} M (Inset Stern-Volmer model). (A colour version of this figure can be viewed online.)

a fluorescence sensor the detection level was in μM range [60].

To assess the possibility of the analytical application of our nanosensor CQDs in terms of its sensitivity, the effect of different concentration ratios of several nitrocompounds (2,6DC-4NA, 2,5DC-4NA and 6C-2,4DNA) to that of 4C-2,6DNA (8.0×10^{-5} M), on the fluorescence intensity of CQDs@PAMAM-NH_2 was studied. The fluorescence intensities of CQDs@PAMAM-NH_2, at different concentration ratios (3:1; 1:1 and 1:3) were measured in separate sets of experiments and the results are summarized in Table 4 and (Fig S6). Recoveries are the quantities observed value obtained using an analytical procedure that involves a calibration graph [61]. 4C-2,6DNA shows recoveries between 100 and 117% and an accuracy as between 1.0 and 2.8% as RSD. The proposed method demonstrates its feasibility of the CQDs@PAMAM-NH_2 nanoparticle application as 4C-2,6DNA sensor.

The results presented in this study indicate that the fluorescent-CQDs@PAMAM-NH_2 CQDs are a feasible medium for detecting explosives. They show the high sensitivity and selectivity for the specific nitrocompounds detection. Sensing is based on a marked quenching in the fluorescence signal.

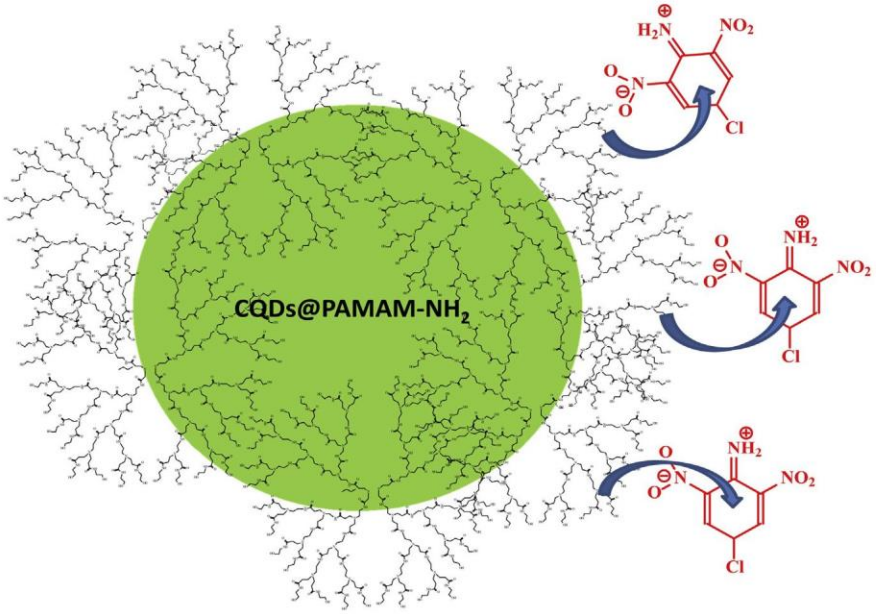

Fig. 7. Possible charge transfer mechanism of CQDs@PAMAM-NH_2 in presence of 4C-2,6DNA. (A colour version of this figure can be viewed online.)

Table 3
Lifetime intensity decays of CQDs@PAMAM-NH_2 nanoparticles in H_2O in the presence of 4C-2,6DNA.

4C-2,6DNA (M)	τ (ns)
0	3.09
1.0×10^{-5}	3.31
2.0×10^{-5}	3.30
4.0×10^{-5}	3.60
8.0×10^{-5}	3.25
1.2×10^{-4}	4.08

Table 4
Interferences of other related nitrocompounds on the determination of the 4C-2,6DNA (8.0×10^{-5} M), expressed in recoveries (%) for n =3.[a]

Recovery (%)			
	3:1	1:1	1:3
6C-2,4DNA	101.9 (1.03)	105.9 (1.35)	117.8 (2.46)
2,5DC-4NA	100.5 (1.22)	116.5 (1.96)	104.0 (2.67)
2,6DC-4NA	104.1 (1.66)	104.0 (2.67)	102.8 (2.03)

[a] In parenthesis the standard deviation.

4. Conclusions

In summary, a novel approach for the fluorimetric sensing of nitroaromatic explosives using carbon quantum dots coated with PAMAM-NH_2 dendrimer nanoparticles has been reported. The presence of the explosive 4C-2,6DNA in an aqueous solution was detected at a low concentration based on the change of a fluorescence signal as a result of CQDs-target molecule interactions. In particular, the functionalization of the external surface with the PAMAM-NH_2 dendrimer, and its interactions with electron-deficient groups of the explosive 4C-2,6DNA (to enhance or tune selectivity), which lead to the strong signal, make this approach appealing for the potential sensing applications.

Acknowledgements

Authors are gratefully to Grant SFRH/BD/84318/2012 to FCT (Lisbon, Portugal). Portugal), and Economy and Competitiveness Ministry (CTQ 2015-68951-C3-3-R), Junta de Andalucía (P12-RNM 1565) and FEDER funds (project CTQ2016).

Appendix A. Supplementary data

Supplementary data related to this article can be found at http://dx.doi.org/10.1016/j.carbon.2016.05.030.

References

[1] C.B. Murray, C.R. Kagan, M.G. Bawendi, Synthesis and characterization of monodisperse nanocrystals and close packed nanocrystal assemblies, Annu. Rev. Mater. Res. 30 (2011) 545–610.
[2] W.J. Parak, R. Boudreau, M. Le Gros, D. Gerion, D. Zanchet, C.M. Micheel, S.C. Williams, A.P. Alivisatos, C. Larabell, C. Larabell, Cell motility and metastatic potential studies based on quantum dot imaging of phagokinetic tracks, Adv. Mater. 14 (2002) 882–885.
[3] I.L. Medintz, H.T. Uyeda, E.R. Goldma, H. Mattoussi, Quantum dot bioconjugates for imaging, labeling and sensing, Nat. Mater. 4 (2005) 435–446.
[4] X. Michalet, F.F. Pinaud, L.A. Bentolila, J.M. Tsay, Li JJ. Doose, G. Sundaresan, A.M. Wu, S.S. Gambhir, S. Weiss, Quantum dots for live cells, in vivo imaging, and diagnostics, Science 307 (2005) 538–544.
[5] U. Resch-Genger, M. Grabolle, S. Cavaliere-Jaricot, R. Nitschke, T. Nann, Quantum dots versus organic dyes as fluorescent labels, Nat. Methods 5 (2008) 763–775.
[6] V. Gupta, N. Chaudhary, R. Srivastava, G.D. Sharma, R. Bhardwaj, S. Chand, Luminescent graphene quantum dots for organic photovoltaic devices, J. Am. Chem. Soc. 133 (2011) 9960–9963.
[7] K. Hoshino, A. Gopal, M.S. Glaz, B. Vanden, A. David, X. Zhang, Nanoscale fluorescence imaging with quantum dot near-field electroluminescence, Appl. Phys. Lett. 101 (2012) 043118.
[8] G. Vastola, Y.W. Zhang, V.B. Shenoy, Experiments and modelling of alloying in self-assembled quantum dots, Curr. Op. Solid State Mater. Sci. 16 (2012) 64–70.
[9] J. Zhao, M. Holmes, A. Michael, F.E. Osterloh, Quantum confinement controls photocatalysis: a free energy analysis for photocatalytic proton reduction at CdSe nanocrystals, ACS Nano 7 (2013) 4316–4325.
[10] M. Algarra, M. Pérez-Martín, M. Cifuentes-Rueda, J. Jiménez-Jiménez, J.C.G. Esteves da Silva, T.J. Bandosz, E. Rodríguez-Castellón, J.T. López-Navarrete, J. Casado, Carbon dots obtained using hydrothermal treatment of formaldehyde. Cell imaging in vitro, Nanoscale 6 (2014) 9071–9077.
[11] B.B. Campos, M. Algarra, B. Alonso, C.M. Casado, J. Jimenez-Jimenez,

E. Rodríguez-Castellon, J.C.G. Esteves da Silva, Fluorescent sensor for Cr(VI) based in functionalized silicon quantum dots with dendrimers, Talanta 144 (2015) 862–867.
[12] X. Xu, R. Ray, Y.L. Gu, H.J. Ploehn, L. Gearheart, K. Raker, W. Scrivens, Electrophoretic analysis and purification of fluorescent single-walled carbon nanotube fragments, J. Am. Chem. Soc. 126 (2004) 12736–12737.
[13] J.C.G. Esteves da Silva, H.M.R. Goncalves, Analytical and bioanalytical applications of carbon dots, TRAC-Trends Anal. Chem. 30 (2011) 1327–1336.
[14] H. Li, Z. Zang, Y. Liu, S.T. Lee, Carbon nanodots: synthesis, properties and applications, J. Mater. Chem. 22 (2012) 24230–24253.
[15] Y. Wang, A. Hu, Carbon quantum dots: synthesis, properties and applications, J. Mater. Chem. C 2 (2014) 6921–6939.
[16] S.Y. Lim, W. Shen, Z. Gao, Carbon quantum dots and their applications, Chem. Soc. Rev. 41 (2015) 362–381.
[17] S. Chandra, P. Patra, S.H. Pathan, S. Roy, S. Mitra, A. Layek, R. Bhar, P. Pramanik, D.A. Goswami, Luminescent S-doped carbon dots: an emergent architecture for multimodal applications, J. Mater. Chem. B 18 (2013) 2375–2382.
[18] X. Zhang, Y. Zhang, Y. Wang, S. Kalytchuk, S.V. Kershaw, Y. Wang, P. Wang, T. Zhang, Y. Zhao, H. Zhang, T. Cui, Y. Wang, J. Zhao, W.W. Yu, A.L. Rogach, Color-switchable electroluminescence of carbon dot light-emitting diodes, ACS Nano 7 (2013) 11234–11241.
[19] M.A. Sk, A. Ananthanarayanan, L. Huang, K.H. Lim, P. Chen, Revealing the tunable photoluminescence properties of graphene quantum dots, J. Mater. Chem. C 2 (2014) 6954–6960.
[20] J. Peng, W. Gao, B.K. Gupta, Z. Liu, R. Romero-Aburto, L.H. Ge, L. Song, L.B. Alemany, X.B. Zhan, G.H. Gao, S.A. Vithayathil, B.A. Kaipparettu, A.A. Marti, T. Hayashi, J.J. Zhu, P.M. Ajayan, Graphene quantum dots derived from carbon fibers, Nano Lett. 12 (2012) 844–849.
[21] J. Zhou, Q. Liu, W. Feng, Y. Sun, F. Li, Upconversion luminescent materials: advances and applications, Chem. Rev. 115 (2015) 395–465.
[22] G. Chen, H. Qiu, P.N. Prasad, X. Chen, Upconversion nanoparticles: design, nanochemistry, and applications in theranostics, Chem. Rev. 114 (2014) 5161–5214.
[23] Y. Wang, A. Hu, Carbon quantum dots: synthesis, properties and applications, J. Mater. Chem. C 2 (2014) 6921–6939.
[24] Q.L. Zhao, Z.L. Zhang, B.H. Huang, J. Peng, M. Zhang, D.W. Pang, Facile preparation of low cytotoxicity fluorescent carbon nanocrystals by electrooxidation of graphite, Chem. Comm. 41 (2008) 5116–5118.
[25] M. Bottini, C. Balasubramanian, M.I. Dawson, A. Bergamaschi, S. Bellucci, T. Mustelin, Isolation and characterization of fluorescent nanoparticles from pristine and oxidized electric arc-produced single-walled carbon nanotubes, J. Phys. Chem. B 110 (2006) 831–836.
[26] R. Prathik, P.C. Chen, A.P. Periasamy, Y.N. Chen, H.T. Chang, Photoluminescent carbon nanodots: synthesis, physicochemical properties and analytical applications, Mater. Today 18 (2015) 447–458.
[27] L. Zheng, Y. Chi, Y. Dong, J. Lin, B. Wang, Electrochemiluminescence of water-soluble carbon nanocrystals released electrochemically from graphite, J. Am. Chem. Soc. 131 (2009) 4564–4565.
[28] X.M. Wei, Y. xu, Y. Hao, X.B. Yin, X.W. Hea, Ultrafast synthesis of nitrogen-doped carbon dots via neutralization heat for bioimaging and sensing applications, RSC Adv. 4 (2014) 44504–44508.
[29] C. López, M. Zougagh, M. Algarra, E. Rodríguez-Castellón, B.B. Campos, J.C.G. Esteves da Silva, J.J. Jiménez-Jiménez, A. Ríos, Microwave-assisted synthesis of carbon dots and its potential as analysis of four heterocyclic aromatic amines, Talanta 132 (2015) 845–850.
[30] M. Algarra, B.B. Campos, K. Radotić, D. Mutavdžić, T.J. Bandosz, J. Jiménez-Jiménez, E. Rodríguez-Castellón, J.C.G. Esteves da Silva, Luminescent carbon nanoparticles: effects of chemical functionalization, and evaluation of Ag+ sensing properties, J. Mater. Chem. A 2 (2014) 8342–8351.
[31] H. Li, X. He, Y. Liu, H. Huang, S. Lian, S.T. Lee, Z. Kang, One-step ultrasonic synthesis of water-soluble carbon nanoparticles with excellent photoluminescent properties, Carbon 49 (2011) 605–609.
[32] Z.F. Ding, B.M. Quinn, S.K. Haram, L.E. Pell, B.A. Korgel, A.J. Bard, Electrochemistry and electrogenerated chemiluminescence from silicon nanocrystals quantum dots, Science 296 (2002) 1293–1297.
[33] N. Fuyuno, D. Kozawa, Y. Miyauchi, S. Mouri, R. Kitaura, H. Shinohara, T. Yasuda, Komatsu, K. Matsuda, Drastic change in photoluminescence properties of graphene quantum dots by chromatographic separation, Adv. Opt. Mater. 2 (2014) 983–989.
[34] A. Sachdev, I. Matai, S.U. Kumar, B. Bhushan, P. Dubey, P. Gopinat, A Novel One-step Synthesis of PEG Passivated Multicolour Fluorescent Carbon Dots for Potential Biolabeling Application, 3, 2013, pp. 16958–16961.
[35] R.J. Fana, Q. Suna, L. Zhanga, Y. Zhangb, A.H. Lu, Photoluminescent carbon dots directly derived from polyethylene glycol and their application for cellular imaging, Carbon 71 (2014) 87–93.
[36] S.L. Hu, K.Y. Niu, J. Sun, J. Yang, N.Q. Zhao, X.W. Du, One-step synthesis of fluorescent carbon nanoparticles by laser irradiation, J. Mater. Chem. 19 (2009) 484–488.
[37] B.B. Campos, M. Moreno-Oliva, R. Contreras-Cáceres, E. Rodríguez-Castellón, J. Jiménez-Jiménez, J.C.G. Esteves da Silva, M. Algarra, Carbon dots on based folic acid coated with PAMAM dendrimer as platform for Pt(IV) detection, J. Coll. Interf. Sci. 65 (2016) 165–173.
[38] Y. Dong, R. Wang, H. Li, Chi Y. Shao, X. Lin, G. Chen, Polyamine-functionalized carbon quantum dot Js for chemical sensing, Carbon 50 (2012) 2810–2815.
[39] Y. Liu, J. Hu, Y. Li, H.P. Wei, X.S. Li, X.H. Zhang, S.M. Chen, X.Q. Chen, Synthesis of polyethyleneimine capped carbon dots for preconcentration and slurry sampling analysis of trace chromium in environmental water samples, Talanta 134 (2015) 16–23.
[40] Y. Dong, R. Wang, G. Li, C. Chen, Y. Chi, G. Chen, Polyamine-functionalized carbon quantum dots as fluorescent probes for selective and sensitive detection of copper ions, Anal. Chem. 84 (2012) 6220–6224.
[41] K. Sato, J.J. Anzai, Dendrimers in layer-by-layer assemblies: synthesis and applications, Molecules 18 (2013) 8440–8460.
[42] B. Pan, D. Cui, P. Xu, C. Ozkan, G. Feng, M. Ozkan, T. Huang, B. Chu, Q. Li, R. He, G. Hu, Synthesis and characterization of polyamidoamine dendrimer-coated multi-walled carbon nanotubes and their application in gene delivery systems, Nanotech. 20 (2009) 125101.
[43] A.M. Brouwer, Standards for photoluminescence quantum yield measurements in solution (IUPAC technical report), Pure Appl. Chem. 83 (2011) 2213–2228.
[44] S. Pandey, A. Mewada, G. Oza, M. Thakur, N. Mishra, Sharon, M. Sharon, Synthesis and centrifugal separation of fluorescent carbon dots at room temperature, Nanosci. Nanotech. 5 (2013) 775–779.
[45] R. Liu, D. Wu, S. Liu, K. Koynov, W. Knoll, Q. Li, An aqueous route to multicolor photoluminescent carbon dots using silica spheres as carriers, Angew. Chem. 121 (2009) 4668–4671.
[46] J.F. Moulder, W.F. Stickle, P.E. Sobol, K.D. Bomben, Handbook of X-ray Photoelectron Spectroscopy, Perkin-Elmer Corp, Eden Prairie, MN, 1992.
[47] G. Zorn, L.H. Liu, L. Árnadóttir, H. Wang, L.J. Gamble, D.G. Castner, M. Yan, X-ray photoelectron spectroscopy investigation of the nitrogen species in photoactive perfluorophenylazide-modified surfaces, J. Phys. Chem. C Nanomater. Interface 118 (2014) 376–383.
[48] K. Dimos, Carbon quantum dots: surface passivation and functionalization, Curr. Org. Chem. 20 (2016) 682–695.
[49] K. Kúsová, I. Pelant, J. Valenta, Bright trions in direct-bandgap silicon nanocrystals revealed by low-temperature single-nanocrystal spectroscopy Light, Sci. Appl. 4 (2012) 1–8 e336.
[50] H. Szmacinski, J.R. Lakowicz, Lifetime-based sensing, in: J.R. Lakowicz (Ed.), Topics in Fluorescence Spectroscopy: v. 4 Probe Design and Chemical Sensing, Plenum Press, New York, 1994, p. 295.
[51] Bretherick's Handbook of Reactive Chemical Hazards, fourth ed., Butterworth & Co Publishers, UK, 1990.
[52] M. Jefraim, J. Donald, R. Hartter, A critical Re-evaluation of the Hammett acidity function at moderate and high acid concentrations of sulfuric acid. New H_0 values based Solely on a set of primary aniline indicators, J. Am. Chem. Soc. 85 (1963) 878–883.
[53] Y. Niu, L. Sun, R.M. Crooks, Determination of the intrinsic proton binding constants for poly(amidoamine) dendrimers via potentiometric pH titration, Macromolecules 36 (2003) 5725–5731.
[54] S. Hughes, S.S.R. Dasary, S. Begum, N. Williams, H. Yu, Meisenheimer complex between 2,4,6-trinitrotoluene and 3-aminopropyltriethoxysilane and its use for a paper based sensor, Sens. Bio Sens. Res. 5 (2015) 37–41.
[55] J.R. Lakowicz, Principles of Fluorescence Spectroscopy, Plenum Press, New York, 1983.
[56] R.C. Stringer, S. Gangopadhyay, S.A. Grant, Detection of nitroaromatic explosives using a fluorescent-labeled imprinted polymer, Anal. Chem. 82 (2010) 4015–4019.
[57] R. Tu, B. Liu, Z. Wang, D. Gao, F. Wang, Q. Fang, Z. Zhang, Amine-capped ZnS-Mn^{2+} nanocrystals for fluorescence detection of trace TNT explosive, Anal. Chem. 80 (2008) 3458–3465.
[58] M. Algarra, B.B. Campos, M.S. Miranda, J.C.G. Esteves da Silva, CdSe quantum dots capped PAMAM dendrimer nanocomposites for sensing nitroaromatic compounds, Talanta 83 (2011) 1335–1340.
[59] Y. Salinas-Soler, A. Agostini, E. Pérez-Esteve, R. Martínez-Máñez, F. Sancenón, M.D. Marcos, J. Soto, A.M. Costero, S. Gila, M. Parra, P. Amorós, Fluorogenic detection of Tetryl and TNT explosives using nanoscopic-capped mesoporous hybrid materials, J. Mater. Chem. A 1 (2013) 3561–3564.
[60] L. Zhang, Y. Han, J. Zhu, Y. Zhai, S. Dong, Graphene nanoribbon-supported PtPd concave nanocubes for electrochemical detection of TNT with high sensitivity and selectivity, Anal. Chem. 87 (2015) 2033–2036.
[61] D.T. Burns, K. Danzer, A. Townshend, Use of the term "recovery" and "apparent recovery" in analytical procedures (IUPAC Recommendations 2002), Pure Appl. Chem. 74 (2002) 2201–2205.

7.2 Supplementary Data

Carbon Dots as Fluorescent Sensor for Detection of Explosive Nitrocompounds

Bruno B. Campos, Rafael Contreras-Cáceres, Teresa J. Bandosz, Enrique Rodríguez-Castellón, Joaquim C.G. Esteves da Silva, Manuel Algarra

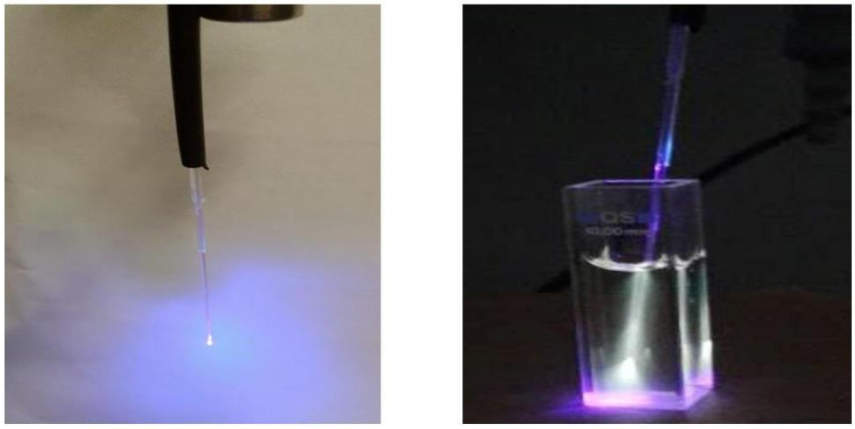

Fgure S1. Fluorescence emission under UV light

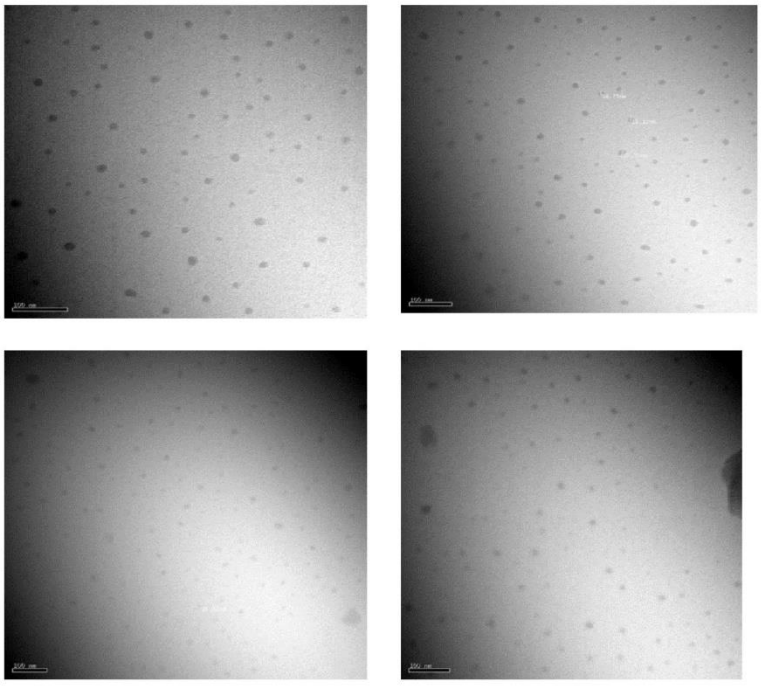

Figure S3A. TEM images obtained for CQDs to obtain the size histogram distribution

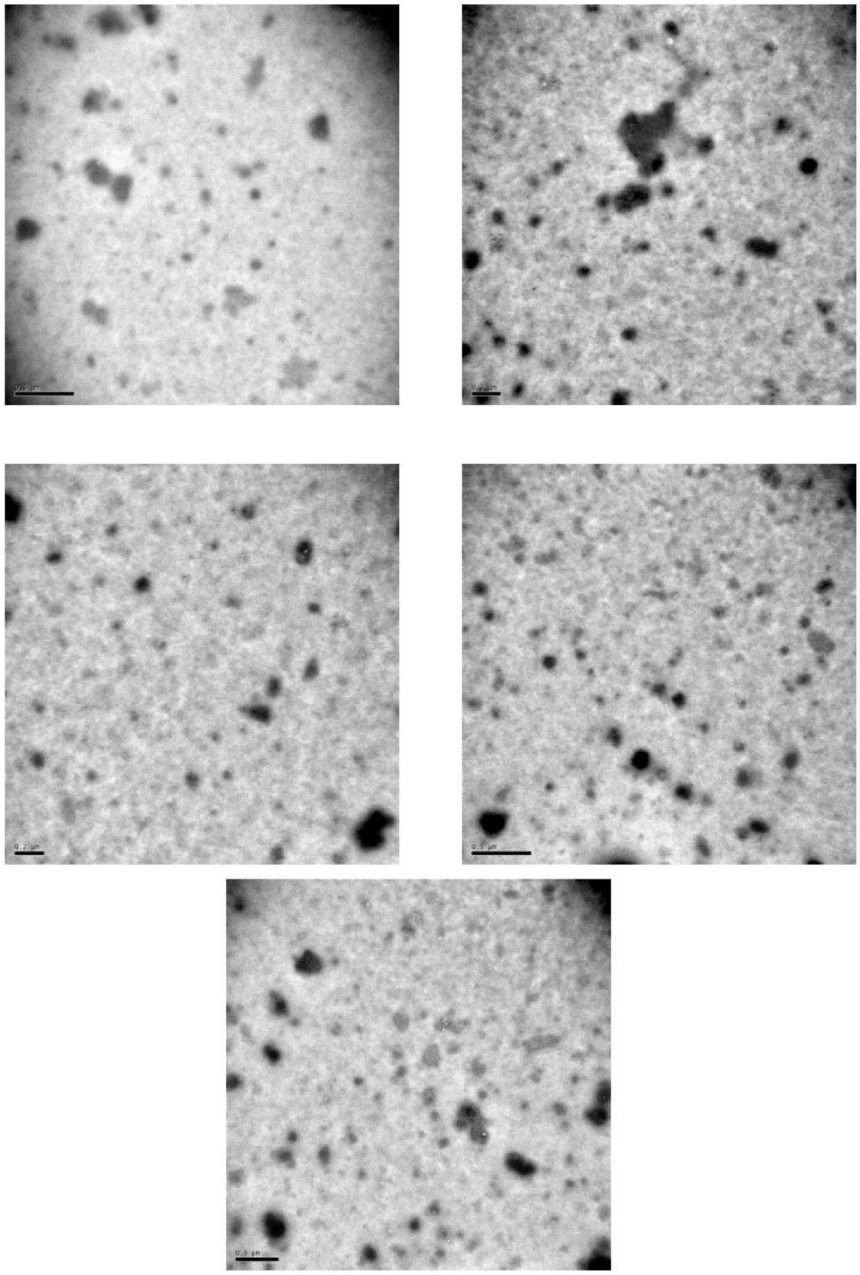

Figure S3B. TEM images obtained for and CQDs@PAMAM-NH_2 to obtain the size histogram distribution

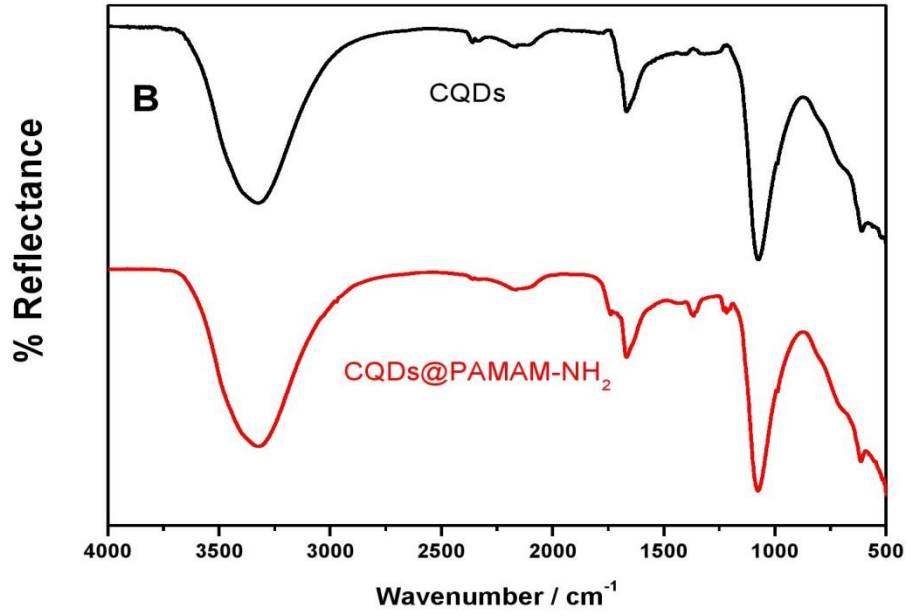

Figure S3. ATR-FTIR spectra of purified CQDs and functionalized with PAMAM dendrimer (CQDs@PAMAM-NH_2)

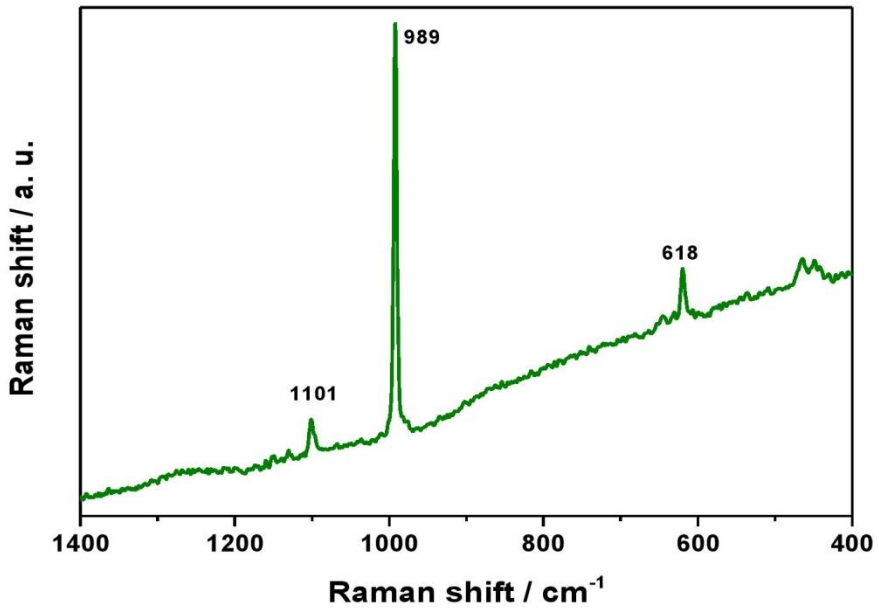

Figure S4. Raman spectra corresponding to CQDs from activated carbon and

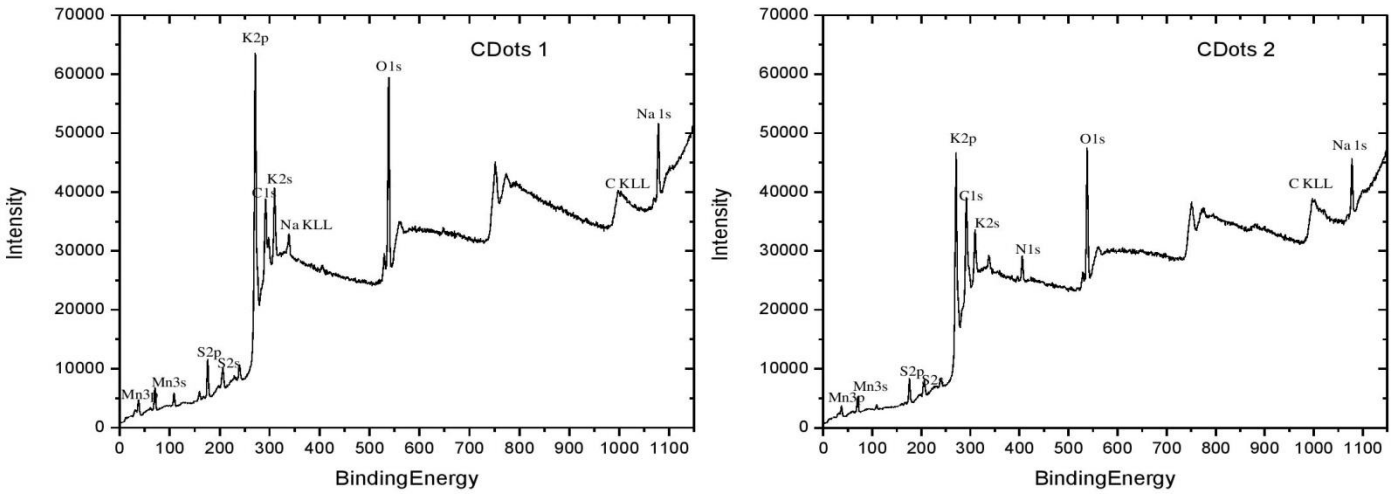

Figure S5. XPS survey scan corresponding to **A**) CQDs from activated carbon and **B**) CQDs@PAMAM-NH_2

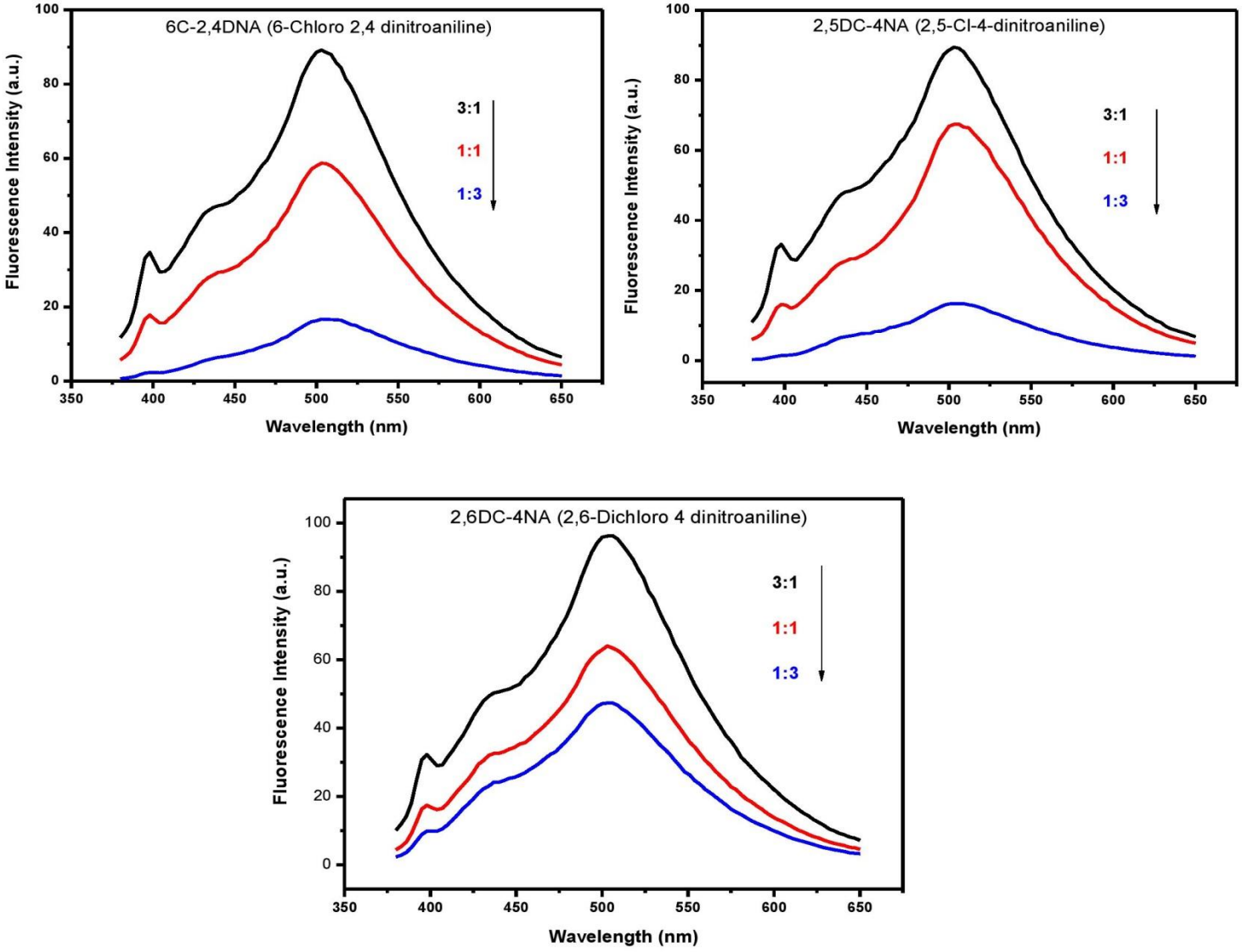

Figure S6. Fluorescence spectra of CQDs@PAMAM-NH_2 when mixed 4C-2,6DNA with other nitrocompounds, at different ratios concentrations. In figures the ratios is showed as (4C-2,6DNA : Other Nitrocompound)

Chapter 8

Fluorescent Sensor for Cr(VI) Based in Functionalized Silicon Quantum Dots with Dendrimers

8.1 Contribution to this Paper

My contribution to this paper included the bibliographic research and writing about silicon QDs, dendrimers and then the experimental planning. The synthesis, purification and functionalization with dendrimers were performed, even all the complementary studies including the effect of some parameters such as pH, ionic strength and the tolerance to some ions on the excitation/emission matrix. The data obtained by the characterization methods was analyzed and interpreted. The determination of analytical parameters and the application to real samples was also performed by collecting real samples *in situ* and assayed with the fluorescent nanosensor. This paper was submitted as a scientific article and until the acceptation it passes through some adjustments required by the reviewers and under supervision of my advisor Professor Joaquim Esteves da Silva and co-advisor Doutor Manuel Algarra.

Talanta 144 (2015) 862–867

Contents lists available at ScienceDirect

Talanta

journal homepage: www.elsevier.com/locate/talanta

Fluorescent sensor for Cr(VI) based in functionalized silicon quantum dots with dendrimers ☆

B.B. Campos [a], M. Algarra [b,*], B. Alonso [c], C.M. Casado [c], J. Jiménez-Jiménez [b], E. Rodríguez-Castellón [b], J.C.G. Esteves da Silva [a]

[a] Centro de Investigação em Q uímica, Departamento de Química e Bioquímica, Faculdade de Ciências da Universidade do Porto, Porto, Portugal
[b] Departamento de Química Inorgánica, Facultad de Ciencias, Universidad de Málaga, Campus de Teatinos s/n, 29071 Málaga, Spain
[c] Departamento de Química Inorgánica, Universidad Autónoma de Madrid, Cantoblanco 28049, Madrid, Spain

ARTICLE INFO

Article history:
Received 18 April 2015
Received in revised form
5 July 2015
Accepted 12 July 2015
Available online 15 July 2015

Keywords:
Silicon dots
Dendrimers
Fluorescent sensors
Chromate

ABSTRACT

Highly luminescent nanoparticles based in Silicon quantum dots, coated by hydroxyl PAMAM dendrimer (PAMAM-OH) of 5th generation, were obtained by one step process by hydrothermal treatment of 3-Aminopropyl)triethoxysilane (APTES) in aqueous solution. Previous to the optimization of the synthesis procedure, different dendritic molecules of 5th generation were tested to obtain the most intense fluorescence signal. The influence of different parameters such ratio APTES/PAMAM-OH, pH and ionic strength on the fluorescence intensity was studied. The fluorescence spectra showed maximum excitation and emission wavelengths at 370 and 446 nm, respectively. The obtained silicon nanoparticles (SiQDs@PAMAM-OH) were characterized by TEM, DLS and XPS, and were found to detect selectively Cr (VI) in aqueous solutions at 2.7 μM level of detection, sensitivity of 0.2 μM with a RSD of 0.16% ($n=10$). To study the feasibility of the proposed system for Cr(VI) detection, it was tested in real electrochemical solution bath and a tanning effluent obtained from electrochemical industry and with two certified waters, demonstrating promising outcomes as nano-sensor.

1. Introduction

Research in quantum dots (QDs) devices dates back to the late 1980s, and new routes and raw materials of synthesis and applications have been developed over the last years [1–4]. So far, Cd*X* (*X*=Te, S and Se) are the most investigated QDs due to their excellent optical and electrochemical properties [5]. Major optical features of QDs include broad absorption spectrum, size-dependent emission spectrum, long fluorescence lifetime, high quantum yield and high stability against photobleaching [6]. QDs have therefore found potential applications in a range of technological fields, including optoelectronic devices, solar cells and fluorescent labeling agents in biomedicine [7]. Later, with the demand for more biocompatible QDs, cadmium-free QDs were introduced, such as silicon QDs (SiQDs), carbon dots, and graphene QDs [8–12]. The strongest advantage of Si QDs lies in their good biocompatibility, at least 10 times safer than Cd-based QDs under UV irradiation, [13] SiQDs are fluorescent zero-dimensional silicon nanoparticles, [10] ranging from 1 to 10 nm in diameter [14,15], resistant to photobleaching [16,17] and a tunable quantum confinement [18] controlled by the surface functionalization [19].

The synthesis of SiQDs nanoparticles is based on the synthesis of the bulk Si–H nanoparticles followed by its coating, by means of the two well-known bottom-up and top down methodologies [15]. The common bottom-up approaches are driven by chemical reactions developed from precursors with final reduction treatments [20,21], decompositions based in laser induced pyrolysis [22] or plasma induced thermolysis [23,24]. The usual top-down approaches may include physical methods, as the laser ablation [25,26], ball-milling [27,28] and chemical catalyzed etching [29,30].

Just a few studies related to water-soluble SiQDs synthesis are found in the literature. These synthesis yield Si–H bonds in the surface being susceptible of degradation by oxidative processes in aqueous media, therefore its surface stabilization is necessary to preserve their optical properties [31-33]. The most used methods for this stabilization are based in hydrosilation/polymerization reactions catalyzed by thermal or UV processes, or reactions with alkene terminal groups [34–36]. Other methods are based in the direct functionalization using the Zintl salt, a method to obtain by direct reaction of nucleophilic groups with NaSi, MgSi or KSi, which are strong electrophilic systems [37].

In view of the above mentioned issues, we present an

☆Presented in VII Workshop in Analytical Nanoscience and Nanotechnology, Salamanca (Spain), July 6-8. 2015.

* Corresponding author. Fax: +34 952132000.
E-mail address: malgarra67@gmail.com (M. Algarra).

http://dx.doi.org/10.1016/j.talanta.2015.07.038
0039-9140/

alternative pathway to obtain functionalized SiQDs, inspired in our previous experience with CdSe and ZnS:Mn QDs coated by different dendrimers which achieved results with C-Reactive Protein and Cd(II), respectively [38,39]. Hydroxyl terminated poly(amidoamine) dendrimer (PAMAM-OH) is one of the most used dendrimers with high adsorption capacity for some anions, as chromate, arsenate or phosphate [40]. This high affinity for chromate anions presents a huge advance in the retention and determination of a hazard pollutant which is strongly oxidizing and carcinogenic, leading to pulmonary and skin diseases [41]. The environmental available chromate occurs in nature by the trace mineral crocoite but the majority is discharged by chemical, metallurgical and refractory industries related to tanning, corrosion inhibition, electroplating, glassware-cleaning solutions, wood preservatives, stainless steel welding, pigments, leather tanning and metal finishing [42,43].

In this paper a high fluorescent and water soluble nano-sensor based in SiQDs coated with PAMAM-OH dendrimer which is selective and sensitive to Cr(VI) is reported. This SiQDs dendrimer passivated nano-sensor is the first nanomaterial synthesized using a passivating dendrimer strategy for SiQDs.

2. Experimental

2.1. Chemicals

(3-Aminopropyl)triethoxysilane (99%, APTES) and hydroxyl-terminated 5th generation poly(amidoamine) dendrimer (PAMAM-$OH_{G=5}$) in methanol, were purchased from Sigma-Aldrich Química S.A. (Spain), and used as received without further purification. 5th generation thiolate poly(propyleneimine) dendrimer (S-$DAB_{G=5}$) [44] and 4th generation cobaltocenium poly (propyleneimine) dendrimer (Cob-$DAB_{G=4}$) [45,46] were synthesized according literature procedures. Certified reference materials SRM 1643d (trace elements in water) and SRM 1640 (trace elements in natural water) from NIST, USA, containing 18.53 ± 0.20 μg L^{-1} and 38.6 ± 1.6 μg Kg^{-1} of total chromium, respectively, were analyzed and also used for recovery experiments. All solutions were prepared using Millipore water that had a resistivity greater than 18.8 MΩ cm.

2.2. Functionalized SiQDs with PAMAM-OH dendrimer (SiQDs@PAMAM-OH)

Functionalized SiQDs nanoparticles were obtained as follows: 100 μL of APTES were mixed with 100 μL of PAMAM-OH dendrimer in 800 μL of H_2O in a Teflon-lined stainless-steel autoclave reactor, which was set for 3 h at 200 °C. Finally, the highly blue fluorescent solution was dialyzed against H_2O for 1 h to obtain SiQDs@PAMAM-OH.

2.3. Characterization methods and data analysis

The morphology was analyzed by transmission electron microscopy (TEM) and examined under a Philips CM-200 (SCAI-UMA). The fluorescence measurements were carried out with a Jovin Yvon Fluoromax 4 TCSPC (Horiba), and measured between 400 and 700 nm using an integration time of 0.1 s and 5 nm slits for excitation and emission. X-ray photoelectron spectroscopy (XPS) studies were performed on a Physical Electronic PHI 5700 spectrometer using non-monochromatic Mg-Kα radiation (300 W, 15 kV, 1253.6 eV) for analyzing the core-level signals of the elements of interest with a hemispherical multichannel detector. The spectra of powdered samples were recorded with a constant pass energy value at 29.35 eV, using a 720 μm diameter circular analysis area. The X-ray photoelectron spectra obtained were analyzed using the PHI ACESS ESCA-V6.0 F software and processed using Multipak 8.2B package. The binding energy values were referenced to adventitious carbon C 1*s* signal (284.8 eV). Shirley-type background and Gauss–Lorentz curves were used to determine the binding energies.

2.4. Metal study

Before the quenching effect of Chromate (Cr(VI)), the presence of the species Zn(II), Cd(II), Ni(II), Tl(I), Sb(III), Pt(II), Pb(II), MnO_{4-}, Cu(II), Fe(II), Fe(III), Hg(II), Cr(III), Co(II), CN^-, Al(III) and Ag(I) in the solution, in separate experiments of the different metals, 0.25 mM were added to 500 μL of SiQDs@PAMAM-OH to the desired concentrations levels in 1 mL of volume, filled up by H_2O. The solution mixture was then equilibrated at room temperature for 5 min before the spectral measurements at 440 nm.

2.5. Sewage samples

Wastewater from an electroplating industry (Progaelectric S.A. situated in Montilla, Cordoba (Spain)) was used to test the efficiency of SiQDs@PAMAM-OH as sensor probe for Cr(VI). A water sample from tanning effluent of the mentioned industrial activity was collected to be analyzed.

3. Results and discussion

3.1. SiQDs coated by PAMAM-OH dendrimer

A novel approach was developed to obtain fluorescent silicon nanoparticles, following a bottom-up synthesis procedure. From the direct use of APTES, by means of a solvothermal process, provided us functionalized SiQDs nanoparticles with PAMAM-OH dendrimer of ~7 nm in one step as showed in the TEM image (Fig. 1). In supplementary information is showed the emission under UV light (Fig. SI.1)

Until now, APTES was used as coating agent of different substrates, to enhance the formation of multiple bonds [47]. In order to obtain fluorescent SiQDs with high fluorescence intensity

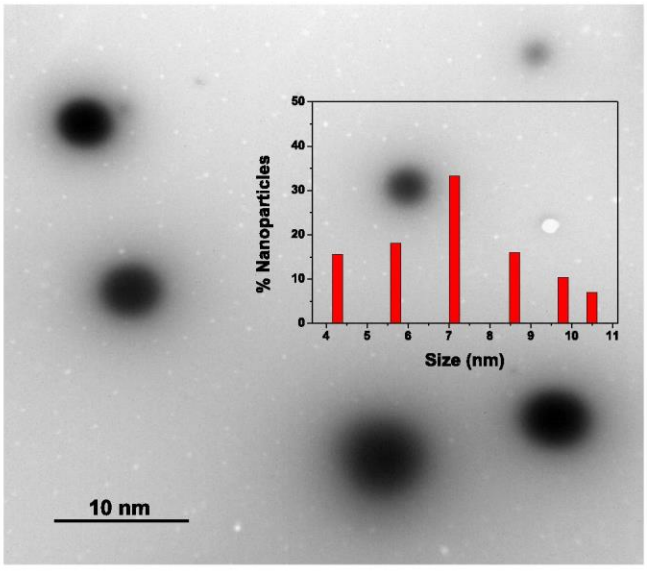

Fig. 1. TEM image of SiQDs@PAMAM-OH obtained hydrothermally from APTES at 200 °C.

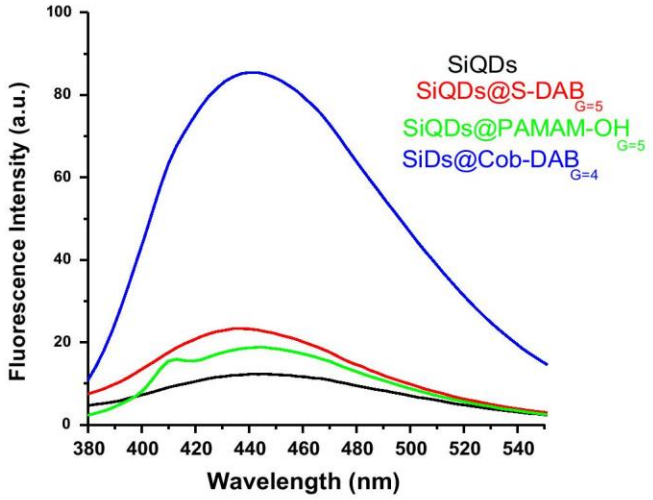

Fig. 2. Emission spectra of SiQDs functionalized with different dendrimers.

different parameters were studied such as (v/v), the passivation agents and the reaction time, with a particularity that all reactions were done by hydrothermal process at 200 °C. Maintaining the volume of APTES constant (100 μL), setting up the time reaction for 1 h and increasing APTES/PAMAM-OH ratio PAMAM-OH volume (20, 60 and 100 μL), the optical properties of raw SiQDs changed significantly when the proportion (APTES:PAMAM-OH) reached a 1:1 value with a fluorescence increasing of ~1.50 times upper with a blue shift emission of ~12 nm (shifting from 449 to 437 nm) (Fig. SI.2).

Once founded the best ratio between the silicon source and dendrimer, the influence of others passivation agents dendrimer based, with 1:1 ratio, such as thiolated poly(propyleneimine) dendrimer generation 5 (S-$DAB_{G=5}$) and cobaltocenium dendrimer generation 4 (Cob-$DAB_{G=4}$) (Fig. 2) was assessed. The Cob-$DAB_{G=4}$ showed the highest increase in fluorescence but as will be forward demonstrated, the recovery values for Cr(VI) sensing are higher for the SiQDs functionalized with PAMAM-OH.

Finally, the influence of the reaction time in the fluorescence intensity was studied. For the above proposed synthesis, 10 μL of SiQDs@PAMAM-OH were hourly picked up during 5 h. The optimal reaction time was achieved after 3 h with a fluorescence increase of ~8 times upper and a right shift emission from 437 nm to 443 nm, comparing to 1 h sample, achieving the quantum yield of 0.15. Actually, the conjugation of the optimal synthesis conditions to the functionalization of SiQDs with PAMAM-OH improved the fluorescent signal through the increasing of hydroxyl groups in the surface of SiQDs core. The effect of the ionic strength and pH were also analyzed by using increasing concentration of NaCl, the proposed nano-sensor presents a high tolerance to variations of ionic strength (1.25 mM to 2.06 M), did not exceeding 6.57% of fluorescence intensity in changing. Relating to the pH, the nano-sensor has a pH of 10.06, the SiQDs@PAMAM-OH exhibited slightly decreases in the fluorescence intensity for a pH below 6 and above 11 (up to 11.6%) and in the range of 6–10 the fluorescence did not showed significantly changes (Fig. SI.3). These soluble nanoparticles showed a slightly positive ζ (1.77 mV) and when coated with PAMAM-OH was increased (5.29 mV).

3.2. XPS analysis

The XPS analysis can identify the nature of the chemical groups present at the surface. The C 1*s* signal for sample SiQDs@PAMAM-OH (see Fig. 3A) can be decomposed in three contributions at 284.8 eV (77.0%), 286.0 eV (19.7%) and 287.7 eV (3.3%). The

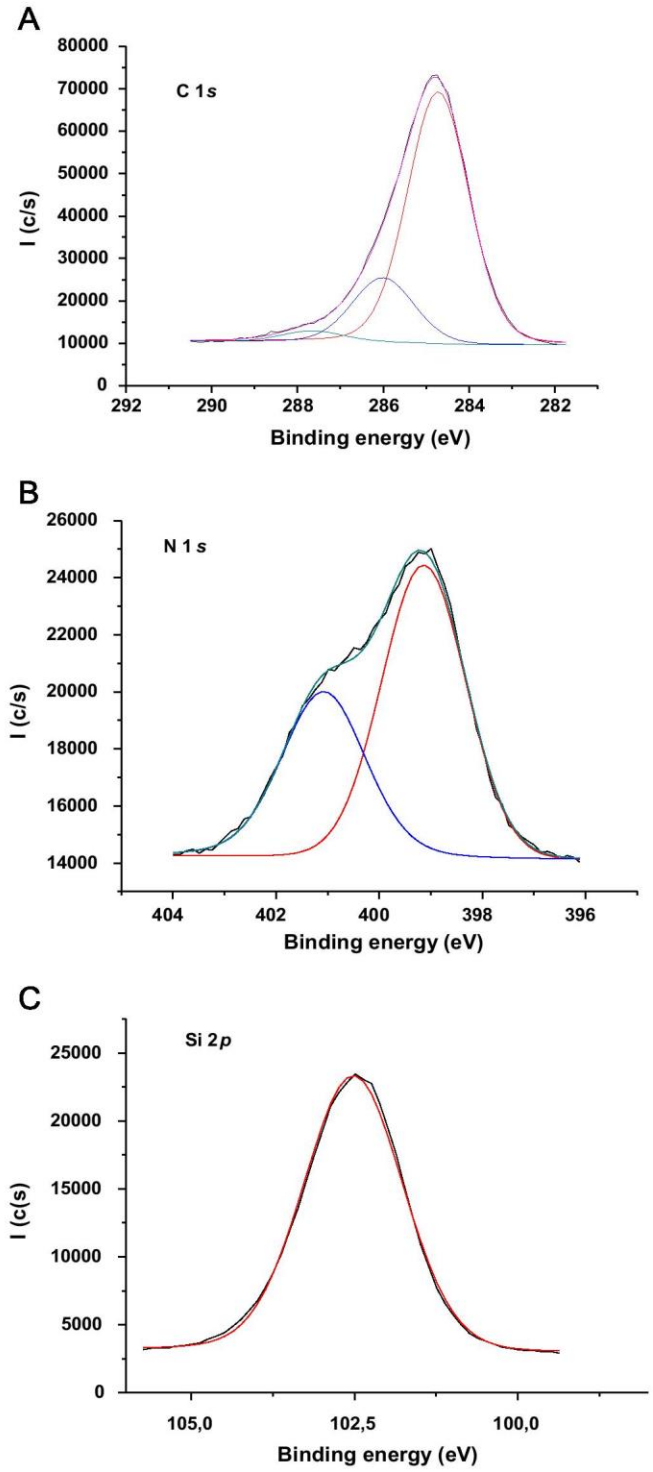

Fig. 3. Core levels spectra of (**A**) C 1*s* and (**B**) N 1*s* for SiQDs@PAMAM-OH.

contribution at 286.0 eV is assigned to the presence of terminal C-OH groups and C–N–H of the polyamide chain. The weak contribution at 287.7 eV is assigned to carbonyl groups of the polyamide chain. This relative weak intensity is due to the core position of the polyamide chain. The N 1*s* signal shows two clear contributions (Fig. 3B) at 399.1 eV (62.1%) and 401.1 eV (37.9%). The former contribution is assigned to the N–H polyamide groups while the later, with a lower intensity, is assigned to protonated amino groups. The O 1*s* signal shows a slight asymmetry at low

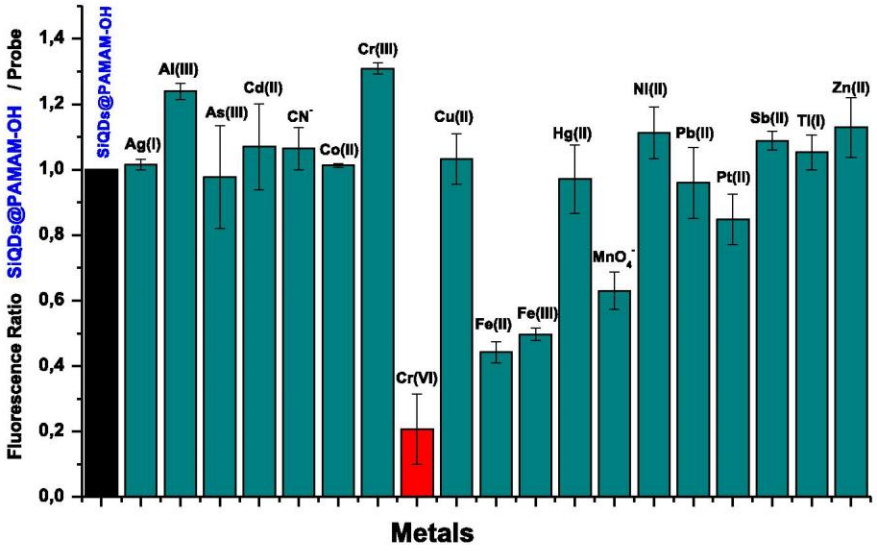

Fig. 4. Fluorescence intensity of SiQDs@PAMAM-OH after addition of different metals and anions.

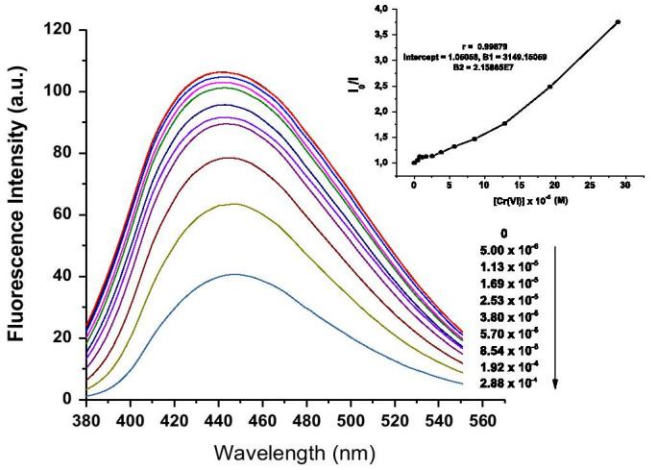

Fig. 5. Influence of the [Cr(VI)] (M) on the fluorescence intensity of SiQDs@PAMAM-OH. Inset: Stern–Volmer representation of the concentration effect of Cr(VI).

binding energy and can be decomposed in two contributions at 532.1 eV (94.1%) and 530.6 eV (5.9%). The main contribution is due to the silica and the weak contribution to the terminal C-OH groups. The Si 2*p* signal is symmetric and centered at 102.5 eV. This value corresponds to tetravalent silicon (Fig. 3C).

3.3. Fluorescent response of SiQDs@PAMAM-OH in the presence of metal ions

In order to find applicability to the proposed nano-sensor, the response of SiQDs@PAMAM-OH was firstly tested in solutions containing individual metal ions. An enhancement (in %) was observed for the ions Ag(I) (0.4), Al(III) (25.7), As(III) (8.9), Cd(II) (16.3), CN^- (11.0), Co(II) (1.7), Cr(III) (32.2), Cu(II) (8.7), Ni(II) (16.9), Sb(II) (10.9), Tl(I) (9.1) and Zn(II) (19.4).

A quenching effect (in %) was also observed when the ions Cr (VI) (71.1), Fe(II) (53.5), Fe(III) (51.6), Hg(II) (10.2), MnO_4- (37.0), Pb(II) (11.7) and Pt(II) (15.2) were tested (Fig. 4). Comparing all the fluorescent profiles, the nano-sensor showed a high affinity for the hexavalent chromium, exhibiting a markedly quenching (71.1) instead of that observed for trivalent chromium which gave a moderate enhancement response (32.2) and highlighted for the systems Fe(II)/ and Fe(III) with 53.5% and 51.6% respectively. The solution that contained Cr(VI) is remaining from a dichromate solution, at a basic pH, which formed the anion chromate. Due to its strong oxidizing property the MnO_4- anion was also tested for the purpose of assess if the quenching was concerning to the oxidation of the SiQDs@PAMAM-OH surface or one of the known quenching mechanisms. With the same concentration, the MnO_4- anion did not show a marked quenching (37.0) as the chromate anion, thus excluding the oxidation as the main effect in the fluorescence quenching.

As previously related, the fact of choosing PAMAM-OH dendrimer instead of the others dendrimers and raw SiQDs is because of the recovery response of the nano-sensor in the presence of Cr (VI) (Fig. SI.4). The functionalized SiQDs by dendrimers offer more affinity for the Cr(VI) anion than without and, comparatively, the SiQDs functionalized with PAMAM-OH are the best combination to achieve the highest quenching profiles for Cr(VI) sensing (from 30% to 70%).

3.4. Calibration curve of SiQDs@PAMAM-OH with CR(VI) ions

The concentration effect of Cr(VI) was studied in the range comprised between 5.0 and 288 μM (Fig. 5). The SiQDs@PAMAM-OH nano-sensor gave a linear response ($r=0.9890$) in function of the Cr(VI) concentration. The quenching phenomena as evaluated through the Stern–Volmer plot which showed an upward curvature indicating the occurrence of static and dynamic effects conjugated in the fluorescence decay (inset Fig. 5). It is assumed that the same quencher acts in the fluorophore by collision and complex formation, the modified Stern–Volmer Eq. (1) reflects the fractional fluorescence remaining.

$$\frac{I_0}{I} = (1 + K_D Q)(1 + K_S Q) \quad (1)$$

Where I_0 and I are the fluorescence intensity without and with a quencher, respectively. Q is the concentration of the quencher and K_D and K_S are the dynamic and static quenching constants, respectively. Rearranging Eq. (1)

$$\frac{\frac{I_0}{I} - 1}{Q} = (K_D . K_S)Q + (K_D + K_S) \quad (2)$$

Where the slope is $K_D.K_S$ and the interception is K_D+K_S. The collisional portion can be calculated by lifetimes measurements (Table 1) through $\tau_0/\tau=K_DQ+1$.

Table 1
Components of lifetime decay ($1.05 < \chi < 1.23$).

[Cr(VI)] (M)	τ_1 (ns)	τ_2 (ns)	τ_3 (ns)
0	3.70 (0.23)	7.30 (0.60)	7.56 (0.74)
2.53×10^{-5}	3.23 (0.10)	1.23 (0.02)	2.00 (0.37)
3.80×10^{-5}	3.10 (0.11)	1.22 (0.03)	1.84 (0.17)
5.70×10^{-5}	3.14 (0.06)	1.22 (0.01)	1.74 (0.26)
8.54×10^{-5}	2.97 (0.15)	1.20 (0.03)	1.80 (0.13)
1.28×10^{-4}	3.15 (0.05)	1.21 (0.03)	1.75 (0.21)

The linear fitting of lifetime was performed by the first lifetime component resulting in the equation $\tau_0/\tau = 2075.5\ [Cr(VI)] + 1.095$ ($r = 0.999$) where dynamic constant is 2075.5 M^{-1}. Adjusting the data points to Eq. (2) was obtained 1.62×10^{-7} for slope and 4763.9 for interception ($r = 0.999$) where the calculated static constant it is 2981.8 M^{-1}. Analyzing the dynamic and static constants, it is observed that the complex formation is predominant up to the collisional fraction predicting that 63% of the fluorophore ground-state are complexed with Cr(VI) ions. The limit of detection and quantification were 2.17 and 7.24 μM, respectively, with an excellent accuracy as relative standard deviation (RSD, $n = 10$) = 0.16% and a sensitivity of 0.20 μM.

3.5. Tolerance to interfering species

In order to assess the potentiality of the proposed nano-sensor for an analytical application in the chromate sensing, the fluorescent intensity variation of the nano-sensor was studied, with a specific concentration of Cr(VI) (1.69×10^{-5} M), in the presence of different interfering species whose concentration was variable in relation to the chromate concentration. The selected interfering species were chosen accordingly to study done in the Section **3.2** where the Al(III), Cr(III), Fe(II), Fe(III) and MnO_4- had caused the highest change in the fluorescence intensity. Moreover these species were used individually at different [Cr(VI)]/[Interferent] ratios (1:5, 1:1 and 5:1) in the same solution containing the SiQDs@PAMAM-OH and a constant = 1.69×10^{-5} M), which is the control solution without the interference, the results are summarized in Table 2.

In fact the results are very satisfactory, indeed because the majority of interfering species showed recovery values superior to 90% for the 1:1 and 5:1 ratios and the lower recovery (72.45%) is attributed to the higher concentration of MnO_4^- (1:5 ratio) because permanganate has a strong oxidizing property, more than chromate, and besides the Cr(VI)-SiQDs@PAMAM-OH complex formed the permanganate could oxidize the accessible groups of the surface causing defects and consequently the loss of fluorescence by alternative decay pathways.

3.6. Application to real samples

The chemical, metallurgical and refractory industries are the main producers of chromate waste and the chrome plating is one of the major responsible methods which produce greater amounts of chromate wasting. To assess the applicability of the nano-sensor to real samples, wasted sample was collected from chrome plating and different chromate concentrations prepared by dilution. The concentration of wasted chromate samples were determined by ICP and resulted in a concentration of 170.1 ± 0.5 g/L. The results summarized in Table 3 shows the Cr(VI) concentrations of 5 samples obtained by a calibration curve whose parameters are $I_F = -2.29 \times 10^{-10}\ [Cr(VI)] + 1.07 \times 10^{-7}$ ($r = 0.999$) in the range of 2.50×10^{-5} M–1.28×10^{-4} M (Fig. 6). The results given by the nano-sensor for real chromate samples are reproducible being a valid method for Cr(VI) sensing.

To validate the analytical procedure at a low range of Cr(VI) concentrations, by means certified materials and a the sample taken from a effluent were used and analyzed under the same optimal analytical conditions. In Table 4 are showed the results of spiked samples, whose experiments were carried out by triplicate, and all the relative standard deviation were very acceptable. The initial concentrations of Cr(VI) in the certified water samples NIST 1640 and NIST 1643b were not detected by the proposed method

Table 2
Recovery (%) values for SiQDs@PAMAM-OH in the presence of chromate (1.69×10^{-5} M) plus different concentration ratios of interfering species.

	1:5	1:1	5:1
Al(III)	100.98(1.19)	101.40(2.94)	100.03(1.60)
Cr(III)	9951(1.19)	97.67(1.66)	97.60(1.18
Fe(II)	86.31(2.93)	92.16(2.309	95.66(3.06)
Fe(III)	91.09(2.09)	91.92(1.75)	94.39(1.51)
MnO_4^-	72.45(4.20)	82.87(4.06)	95.99(4.80)

Table 3
Determination of [Cr(VI)] $\times 10^{-5}$ M in real samples by SiQDs@PAMAM-OH.

$[Cr(VI)]_{st}$ ($\times 10^{-5}$ M))	[Cr(VI)] sample ($\times 10^{-5}$ M)	Accuracy %
2.531	2.654 (0.070)	4.83
3.797	3.611 (0.195)	4.88
5.695	5.285 (0.349)	7.21
8.543	8.554 (0.770)	0.13
12.814	12.834 (1.355)	0.15

4. Conclusions

In summary, a fluorescent nano-sensor has been proposed for the detection of Cr(VI) based on the quenching effect on the fluorescence intensity at 450 nm of the silicon quantum dots coated by hydroxyl terminated PAMAM dendrimer (SiQDs@PAMAM-OH). The fluorescent nanoparticles were obtained by direct hydrothermal treatment of APTES with PAMAM-OH dendrimer at 1:1 ratio. Amino, amide and hydroxyl groups are suggested to function as fluorophore attached to the SiQDs surface. Under the optimum conditions, fluorescence intensity was linearly

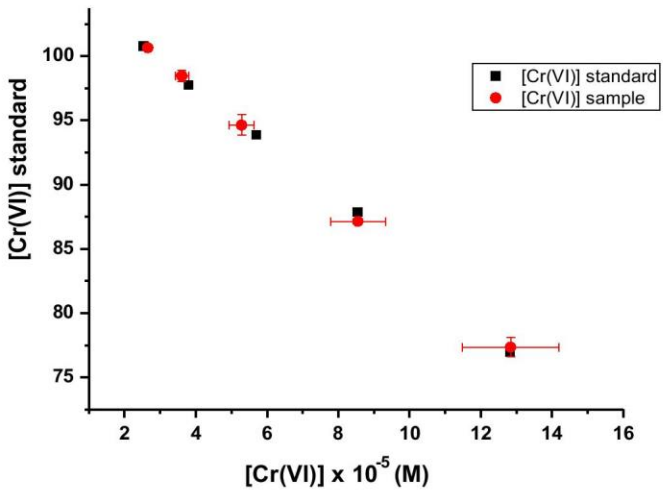

Fig. 6. Results obtained for the standard and sample concentrations.

Table 4
Analytical results of Cr(VI) in spiked samples.

Sample	Chromium concentration (mg L^{-1})*		
	Cr(VI) initial	Cr(VI) added	Cr(VI) found
Water NIST 1640	ND	0.10	0.105 (0.001)
		0.25	0.263 (0.002)
		0.30	0.390 (0.002)
		0.40	0.425 (0.003)
Water NIST 1643d	ND	0.10	0.187 (0.002)
		0.30	0.332 (0.002)
		0.60	0.650 (0.001)
Tanning effluent	1.6 ± 0.2**	0.50	2.31 (0.12)
		0.80	2.48 (0.23)
		1.0	2.98 (0.21)

* Standard deviation ($n=3$).
** Data obtained for IPC.

proportional at μM level of Cr(VI) concentration. The probe had remarkably high selectivity and moderate sensitivity when was applied to real electrochemical wastewater, certified materials and tanning effluent sample used to validated at low concentrations.

Acknowledgments

Authors are gratefully to Grant SFRH/BD/84318/2012 to FCT (Lisbon, Portugal). This work was supported by the projects P12-RNM-1565 (Junta de Andalucía (Spain) and CTQ2012-37925-C03-03 (Ministerio de Economía y Competitividad (Spain) and FEDER Funds).

Appendix A. Supplementary material

Supplementary data associated with this article can be found in the online version at doi:10.1016/j.talanta.2015.07.038.

References

[1] L. Medintz, H.T. Uyeda, E.R. Goldman, H. Mattoussi, Nature Mater. 4 (2005) 435.
[2] D. Bera, L. Qian, T.K. Tseng, P.H. Holloway, Materials 3 (2010) 2260.
[3] W.R. Algar, A.J. Tavares, U.J. Krull, Anal. Chim. Acta 673 (2010) 1.
[4] V. Wood, V. Bulovic, Nano Rev. 1 (2010) 5202.
[5] C.B. Murray, D.J. Norris, M.G. Bawendi, J. Am. Chem. Soc. 115 (1993) 8706.
[6] M. Nirmal, L. Brus, Acc. Chem. Res. 32 (1999) 407.
[7] A. Al-Ahmadi, Quantum A Variety of New Applications (InTech, Rijeka), 2012.
[8] L. Cao, X. Wang, M.J. Meziani, F. Lu, H. Wang, P.G. Luo, Y. Li, B.A. Harruff, L. M. Veca, D. Murray, S.Y. Xie, Y.P. Sun, J. Am. Chem. Soc. 129 (2007) 11318.
[9] J.H. Shen, Y.H. Zhu, X.L. Yang, C.Z. Li, Chem. Commun. 48 (2012) 3686.
[10] Y. Zhong, F. Peng, F. Bao, S. Wang, X. Ji, L. Yang, Y. Su, S.T. Lee, Y. He, J. Am. Chem. Soc. 135 (2013) 8350.
[11] H.T. Li, Z.H. Kang, Y. Liu, S.T. Lee, J. Mater. Chem. 22 (2012) 24230.
[12] K. Fujioka, M. Hilruoka, K. Sato, N. Manabe, R. Miyasaka, S. Hanada, A. Hoshino, R.D. Tilley, Y. Manome, K. Hirakuri, K. Yamamoto, Nanotechnology 19 (2008) 415102.
[13] Y. Yi, G. Zhu, C. Liu, Y. Huang, Y. Zhang, H. Li, J. Zhao, S. Yao, Anal. Chem. 85 (2013) 11464.
[14] O. Akcakir, J. Therrien, G. Belomoin, N. Barry, J.D. Muller, E. Gratton, M. Nayfeh, Appl. Phys. Lett. 76 (2000) 1857.
[15] J.C.G. Esteves da Silva, Carbon and silicon fluorescent nanomaterials, in: M. Muzibur Rahman (Ed.), Nanomaterials, Intech, 2011 Chapter 10.
[16] B. Gelloz, H. Sano, R. Boukherroub, D.D.M. Wayner, D.J. Lockwood, N. Koshida, Appl. Phys. Lett. 83 (2003) 2342.
[17] J.H. Warner, A. Hoshino, K. Yamamoto, R.D. Tilley, Angew. Chem. Int. Ed. 44 (2005) 4550.
[18] H. Nishimura, K. Ritchie, R.S. Kasai, M. Goto, N. Morone, H. Sugimura, K. Tanaka, I. Sase, A. Yoshimura, Y. Nakano, T.K. Fujiwara, A.J. Kusumi, J. Cell Biol. 202 (2013) 967.
[19] S. Chinnathambi, S. Chen, S. Ganesan, N. Hanagata, Adv. Healthc. Mater. 3 (2014) 10.
[20] N. Shirahata, Phys. Chem. Chem. Phys. 13 (2011) 7284.
[21] J.G.C. Veinot, Chem. Commun. (2006) 4160.
[22] K. Dohnalová, T. Gregorkiewicz, K. Kůsová, J. Phys.: Condens. Matter 26 (2014) 173201.
[23] L. Mangolini, E. Thimsen, U. Kortshagen, Nano Lett. 5 (2005) 655.
[24] B.N. Jariwala, N.J. Kramer, M.C. Petcu, D.C. Bobela, M.C.M. van de Sanden, P. Stradis, C.V. Ciobanu, S. Agarwal, J. Phys. Chem. C 115 (2011) 20375.
[25] D. Tan, B. Xu, P. Chen P, Y. Dai, S. Zhou, G. Ma, J. Qiu, RSC Adv. 2 (2012) 8254.
[26] V. Švrček, D. Mariotti, T. Nagai, Y. Shibata, I. Turkevych, M. Kondo, J. Phys. Chem. C 115 (2011) 5084.
[27] K. Dohnalová, L. Ondič, K. Kůsová, I. Pelant, J.L. Rehspringer, R.R. Mafouana, J. Appl. Phys. 107 (2010) 053102.
[28] K. Dohnalová, K. Kůsová, I. Pelant, Appl. Phys. Lett. 94 (2009) 10.
[29] K. Shinoda, S. Yanagisawa, K. Sato, K. Hirakuri, J. Cryst. Growth 288 (2006) 84.
[30] K. Matsuhisa, M. Fujii, K. Imakita, S. Hayashi, J. Lumin. 132 (2012) 1157.
[31] J.J. Gooding, S. Ciampi, Chem. Soc. Rev. 40 (2011) 2704.
[32] X. Li, Y. He, M.T. Swihart, Langmuir 20 (2004) 4720.
[33] X. Pi, T. Yu, D. Yang, Part. Part. Syst. Charact. 31 (2014) 751.
[34] R.D. Tilley, K. Yamamoto, Adv. Mater. 18 (2006) 2053.
[35] Y. Yu, C.M. Hessel, T. Bogart, M.G. Panthani, M.R. Rasch, B.A. Korgel, Langmuir 29 (2013) 1533.
[36] X. Cheng, S.B. Lowe, P.J. Reece, J.J. Gooding, Chem. Soc. Rev. 43 (2014) 2680.
[37] D. Mayeri, B.L. Phillips, M.P. Augustine, S.M. Kauzlarich, Chem. Mater. 13 (2001) 765.
[38] M. Algarra, B.B. Campos, D. Gomes, B. Alonso, C.M. Casado, M.M. Arrebola, M. J. Diez de los Rios, M.E. Herrera-Gutiérrez, G. Seller-Pérez, J.C.G. Esteves da Silva, Talanta 99 (2012) 574.
[39] B.B. Campos, M. Algarra, K. Radotić, D. Mutavdžić, E. Rodríguez-Castellón, J. Jiménez-Jiménez, B. Alonso, C.M. Casado, J.C.G. Esteves da Silva, Talanta 134 (2015) 317.
[40] D.G. Barceloux, Chromium 37 (1999) 73.
[41] J. Kotaś, Z. Stasicka, Environ. Pollut. 107 (2000) 263.
[42] J. Barnhart, Regul. Toxicol. Pharmacol. 26 (1997) S3.
[43] G. De Ruiter, T. Gupta, M.E. Van Der Boom, J. Am. Chem. Soc. 130 (2008) 2744.
[44] M. Algarra, B.B. Campos, B. Alonso, M.S. Miranda, A.M. Martínez, C.M. Casado, J.C.G. Esteves da Silva, Talanta 88 (2012) 403.
[45] B. González, C.M. Casado, B. Alonso, I. Cuadrado, M. Morán, Y. Wang, A. Kaifer, Chem. Commun. 2569 (1998).
[46] K. Takada, D.J. Díaz, H.D. Abruña, I. Cuadrado, B. González, C.M. Casado, B. Alonso, M. Morán, J. Losada, Chem. Eur. J. 7 (2001) 1109.
[47] Y. Huang, X.F. Duan, Q.Q. Wei, C.M. Lieber, Science 291 (2001) 630.

8.2 Supplementary Data

Supplementary Information

Fluorescent Sensor for Cr(VI) Based in Functionalized Silicon Quantum Dots with Dendrimers

B. B. Campos, M. Algarra, B. Alonso, C.M. Casado, J. Jiménez-Jiménez,
E. Rodríguez-Castellón, J.C.G. Esteves da Silva

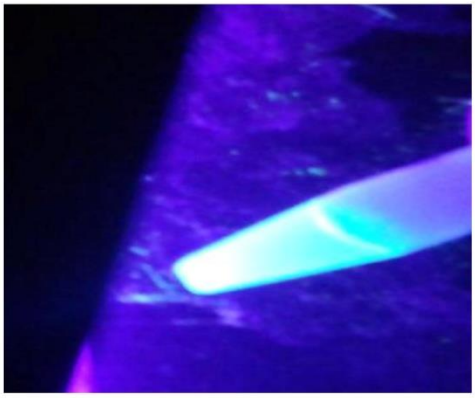

Figure SI.1. Fluorescence emission of SiQDs@PAMAM-OH when irradiated under UV light

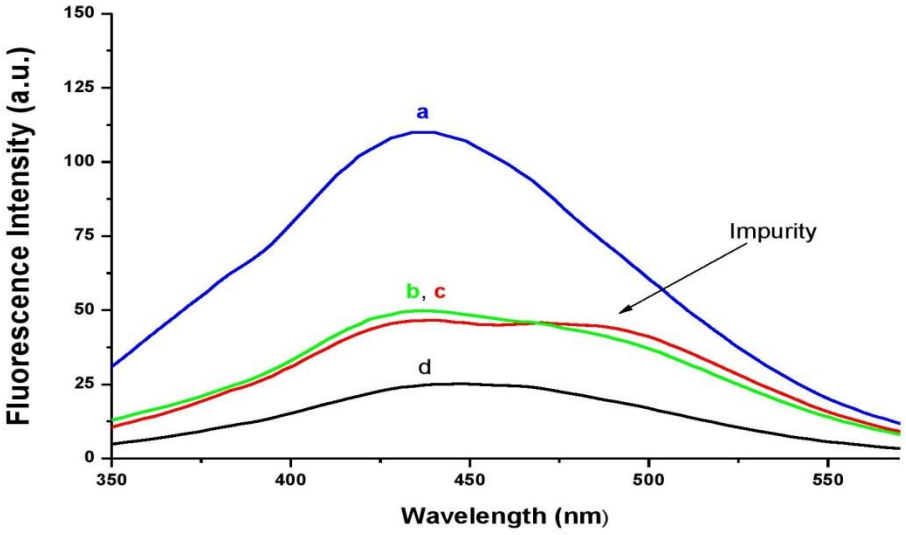

Figure SI.2. Influence of the APTES/PAMAM-OH ratio (v/v) on the fluorescence intensity of SiQDs: **a)** 1:1; **b)** 5:3; **c)** 5:1 and **d)** raw SiQDs.

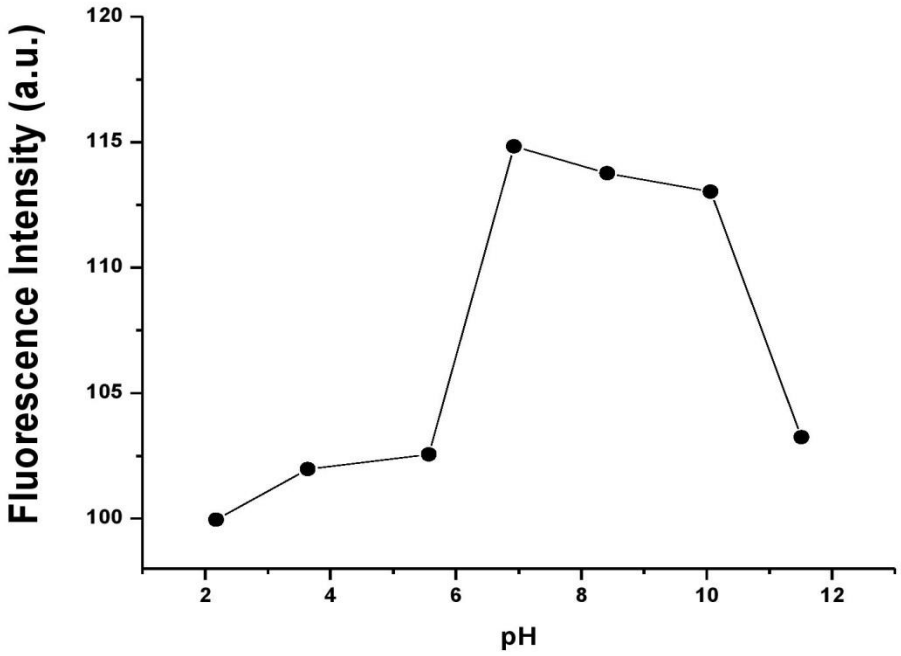

Figure SI.3. Influence of the pH on the fluorescence intensity of SiQDs@PAMAM-OH.

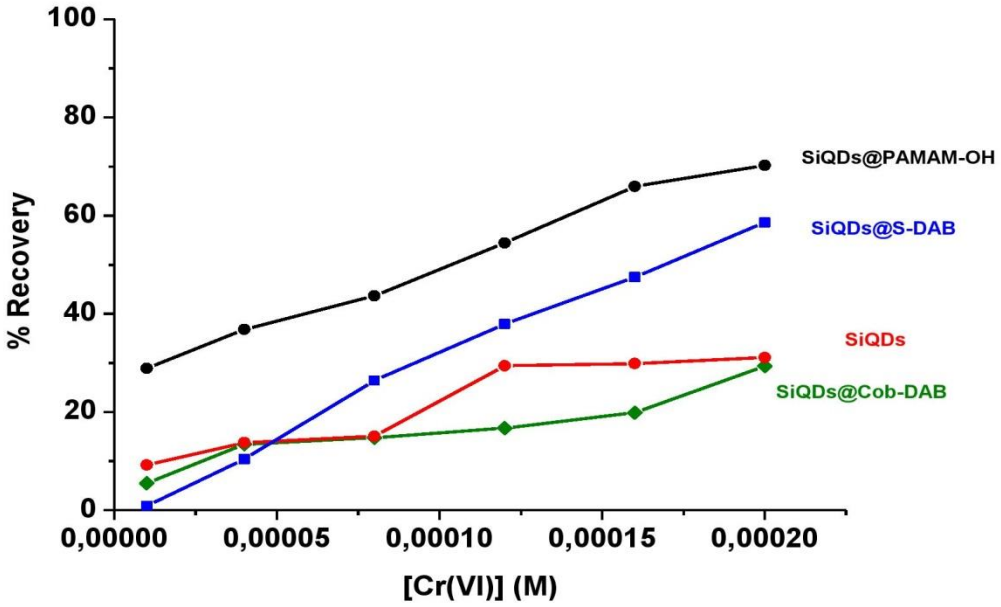

Figure SI.4. Recovery performance of SiQDs functionalized with different dendrimers for the sensing of Cr(VI).

Chapter 9

Characterization of cellulose membranes modified with luminescent silicon quantum dots nanoparticles

9.1 Contribution to this Paper

My contribution to this paper started with the bibliographic research and writing about immobilization of QDs on cellulose membranes and then the experimental planning. The synthesis, purification and functionalization with dendrimers were performed and sent to specialized group on Electrokinetic Characterization about Membranes and Interphases at Faculty of Sciences of Málaga University, which conducted the immobilization studies and the complementary assays such as thermal and optic analysis and impedance spectroscopy. The data obtained by the characterization methods was analyzed and interpreted. This paper was submitted as a scientific article and until the acceptation it passes through some adjustments required by the reviewers and under supervision of my advisor Professor Joaquim Esteves da Silva and co-advisor Doutor Manuel Algarra.

Carbohydrate Polymers 151 (2016) 939–946

Contents lists available at ScienceDirect

Carbohydrate Polymers

journal homepage: www.elsevier.com/locate/carbpol

Characterization of cellulose membranes modified with luminescent silicon quantum dots nanoparticles

B.B. Campos[a], L. Gelde[b], M. Algarra[c,*], J.C.G. Esteves da Silva[a], M.I. Vázquez[b], J. Benavente[b]

[a] Centro de Investigação em Química, Departamento de Química e Bioquímica, Faculdade de Ciências da Universidade do Porto, Porto, Portugal
[b] Grupo Caracterización Electrocinética en Membranas e Interfases, Departamento de Física Aplicada I, Facultad de Ciencias, Universidad de Málaga, 29071 Málaga, Spain
[c] Departamento de Química Inorgánica, Facultad de Ciencias, Universidad de Málaga, Campus de Teatinos s/n, 29071 Málaga, Spain

ARTICLE INFO

Article history:
Received 9 March 2016
Received in revised form 26 May 2016
Accepted 27 May 2016
Available online 11 June 2016

Keywords:
Nanoparticle
Silicon quantum dots
Dendrimer
Cellulose

ABSTRACT

A highly hydrophilic planar membrane fabricated with regenerated cellulose (RC-4 membrane), a biocompatible polymer, was modified by inclusion of water-soluble silicon quantum dot nanoparticles (SiQDs). Both bare SiQDs and SiQDs coated with a PAMAM-OH dendrimer were employed in order to obtain luminescent and thermally stable membrane systems (RC-4/SiQDs and RC-4/SiQDs-PAMAM-OH membranes). Original and SiQDs-modified membranes were characterized by fluorescence spectroscopy (steady and confocal), derivative thermogravimetric analysis and impedance spectroscopy measurements. According to these results, both SiQDs-regenerated cellulose composite membranes present luminescent character as well as higher thermal resistance and conductivity than the original sample, although the dendrimer coverage of the SiQDs might partially shield such effects. Moreover, the permanence of SiQDs nanoparticles in the structure of the cellulosic support in aqueous environments and their effect on diffusive transport were determined by water uptake as well as by membrane potential measurements at different concentrations of a model electrolyte (KCl). These results demonstrate the possible use of these stable nano-engineered membranes, which are based on SiQDs nanoparticles, in electrochemical devices under flow conditions.

1. Introduction

Quantum dots (QDs) based on Cd or Se have attracted great attention due to their semiconductor behavior and unique optical properties (Chen & Liang, 2014; Choi et al., 2015; Loef, Houtepen, Talgorn, Schoonman, & Goossens, 2009), and they have been studied for a great variety of applications such as sensing systems, catalysis, energy storage, and bio-imaging (Algarra, Campos, Aguiar, Rodríguez-Borges, & Esteves da Silva, 2012; Hod et al., 2011; Liu et al., 2015; Nann & Skinner, 2011; Tan, Wan, & Li, 2014; Tomasulo, Yildiz, & Raymo, 2006; Vanacore et al., 2014; Zhao et al., 2012). However, the application of these systems seems to be limited due to the toxicity of the heavy metals employed (Chou & Chan, 2012). Lately, due to the demand of biocompatible, heavy metal free QDs for environmental and medical applications, silicon, carbon, and graphene quantum dots (SiQDs, CQDs and GQDs, respectively) have been considered (Esteves da Silva, 2011). Although the toxicities of these new QDs are lower than that presented by classical QDs, and they also exhibit good optical characteristics, they have not been widely used to date. Research on both the production of water-dispersible SiQDs and CQDs and their incorporation into highly hydrophilic structures or hydrogels have been reported recently since water-dispersible QDs might lead to applications in diagnostics or facilitate their use in electrochemical devices or liquid media sensors (Algarra, Campos, et al. 2014; Algarra, Pérez-Martin, et al. 2014; Campos et al., 2015; English, Pell, Yu, Barbara, & Korgel, 2002; Erogbogbo et al., 2008; Goh et al., 2012; Junka, Guo, Filpponen, Laine, & Rojas, 2014; Li et al., 2014; Pereira, Vasilopoulos, & Peeters, 2007; Shiohara et al., 2010). In this context, it should be pointed out that flat sheets of regenerated cellulose (RC), the most abundant biopolymer in nature and a highly hydrophilic material, have already been used for the incorporation of different nanoparticles and even QDs (Algarra, Alonso, Casado, Esteves da Silva, & Benavente, 2013; Mansur, Mansur, Curti, & de Almeida, 2012; Vázquez, Algarra, & Benavente, 2015). As it has been demonstrated, the high degree of swelling of the RC supports favors

* Corresponding author.
E-mail address: malgarra67@gmail.com (M. Algarra).

http://dx.doi.org/10.1016/j.carbpol.2016.05.097
0144-8617/

the inclusion of nanoparticles into the cross-linked structure of the cellulose sheets, which might affect the mass and charge transport across these new nanocomposite structures.

In this paper, we show the feasibility of obtaining luminescent and thermally stable membranes by inclusion of SiQDs into a regenerated cellulose support by a simple and chemically friendly technique. Dry samples of original regenerated bare cellulose support (RC-4 sample), cellulose support modified by SiQDs (RC-4/SiQDs) and SiQDs/dendrimer-covered (RC-4/SiQDs-PAMAM-OH) membranes have been characterized by different techniques, such us luminescent spectroscopy, derivative thermogravimetry and impedance spectroscopy in order to observe differences in their physicochemical properties for possible application in bioanalytical techniques. In addition, for establishing their use in electrolyte flow devices, electrochemical characterization of the QDs-modified cellulose supports using KCl solution at different concentrations was also performed.

2. Material and methods

2.1. Chemicals

(3-Aminopropyl)triethoxysilane (99%, APTES) and hydroxyl-terminated 5th generation poly(amidoamine) dendrimer (PAMAM-$OH_{G=5}$) in methanol were purchased from Sigma–Aldrich Química S.A. (Spain), and used as received without further purification. Ultrapure Millipore™ water was used throughout all experiments. A flat sheet of regenerated cellulose (RC) from Cellophane Española, S.A. (Burgos, Spain) with a RC content of 0.04 kg m^{-2} was used as support membrane (sample RC-4).

2.2. Synthesis of SiQDs and SiQDs-PAMAM-OH dendrimer

Raw SiQDs and functionalized SiQDs nanoparticles were obtained as follows: 100 μL of APTES were mixed with 100 μL of PAMAM-OH dendrimer in 800 μL of H_2O in a Teflon-lined stainless-steel autoclave reactor, which was set for 3 h at 200 °C. Finally, the highly blue fluorescent solution was dialyzed against H_2O for 1 h to obtain SiQDs/PAMAM-OH. The same procedure, but without dendrimer, was repeated to obtain raw SiQDs.

2.3. Preparation of the RC-4/SiQDs and RC-4/SiQDs-PAMAM-OH

Pieces of the RC-4 membrane were immersed in an aqueous solution of SiQDs or SiQDs/PAMAM-OH at room temperature for 46 h, then the modified membranes were taken off and their surfaces gently dried with paper; these samples will be hereafter named as RC-4/SiQDs and RC-4/SiQDs-PAMAM-OH respectively. The membrane thicknesses of the studied samples were measured with a digital micrometer, while the membrane water content or solution uptake (SU) was determined from the difference in weight between dried (W_d) and swollen (W_w) samples generated from their immersion in distilled water. Then, the samples were taken out and their surfaces were wiped with filter paper before weighting: $SU = [(W_w - W_d)/W_w] \times 100$. These latter measurements were performed after keeping the samples in distilled water for varying amounts of time.

2.4. Fluorescence characterization

Fluorescence measurements and fluorescence lifetime analyses were performed using an Edinburgh Instruments FLS920, equipped with a Xe lamp (450 W) as excitation source for steady state fluorescence measurements, and monochromatic LEDs (PicoQuant PLS) controlled by a PDL 880-B system. The spectra of SiQDs on the solid support were measured in the front-face configuration of the measuring cavity. The slits on the excitation and emission beams were fixed at 4 nm and 2 nm respectively. The integration time was 0.1 s. The spectra were corrected for dark counts. In each measurement three scans were averaged. Fluorescence decays were interpreted in terms of a multi-exponential equation: $I(t) = A + \sum B_i \exp^{-t/\tau_i}$, where A is the pre-exponential factor, B_i is the relative amplitude and τ_i is the average component lifetime.

2.5. Thermal characterization

Derivative thermo-gravimetric analysis (TGA) and differential scanning calorimetry (DSC) measurements were performed through a TG/DSC 1 Star System (Mettler-Toledo) coupled with a MS-Thermostar GSD320 (Pfeiffer Vacuum) Mass Spectrometer. TG/DSC curves were measured with Pt crucibles, in N_2 flow (20 mL min^{-1}) and using a heating rate of 5 °C min^{-1} in the range 25–1600 °C by a HT1600 oven connected to a MX5 microbalance (thermostatic at 22 °C). The process was controlled by STARe software v.10.0 (Mettler Toledo). All the samples were air dried in an oven at a temperature of 60 °C for one week to remove the excess of water, mainly in the samples subjected to high humidity conditions.

2.6. Confocal laser scanning microscopy

Confocal laser scanning microscopy (CLSM) was performed with a Leica TCS NT confocal laser scanning microscope (Leica, Heidelberg, Germany) and images were processed using the Solid algorithm, which is a direct composition with diffuse gradient shading (Leica TCS software). Small pieces of the modified samples were put on microscope slides under a coverslip and the fluorescence of the samples was studied by CLSM. Generally, an excitation beam splitter DD488/568 was used. For visualization of multispectral image data, the selected channel was associated with a color value on the display system, blue in this case, using a band pass filter (BP) of 515–565 nm.

2.7. Impedance spectroscopy measurements

The test cell for impedance spectroscopy (IS) measurements consists of two Teflon half-cells, with one Pt electrode each, where the membranes were placed and the cell mounted (system: electrode/membrane/electrode). The electrodes were connected to a frequency response analyzer (FRA, Solartron 1260, England) and 100 data points were recorded at a frequency ranging between 1 Hz and 10^7 Hz at a maximum voltage of 0.01 V. The impedance, Z, is a complex number, $Z = Z_{real} + jZ_{img}$, which can be separated into real and imaginary parts using algebraic rules. Z_{real} and Z_{img} components are related to the transport of charge across the system (electrical resistance, R) and charge storage (capacitance, C): $Z_{real} = R/[1 + (\omega RC)^2]$ and $Z_{img} = -\omega R^2 C/[1 + (\omega RC)^2]$, where $\omega = 2\pi f$ is the angular frequency. R and C parameters can be determined from impedance plots by using equivalent circuits as models (Asaka, 1990; Benavente, García, de la Campa, & de Abajo, 1996; Benavente, García, Riley, Lozano, & de Abajo, 2000). IS measurements were performed at atmospheric conditions (54% humidity).

2.8. Membrane potential measurements

The equilibrium electrical potential difference at both sides of a membrane separating two solutions of one electrolyte with different concentrations (membrane potential, $\Delta\Phi_{mbr}$), was measured in a dead-end test cell similar to that described previously (Peláez, Vázquez, & Benavente, 2010), and the solutions were stirred at a rate of 520 rpm to minimize the concentration polarization at the

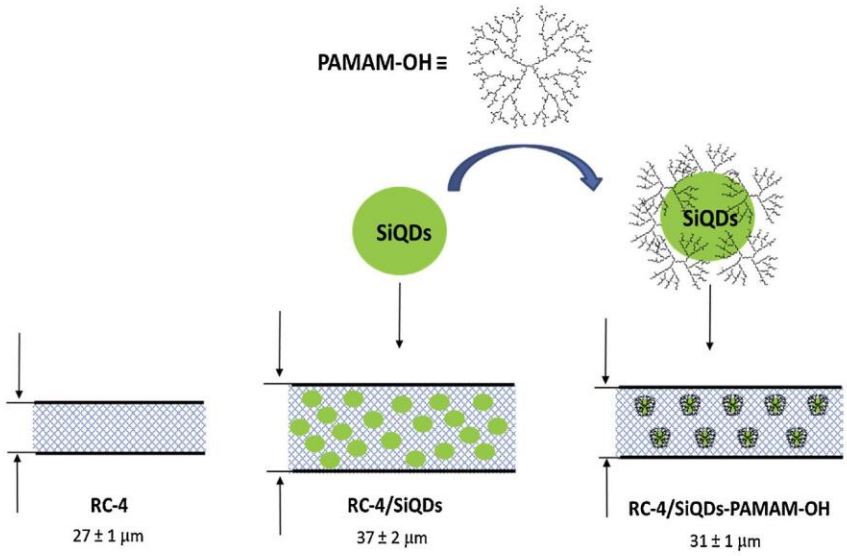

Fig. 1. Schematic representation of the RC-4 membrane and the modified RC-4/SiQDs and RC-4/SiQDs-PAMAM-OH membranes, with indication of their average thickness.

membrane surfaces (Romero, Vázquez, & Benavente, 2013). A typical electrolyte model, KCl, was chosen for these measurements to avoid the possible contribution of the solution potential in $\Delta\Phi_{mbr}$ values due to the similarity in cation and anion transport numbers in solution (Robinson & Stokes, 1955).

The electromotive force in the steady-state between the two solutions with different concentrations on each membrane side (ΔE) was measured with two reversible Ag/AgCl electrodes connected to a digital voltmeter (Yokohama 7552, 1 GΩ input resistance). Measurements were carried out by keeping the concentration of one of the KCl solutions constant ($C_c = 0.01$ M) and gradually changing the concentration of the solution on the other side of the membrane ($0.004 \leq C_v$ (M) ≤ 0.1). The membrane potential value for each pair of solution concentrations (C_v, C_c) was obtained by subtracting the corresponding electrode potential, $\Delta\Phi_{elect} = (RT/z)\ln(C_v/C_c)$, from the measured ΔE potential: $\Delta\Phi_{mbr} = \Delta E - \Delta\Phi_{elect}$.

2.9. FESEM and EDS analysis

The surface morphology of the MNPs composite was studied by field-emission scanning electron microscope (FE-SEM), double beam Helios Nanolab 650 de FEI Company (Oxford, UK) with detector for EDX analysis.

3. Results and discussion

Fig. 1 shows a scheme of the analyzed RC-4, RC-4/SiQDs and RC-4/SiQDs-PAMAM-OH dry samples with indication of the corresponding thickness. As can be observed, the inclusion of the SiQDs causes a separation of the RC chains and, consequently, a more open structure; however, coverage of SiQDs by the PAMAM-OH dendrimer partially reduces this effect as a result of its linkage with the RC chains, giving rise to a more closed structure.

3.1. FESEM and EDS analysis

High-resolution field emission scanning electron microscopy (FESEM) images show the presence of SiQDs nanoparticles (both isolated and aggregated) on the surface of the RC-4 support (Fig. 2A), but primarily aggregations seems to exist when the SiQDs are coated with PAMAM-OH dendrimer (Fig. 2B). These images also show the regular spherical shape of the SiQDs, with an average particle size of around 50 ± 8 nm, which correlates well with those previously obtained by TEM (Campos et al., 2015).

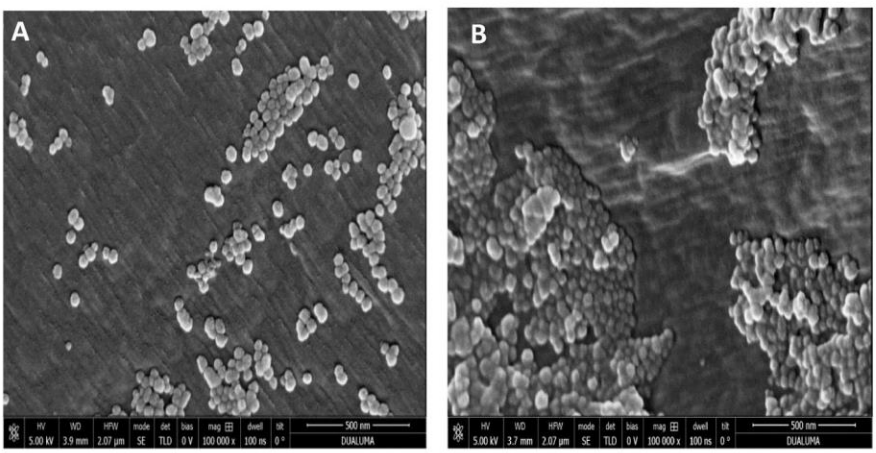

Fig. 2. Field emission scanning electron microscope images of a RC-4 cellulose membrane modified with: (A) SiQDs and (B) SiQDs-PAMAM-OH nanoparticles observed at high magnification (60 000).

Table 1
Chemical composition (%) by EDS spectroscopy.

Membrane	Si (%)	C (%)	O (%)
Unmodified RC-4		84.43	14.95
RC-4/SiQDs	3.75	75.08	20.90
RC-4/SiQDs-PAMAM-OH	3.06	80.55	16.21

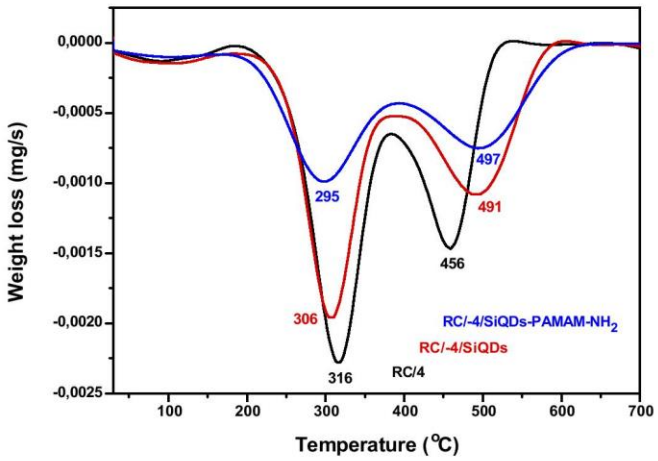

Fig. 3. DTG curves for cellulose membranes: RC-4, RC-4/SiQDs and RC-4/SiQDs-PAMAM-OH.

The chemical composition of RC-4, RC-4/SiQDs and RC-4/SiQDs-PAMAM-OH membranes was investigated by energy-dispersive X-ray spectroscopy (EDS) elemental analysis and the values obtained are shown in Table 1. As expected, these results confirm the presence of Si in the as-prepared samples and higher content of carbon for the SiQDs-dendrimer coated sample.

3.2. Thermal analysis

Differences in the TGA curves and thermal characteristic parameters obtained for the three studied membranes are shown in Fig. 3 and Table 2, respectively. For further insight into these data, the following membrane characteristics are indicated in Table 2: initial temperature at which thermal decomposition starts (T_{onset}), temperature at which maximal degradation is registered (T_{peak}), and temperature at which the investigated process ends (T_{endset}). Additionally, the percentage of mass loss in each step (W%) and the quantity of residue remaining (Re_{left}), are also shown. As can be observed from the results represented in Table 2 and Fig. 3, cellulose modified RC-4/SiQDs and RC-4/SiQDs-PAMAM-OH membranes show similar thermal behavior, but they differ clearly from the original RC-4 membrane. In particular, both SiQDs-modified membranes exhibit higher thermal stability than the RC-4 untreated membrane.

As can be observed in Fig. 3, the thermal degradation consists of two exothermic degradation steps and all three membranes present the same behavior during the first degradation (temperature interval between 186 °C and 208 °C). The mass loss in the case of the RC-4 membrane is originated by the degradation of

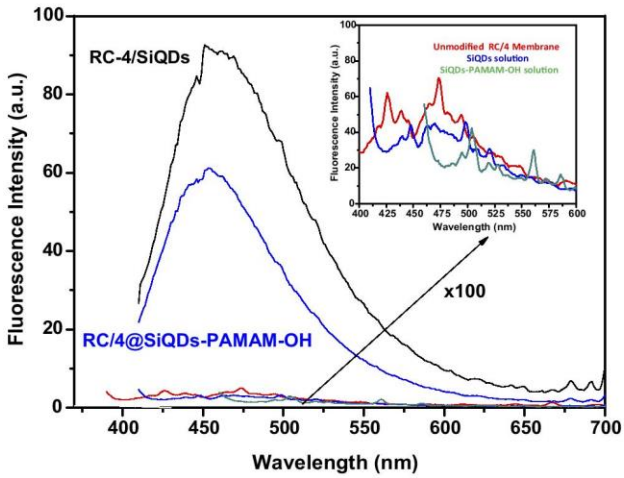

Fig. 4. Fluorescence spectra of the studied modified membranes. In the bottom, compared with the dissolutions of prepared SiQDs and SiQDs-PAMAM-OH nanoparticles and un-functionalized RC/4. (λ_{ex} = 380 nm).

cellulose chains, i.e. the pyrolysis of the polymer skeleton backbone, but the inclusion of SiQDs reduces this loss. The temperature for the second degradation step starts at 389 °C for the original RC-4 membrane but around 409 °C for the SiQDs-modified samples; moreover, the minima of the curves for these latter samples appear at higher temperatures and they show a remarkable reduction in the mass loss, which confirms the thermal stability of these membranes, as proposed previously (Arthanareeswaran, Thanikaivelan, Srinivasn, Mohan, & Rajendran, 2004; Coutinho, Delpech, Alves, & Ferreira, 2003; Shieh & Chung, 1998). Similarly, it has been shown that SiQDs-cellulose supported membranes exhibit higher thermal stability than those modified with CdSe QDs (Zhenhua et al., 2012).

3.3. Fluorescence analysis

To study the emission behavior of the modified membranes, fluorescence spectra for RC-4/SiQDs and RC.4/SiQDs-PAMAM-OH samples were recorded, with excitation at 380 nm, and compared with the RC-4 original membrane as it is shown in Fig. 4. As can be observed, the raw RC-4 membrane does not show any fluorescent emission, while the inclusion of SiQDs nanoparticles clearly increases the fluorescent effect in the modified samples at 455 nm, but with different relative intensities. The lower intensity exhibited by the RC-4/SiQDs-PAMAM-OH membrane is attributed to dendrimer coverage of SiQDs previously indicated (see Fig. 1), which might shield the light emission. In particular, the presence of PAMAM-OH reduces, by two orders of magnitude, the fluorescence intensity of this membrane. Moreover, the fluorescent lifetimes for the SiQDs and SiQDs-PAMAM-OH cellulose modified membranes were also calculated. The fluorescent decay curve was fitted to a model with two exponential decay components, and Table 3 shows the fluorescence lifetime parameters (A, B_i and τ_i) and the fit (χ^2) values. The overall complex behavior of the emission spectra is apparently associated with a variety of emission centers present in the SiQDs. The average fluorescence lifetimes

Table 2
Thermogravimetric characteristics of RC-4 and the modified RC-4/SiQDs and RC-4/SiQDs-PAMAM-OH.

Membrane	Thermal degradation step I				Thermal degradation step II				Re_{left} (%)
	T_{onset} (°C)	T_{peak} (°C)	T_{endset} (°C)	W (%)	T_{onset} (°C)	T_{peak} (°C)	T_{endset} (°C)	W (%)	
Unmodified RC-4	186	316	381	55.39	389	456	538	36.77	3.8293
RC-4/SiQDs	208	306	381	50.18	414	491	601	36.73	13.0866
RC-4/SiQDs-PAMAM-OH	191	295	390	45.26	420	497	632	39.69	10.7104

Table 3
Tabular representation of fluorescence lifetime calculations of RC/4@SiQDs and RC/4@SiQDs-PAMAM-OH.

Membrane	A	B_1	B_2	τ_1 (ns)	τ_2 (ns)	χ^2
RC-4/SiQDs	3.571	495.57	547.80	3.80 (26.0%)	9.788 (74.0%)	1.216
RC-4/SiQDs-PAMAM-OH	4.815	887.85	700.87	4.45 (34.4%)	10.764 (65.6%)	1.181

(τ_1 and τ_2) of both membranes are in the nanosecond regime, which is similar to that exhibited by QDs, and reveals the radiative recombination nature of the excitations (Kůsová, Pelant, & Valenta, 2015), and the lifetimes indicate that both RC-4/SiQDs and RC-4/SiQDs-PAMAM-OH membranes are potentially suitable for fluorescence applications. Moreover, Fig. 4 also shows the fluorescent spectra of SiQDs and SiQDs-PAMAM-OH nanoparticle solutions, which show clearly lowest intensity than the obtained for the corresponding modified membranes due to the different nanoparticles interactions with solid/liquid supports (Lackowiz, 1999).

3.4. Confocal microscopy analysis

The fluorescent nature of RC-4/SiQDs and RC-4/SiQDs-PAMAM-OH membranes was confirmed by confocal fluorescence microscopy analysis. Fig. 5 shows fluorescence images for both SiQDs-modified samples and the original RC-4 membrane. These images demonstrate the possibility of obtaining luminescent cellulose-based membranes through incorporation of biocompatible SiQDs by a simple dip coating procedure, as well as the fact that SiQDs-coverage by PAMAM-OH dendrimer only causes a certain attenuation of the fluorescent intensity.

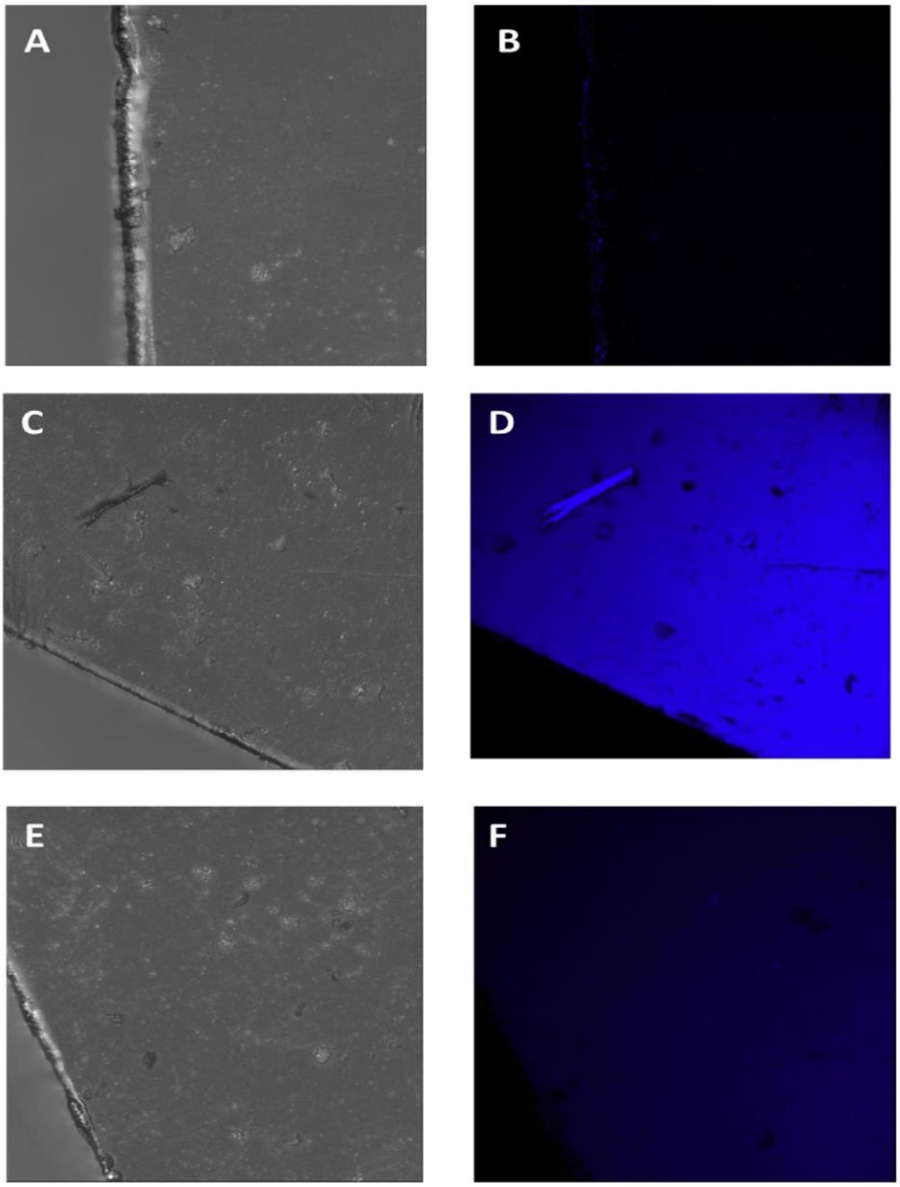

Fig. 5. Confocal images of the original RC-4 membrane without UV irradiation (A) and under excitation (B); RC-4/SiQDs membrane without irradiation (C) and under excitation (D); RC-4/SiQDs-PAMAM-OH membrane without irradiation (E) and under excitation (F).

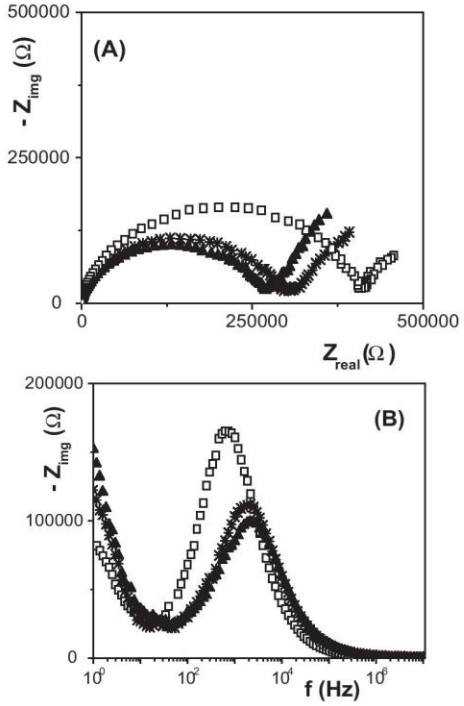

Fig. 6. Impedance curves: (A) Nyquist plot and (B) Bode plot for (□) RC-4 membrane, (▲) RC-4/SiQDs membrane, (*) RC-4/SiQDs-PAMAM-OH membrane.

3.5. Impedance spectroscopy (IS) analysis

Electrical response can also give information on differences among original and SiQDs-modified membranes. Fig. 6 shows a comparison of the impedance curves obtained with the three studied samples. Fig. 6A shows the Nyquist plot ($-Z_{img}$ vs. Z_{real}), where clear differences can be observed when the IS data obtained for both SiQDs-modified membranes are compared with the original RC-4 sample; in all cases, the curves represent a semi-circle and their equivalent circuits correspond to a parallel association of a resistance and a capacitor, according to IS models (Benavente et al., 2000; Macdonals, 1987). Fig. 6B shows the Bode plot ($-Z_{img}$ vs. frequency), where a shift of the $-Z_{img}$ maximum value to high frequency values for both SiQD-modified membranes can be observed, which is usually associated with more conductive materials (f_{max} for common electrolyte solutions around 10^6 Hz). According to these results, the inclusion of SiQDs in the structure of the cellulose membranes increases the electrical character of the samples, causing a reduction in their electrical resistance, although the SiQDs coverage by the PAMAM-OH dendrimer slightly decrease this effect. In particular, the analysis of the Nyquist plots using a non-linear Z-plot program (Algarra, Vázquez, et al., 2014) allows us the estimation of the electrical resistance (R_m) and capacitance (C_m) of the studied membranes.

Characteristic intensive (independent of the sample geometry) material parameters such as conductivity and dielectric constant can be determined from IS results, taking into account electrical relationships for (Benavente, 2012): (i) resistance/conductivity, $R_m = \Delta x_m/(\sigma_m \cdot S)$, where σ_m, Δx_m and S represent the membrane conductivity, thickness and area, respectively; (ii) capacitance of a plane-parallel capacitor, $C_m = (\varepsilon_o \varepsilon_m \cdot S)/\Delta x_m$, where ε_m and ε_o are the membrane permittivity and dielectric constant of vacuum, respectively. Table 4 shows the values of conductivity and dielectric constant determined for the three studied membranes. According to these results, the inclusion of the SiQDs into the structure of the RC-4 membranes: (a) significantly increases the conductivity of both samples (97% for the RC-4/SiQDs, but 55% for the RC-4/SiQDs-PAMAM-OH due to dendrimer coverage of the QDs); (b) slightly reduces the value of their dielectric constant (around 10% and 20% for the RC-4/SiQDs, and RC-4/SiQDs-PAMAM-OH samples, respectively), which could be related to a reduction in the water content of both modified samples.

Table 4
Membrane conductivity, σ_m, and dielectric constant, ε_m, for the studied membranes.

Membrane	σ_m (Ω m)$^{-1}$	ε_m
Unmodified RC-4	0.68×10^{-6}	12.4
RC-4/SiQDs	1.34×10^{-6}	11.2
RC-4/SiQDs-PAMAM-OH	1.05×10^{-6}	10.0

3.6. Characterization of membranes under diffusive flow

Electrochemical devices usually work in contact with solutions; thus, studying the behaviors of the bare and modified RC-4 membranes in aqueous electrolytes solutions are of great interest. Due to the pronounced hydrophilic character of the cellulose (RC-4 support material), before electrochemical characterization of the membranes, information on their water uptake (Sw) is necessary. Fig. 7 shows time variation of Sw values obtained for the three membranes. As can be observed, the inclusion of both modifying substances, SiQDs and SiQDs-PAMAM-OH, clearly reduces the water uptake of the RC-4 support, but does not seem to affect membrane stability according to the time constancy of the Sw values. Consequently, the following average values were determined: $Sw_{RC-4} = 105.4\ (\pm 1.3)\%$, $Sw_{RC-4/SiQDs} = 61.4\ (\pm 2.8)\%$ and $Sw_{RC-4/SiQD-PAMAM-OH} = 72.5\ (\pm 2.3)\%$. The pronounced hydrophilic character of cellulose corroborates the significant swelling degree of sample RC-4 (higher than 100%), as was previously reported by other authors for these kinds of materials (Gilbert, Okano, Miyata, & Kim, 1988; Ramos et al., 2010).

Once the permanence of the SiQDs nanoparticles into the structure of the cellulosic RC-4 membrane was established and the stability of the modified membranes in the most adverse conditions (water environment) was determined, their electrochemical characterization using KCl solutions was performed. The effective membrane fixed charge, X_{ef}, and the ion transport number, t_i, or fraction of the total current transported for one ion ($t_i = I_i/I_T$), are two significant parameters related to the transport of electrolyte solutions through charged membranes, which are commonly obtained from membrane potential values ($\Delta\Phi_{mbr}$) (Ramos et al., 2010). According to the Teorell–Meyer–Sievers model (Meyer & Sievers, 1936; Teorell, 1956), the membrane potential can be considered as the sum of two Donnan potentials ($\Delta\Phi_{Don}$, one at

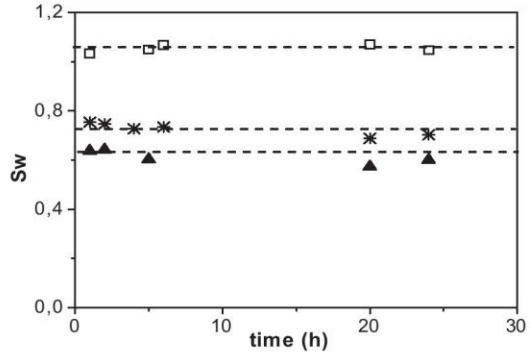

Fig. 7. Time variation of water uptake by the studied membranes: (□) RC-4 membrane, (▲) RC-4/SiQDs membrane, (*) RC-4/SiQDs-PAMAM-OH membrane.

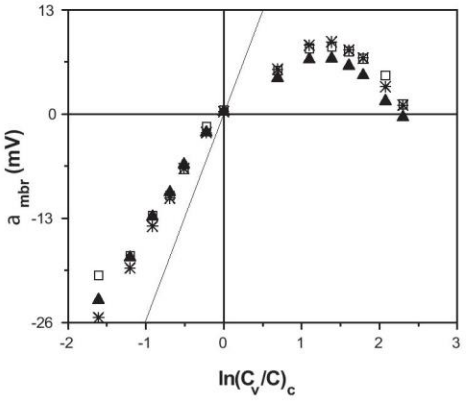

Fig. 8. Membrane potential vs KCl solutions concentration ratio (C_c = 0.01 M) for membranes: RC-4 (□), RC-4/SiQDs (▲) and RC-4/SiQDs-PAMAM-OH (*). Solid line corresponds to an ideal cation-exchange membrane (t_+ = 1 and t_- = 0).

each membrane-solution interface) associated with the exclusion of co-ions (ions with the same sign as the membrane charge), plus a diffusion potential in the membrane bulk ($\Delta\Phi_{dif}$) due to the different mobilities of both ions in the membrane, that is, $\Delta\Phi_{mbr} = \Delta\Phi_{Don(I)} + \Delta\Phi_{dif} + \Delta\Phi_{Don(II)}$.

The total membrane potential can be expressed as (Lakshminarayanaiah, 1969):

$$\Delta\Phi_{mbr} = -\frac{RT}{wzF}\left[U\ln\frac{\sqrt{4y_v^2+1}+wU}{\sqrt{4y_f^2+1}+wU} - \ln\frac{c_f}{c_v}\frac{\sqrt{4y_v^2+1}+w}{\sqrt{4y_f^2+1}+w}\right]z$$

where $w = -1/+1$ for negatively/positively charged membranes, R and F are the gas and Faraday constants, respectively, T is the temperature of the system, U is a parameter related to the transport number of the ions ($U = t_+ + t_-$), and $y_i = K_{s,i}\cdot c_i/|X_{ef}|$, where $K_{s,j}$ is the partition coefficient or membrane/solution concentration ratio ($c^m_{s,i}/c_{s,i}$) (Romero et al., 2013); in these expressions 1:1 electrolytes ($|z_+| = |z_-| = 1$) and diluted solutions are assumed (concentrations instead of activities are used).

Fig. 8 shows the membrane potentials for the original and modified membranes as a function of the KCl concentration ratio; for comparison, membrane potentials for an ideal cation-exchanger membrane ($t_- = 1$) is also represented by a solid line. As can be observed, two different $\Delta\Phi_{mbr} - \ln(C_v/C_c)$ relationships, depending on C_v values, were obtained for the three membranes: (i) when C_v ranged between 0.002 M and 0.03 M (i.e. at low concentrations), the tendency of the membrane potential is similar to that shown by the ideal cation-exchanger (although it presents lower absolute values), due to the Donnan exclusion of the co-ions (anion exclusion) associated with the negative charge in the membranes; (ii) for $C_v > 0.03$ M, a change in the tendency of the membrane potential values was observed, which might be caused by the reduction of the electrical interactions at high solution concentrations (anion exclusion can be reduced and even neglected when $C \gg X_{ef}$), and the membrane potentials are mainly due to the diffusion of both counter-ions (t_+) and co-ions (t_-) into the membrane structure.

Effective membrane fixed charge (X_{ef}) can be obtained by the maximum concentration, C_{max}, and the slope of the straight-line at high C_v values associated with diffusion contribution (U) by: $C_{max} = 2X_{ef}U/(1-U^2)^{1/2}$ (Demish & Pusch, 1979). The cation transport number in the membrane was determined from the latter parameter by: $U = (RT/F)\cdot[1-2t_+]$. The values of X_{ef} and t_+ obtained for the three studied membranes are indicated in Table 5.

According to these results, inclusion of the SiQDs seems to slightly reduce (~20%) the weak electronegative character of the cellulosic support membrane (Gilbert et al., 1988; Van Oss, 1963), but their coverage by the dendrimer PAMAM-OH seems to work in the opposite way, reducing that effect. A comparison of K^+ transport number in the membranes with that of KCl in aqueous solution [$t^\circ_{K^+} = 0.49$ (Robinson & Stokes, 1955)] clearly shows the influence of the negative character of the membranes in the transport of the ions, with $t_+ > t_+^\circ$ in all cases. On the other hand, taking into account the correlation between the ion transport number ratio and ionic diffusion coefficients ratio, $t_+/t_- = D_+/D_-$ (Robinson & Stokes, 1955), this latter parameter was also determined and their values for the studied membranes are also indicated in Table 5. A comparison of D_{K^+}/D_{Cl^-} values in the membrane with those corresponding to aqueous solutions, $(D_{K^+}/D_{Cl^-})^\circ = 0.96$, clearly shows the effect of the three membranes in the diffusive transport across them, which might be of interest for their application in electrochemical devices.

Table 5
Effective fixed charge in the membrane, X_{ef}, cation transport number, t_{K^+}, and ionic diffusion coefficients ratio, D_{K^+}/D_{Cl^-}.

Membrane	X_{ef} (M)	t_{K^+}	D_{K^+}/D_{Cl^-}
Unmodified RC-4	−0.023	0.681	2.13
RC-4/SiQDs	−0.018	0.662	1.96
RC-4/SiQDs-PAMAM-OH	−0.020	0.671	2.04

4. Conclusions

In summary, luminescent biocompatible transparent membranes were obtained by the inclusion of SiQDs in the structure of a regenerated cellulose support membrane by dip coating. According to our results, the presence of the SiQDs in the cellulose structure improves the thermal stability and increases the conductivity of these new membranes in dry conditions, but partial attenuation of these effects by PAMAM-OH dendrimer coverage of the SiQDs was also observed. The stability of the cellulose SiQDs-modified membranes in aqueous environments was also established, with a reduction of 40% and 30% in the water uptake of the cellulosic RC-4 support when modified by SiQDs and SiQDs-PAMAM-OH, respectively, but SiQDs inclusion also affects the diffusive transport of cations (K^+). Consequently, these results support the possible manufacture of stable nano-engineered biocompatible membranes based on SiQDs nanoparticles with luminescent properties for application as dry samples or in flow devices.

Appendix A. Supplementary data

Supplementary data associated with this article can be found, in the online version, at doi:10.1016/j.carbpol.2016.05.097.

References

Algarra, M., Alonso, B., Casado, C. M., Esteves da Silva, J. C. G., & Benavente, J. (2013). Inclusion of thiol DAB dendrimer/CdSe quantum dots based in a membrane structure: Surface and bulk membrane modification. *Electrochimica Acta, 89*, 652–659.

Algarra, M., Campos, B. B., Aguiar, F. R., Rodríguez-Borges, J. E., & Esteves da Silva, J. C. G. (2012). Novel β-cyclodextrin modified CdTe quantum dots as fluorescence nanosensor for acetylsalicylic acid and metabolites. *Materials Science and Engineering C, 32*, 799–803.

Algarra, M., Campos, B. B., Radotić, K., Mutavdžić, D., Bandosz, T. J., Jiménez-Jiménez, J., et al. (2014). Luminescent carbon nanoparticles: Effects of chemical functionalization, and evaluation of Ag^+ sensing properties. *Journal of Materials Chemistry A, 2*, 8342–8351.

Algarra, M., Pérez-Martin, M., Cifuentes-Rueda, M., Jiménez-Jiménez, J., Esteves da Silva, J. C. G., Bandosz, T. J., et al. (2014). Carbon dots obtained using hydrothermal treatment of formaldehyde. Cell imaging in vitro. *Nanoscale, 6*, 9071–9077.

Algarra, M., Vázquez, M. I., Alonso, B., Casado, C. M., Casado, J., & Benavente, J. (2014). Characterization of an engineered cellulose based membrane by thiol dendrimer for heavy metals removal. *Chemical Engineering Journal, 253*, 472–477.

Arthanareeswaran, G., Thanikaivelan, P., Srinivasn, K., Mohan, D., & Rajendran, M. (2004). Synthesis, characterization and thermal studies on cellulose acetate membranes with additive. *European Polymer Journal*, *40*, 2153–2159.
Asaka, A. (1990). Dielectric properties of cellulose acetate reverse osmosis membranes in aqueous salt solutions. *Journal of Membrane Science*, *50*, 71–82.
Benavente, J. (2012). Use of impedance spectroscopy for characterization of membranes and the effect of different modifications. In N. Hilal, M. Khayet, & C. J. Wright (Eds.), *Membrane modification: Technology and applications* (pp. 21–40). Boca Raton, FL, USA: CRC Press.
Benavente, J., García, J. M., de la Campa, J. G., & de Abajo, J. (1996). Determination of some electrical parameters for two novel aliphatic-aromatic polyamide membranes. *Journal of Membrane Science*, *114*, 51–57.
Benavente, J., García, J. M., Riley, R., Lozano, A. E., & de Abajo, J. (2000). Sulfonated poly(ether ether sulfones): Characterization and study of dielectrical properties by impedance spectroscopy. *Journal of Membrane Science*, *175*, 43–52.
Campos, B. B., Algarra, M., Alonso, B., Casado, C. M., Jiménez-Jiménez, J., Rodríguez-Castellón, E., et al. (2015). Fluorescent chemosensor for pyridine based on N-doped carbon dots. *Talanta*, *144*, 862–867.
Chen, Y., & Liang, H. J. (2014). Applications of quantum dots with upconverting luminescence in bioimaging. *Photochemistry and Photobiology B*, *135*, 23–32.
Choi, M. K., Yang, Y., Kang, K., Kim, D. C., Choi, C., Park, C., et al. (2015). Wearable red-green-blue quantum dot light emitting diode array using high resolution intaglio transfer printing. *Nature Communications*, *6*, 7149
Chou, L. Y. T., & Chan, W. C. W. (2012). Nanotoxicology: No signs of illness. *Nature Nanotechnology*, *7*, 416–417.
Coutinho, F. M. B., Delpech, M. C., Alves, T. L., & Ferreira, A. A. (2003). Degradation profile of polyurethane and poly(urethane-urea) aqueous dispersions based on hydroxyterminated polybutadiene and different diisocyanates. *Polymer Degradation and Stability*, *81*, 19–27.
Demish, H. U., & Pusch, W. J. (1979). Electric and electrokinetic transport properties of homogeneous weak ion exchange membranes. *Journal of Colloid and Interface Science*, *69*, 247–270.
English, D. S., Pell, L. E., Yu, Z., Barbara, P. F., & Korgel, B. A. (2002). Size tunable visible luminescence from individual organic monolayer stabilized silicon nanocrystal quantum dots. *Nano Letters*, *2*, 681–685.
Erogbogbo, F., Yong, K. T., Roy, I., Xu, G., Prasad, P. N., & Swihart, M. T. (2008). Biocompatible luminescent silicon quantum dots for imaging of cancer cells. *ACS Nano*, *2*, 873–878.
Esteves da Silva, J. C. G. (2011). Carbon and silicon fluorescent nanomaterials. In M. M. Rahman (Ed.), *Nanomaterials*. Intech (chapter 10).
Gilbert, D. L., Okano, T., Miyata, T., & Kim, S. W. (1988). Molecular diffusion through collagen membranes. *International Journal of Pharmaceutics*, *47*, 79–86.
Goh, E. J., Kim, K. S., Kim, Y. R., Jung, H. S., Beack, S., Kong, W. H., et al. (2012). Bioimaging of hyaluronic acid derivatives using nanosized carbon dots. *Biomacromolecules*, *13*, 2554–2561.
Hod, I., González-Pedro, V., Tachan, Z., Fabregat-Santiago, F., Mora-Seró, I., Bisquert, J., et al. (2011). Dye versus quantum dots in sensitized solar cells: Participation of quantum dot absorber in the recombination process. *Journal of Physical Chemistry Letters*, *2*, 3032–3035.
Junka, K., Guo, J., Filpponen, I., Laine, J., & Rojas, O. J. (2014). Efficient intracellular delivery of molecules with high cell viability using nanosecond-pulsed laser-activated carbon nanoparticles. *Biomacromolecules*, *15*, 876–881.
Kůsová, K., Pelant, I., & Valenta, J. (2015). Bright trions in direct-bandgap silicon nanocrystals revealed by low-temperature single-nanocrystal spectroscopy. *Light: Science & Applications*, *4*, e336.1–8.
Lackowiz, J. R. (1999). *Principles of fluorescence spectroscopy* (2nd ed.). New York, NY: Springer.
Lakshminarayanaiah, N. (1969). *Transport phenomena in membranes*. New York, USA: Academic Press.
Li, L., Wu, G., Hong, T., Yin, Z., Sun, D., Abdel-Halim, E. S., et al. (2014). Graphene quantum dots as fluorescence probes for turn-off sensing of melamine in the presence of Hg^{2+}. *ACS Applied Materials & Interfaces*, *6*, 2858–2864.
Liu, J., Cao, L., LeCroy, G., Wang, P., Meziani, M. J., Dong, Y., et al. (2015). Carbon "quantum" dots for fluorescence labeling of cells. *ACS Applied Materials & Interfaces*, *7*, 19439–19445.
Loef, R., Houtepen, A. J., Talgorn, E., Schoonman, J., & Goossens, A. (2009). Study of electronic defects in CdSe quantum dots and their involvement in quantum dot solar cells. *Nano Letters*, *9*, 856–859.
Macdonals, J. R. (1987). *Impedance spectroscopy*. New York: Wiley.
Mansur, H. S., Mansur, A. A. P., Curti, E., & de Almeida, M. V. (2012). Bioconjugation of quantum-dots with chitosan and N,N,N-trimethyl chitosan. *Carbohydrate Polymers*, *90*, 189–196.
Meyer, K. H., & Sievers, J. F. (1936). La perméabilité des membranes I. Theorie de la perméabilité ionique. *Helvetica Chimica Acta*, *19*, 646–651.
Nann, T., & Skinner, W. M. (2011). Quantum dots for electro-optic devices. *ACS Nano*, *5*, 5291–5295.
Peláez, L., Vázquez, M. I., & Benavente, J. (2010). Interfacial and fouling effects on diffusional permeability across a composite ceramic membrane. *Ceramics International*, *36*, 797–801.
Pereira, J. M., Jr., Vasilopoulos, P., & Peeters, F. M. (2007). Tunable quantum dots in bilayer graphene. *Nano Letters*, *7*, 946–949.
Ramos, J. D., Milano, C., Romero, V., Escalera, S., Alba, M. C., Vázquez, M. I., et al. (2010). Water effect on physical–chemical and elastic parameters for a dense cellulose regenerated membrane: Transport of different aqueous electrolyte solutions. *Journal of Membrane Science*, *352*, 153–159.
Robinson, R. A., & Stokes, R. H. (1955). *Electrolyte solutions*. London: Butterworths Scientific.
Romero, V., Vázquez, M. I., & Benavente, J. (2013). Study of ionic and diffusive transport through a regenerated cellulose nanoporous membrane. *Journal of Membrane Science*, *433*, 152–159.
Shieh, J. J., & Chung, T. S. (1998). Effect of liquid–liquid demixing on the membrane morphology, gas permeation, thermal and mechanical properties of cellulose acetate hollow fibers. *Journal of Membrane Science*, *140*, 67–79.
Shiohara, A., Hanada, S., Prabakar, S., Fujioka, K., Lim, T. H., Yamamoto, et al. (2010). Chemical reactions on surface molecules attached to silicon quantum dots. *Journal of the American Chemical Society*, *132*, 248–253.
Tan, L., Wan, A., & Li, H. (2014). Synthesis of near-infrared quantum dots in cultured cancer cells. *ACS Applied Materials & Interfaces*, *6*, 18–23.
Teorell, T. (1956). Transport phenomena in membranes eighth Spiers Memorial Lecture. *Discussion Faraday Society*, *21*, 9–26.
Tomasulo, M., Yildiz, I., & Raymo, F. M. (2006). pH-sensitive quantum dots. *Journal of Physical Chemistry B*, *110*, 3853–3855.
Van Oss, C. J. (1963). Ultrafiltration membrane performance. *Science*, *139*, 1123–1124.
Vanacore, G. M., Hu, J., Liang, W., Bietti, S., Sanguinetti, S., & Zewail, A. H. (2014). Diffraction of quantum dots reveals nanoscale ultrafast energy localization. *Nano Letters*, *14*, 6148–6154.
Vázquez, M. I., Algarra, M., & Benavente, J. (2015). Modification of regenerated cellulose membrane based on thiol dendrimer. *Carbohydrate Polymers*, *131*, 273–279.
Zhao, Y., Riemersma, C., Pietra, F., Koole, R., Donegá, C. M., & Meijerink, A. (2012). High-temperature luminescence quenching of colloidal quantum dots. *ACS Nano*, *6*, 9058–9067.
Zhenhua, Y., Shiyan, C., Weili, H., Na, Y., Wen, Z., Cao, X., et al. (2012). Flexible luminescent CdSe/bacterial cellulose nano-composite membranes. *Carbohydrate Polymers*, *88*, 173–178.

9.2 Supplementary Data

Supporting Information

Characterization of cellulose membranes modified with luminescent silicon quantum dots nanoparticles

Bruno B. Campos , Lourdes Guelde, Manuel Algarra, M Isabel Vázquez, Joaquim C.G. Esteves da Silva and Juana Benavente

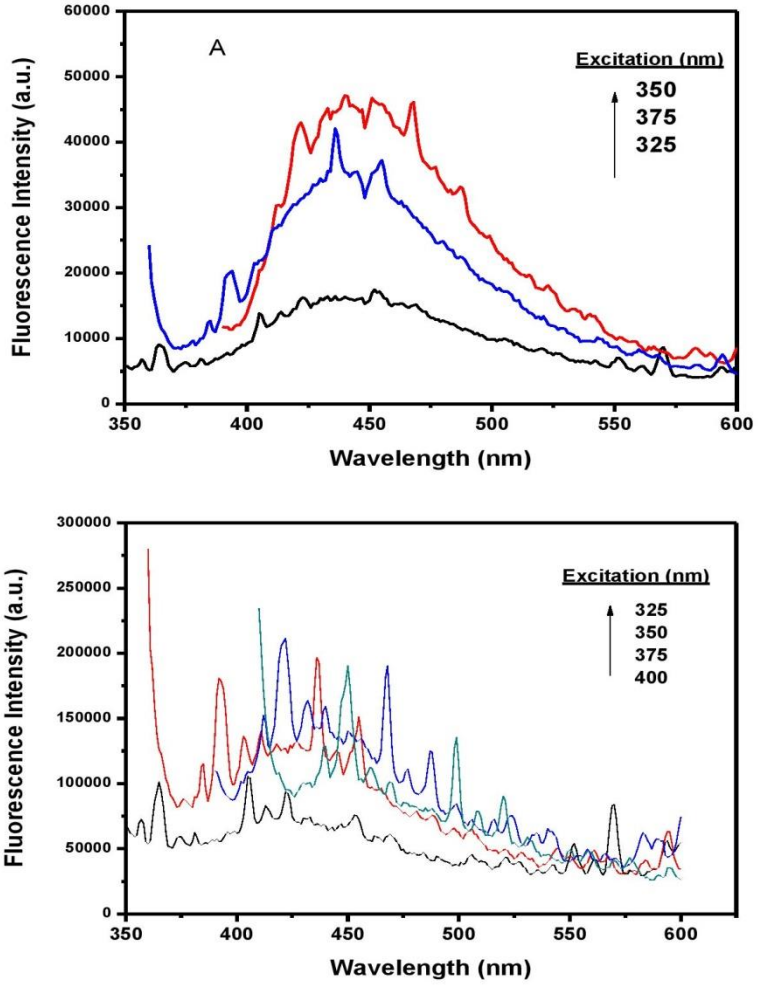

Figure 4. Fluorescence spectra of modified membranes after the treatment in KCl disolutions. **A**) SiQDs and B) SiQDs-PAMAM-OH nanoparticles.

Conclusions and Future Perspectives

The main goal of this thesis was the synthesis of fluorescent nanosensors without the classical QDs made of cadmium. This proposal was successfully achieved resulting in nanosensors made of Zn, Si and C. Other concerning issue which influences the bandgap emission and the selectivity of the nanosensor is the funcionalization. In spite of the title of the thesis contemplated the use of dendrimers, were used other organic molecules which presented interesting results. The quantum yield and the selectivity are parameters which were taking account in the framework of the experiments, as the examples of the works were was used different raw materials, different heating process, different dehydrating agents, doping agents and different passivation molecules. Resulting in optimized nanosensors with unique optical properties, exhibiting ratiometric bands and FRET phenomenon. These optimal conditions allowed the application of the nanosensors in real samples with excellent analytical results in the sensing of a wide range of molecules and atoms with harmful characteristics to human health and environment. The quality of the work done is reflected in the articles published in journals of high impact.

Assessing briefly each work, the novelty of ZnS:Mn@PAMAM-$OH_{G=3}$ fluorescent nanocomposite is based on the ratiometric response by the quenching of blue shift band and enhancing of red shift band in the presence of Cd^{2+} in water, which differed from the response of separately raw bands, and the reproducibility of the nanosensor was also founded on real water samples.

The fluorescent nanosensors based on carbon were focused on the synthesis of CQDs and the funcionalization with dendrimers and other molecules. Concerning to CQDs-MSA, this fluorescent nanocomposite presented the highest fluorescence intensity among the other CDs-ligands, and showed a pronounced quenching of the emission signal in the presence of Ag^{+}, suggesting a formation of a complex between the soft bases of thiol groups on the flourophore surface and the soft acid Ag^{+}.

The synthesis of CQDs doped with nitrogen under a basic mild, increased the QY comparing to un-doped CQDs. N-CQDs showed also sensitivity towards to pyridine in aqueous solutions by the enhancing of the fluorescent emission band proportionally to the pyridine concentration, suggesting an energy transfer process by the formation of a

complex based on the electrostactic attraction between the electronegative groups on the surface of N-CQDs and the positively charged pyridine.

The functionalization of CQDs with Vitamin B12 resulted on a fluorescent nanosensor with ratiometric properties based on a FRET phenomenon, because the negatively charged CQDs which transfer the excitons to the positively cobalt complexed in the center of VB12, promoting the appearance of 550 nm band. This ratiometric FRET-based nanosensor proved to be selective in the determination of CBFP pesticide even in solution and in real samples of soy sauce. The ratiometric response of this nanosensor is an advantage over others one band CQDs due to high selectivity and low interference of scattered light and energy fluctuation.

The previous functionalization of CQDs with PAMAM-NH_2 dendrimer increased on the surface the amine groups resulting in a blue shift emission and a fluorescence enhancement. The functionalization of the acid folic CQDs with a positively charged dendrimer raised the selectivity of the nanosensor in the sensing of chloroplatinate ions because it high negative charge.

Taking advantage of the studies previously done, was synthesized CQDs from activated carbon by chemical exfoliation and functionalized with PAMAM-NH_2. Once again, the addition of PAMAM-NH_2 leaded to a fluorescence enhancement and a blue shift emission. The particularity of this fluorescent nanocomposite is regarding to the selective ratiometric response in the determination of 4C-2,6DNA and the formation of a Meisenheimer complex, supported by the quenching profile which showed a formation of a complex.

The addition of PAMAM-$OH_{G=5}$ to SiQDs enhanced considerably the fluorescence signal as well as the recovery response in the detection of Cr(VI). In fact, the addition of PAMAM-$OH_{G=5}$ dendrimer caused a nitrogen enrichment and an increasing of negative dipoles attributed to amide and hydroxyl groups influencing the fluorescence intensity and the sensitivity, respectively. The reproducibility of the nanosensor was also proved to real electrochemical wastewater, certified materials and tanning effluent sample and after submitted to an inclusion in the structure of a regenerated cellulose support membrane by dip coating. Contrary of previous results, the bare inclusion of SiQDs showed better results comparing with SiQDs-PAMAM-OH in terms of conductivity and thermal stability of the membranes, in dry conditions. In aqueous solutions, the water uptake of the membrane is improved by SiQDs-PAMAM-OH due to the negatively charged dipoles originated by the amide and hydroxyl groups at the surface. These

results corroborates with the premise to manufacture a biocompatible membrane including the SiQDs-PAMAM-OH nanocomposite to detect in water samples the presence of Cr(VI).

In a general way, can be concluded that the bandgap emission of the QDs can be tuned taking account the functional groups presented in the carbon source, the dehydrating agent and the passivation molecules, including as well the heating process. The dendrimers showed a high functionality and interference also in the bandgap emission of the QDs and in the selective sensing of molecules and/or atoms. Presenting a disadvantage of the final production cost of the nanosensor which increases with the use of dendrimers, because they are a bit expensive in relation to the others passivation molecules used in this thesis. Besides, the inherent cytotoxicity to the positive surface dendrimers, as the PAMAM-NH_2. The future works should include the cytotoxicity studies of the fluorescent nanocomposites made and extend the inclusion of these nanocomposites on membranes in order to give a real application to real samples.

Errata

Page 26, Figure 1: **generation 4th** instead of ~~generation 5th~~

Page 38, Column 1, Line 21: Erase ~~and MAA~~

Page 38, Column 2, Line 23: **confirm** instead of ~~conform~~

Page 39, Column 2, Line 58:

$\alpha' = 1253.6 - KE(ZnLMM) + KE\left(Zn\ 2p_{3/2}\right)$ instead of ~~$\alpha' = 1253.6 + KE(ZnLMM) - KE\left(Zn\ 2p_{3/2}\right)$~~

Page 4, Table 2: **2.25x10^{-4} M** instead of ~~2.25x10^{-7} M~~

Page 49, Figure SI5: **wavenumber (cm^{-1})** instead of ~~wavelength (nm)~~

Page 53, Figure SI11: Add **at 595 nm (λ_{em})**

Page 60, Figure 1: **lactose** instead of ~~sacarose~~

Page 61, Column 2, Line 4: **CDs-MSA** instead of ~~CDs~~

Page 62, Figure 4: **(A) Fluorescence spectra of raw CDs (black); functionalized with MSA (red). (B) Influence of passivating agents in the CDs emission. (C) Emission spectra of CDs-MSA complexed with Ag^{+}** instead of ~~(A) Fluorescence spectra of raw CDs (black); functionalized with MSA (blue), MAA (brown) and MPA (red). (B) Influence of MSA concentration: (a) 0; (b) 0.02 M; (c) 0.05 M, (d) 0.01 M; (e) 0.2 M; (f) 0.4 M and (g) 0.6 M~~

Page 63, Column 2, Line 15: **CDs** instead of ~~QDs~~

Page 64, Figure 7: Add **(C) Modified Stern-Volmer representation of CDs-MSA complexed with Ag^{+}**

Page 66, Column 1, Line 4: **Fig. SI7A and B** instead of ~~Fig. S7A and B~~

Page 70, Figure SI.5: Add **Graphic representation of lifetime decays corresponding to CDs-MSA@Ag^{+} with different concentrations of Ag^{+}**

Page 73, Figure SI.7: Add **Emission spectra presenting the influence on the fluorescence intensity with the increasing of the Ag^{+} concentrations in the (B) presence and in the (A) absence of AgNPs**

Page 74: Add **Fig. SI.8**

Page 78, Column 2, Line 38: **H_2O** instead of ~~H_2O_2~~

Page 81, Figure 5: **(B) TG and (A) DSC curves** instead of ~~(A) TG and (B) DSC curves~~

Page 80, Column 2, Line 17: **0.48% and 3.85%** instead of ~~3.85% and 0.48%~~

Page 82, Column 1, Line 2: **biexponential** instead of ~~mono-exponential~~

Page 82, Figure 8: **(a) Initial taken as reference (0h); (b) 3h; (c) 3 days and (d) 5 days** instead of ~~(a) 5 days; (b) 3 days; (c) 3h and (d) Initial taken as reference (0h)~~.

Page 91, Abstract, Line 8: **linearly increased** instead of ~~linearly decreased~~

Page 92, Column 2, Line 26: **Ethyl Acetate** instead of ~~Acetonitrile~~

Page 92, Equation (1): $\boldsymbol{Ratio} = \frac{\left(\frac{I417}{I550}\right)_{\boldsymbol{CQDs@VitB12:CBFP-Interference}}}{\left(\frac{I417}{I550}\right)_{\boldsymbol{CQDs@VitB12:CBFP}}}$ instead of

$$Ratio = \frac{\left(I_{417}/I_{550}\right)_{CQDs@VitB_{12}\ -Interferen\ ce}}{\left(I_{417}/I_{550}\right)_{CQDs@VitB_{12}-\mathrm{CBFP}}}$$

Page 93, Column 1, Line 37: **The efficiency (1-($\tau_{CQDs@VB12}$/ τ_{CQDs})x100) of FRET process calculated using mean lifetime decays data is 48%** instead of ~~The efficiency ($\phi_{CQDs@VB12}/\phi_{CQDs}$) of the FRET process calculated using steady state fluorescence data is 61%~~

Page 95, Figure 2: **ATR-FTIR spectra of raw CQDs** instead of ~~ATR-FTIR spectra of the obtained CQDs@VB12after purification in ethyl acetate, compared with the raw CQDs~~

Page 96, Table 2: **CBFK** instead of ~~CBFP~~

Page 97, Column 1, Line 10: Erase ~~Table 3~~

Page 112, Figure 7: **$I_0/I=8381[(PtCl_6)^{2-}]+0.9664$** instead of ~~$I_0/I=11333[(PtCl_6)^{2-}]+0.9664$~~

Page 113, Column 1, Line 2: **2.2 µM** instead of ~~2.2 mM~~

Page 116: **Carbon dots on based folic acid coated with PAMAM dendrimer as platform for Pt(IV) detection** instead of ~~P-doped Carbon Dots Funcionalized with PAMAM Dendrimer for Pt (IV) Detection.~~

Page 116, Figure ESI 1: **PAMAM-NH_2 dendrimer (B)** instead of ~~PAMAM-NH_2 dendrimer~~

Page 123, Column 2, Line 56: Erase ~~Rhodamine~~

Page 123, Column 1, Line 16: **top-down** instead of ~~bottom-up~~.

Page 125, Column 1, Line 42: **of the C and N** instead of ~~of in the C and N~~

Page 125, Column 2, Line 1: **non radiative** instead of ~~radiative~~

Page 127, Figure 6.A: **CQDs@PAMAM-NH_2** instead of ~~GQDs@PAMAM-NH_2~~.

Page 130: **Figure S2A** instead of ~~Figure S3A~~

Page 131: **Figure S2B** instead of ~~Figure S3B~~

Page 132, Figure S4: Erase ~~and~~

Figure 132, Figure S3: **%Transmittance** instead of ~~%Reflectance~~

Page 139, Figure 3: Add **(C) Si 2p**

Page 138, Figure 1: **SiQDs** instead of ~~SiQDs@PAMAM-OH~~

Page 141, Table 2: **99.51** instead of ~~9951~~

Page 141, Column 1, Line 6: **2688.4 M^{-1}** instead of ~~2981.8 M^{-1}~~

Page 141, Column 1, Line 8: **56%** instead of ~~63%~~

Page 141, Column 1, Line 12: **2.03 µM** instead of ~~0.20 µM~~

Page 148, Column, 1 Line 48: **SU=[(W_w-W_d)/W_d)]x100** instead of ~~SU=[(W_w-W_d)/W_w)]x100~~

Page 149, Figure 2: **100000** instead of ~~60000~~

Page 150, Column 1, Line 24: **endothermic** instead of ~~exothermic~~

Page 151, Column 2, Line 8: **immersion** instead of ~~dip coating~~

Page 152, Table 4: **permittivity** instead of ~~constant~~

Page 152, Column 1, Line 33: **permittivity** instead of ~~constant~~

Page 152, Column 2, Line 4: **permittivity** instead of ~~constant~~

Page 153, Figure 8, Y Axis: **$\Delta\Phi_{mbr}$ (mV)** instead of ~~a_{mbr} (mV)~~.

Page 153, Figure 6, X Axis: **$\ln(C_v/C_c)$** instead of ~~$\ln(C_v/C)_c$~~

Page 153, Column 2, Line 18: **immersion** instead of ~~dip coating~~